

uOttawa

Optimizing the Cold Spray Process Performance: Influence of the Initial Substrate, Coating, and Particle Impact Temperatures

Thesis submitted to the University of Ottawa in partial fulfillment of the requirements for the Doctorate in Philosophy in Mechanical Engineering

Department of Mechanical Engineering

Faculty of Engineering

University of Ottawa

© Roberto Ortiz Fernandez, Ottawa, Canada, 2022

Abstract

It is well-known that the performance of the CS process is enhanced by increasing the process gas stagnation temperature, as this increases the gas velocity, and thus the particle velocity (kinetic energy). However, the influence of the initial substrate, coating, and particle impact temperatures on the CS process performance is still a topic that has barely been studied. This work focuses on establishing in a more systematic way how the initial substrate, coating, and particle impact temperatures affect the CS process performance by decoupling these three variables from the general spray parameters, namely the gas stagnation temperature. This decoupling is of crucial importance if one wants to be able to study the effect of each temperature and this approach has never been reported anywhere so far.

In this work, two feedstock powder materials are used: pure aluminum and Inconel 718. The substrate material selected is Ti-6Al-4V. Therefore, the observations provided in this thesis are valid for the deposition of aluminum-on-Ti-6Al-4V and Inconel718-on-Ti-6Al-4V. To increase and control the initial substrate and coating temperatures while ensuring proper decoupling of other spray parameters, an induction heating system is used with the CS process. To control the initial particle temperature, independently from the gas stagnation temperature, powder preheater units are used. The powder is fed in the diverging section of the nozzle to avoid the uncontrollable heating usually observed by feeding the powder in the converging section.

Single-particle impact testing and splat adhesion strength testing are carried out to evaluate the effect of the initial substrate temperature on individual particles. This is investigated using pure aluminum as the feedstock powder material. A finite element modeling is also carried out to complement the experimental results. The influence of the initial substrate temperature on the deposition process is quantified by measuring the

deposition efficiency and coating porosity values. Micro-hardness testing and adhesion strength testing are used to characterized the as-sprayed coating mechanical properties.

To study the influence of the coating temperature on the CS process performance, both powders, pure aluminum and Inconel 718, are used. The role of the coating temperature on the CS process is assessed by measuring the deposition efficiency and coating porosity values for the deposition of both powders. Micro-hardness, adhesion, and tensile strength measurements of the pure aluminum coatings is carried out. For the Inconel 718 coatings, only micro-hardness testing is conducted.

To characterize the influence of the particle impact temperature on the CS process, Inconel 718 is used. The particle impact temperature is predicted using a computational fluid dynamics model. Deposition efficiency, coating porosity values, and micro-hardness testing are used to characterize the influence of the particle impact temperature on the CS process.

The results in this thesis provide a path to optimize the CS process performance based on the influence of the initial substrate, coating, and particle impact temperatures. This work also demonstrates that other variables, such as particle impact velocity and feedstock powder material hardness, must also be considered to optimize the CS process performance through the use of different temperatures.

Acknowledgements

I would like to thank my supervisor Dr. Bertrand Jodoin for his support, guidance, and feedback to all my work. It has been an honor and pleasure to work together. I am sad that I won't be able to see the "Star Wars" mid term again. Doing my PhD under your supervision changed my life (literally), and for that I will always be grateful.

I would also like to thank Dr. Michel Nganbe for facilitating the use of his induction heating system. Without this equipment, this thesis wouldn't exist. I would also like to thank Dr. Richard Chromik for facilitating the use of his single-splat adhesion strength testing equipment. This machine was of paramount importance to further understand the role of the initial substrate temperature on the CS process.

This achievement is a collective effort form my family in Mexico and in Canada. Thanks to my mom for all her support through this journey. My achievements and the person I am today is all thanks to you. I like save the best for last. I would like to thank my wife Aurea. Thank you very much for proofreading ALL my work, thanks for your advice and tips to improve my writing skills, BUT more importantly for being my partner in this journey. I will always love you.

To God be the glory!

Table of Contents

Abstract ii

Acknowledgements iv

Table of Contents v

List of Tables x

List of Figures xi

List of Symbols xv

Subscripts and Superscripts xvii

Chapter 1 - Introduction 1

1.1 Background 1

1.2 Motivation and General Objectives 2

1.3 Outline of the Proposal 2

Chapter 2 - Literature Review 4

2.1 Cold Gas Dynamic Spray 4

2.1.1. Background 4

2.1.2. Process Overview 5

2.1.3. Gas Dynamics in Cold Spray 7

2.1.4. Fluid Flow in a Variable Area Nozzle 7

2.1.5. Stagnation Properties 8

2.1.6. Particle Acceleration 9

2.1.7. Critical Velocity 10

2.1.8. Bonding Mechanisms 11

2.1.9. Initial Substrate Temperature 14

2.1.10. Coating Temperature 17

2.1.11. Particle Impact Temperature 18

2.1.12. Dimensionless Parameter Eta (η) 20

2.1.13. The Role of the Particle/Substrate Strength on the CS Deposition Process 21

2.2 Substrate Material 22

2.2.1. Ti-6Al-4V (Ti64) 22

2.3 Feedstock Powder Materials 23

2.3.1. Aluminum 24

2.3.2. Inconel 718 (In718) 24

2.4 Induction Heating Process 24

2.4.1. Overview of Induction Heating 24

2.4.2. Material Properties Affecting the Induction Heating Process 29

2.4.3. Electrical Resistivity 29

2.4.4. Relative Magnetic Permeability 31

2.4.5. Spatial Configuration Phenomena Controlling the Eddy Current Density Distribution 32

2.4.5.1. Skin Effect 32

2.4.5.2. Proximity Effect 34

2.4.5.3. Electromagnetic Ring Effect 35

Chapter 3 - Description of the Research Objectives 37

3.1 Evaluate the Role of the Initial Substrate Temperature on the CS Deposition Process 39

3.1.1. Evaluate the Particle/Substrate Deformation Behavior and the Adhesion Strength at a Single-particle Level 39

3.1.2. Measure the Substrate Time-temperature History 41

3.1.3. Measure the Deposition Efficiency and Coating Thickness 41

3.1.4. Measure the Coating Mechanical Properties 41

3.2 Characterize the Influence of the Coating Temperature on the CS Process 42

3.2.1. Predict the Coating Eddy Current Density Distribution 43

3.2.2. Measure the Coating Time-temperature History 44

3.2.3. Measure the Deposition Efficiency and Coating Thickness 44

3.2.4. Measure the Coating Mechanical Properties 44

3.3 Assess the Importance of the Particle Impact Temperature on the Performance of the CS Process 45

3.3.1. Decouple the Initial Particle Temperature from the Gas Stagnation Temperature 46

3.3.2. Predict the Particle Impact Temperature 46

3.3.3. Characterize the CS Deposition Process as a Function of the Particle Impact Temperature 47

3.4 Enhance the CS Process Performance Based on the Findings of the Previous Objectives 47

Chapter 4 - Research methodology 48

4.1 Feedstock Material 48

4.1.1. Substrate Material 48

4.1.2. Feedstock Powder Material 50

4.2 Experimental Equipment 52

4.2.1. Cold Spray System 52

4.2.2. Powder Feeding 53

4.2.3. Controlled Powder Preheating Units 53

4.2.4. Induction Heating System 56

4.2.5. Sample Preparation for Optical and Scanning Electron Microscope 58

4.2.6. Scanning Electron Microscope 60

4.2.7. Micro-hardness Testing 60

4.2.8. Splat Adhesion Strength Testing 61

4.2.9. Particle Distribution 62

4.2.10. Tensile Strength 63

4.2.11. Adhesion Strength 63

4.2.12. Deposition Efficiency....63
4.2.13. Other Relevant Tools and Equipment....64
4.3 Numerical Model Structure....65
4.3.1. Electromagnetic Model: Eddy Current Density Distribution....65
4.3.2. Single-Particle Impact and Adhesion Strength Bonding Simulation....70
4.3.3. Computational Fluid Dynamic Model: Gas and particle interaction....74
Chapter 5 - Results....81
5.1 Induction Heating System Evaluation....82
5.2 Influence of the Substrate and Coating Temperatures on the CS process using the Soft-on-Hard Material Combination – Part I....87
5.3 Influence of the Substrate and Coating Temperatures on the CS process using the Soft-on-Hard Material Combination – Part II....104
5.4 Influence of the Initial Substrate Temperature on the CS process at the Single-Particle Level using the Soft-on-Hard Material Combination....119
5.5 Influence of the Coating and Particle Impact Temperatures On the CS Process using the Hard-on-Hard Material Combination....134
Chapter 6 - Conclusions and Future work....176
6.1 Conclusions....176
6.2 Future Work....179
References....181

List of Tables

Table 3.1 Research objectives, a brief description of the tasks done to fulfill the objectives, and the material combination used. 38

Table 4.1 AC source boundary conditions 68

Table 4.2 Material properties of the different materials used in the electromagnetic models [73,76,99]. 69

Table 5.1 Objectives and specific section addressing each objectives 81

List of Figures

Figure 2.1 Comparison of the particle velocity and gas velocity for various thermal spray processes Republished from [4] with permission of Springer; permission conveyed through Copyright Clearance Center, Inc. 5

Figure 2.2 Schematic of a typical cold spray process. Republished from [17] with permission of Springer; permission conveyed through Copyright Clearance Center, Inc. 6

Figure 2.3 Representation of differences in flow behavior for subsonic and supersonic flows in a variable area nozzle. Ma is the Mach number. Republished from [19] with permission of John Wiley & Sons; permission conveyed through Copyright Clearance Center, Inc. 8

Figure 2.4 Experimentally determined critical velocities for various material. Republished from [24] with permission of Springer; permission conveyed through Copyright Clearance Center, Inc. 11

Figure 2.5 Mechanical bonding at the interface between a soft copper coating (top) and a hard steel substrate (bottom). Adapted [38] with permission of Springer; permission conveyed through Copyright Clearance Center, Inc. 12

Figure 2.6 Schematic of the bonding process in the cold welding process. Adapted from [46] with permission of Springer; permission conveyed through Copyright Clearance Center, Inc. 13

Figure 2.7 Pure aluminum particle deposited on a Ti-6Al-4V substrate. a) cross-sectional image of an individual particle bonded to the substrate, b) top view of a particle deposited onto the substrate, and c) evidence of a metallic bond Black arrows in a) indicate partial contact between the substrate and the particle. Adapted from [42] with permission of Springer; permission conveyed through Copyright Clearance Center, Inc. 14

Figure 2.8 Classified four cases of particle impact on substrate: (a) soft/soft (Al particle onto Al substrate, (b) hard/hard (Ti particle onto Ti substrate, (c) soft/hard (Al particle onto mild steel substrate), (d) hard/soft (Ti particle onto Al substrate). Reprinted from [41] with permission of Elsevier; permission conveyed through Copyright Clearance Center, Inc.. 22

Figure 2.9 Powder sprayability as a function of the propellant gas velocities and mechanical properties. 23

Figure 2.10 Schematic of the induction heating process. Adapted from [110]. 25

Figure 2.11 Classification of materials based on their electrical resistivity. 30

Figure 2.12 a) Bar positioned in the middle of a multiturn coil, b) Eddy current density distribution along the radius of the cylinder presented in a) at two different frequencies, and c) current and power density profiles owing to skin effect. Adapted from [104] with permission of Taylor and Francis; permission conveyed through Copyright Clearance Center, Inc. 33

Figure 2.13 a) Proximity effect current distribution within two wires having opposite current directions, and b) proximity effect in single-turn coil with nonsymmetrical positioning of the workpiece. Adapted from [104] with permission of Taylor and Francis; permission conveyed through Copyright Clearance Center, Inc. 34

Figure 2.14 a) Ring effect in a round conductor, and b) eddy current distribution on a cylindrical geometry positioned in the middle of a multiturn coil due to the ring effect. Adapted from [104] with permission of Taylor and Francis; permission conveyed through Copyright Clearance Center, Inc. 36

Figure 4.1 Particle/substrate interfacial deformation for a) the soft-on-hard material and b) hard material deformation under significant thermal softening upon impact. Reprinted

from [41] with permission of Elsevier; permission conveyed through Copyright Clearance Center, Inc. 49

Figure 4.2 Feedstock powder materials used in this work. a) Pure aluminum and in b) Inconel 718. 51

Figure 4.3 SST-EPX cold spray system. a) Overview of the of the spraying system, and b) interior of the safety cabinet. 52

Figure 4.4 Downstream injection configurations using: a) no powder preheating, b) a commercially available controlled powder preheating unit, and c) an in-house controlled powder preheating unit. The insulation around the mixing coil in c) has been removed to provide a detailed perspective of the in-house controlled powder preheating unit. 55

Figure 4.5 In-house powder preheater. Hot and cold gases are brought together and mixed inside a stainless steel coil. The insulation around the mixing coil has been removed to provide a detailed perspective of the in-house controlled powder preheating unit. .. 56

Figure 4.6 Induction heating system setup. In a) Induction heating system positioned behind the spray cabinet, in b) perforated holes that allow the copper coil connection to the induction heating system located behind the spray cabinet, in c) the copper coil covered in epoxy resin, in d) copper coil inside the spray cabinet, in e) zoomed-in image of the copper coil after the spraying process. Cross- sectional schematic view of the rectangular and cylindrical substrate configurations in f) and g), respectively. 58

Figure 4.7 a) Secotom-10 precision cut-off saw, b) LaboPress-3 mounting machine, c) TegraPol-31 grinding and polishing machine and d) VHX-2000E optical microscope. 59

Figure 4.8 EVO-10MA scanning electron microscope. 60

Figure 4.9 Micro-combi scratch tester. In a) overall setup of the equipment, in b) zoom-in image of the testing zone, in c) light-optical microscope objective, and in d) the output of the light-optical microscope objective..... 62

Figure 4.10 Calibration of the RAYGPRSF non-contact infrared thermometer for a Ti64 substrate in the 25 to 300 °C range. 65

Figure 4.11 Computer aided designed geometries used to predict the eddy current density distribution within a 100 µm coating. The copper coil used in the experimental section of this work is presented in a) and in b) the CAD copper coil used for the electromagnetic simulations. Substrates with a 100 µm coating on top of the rectangular and cylindrical substrates are presented in c) and d), respectively..... 67

Figure 4.12 Ansys Maxwell frequency-dependent solution steps. 70

Figure 4.13 Illustration of the Coupled algorithm approach used by Ansys Fluent to solve the governing flow equations. 79

Figure 5.1 Finite element electromagnetic model of the Ti64 substrates and 100 µm coating. Isometric view a) the rectangular substrate configuration, and in b) of the cylindrical substrate configuration. c) to f) eddy current density distribution in a 100 µm coating. In c) and d), the coating is modeled as pure aluminum, while in e) and f) In718 is used as the coating material. The IH parameters were 58 A and 192 kHz. All the values are shown at the peak values of the sinusoidal AC source. 84

Figure 5.2 Finite element electromagnetic model of the Ti64 substrates and 100 µm pure aluminum coating using different IH parameters. 86

List of Symbols

Nomenclature

Symbol	Description	Units
c	Speed of sound	m/s
K_S	Bulk modulus	N/m
ρ	Density	kg/m^3
P	Pressure	Pa
C_p	Gas specific heat at constant pressure	kJ/kg·K
C_v	Gas specific heat at constant volume	kJ/kg·K
γ	Specific heat ratio	(-)
R	Gas constant	J/kg·K
T	Temperature	K
M	Mach number	(-)
V, $\vec{v}$	Velocity	m/s
A	Cross-sectional flow area of a nozzle	m^2
F	Force	N
C_D	Drag force coefficient	(-)
$A_{projected}$	Projected area	m^2
a	Acceleration	m/s^2
m	Mass	kg
V_{crit}	Critical velocity	m/s
k1	particle size-dependent dimensionless fitting parameter	(-)
$T_{melting}$	Melting temperature	K
σ_y	Yield Strength	MPa
V_{imp}	Particle impact velocity	m/s
η	Eta	(-)
μ	Magnetic permeability	H/m
ε	Electric permitivity	F/m
r	Electrical resistivity	Ω·m
D	Electric displacement field	C/m^2
J	Electric current density	A/m^2
H	Magnetic field	A/m
E	Electric field	V/m
$\varphi_{freecharge}$	Volume free electric charge density	C/m^3
B	Magnetic flux density	T
σ	Electrical conductivity	S/m

j	Complex part of the current	(-)
w	Angular frequency	rads/s
r	Electrical resistivity	Ω·m
δ	Penetration depth	m
f	Frequency	Hz
y	Radial distance	m
L_{small}	Smallest element dimension	μm
W	Dilatation wave speed	m/s
E_{Young}	Young Modulus	MPa
E_m	Internal energy per unit mass	J/kg
p_{bv}	Pressure due to bulk viscosity	Pa
$\dot{e}$	Deviatoric part of strain rate	1/s
S	Deviatoric stress tensor	GPa
$\dot{Q}$	Heat transfer rate per unit mas	J/kg
p_H	Hugoniot pressure	Pa
Γ	Mie- Grüneisen constant	(-)
E_H	Specific energy per unit mass	J/kg
s	Hugoniot slope	(-)
G_e	Elastic shear modulus	GPa
e^{dev}	Deviatoric elastic strain	μm/μm
A,B,C	Johnson-Cook material parameters	A and B = MPa
$\dot{\varepsilon}$	Strain rate	1/s
$\bar{\varepsilon}$	Equivalent strain	μm/μm
n	Strain rate hardening constant	(-)
m	Thermal softening power coefficient	(-)
M_w	Molecular weight	g/mol
S_m	Mass added	kg
$\vec{F}$	External Body Forces vector	N
$\vec{g}$	Gravity vector	m/s^2
μ	Dynamic viscosity	m^2/s
$\vec{J}_j$	Diffusion flux vector	Atoms $/m^2 \cdot s$
k	Thermal conductivity	W/m·K
P_r	Prandtl Number	(-)
$\bar{\bar{\tau}}$	Viscous stress tensor	Pa
S_h	Heat sources	$kg/m \cdot s^3$
En	Energy	J/kg
h_s	Sensible Enthalpy	J/kg

Y_j	Mass fraction of the species	(-)
h_j	Enthalpy of the species	J/kg
Br	Brinkman Number	(-)
u_i	Gas velocity component in i-direction	m/s
x_i	Cartesian coordinate in the i-direction	m
K	Turbulent Kinetic Energy	m^2/s^3
ϵ	Turbulent dissipation rate	m^2/s^2
G_K	Generation of turbulent kinetic energy due to mean velocity gradients	$kg/m{\cdot}s^3$
G_b	Generation of turbulent kinetic energy due to buoyancy	$kg/m{\cdot}s^3$
Y_M	Contribution of the fluctuating dilatation in compressible turbulence to the overall dissipation rate	$kg/m{\cdot}s^3$
S_K	User defined source term	(-)
α_K	Inverse effect Prandtl number for K	(-)
α_ϵ	Inverse effect Prandtl number for ϵ	(-)
$C_{1\epsilon}, C_{2\epsilon}, C_{3\epsilon}$	Model constants	(-)
C_{vx}	Yakhot's formula constant	(-)
S_ϵ	User defined source term	(-)

Subscripts and Superscripts

gas Gas property

0 Flow stagnation properties

B Back pressure or chamber discharge conditions

Drag Drag

particle Particle conditions

r Relative

D Displaced current

Eddy Eddy current

Total Total

S source

Vac Vacuum

y	Distance *y* from the surface
Surf	Surface
Hot	Hot
Cold	Cold
Mixed	Mixed
n	Normal
t	Tangential
ref	Reference
Plastic	Plastic
JCref	Reference to obtain Johnson-Cook material constants
op	Operating pressure (Atmospheric)
local	Local static pressure
eff	Effective

Chapter 1 - Introduction

1.1 Background

Cold Gas Dynamic Spray (CGDS), or Cold Spray (CS), is one of the most recent thermal spray processes developed for the production of coatings [1]. In CS, the feedstock material is injected in the spray gun in micron-size powder form. These powders are accelerated to high impact velocities by a supersonic gas stream inside a converging-diverging nozzle. Once the particles exit the nozzle and impact the substrate, approximately 90% of the their kinetic energy is converted into thermal energy, while the rest is transformed into elastic and plastic deformation at high strain rates [1–4]. Bonding can take place once the particles and the substrate enter into intimate contact due to high interfacial pressure. Intimate contact is assumed to be reached when the particle/substrate respective native surface oxides are broken and removed after the impact [1,3–5].

The CS process is characterized by its high deposition rate in comparison to other thermal spray processes. Another benefit is that melting of the powder during the CS deposition is avoided. In consequence, phase transformation of the powder is by-passed and low-oxide content coatings are produced. The CS process also presents a few disadvantages in comparison to other thermal spray processes. For example, the as-sprayed coatings exhibit limited ductility and best results are obtained when ductile powder materials are sprayed.

Several studies have demonstrated that particles are required to impact the substrate above a critical velocity before they can deposit and form a coating. This critical velocity is a material dependent parameter and it is also a function of the particle size. The critical velocity tends to increase as the hardness and yield strength of the material increases because plastic deformation is limited. Additionally, the critical velocity reaches higher values as the particle size decreases. This is caused by the limited plastic deformation,

consequence of the relatively low particle impact temperatures (small particles lose more heat in comparison to large particles), and due to the relatively small grain size of the feedstock powder. Conversely, the critical velocity tends to be lower for large particles and for ductile materials. Reducing the critical velocity for deposition helps optimize the CS process performance because a better coating quality can be achieved. It has been suggested that the initial substrate, coating, and particle impact temperatures might also have an influence on the critical velocity. However, results in the literature are contradictory when the effect of substrate and particle impact temperature on the CS process performance are reported, while in-depth studies evaluating the role of the coating temperature are scarce.

1.2 Motivation and General Objectives

This work focuses on establishing how the initial substrate, coating, and particle impact temperatures affect the CS process performance by trying to decouple these three variables from the general spray parameters, in particular the gas stagnation temperature. To systematically investigate the effect of the initial substrate, coating, and particle impact temperatures on the CS deposition process, the following objectives are set:

1. Evaluate the role of the initial substrate temperature on the CS process.
2. Characterize the influence of the coating temperature on the CS process.
3. Assess the importance of the particle impact temperature on the CS process.
4. Enhance the CS process performance based on the findings of the previous objectives.

1.3 Outline of the Proposal

The thesis is organized in six chapters. The first chapter is dedicated to set the relevant background information for this study. It also includes the motivation and the main objectives of this work. The second chapter provides a review of the relevant literature

for this research project. A description of the CS process as a coating technique is presented. Several other topics are also presented, such as a general overview of the process, the critical velocity criterion, the adhesion mechanisms, the soft-on-hard and the hard-on-hard material combinations, among other topics. Lastly a general overview of the induction heating (IH) process is presented.

The third chapter describes in detail the main objectives of this research work. The main goal of this chapter is to provide a clear path to demonstrate the influence of the initial substrate, coating, and particle impact temperatures on the CS process performance. To do that, the soft-on-hard and the hard-on-hard material combinations are used. The fourth chapter is dedicated to provide a detailed methodology of the research approach to follow in this study. This chapter also describes the equipment and the materials that are used. The testing plans, characterization, analysis and measurement apparatus are also presented in this chapter. The fifth chapter provides the reader with three peer-reviewed studies and one manuscript submitted to the Journal of Thermal Spray Technology (currently under review). These studies address the objectives presented in Chapter 3. The sixth and final chapter summarizes and highlights the importance of the initial substrate, coating and particle impact temperatures on the CS process. It also provides numerous suggestions of future work that could be done towards the application of these temperatures to the CS additive manufacturing subdomain.

Chapter 2 - Literature Review

2.1 Cold Gas Dynamic Spray

2.1.1. Background

The CS process was first conceptualized more than 120 years ago in 1900 by Thurston [6] as a metallic blasting process. Almost 60 years after its first conceptualization, Rocheville introduced the use of a nozzle to the process in order to produce a supersonic flow [7]. Unfortunately, at that time, the mainstream use of the process as a coating method did not materialize as a coating deposition technique [2]. In the mid-80's the CS process was re-discovered at the Institute of Theoretical and Applied Mechanics of the Siberian Division of the Russian Academy of Science in Novosibirsk [2]. However, it was not until 1995 that patents were granted in the United States and Europe to Alkhimov et al. for the cold spray process.

The CS is characterized by its low gas temperatures and fast particle velocities compared to other thermal spray processes [4], as presented in Figure 2.1. While many thermal spray processes require melting to produce a coating, the CS process is classified as a solid-state deposition process [4]. One of the many advantages that CS offers over other thermal spray processes is the possibility of controlling the microstructure of the resulting deposit, as melting and uneven solidification rates of the powder are circumvented[1,4]. The resulting microstructure of the deposits will have a strong resemblance to the original feedstock powder material. Because CS relies on the plastic deformation of the particles to build up a coating [1,2,4], the variety of materials that can be sprayed using this technique is limited. For this reason, CS works almost exclusively with metals, and works best with ductile materials although research in the past decades have allowed to extend the technique to hard materials, cermets, polymers and ceramics, under limited conditions, with research work still underway [8–11].

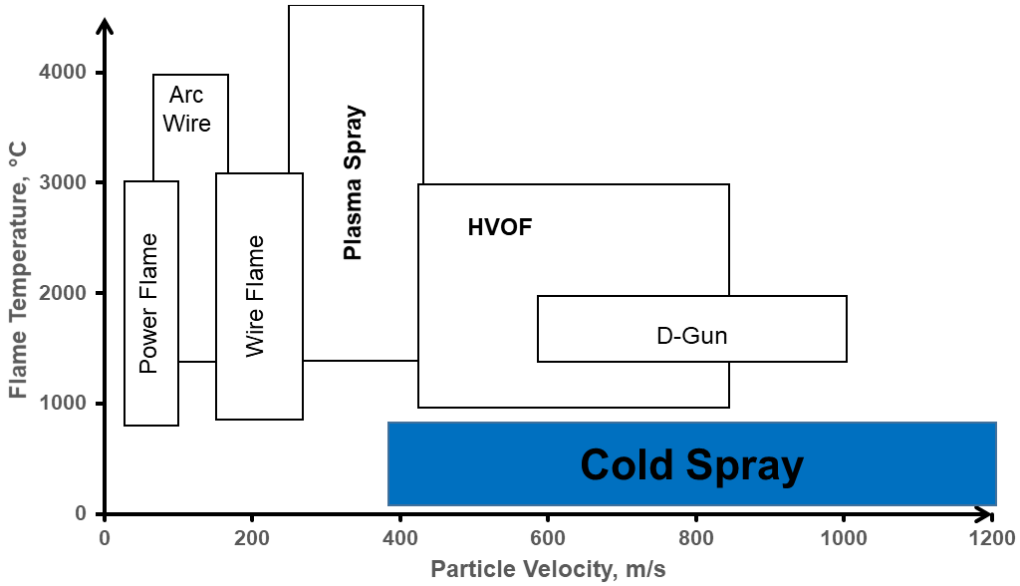


Figure 2.1 Comparison of the particle velocity and gas velocity for various thermal spray processes Republished from [4] with permission of Springer; permission conveyed through Copyright Clearance Center, Inc.

Since the mid-80's the number of CS studies have grown exponentially. These vary from fundamental principles of the CS process to industrial applications [12,13]. Even though the CS process appears to be simple, the physics behind the deposition process are extremely complex. This is because many different fields and areas are involved, such as gas dynamics, heat transfer, solid mechanics, and surface and materials science. Thus, a multidisciplinary endeavor is required to gain a full understanding of the physics behind the deposition and bonding mechanisms in the CS process.

2.1.2. Process Overview

A schematic of the CS process is presented in Figure 2.2. The process starts with a high-pressure source of gas, which usually supplies helium or nitrogen. This gas is often called propellant gas, because it is used to accelerate the feedstock powder material [1,2,4]. The high-pressure gas flow is then passed through a heater, which increases its temperature to provide thermal energy to the propellant gas. Commercial CS systems can increase the gas temperature up to 1100 °C, but temperatures ranging from 500 to 1000 °C are more

commonly used. Once the gas is heated, it is injected into a converging-diverging (de-Laval) nozzle where it expands and accelerates to supersonic speeds (ranging from 400 to 1200 m/s) [1,2,4], as a result of the transformation of thermal energy (enthalpy) of the gas into kinetic energy [1,4]. The gas velocity and temperature at the nozzle exit are a function of the nozzle geometry, nature of the gas, and gas stagnation conditions (pressure and temperature) [1,4,13–16].

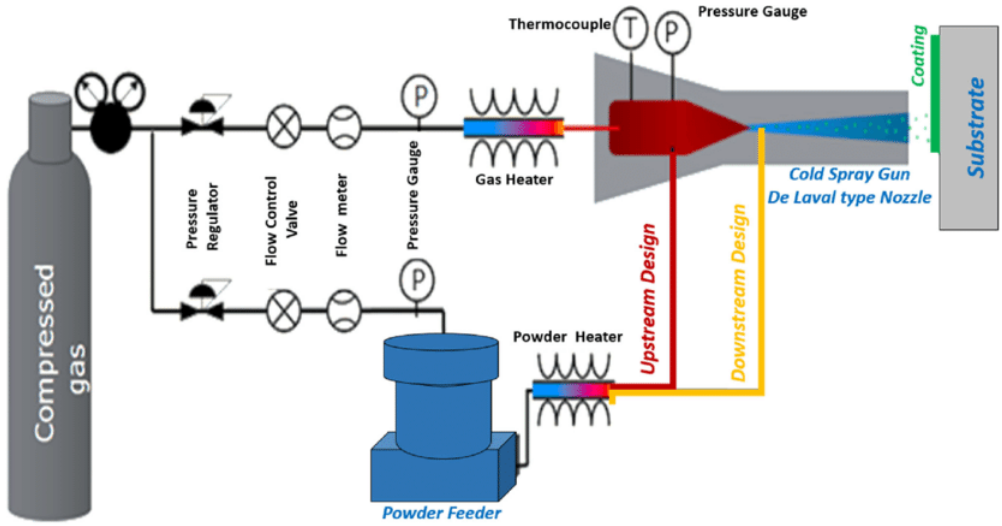


Figure 2.2 Schematic of a typical cold spray process. Republished from [17] with permission of Springer; permission conveyed through Copyright Clearance Center, Inc.

Simultaneously, a second gas flow, also commonly referred to as carrier flow, is fed into the powder feeder, as shown in Figure 2.2. The carrier flow is used to fluidize the powder and feed it into the nozzle. Powders can be fed at the converging (upstream or hot zone) or diverging (downstream or cold zone) regions of the nozzle [18]. After being fed inside the nozzle and accelerated by the propellant gas, the particles will exit and impact the substrate. Upon their impact, the particles will plastically deform, and they may adhere to the substrate surface and form a coating if conditions for bonding are met [12]. To fully understand the bonding conditions and the subsequent building up process, the critical velocity criterion and the bonding mechanisms are presented.

2.1.3. Gas Dynamics in Cold Spray

To understand this process, a gas dynamics analysis using basic concepts of this field will be carried out in this section. The importance of compressibility effects in fluid flow calculations depend on the magnitude of the flow velocity with respect to the speed of sound. In gas dynamics, the Mach number is used to quantify the compressibility of the gas and it is defined by Eq. 2.1.

$$M = \frac{V}{c} = \frac{V}{\sqrt{\gamma RT}} \quad \text{Eq. 2.1}$$

A flow with M < *0.3* is considered incompressible. Therefore, there are no important changes in density with respect of pressure. If $0.3 < M < 1$, the flow is considered a subsonic flow. In this case, compressibility effects may be important. Finally, a supersonic flow ($M > 1$) is said to be present when the fluid velocities are larger than the speed of sound. For this flow conditions, compressibility effects are significant.

2.1.4. Fluid Flow in a Variable Area Nozzle

In CS, the gas reaches supersonic velocities using a converging-diverging nozzle. To understand the effect of a variable area nozzle on an isentropic flow, three governing equations are considered: mass conservation, energy conservation and the second law of thermodynamics. From these three, it is found that:

$$\frac{dV}{V}(1 - M^2) = -\frac{dA}{A} \quad \text{Eq. 2.2}$$

Equation 2.2 shows the relationship between changes in the flow velocity (dV) and the cross sectional area (dA). Additionally, this equation outlines the importance of the Mach number, as it presents the dependence of the flow behavior in a variable area nozzle as a function of the compressibility of the gas. A subsonic flow (M<1) result in dV and dA to have the opposite sign. This produces the well-known behavior for incompressible flows,

in which the velocity increases as the cross-sectional area is reduced. On the other hand, if the M >1 the flow will accelerate in an increasing variable area section. Figure 2.3 presents a summary of the different flow behaviors that can be inferred from Eq. 2.2.

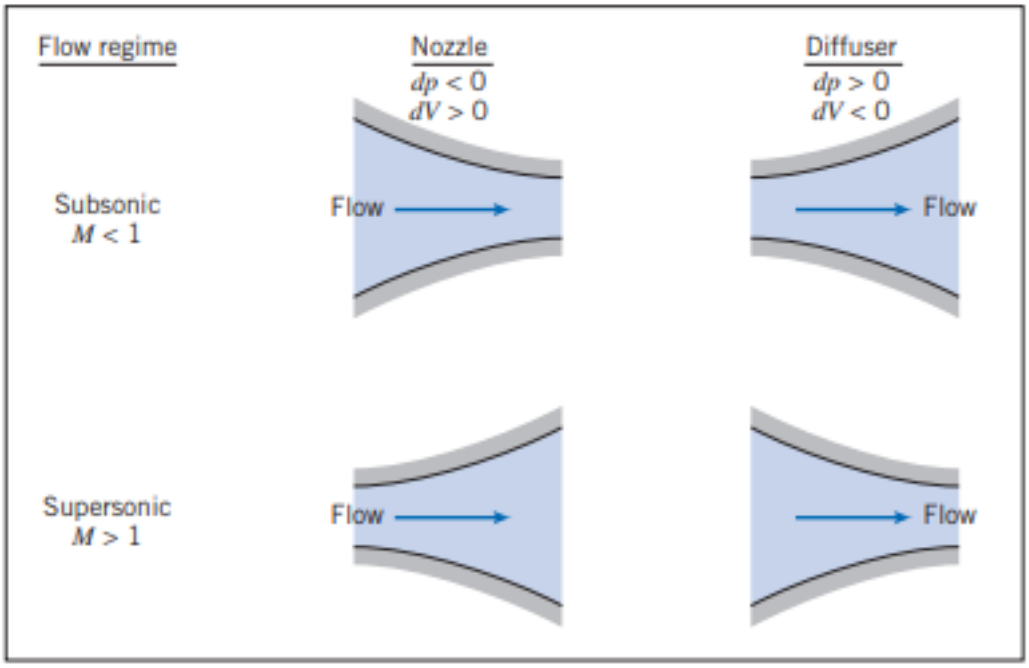


Figure 2.3 Representation of differences in flow behavior for subsonic and supersonic flows in a variable area nozzle. Ma is the Mach number. Republished from [19] with permission of John Wiley & Sons; permission conveyed through Copyright Clearance Center, Inc.

2.1.5. Stagnation Properties

In gas dynamics, the stagnation properties represent the flow conditions when the gas is decelerated isentropically to zero velocity. When a gas is expanded isentropically from its stagnation state through a de-Laval nozzle, the energy is transformed from pressure and thermal energy (the enthalpy of the stagnation state) into kinetic energy. This produces a decrease in temperature and pressure, or enthalpy, as the expansion occurs.

If the gas is assumed to be calorically perfect and the expansion is isentropic, the temperature and pressure at any point of the nozzle are given by Eq. 2.3 and Eq. 2.4, respectively. The subscript $_0$ refers to the stagnation state while the other side of the equations refers to the enthalpy and velocity at any point of the nozzle.

$$\frac{T_0}{T} = 1 + \frac{\gamma-1}{2}M^2 \quad \text{Eq. 2.3}$$

And

$$\frac{P_0}{P} = \left(1 + \frac{\gamma-1}{2}M^2\right)^{\frac{\gamma}{\gamma-1}} \quad \text{Eq. 2.4}$$

The previous equations allow determining the flow conditions at any point in the nozzle.

2.1.6. Particle Acceleration

Particles traveling inside the nozzle are accelerated as a result of the drag force that they experience due to their interaction with the supersonic flow. The drag force (F_D) exerted on the particles can be expressed as follows:

$$F_D = \frac{1}{2}C_D A_{projected}\,\rho_{gas}\left(V - V_p\right)^2 \quad \text{Eq. 2.5}$$

in Eq. 2.5, C_D represents the drag coefficient, $A_{projected}$ is the projected area of a particle, ρ is the gas density and (V-V_p) represents the relative velocity of the flow with respect of the particle. If Eq. 2.5 is combined with Newton's law, then the particle acceleration ($a_{particle}$) can be written as:

$$a_{particle} = \frac{1}{2}C_D A_{projected}\frac{\rho_{gas}}{m_{particle}}(V - V_P)^2 \quad \text{Eq. 2.6}$$

Where $m_{particle}$ is the mass of the particle. From Eq. 2.6 it can be seen that the magnitude of the particle acceleration is a function of the relative gas velocity. It can also be seen that the drag coefficient will have an influence on the particle velocity. As such, significant differences in the particle velocities are expected between particles having a spherical

morphology in comparison with irregular shaped ones, as reported by Jodoin et al [20]. The ratio $A_{projected}$ /$m_{particle}$ hides some features related to the particle size and material. Assuming a spherical particle, the projected area is a function of its diameter squared, while the mass is a function of its volume (diameter cubed). Therefore, the particle acceleration is inversely proportional to the particle diameter. Thus, larger particle will travel at lower velocities in comparison to small as the latter are easier to accelerate. Lastly, the gas density plays a role as the particle acceleration will be proportional to the gas density, which in turn is a function of the gas nature and stagnation properties.

2.1.7. Critical Velocity

Feedstock powders used in the CS process are characterized by a size distribution. Therefore, a particle velocity distribution is obtained at the nozzle exit. This distribution is a function of the particle size and the particle history inside and outside the nozzle prior to impact with the substrate. If the particles have a sufficiently high impact velocity, they will elastically and plastically deform upon impact, bond, and form a coating. Otherwise they will bounce off the substrate surface, or even erode it in some cases. To set a clear distinction between the two previous cases, a criterion has been suggested and confirmed by different studies: the critical velocity [14,15,21–23].

The critical velocity (V_{crit}) is mostly a function of the powder material, as presented on Figure 2.4. For example, it has also been shown that crystallographic lattice structures, stiffness, density, melting temperature, and yield strength have an impact on the critical velocity [15,24,25]. Other factors that have been suggested that could possibly influence the critical velocity are particle impact temperature [16,18], particle size [14,15,18,26], substrate material [27–29], substrate temperature [30,31], and native oxide layer [32–35]. However, studies focused on the influence of the substrate and particle impact temperature have reported contradictory results and conclusions cannot be generalized.

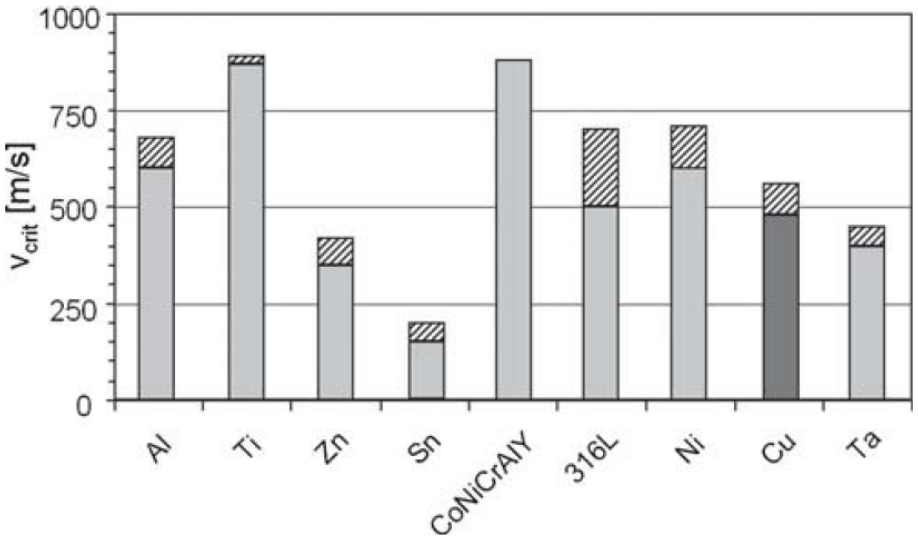


Figure 2.4 Experimentally determined critical velocities for various material. Republished from [24] with permission of Springer; permission conveyed through Copyright Clearance Center, Inc.

In the following section, the bonding mechanisms that occur when enough plastic deformation is reached are discussed.

2.1.8. Bonding Mechanisms

Once the particles exit the nozzle, they can potentially adhere to the substrate if they exceed their critical velocity for deposition [12,15,22]. The adhesion mechanisms can be classified into metallic and mechanical bonding [36,37]. Mechanical bonding, or anchoring, is the type of bonding in which the particles mechanically interlock with the substrate [36,38–40], as shown on Figure 2.5. It is believed that the creation of anchor points is due to the extremely high levels of deformation that take place at the particle/substrate interface during the impact process [22,23,40]. The natural occurrence of mechanical interlocking between the powder and the substrate is commonly observed when these two have a similar strength or when a hard material is sprayed on a soft substrate [37,40,41]. For the soft-on-hard material combination, the natural occurrence of

these anchor points is not expected due to hardness dissimilarity between the two metals [36,38,39,41–43]. Studies have shown that the lack of formation of anchor points can potentially be addressed by preparing the substrate surface before the CS process [36–39]. By doing so, artificial anchor points are created on the surface which in turn increase the mechanical contribution on the overall adhesion strength of the coating [36,38–40], as presented in Figure 2.5

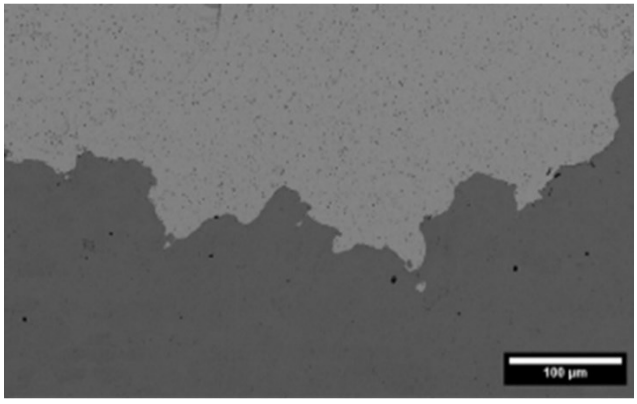


Figure 2.5 Mechanical bonding at the interface between a soft copper coating (top) and a hard steel substrate (bottom). Adapted [38] with permission of Springer; permission conveyed through Copyright Clearance Center, Inc.

Metallic bonding is of the same nature as the one found in bulk metallic materials [12,22,36,37,42]. However, the difference is that for the CS process the electrons are shared between the atoms of the coating and the substrate [36,42,44,45]. In the literature, it has been proposed and accepted that the mechanisms driving the metallic bond formation in the CS process are similar to the mechanisms experienced in the cold welding process [12,34]. To induce metallic bonding, two clean and oxide-free surfaces must be brought into close contact (substrate and particles), and high interfacial contact pressures between the substrate and the particles must be achieved [12,34,35], as summarized by the schematic shown in Figure 2.6.

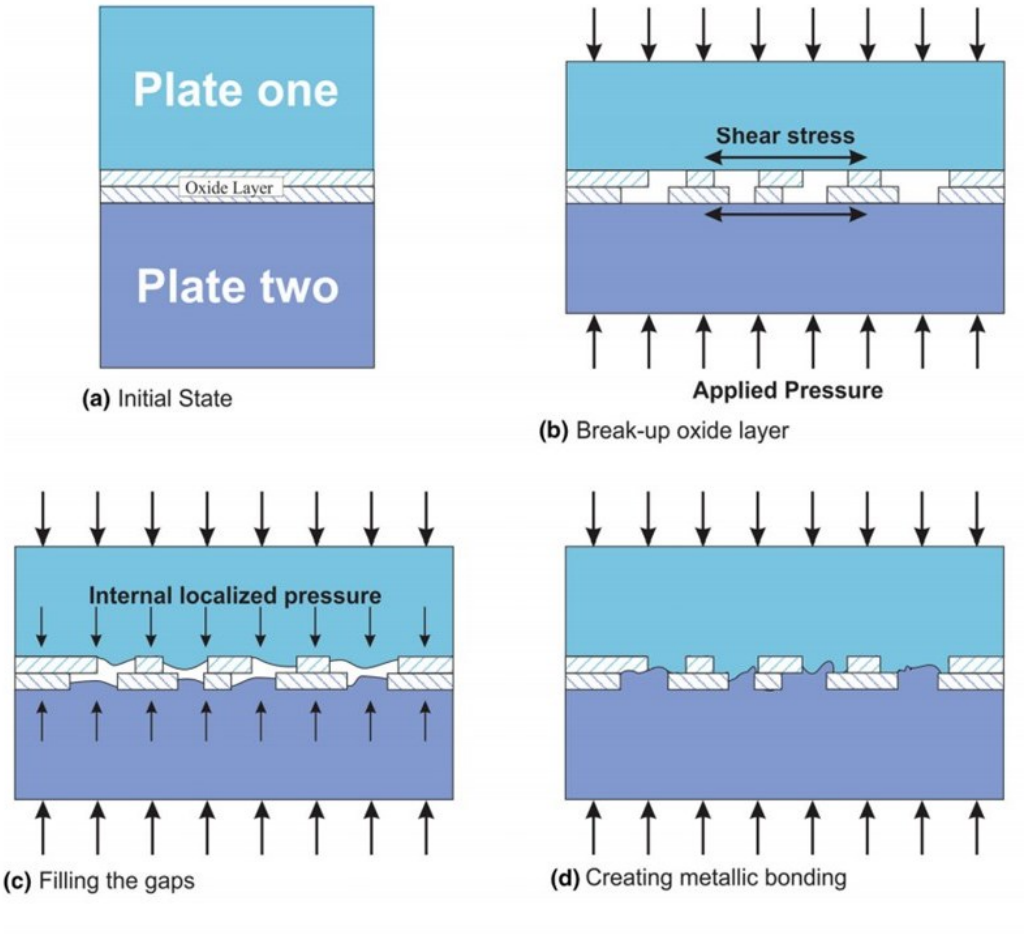


Figure 2.6 Schematic of the bonding process in the cold welding process. Adapted from [46] with permission of Springer; permission conveyed through Copyright Clearance Center, Inc.

In the CS process, metallic bonding is only achieved locally at the regions where both conditions are met [12,34,35]. An example of this bonding mechanism is presented in Figure 2.7. A cross-section of a pure aluminum particle deposited on a Ti-6Al-4V substrate is presented in Figure 2.7 a). It can be seen that for this particular case, no visible substrate deformation occurred, and partial bonding was achieved because gaps are visible between the particle and the substrate (black arrows). For this material combination, the adhesion is mainly attributed to the formation of metallic bonds [36,42]. In Figure 2.7 b) and c), top view images of a pure aluminum particle before and after splat adhesion

strength testing are presented. On these, it can be seen that after the testing procedure, the particle was partially bonded to the substrate. It is said that conditions for bonding were only met where particle remnants can be seen [42,43,47]. Contrarily, for the regions in which the substrate is visible, these conditions were not likely met and bonding did not likely occur [42]. Metallic bonding at the interface is enhanced by substrate deformation and native-free oxide surfaces.

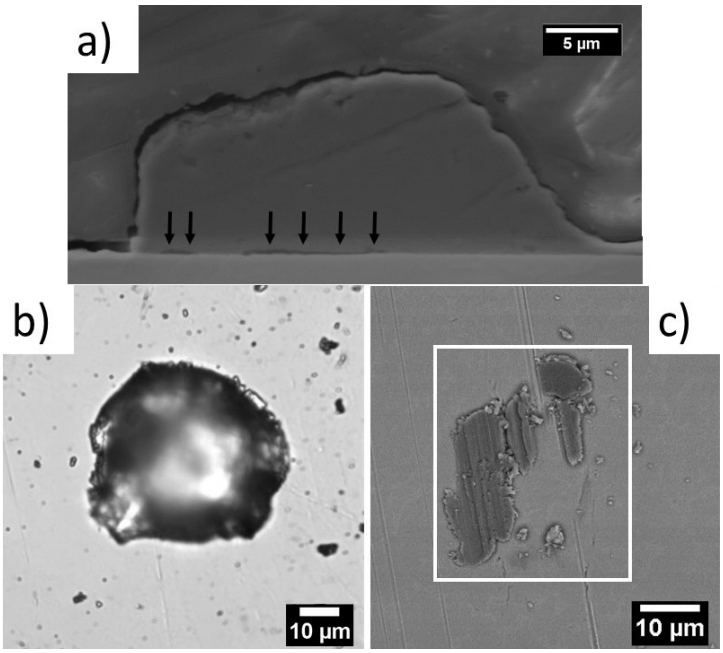


Figure 2.7 Pure aluminum particle deposited on a Ti-6Al-4V substrate. a) cross-sectional image of an individual particle bonded to the substrate, b) top view of a particle deposited onto the substrate, and c) evidence of a metallic bond Black arrows in a) indicate partial contact between the substrate and the particle. Adapted from [42] with permission of Springer; permission conveyed through Copyright Clearance Center, Inc.

2.1.9. Initial Substrate Temperature

The initial substrate temperature has been proposed as a variable that could potentially reduce the critical velocity, and thus, likely improve the CS deposition process. Studies have been devoted to investigate the role of relatively high initial substrate temperatures, but the breadth of results are, in some cases, contradictory. For single particle testing

("wipe tests"), it is clear that the number of deposited particles increases as the initial substrate temperature rises [11,45,48,49]. However, in these studies, the potential mechanisms increasing the number of deposited particles as a function of the temperature has not been explained. In addition to that, the influence of the initial substrate temperature at the single-particle level has been mostly evaluated by looking at cross-sectional images of deposited particles. This approach, however, is limited for the following reasons:

- Results may be misleading because the deposited particles might not be cut through the center of the particle resulting in not representative cross-sectional images.
- The adhesion strength as a function of the initial substrate temperature cannot be quantified.
- The bonded area at the particle/substrate interface as a function of the initial substrate temperature remains unknown.

For the deposition efficiency (DE), the results are contradictory. In the literature, higher DE values for nickel, titanium, aluminum, diamond/Ni60 and copper/alumina have been measured as the initial substrate temperature increases [50–52]. In these studies, a laser coupled to the CS process is used to increase the initial substrate temperature. According to these studies, the substrate temperature is kept at a constant value by increasing the laser power using a closed-loop feedback system connected to the laser equipment [50–53]. The problem with this approach is that it creates a variable heat input (a variable substrate heating rate), and thus, comparing the as-produced coatings is difficult due to the different thermal history. Additionally, so far, no clear explanation has been provided to explain the increase in DE. Efforts to explain the benefit preheating the substrate using a laser have been carried out, some attribute the higher DE results to the laser heating the propellant gas molecules, while others believe that the powder stream is heated. Thus,

so far, no consensus has achieved to explain the higher DE values as a function of the substrate temperature.

On the other hand, the DE for pure aluminum, copper, iron, iron-based, tin, zinc and metallic glass coatings did not increase with respect of the initial substrate temperature [31,45,54,55]. However, in these studies the lack of an increase in DE has not been explained. Additionally, most of the studies did not report the time-temperature history during the spraying process which makes it difficult to draw conclusions. In consequence, this work aims to provide a generalized explanation to understand the influence of the initial substrate temperature on the DE results.

From the few studies that have reported mechanical properties, it is clear that no changes in coating hardness must be expected as the initial substrate temperature increases [49,56]. However, no explanation has been provided to describe the coating micro-hardness behavior. In consequence, this work will also provide an explanation to describe the lack of change in coating micro-hardness values.

Another mechanical property of interest is the coating adhesion strength. According to different authors, an increase in adhesion strength is expected with an increase in initial substrate temperature [11,31,53,56–59], unless a thick oxide layer is formed on the substrate during the preheating step, which ultimately hinders adhesion [31,56]. While the reasons to have higher adhesion strength values have been generally outlined in previous studies, it is still unclear

- how favoring the native oxide growth (due to higher substrate temperatures) can in some cases increase the adhesion strength values, and
- what the mechanisms driving the increase in adhesion strength are.

To answer these questions, in this work, an oxidation-resistant material (Ti-6Al-4V) is used. Selecting this material will help understand how favoring the native oxide growth can

raise the adhesion strength values. To describe the mechanisms driving the increase in adhesion strength, the soft-on-hard material combination (Aluminum on Ti-6Al-4V) is used. This will limit the formation of mechanical anchor points, and thus, any increase in adhesion strength can be attributed to accelerated metallic bond formation.

2.1.10. Coating Temperature

The role of the coating temperature has not been considered at all as a potential variable that could improve the CS deposition process. The main reason for this is that elevating the coating temperature is often difficult due to a constant heat exchange between the gas and the coating. Locally increasing the coating temperature has only been achieved through the use of a laser coupled with the CS process which irradiates on the deposited layers during the spray time. As in other studies, the laser power is controlled using a closed-loop feedback system connected to the laser equipment to keep a constant ***substrate temperature*** [60–62]. This approach has a few problems:

- The coating temperature is not controlled. Authors have used a closed-loop feedback system to keep a constant substrate temperature.
- As the coating thickness increases, more and more energy (or a higher power) is required to keep a constant substrate surface temperature due to heat dissipation by conduction into the coating.
- The coating temperature during the spraying process becomes a function of the substrate temperature. These two variables cannot be decoupled.

In this work, the influence of the coating temperature on the CS deposition process is evaluated by decoupling the substrate and the coating temperatures.

Generally speaking, studies have shown the laser-assisted CS process can increase the DE [60,61]. The laser-assisted CS process has also improved the coating quality in some cases [50,51,60], while it has worsened it in others [61,62]. Because of the contradictory results

the influence of the coating temperature on the CS deposition process becomes difficult to assess. Moreover, most of the studies have been focused on quantifying the deposition efficiency, porosity and micro-hardness values of the produced coatings. While the evaluation of the as-produced coating mechanical properties, such as the adhesion and tensile strength, has been neglected. In consequence, in this work, the influence of the coating temperature on the mechanical properties is investigated.

Until this day, only the use of laser systems has been proposed and no other alternatives have been investigated to increase the coating temperature. It is believed that the induction heating process can potentially be used to increase the coating temperature as a consequence of an eddy current density distribution formed within the coating. Therefore, in this work, the use of an induction heating system as a method to increase the coating temperature independently of the initial substrate temperature is investigated. The soft-on-hard and hard-on-hard material combinations are used to study the influence of the coating temperature on the CS deposition.

2.1.11. Particle Impact Temperature

Studies have been dedicated to understand the role of relatively low and high particle impact temperatures on the spraying process [16,18,63–69]. Higher particle impact temperatures have been found to favor plastic deformation under lower stress flows [18,64,66]. In consequence, the critical velocity for deposition is said to be a function of the particle impact temperature [14,18]. Assadi et al.[14] proposed an equation which expresses the critical velocity, of copper only, in terms of material properties and particle impact temperature:

$$V_{crit} = k_1\sqrt{c_p\left(T_{melting} - T_{particle}\right) + 16\,\frac{\sigma_y}{\rho_{particle}}\left(\frac{T_{melting}-T_{particle}}{T_{melting}-293}\right)} \quad \text{Eq. 2.7}$$

In Eq. 2.7, k_1 is a particle size-dependent dimensionless fitting parameter, C_p is the specific heat of the particle material, $T_{melting}$ is the particle melting temperature, $T_{particle}$ is the particle impact temperature, σ_y is the yield strength of the particle material at 293 K, and $\rho_{particle}$ is the density of the particle material. Equation 2.7 implies that by increasing the particle impact temperature, higher copper deposition rates could potentially be attained as the critical velocity for deposition is reduced [14]. However, studies have not been able to provide a similar equation for other materials, such as aluminum, Inconel 718 or stainless steel. Therefore, the overall effect of the particle impact temperature on the deposition of other materials needs to be investigated.

Despite the good understanding between the critical velocity and the particle impact temperature, the influence of this variable on the overall coating quality is far from being completely understood. For example, it is believed that the use of higher particle impact temperatures must always result in higher deposition efficiencies and lower porosity values [18,64–66]. However, studies have also shown that this is not necessarily the case. Higher particle impact temperatures can also result in higher deposition efficiencies and porosity levels, but until this day, there is no clear explanation that can describe this trend [70–72]. The author of this work believes that this discrepancy exists by the lack of control in the particle impact temperature due to the upstream injection. Feeding the powder at this location causes the stagnation gas, and ultimately particle velocity, and the initial particle temperature to become two intertwined variables. Therefore, any changes in the stagnation gas temperature inevitably have a direct influence on the particle impact temperature. As such, to fully understand the influence of the particle impact temperature on the coating quality, the deposition efficiency, and the porosity values, the stagnation gas and initial particle temperature must be decoupled. In this work, a potential method to do so is proposed and explored. Powder particles are fed in the downstream section of the CS nozzle and controlled powder preheating units are used to investigate different

particle impact temperatures. As a result, the gas stagnation conditions can be kept constant, and thus the particle impact velocity, and the influence of the particle impact temperature on the overall coating quality can be unraveled. To study the influence of the particle impact temperature on the overall coating quality, the hard-on-hard material combination is used.

It has been demonstrated that higher particle impact temperatures have a tendency to decrease the adhesion strength of the coating in comparison to lower particle impact temperatures [18]. The lower coating adhesion strength values are attributed to the fact that substrate deformation is reduced, while particle deformation is favored when higher particle impact temperatures are used. This hinders the breakage of the substrate native-oxide layer leading to lower adhesion values [18]. To clearly demonstrate the influence of the particle impact temperature on the coating adhesion strength, the authors followed the approach suggested in the previous paragraphs. This means that samples are sprayed using similar particle impact velocity, but different particle impact temperatures [18]. These results suggest that the proposed methodology should help explain the influence of the particle impact temperature on the overall coating quality (DE and porosity values).

2.1.12. Dimensionless Parameter Eta (η)

In the literature, the dimensionless parameter η correlates the particle impact velocity (V_{imp}) and the critical velocity as shown in Eq. 2.8 [14]

$$\eta = \frac{V_{imp}}{V_{crit}} \quad \text{Eq. 2.8}$$

From Eq. 2.8, it is evident that deposition starts when η ≥1. Knowing that the critical velocity decreases with particle impact temperature [14], feedstock powder materials

should ideally be sprayed using parameters that simultaneously increase their particle velocity and temperature prior to their impact. In the literature, $\eta \sim 1.5$ is often referred to as the benchmark for a high quality coatings [14]. It should be noted that this value was obtained for copper only with a specific powder size range, microstructure, and native-oxide layer. Therefore, $\eta \sim 1.5$ should be used as a parameter to be optimized for specific powder material and conditions rather than as a hard value.

2.1.13. The Role of the Particle/Substrate Strength on the CS Deposition Process

The mechanical properties of the particle and substrate materials will play an important role during the deposition process [40,41]. Bae et al. [41] proposed four more relevant deposition cases based on the particle/substrate strength combination: soft/soft, soft/hard, hard/soft, and hard/hard. For the soft/soft and hard/hard, both the particle and the substrate experience a similar degree of deformation, as shown in Figure 2.8 a) and b), respectively.

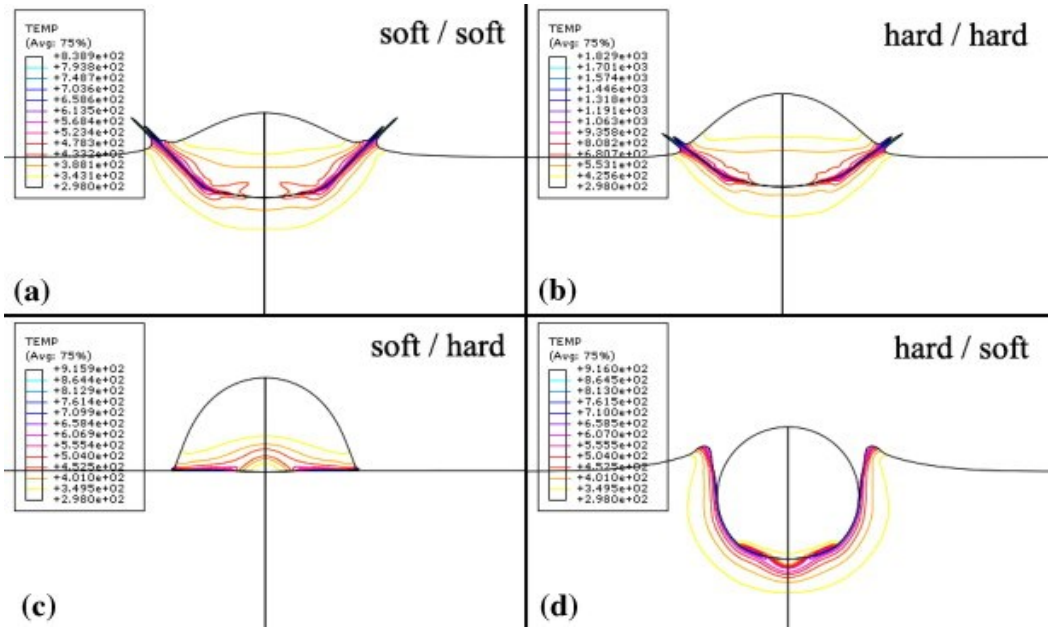


Figure 2.8 Classified four cases of particle impact on substrate: (a) soft/soft (Al particle onto Al substrate, (b) hard/hard (Ti particle onto Ti substrate, (c) soft/hard (Al particle onto mild steel substrate), (d) hard/soft (Ti particle onto Al substrate). Reprinted from [41] with permission of Elsevier; permission conveyed through Copyright Clearance Center, Inc.

For the most extreme cases (soft/hard and hard/soft), the deformation mainly occurs on the soft part, while their hard counterparts remain barely deformed. These two cases are of great interest as the deposition of soft and ductile powders on hard substrates is often accompanied by poor adhesion, due to an improper cleaning process of the substrate native-oxide layer. For the hard-on-soft combination, higher particle velocities and temperatures are expected to properly deform the coating layers and produce a good quality coating.

2.2 Substrate Material

2.2.1. Ti-6Al-4V (Ti64)

Ti64 is used as the hard substrate material in this work. This α-β alloy is characterized by high strength and hardness, its high specific weight-strength ratio, corrosion resistance,

and oxidation resistance at a wide range of temperatures up to 600 °C [73,74]. This alloy was originally developed for aircraft structural applications and it was developed to work under moderate to high temperature applications [73,75]. A thermodynamically stable, protective α-Al_2O_3 phase in combination with TiO_2 will form on the surface [75]. These properties make Ti64 an ideal candidate to study the influence of the initial substrate temperature. A detailed explanation supporting this choice is provided in Chapter 4. The maximum aluminum content is limited to 6 wt.% due to its detrimental effect on ductility. A few drawbacks of this alloy are its poor thermal conductivity, its propensity to strain harden, and its significant decrease in young modulus at temperatures above 600 °C [73,75].

2.3 Feedstock Powder Materials

In Figure 2.4, it was shown that the critical velocity ranges from a couple of hundred meters per second, i.e. tin, up to 750 m/s or higher for materials like MCrAlY. Commonly, materials with relatively low mechanical properties, like tin or zinc, do not require high gas velocities to accelerate the particles above their critical velocity, as shown in Figure 2.9. In the following section, the approaches used to produce aluminum and Inconel 718 coatings are discussed.

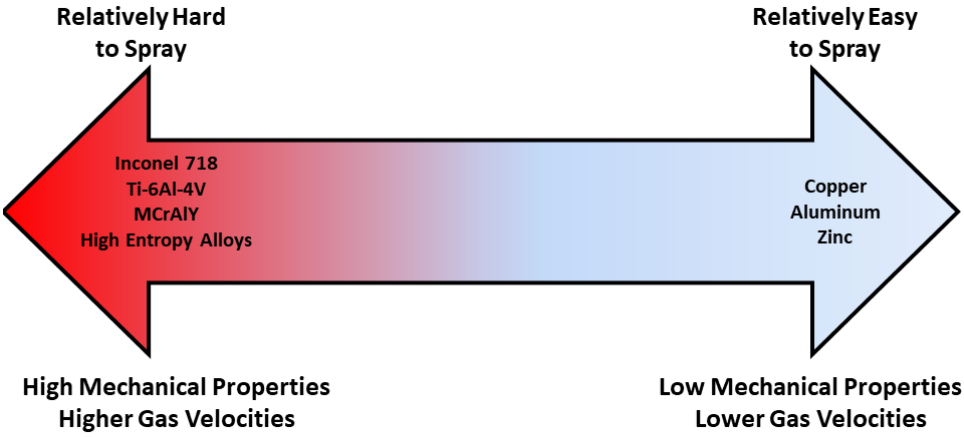


Figure 2.9 Powder sprayability as a function of the propellant gas velocities and mechanical properties.

2.3.1. Aluminum

Aluminum is an FCC metallic element with high ductility at room temperature, high thermal conductivity, low hardness and density. It is one of the easiest materials to spray using the CS process [76]. The critical velocity of pure aluminum is around 600 m/s [12,15,22,24]. These characteristics have also made aluminum one of the flagship materials of the CS technique and many studies in the field have been dedicated to understand the cold-spray deposition of aluminum coatings [18,59,77–82]. Because of these reasons, aluminum is chosen as the soft feedstock powder material. A detailed explanation supporting this choice is provided in Chapter 4

2.3.2. Inconel 718 (In718)

In718 has gained special attention from the CS community in recent years [11,70,83–98]. This superalloy is characterized by its high mechanical properties at a wide range of temperatures (from cryogenic temperatures up to 700 °C) [99–102]. This alloy also exhibits a high performance against corrosion and oxidation at elevated temperatures [100–102]. Therefore, it has become a popular material in the aerospace and aeronautical industries.

The same excellent mechanical properties that characterize this nickel-based superalloy also make the production of coatings using the CS process challenging [70,84,86]. Plastic deformation of this material is highly restricted at temperatures below 750 °C (1400 °F). These properties make In718 an ideal candidate for the hard feedstock powder material. A detailed explanation supporting this choice is provided in Chapter 4.

2.4 Induction Heating Process

2.4.1. Overview of Induction Heating

From a practical perspective, the induction heating (IH) process can be described by the application of alternating voltage to an inductor (coil). This in turn creates an alternating

current (AC) flow on the coil. The AC flow on the coil will then create an alternating electromagnetic field (EMF) with an identical frequency to the AC flow, as described by Ampere's Law [103–109]. The EMF will induce the formation of eddy currents in any metallic piece located in the vicinity of the coil. These currents will have the same frequency as AC flow on the coil; however, their direction is opposite to the coil current, as presented by the schematic in Figure 2.10. The induced eddy currents will heat the metallic piece due to the Joule heating effect. It is worth noting that the eddy current distribution within the metallic workpiece, and thus the temperature gradient, will not be uniform [103,104,106,107].

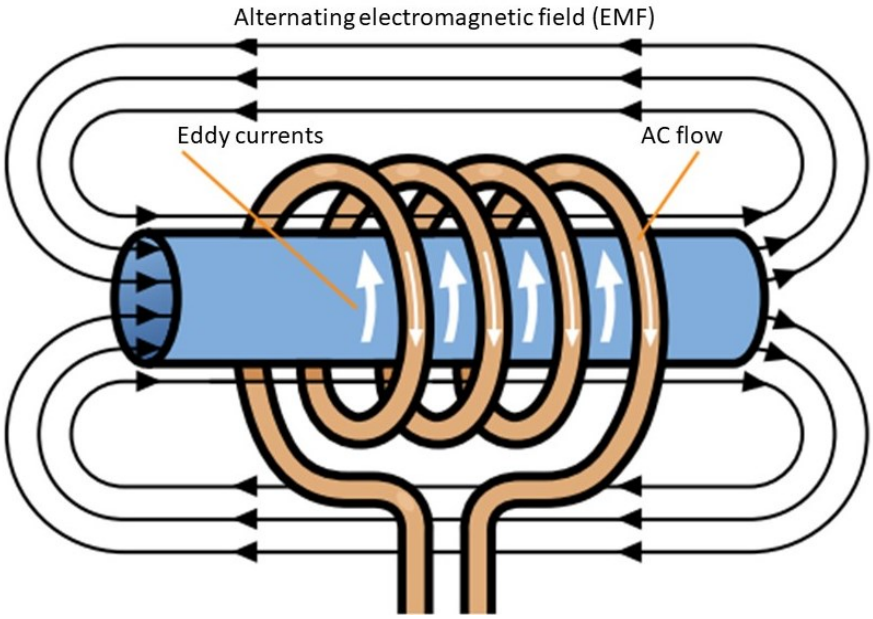


Figure 2.10 Schematic of the induction heating process. Adapted from [110].

From a theoretical perspective, the IH process, and thus, the eddy current density distribution can be described using the well-known Maxwell equations, which are presented in Eq. 2.9-2.12 [105,108,109]:

$$\frac{\partial D}{\partial t} + J = \nabla \times H \text{ (Maxwell-Àmpere equation) Eq. 2.9}$$

$$\frac{\partial B}{\partial t} + \nabla \times E = 0 \text{ (Faraday equation) Eq. 2.10}$$

$$\nabla \cdot D = \varphi_{freecharge} \text{ (Gauss electrical equation) Eq. 2.11}$$

$$\nabla \cdot B = 0 \text{(Gauss magnetic equation) Eq. 2.12}$$

D is the electric displacement field, E is the electric field, H is the magnetic field, B is the magnetic flux density, J is the electric current density, and $\varphi_{freecharge}$ is the volume free electric charge density. D and B are related to E and H by the following constitutive relationships: $D = \varepsilon E$ and $B = \mu H$. ε and μ are defined as electric permittivity and magnetic permeability of a specific medium, respectively [105,108,109].

The Maxwell-Àmpere equation states that the electric current density (J) passing through a surface is equal to the line integral of the magnetic field H on the boundary of that surface. The Faraday equation demonstrates that the time derivative of the flux of the magnetic induction through a given surface is equal to the line integral of that induced electric field on the boundary of that surface. The Gauss electrical equation states that the total charge contained inside a volume is equal to the external flux of the electric induction through the boundary of that volume. Lastly, the Gauss magnetic equation states that magnetic charges do not exist [105,108].

Once the Maxwell equations have been presented, these can be manipulated to describe the formation of eddy currents due to alternating magnetic fields. Despite the fact that eddy currents within a metallic piece must be induced by a time-varying field associated with the current flowing in a coil, it turns out that the displacement current inside the metallic piece can be neglected [108,109]. In other words, the currents inside the metallic part have a quasi-static nature and a non-significant number of displaced currents are formed. To support this argument, it is necessary to first introduce Ohm's Law (Eq. 2.13) and the displacement current density equation (Eq. 2.14) [105,108,109]. If any

displacement current density exists in the metallic geometry, the total current density (J_{Total}) can be calculated as the sum of the current and the displacement current density (J_D), as shown in Eq. 2.15 [108]. In phasor form, for sinusoidal time variation fields E, the sum can be expressed as in Eq. 2.16 [108].

$$J = \sigma E \quad \text{Eq. 2.13}$$

$$\frac{\partial D}{\partial t} = J_{\boldsymbol{D}} = \frac{\partial \varepsilon E}{\partial t} \quad \text{Eq. 2.14}$$

$$J_{total} = \sigma E + \frac{\partial \varepsilon E}{\partial t} = \left(\sigma + \varepsilon \frac{\partial}{\partial t}\right) E \quad \text{Eq. 2.15}$$

$$J_{total} = (\sigma + j\omega\varepsilon) E \quad \text{Eq. 2.16}$$

Where σ is the electrical conductivity of a material, j is the complex part of the current driving the electric field and ω is the angular frequency (2π·frequency) [108].

Typically, metals have a σ in the order of $1x10^7$ Siemens and the maximum frequency used in the IH process is around 10MHz. In this work, the maximum frequency is in the range of 190 kHz and ε= $8.85x10^{-12}$. In consequence, using Eq. 2.16, it can be seen that:

$$J = \sigma E \sim 10^7 |E|$$

and

$$J_D = j\omega\varepsilon E \sim 2 \cdot \pi \cdot 190 \times 10^3 \cdot 8.85 \times 10^{-12} |E| \sim 1 \times 10^{-5} |E|$$

This demonstrates that the displaced currents can be neglected as $|J| \gg |J_D|$. In other words, the eddy current is orders of magnitude larger than the displaced currents, both caused by an alternating magnetic field [108]. Thus, the Maxwell-Àmpere equation (Eq.2.9) becomes $\nabla \times H = J$,and thus, it is said that the approximation of the eddy current density distribution can be done under a quasi-static regime [108,109].

The total current density inside a control volume due to a current density in a source (J_s) and the eddy current density (J_{eddy}) induced within the metallic piece can be expressed as follows [108,109]:

$$J_{total} = J_S + J_{eddy}$$ Eq. 2.17

And so, the Maxwell- Àmpere equation can be re-expressed as [108,109]:

$$\nabla \times H = J_S + J_{eddy}$$ Eq. 2.18

Using the phasor form of Faraday's Law ($\nabla \times E = -j\omega B$), the constitutive relationship between B and H ($B = \mu H$), and assuming an isotropic permeability, Eq. 2.10 can be re-written as presented in Eq. 2.19 [108,109]:

$$\nabla \times E = -j\omega\mu H$$ Eq. 2.19

And multiplying both sides of the previous equation by the curl, Faraday's law can be re-expressed as follows [109]:

$$\nabla \times \nabla \times E = -j\omega\mu \nabla \times H$$ Eq. 2.20

Combining Eq. 2.18 and Eq. 2.20, the following expression is obtained [108,109]:

$$\nabla \times \nabla \times E = -j\omega\mu(J_S + J_{eddy})$$ Eq. 2.21

Making the substitution of $J_{eddy} = \sigma E$ and using the a vector identity ($\nabla \times \nabla \times E = \nabla\nabla \cdot E - \nabla^2 E$), Eq. 2.19 becomes [108,109]:

$$\nabla\nabla \cdot E - \nabla^2 E = -j\omega\mu(J_S + \sigma E)$$ Eq. 2.22

For a zero free volume charge ($\varphi_{freecharge}$ = 0) and by combining Eq. 2.11 and the constitutive relationship between D and E ($D = \varepsilon E$), $\varepsilon \nabla \cdot E = 0$, and Eq. 2.22 is re-written as follows [105,108,109]:

$$(\nabla^2 - j\omega\mu\,\sigma)E = j\omega\mu J_S$$ Eq. 2.23

The previous expression is the governing equation (Eq. 2.23) that can be used to estimate the eddy current density in a metallic piece due to an alternating electric field caused by a current density in a source. Equation 2.23 is valid for problems in one or three-dimensions and is a function of the electric field [108,109]. A similar expression can be inferred as a function of the magnetic field H, as presented in Eq. 2.24 [108,109].

$$(\nabla^2 - j\omega\mu\,\sigma)H = -\nabla \times J_S \quad \text{Eq. 2.24}$$

2.4.2. Material Properties Affecting the Induction Heating Process

In the previous section, it has been shown that the electromagnetic properties have an influence on the eddy current density formation. There are many electromagnetic properties such as electrical resistivity, relative magnetic permeability, coercive force, hysteresis loss, magnetic susceptibility, and magnetic dipole moment [103,104,106–109]. However, from the equations shown in Section 2.4.1, the most relevant electromagnetic properties are electrical conductivity and magnetic permeability of a medium [103,104,106–109,111].

2.4.3. Electrical Resistivity

Generally speaking, metals have high conductivities because of the large numbers of free electrons that have been exited into empty states above the Fermi energy [76]. While the electrical conductivity is of great interest, it is more common to describe a material in term of its electrical resistivity (r). Metallic materials can be classified in low-resistivity metals and high resistivity metals and alloys [76], as shown in Figure 2.11.

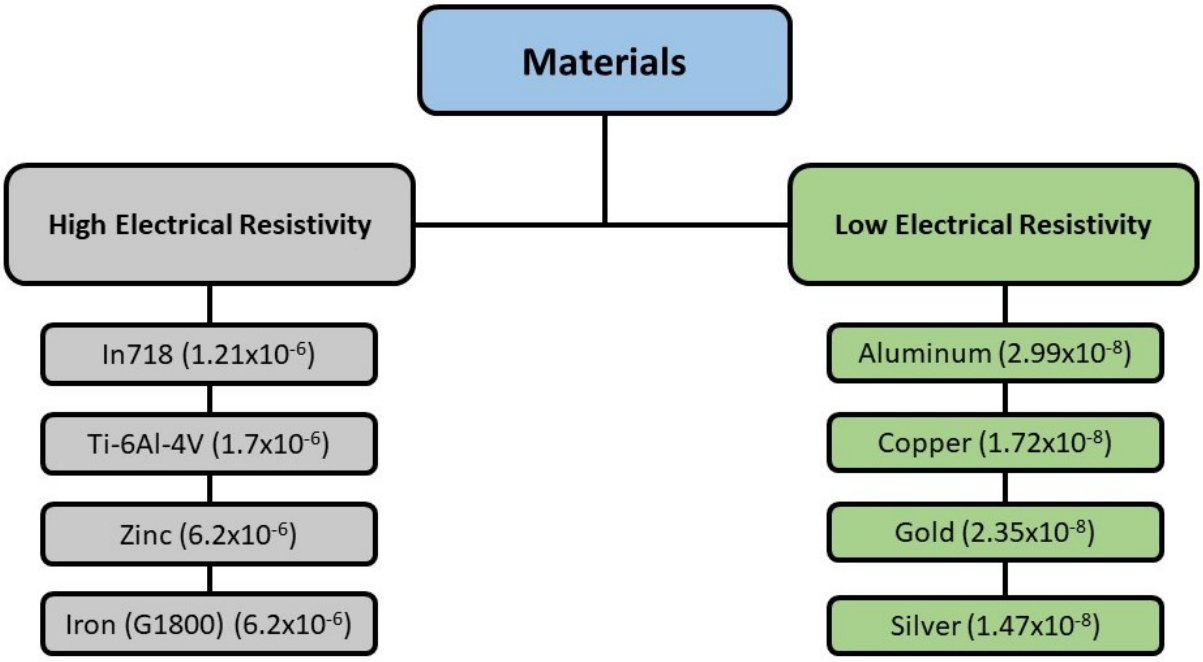


Figure 2.11 Classification of materials based on their electrical resistivity.

As a rule of thumb, the electrical resistivity of metals changes as a function of temperature, chemical composition (impurities), and deformation, as shown in Eq. 2.25 [76,103,104]:

$$r_{total} = r_{temperature} + r_{impurities} + r_{deformation} \quad \text{Eq. 2.25}$$

For most metals, the electrical resistivity commonly increases as the temperature is elevated. This effect is caused by the increased atomic vibration and constant motion of vacancies in the lattice structure limiting the free motion of electrons. [76,103,104,112,113]. However, other metals such as semiconductor materials, like silicon and germanium, exhibit lower resistivity as the temperature increases. This is because at room temperature the valence bands are filled, but by increasing the temperature the electrons in the outermost bands are free to escape the bonding forces and freely move [76].

Alloying elements or impurities also influence the electrical resistivity [76,103,112,114]. For example, in the copper-nickel system, as the nickel content increases, the electrical

resistivity increases. Alloys have higher electrical resistivity because the electron motion is restricted by the alloying elements inside the crystalline structure. Plastic deformation also increases electrical resistivity because the free electron motion inside the crystal lattice is also restricted [76,104,115–118]. Reducing the grain size increases the surface area at the grain boundaries scattering electrons more easily increasing the resistivity [76,119,120]. However, these factors have minimal influence on the resistivity in comparison to the chemical composition and temperature [76,104,112–114]. For cold-sprayed coating specifically, the electrical resistivity increases as the coating porosity values increase and as the coating cohesion strength decreases consequence of the imperfect contact at the particle/particle interface [117,118,121,122].

2.4.4. Relative Magnetic Permeability

The magnetic permeability (of a medium) is the ability of a material to conduct a magnetic flux [76,105,108]. The magnetic permeability of the vacuum (μ_{vac}) is defined as the standard reference value and it is equal to $\mu_{vac} = 1.25x10^{-6}$ [76,105,108]. It is often more convenient to quantify the degree to which the material can be magnetized with respect to the standard value. To do that, the relative permeability (μ_r) is used and it is the ratio of the permeability of a medium over the permeability of vacuum $\mu_r = \frac{\mu}{\mu_{vac}}$ [76,105,108]. Based on the μ_r, materials can be classified as ferromagnetic, paramagnetic and diamagnetic [76]. Materials, such as Cobalt and Iron are ferromagnetic exhibit a $\mu_r >> 1$ (E.g. Iron 99.95% purity has a μ_r =200000) [76,103,104,106,107]. Paramagnetic materials, such as aluminum, exhibit a μ_r close to 1 [76,103,104]. Diamagnetic materials have a $\mu_r < 1$, such as Bismuth (0.999834) [76]. Both diamagnetic and paramagnetic materials are considered non-magnetic because they exhibit magnetization only when in the presence of an external field [76].

The relative magnetic permeability is also a function of temperature [76,123,124]. Ferromagnetic materials become paramagnetic above their Curie temperature [76,124]. Above this temperature the orientations of the atomic magnetic moments become random because magnetic moments have the tendency to rotate with higher temperatures generating no net macroscopic magnetization [76,105]. The relative magnetic permeability also decreases as the magnetic field frequency increases because the atomic moments do not have enough time to re-organize themselves favoring a random direction[103,104,124,125]. However, this effect is significant at frequency values outside of the induction heating range.

2.4.5. Spatial Configuration Phenomena Controlling the Eddy Current Density Distribution

The IH process has been outlined in a mathematical and practical fashion in the previous sections. The most important material properties have also been presented. Now, three of the most common eddy current distribution phenomena as a function of the relative position between a metallic piece and a coil are discussed.

2.4.5.1. Skin Effect

For a direct current (DC) flow, the electrical current distribution through the cross section of a conductor is uniform, but for an AC flow this is not the case [103,104,106,107]. The maximum AC value of the distribution is located at the surface of the conductor, and the values will decrease towards the center [103,104,106,107]. This phenomenon is known as the “skin effect” [103,104,106,107], and it is always present whenever there is an AC flow. A similar effect takes places when eddy currents are formed due to an alternating magnetic field caused by an AC flow. For example, in the cylindrical piece shown in Figure 2.12 a), the maximum current density can be seen at the surface of the workpiece (Figure 2.12 b)). It is also evident that values quickly decay towards the center reaching zero right

at the axis of symmetry (core). It is estimated that about 86% of the total power will be concentrated near the surface layer of the workpiece, as shown on Figure 2.12 c). In the literature this near-surface region is called penetration depth (δ) [103,104,106,107,111].

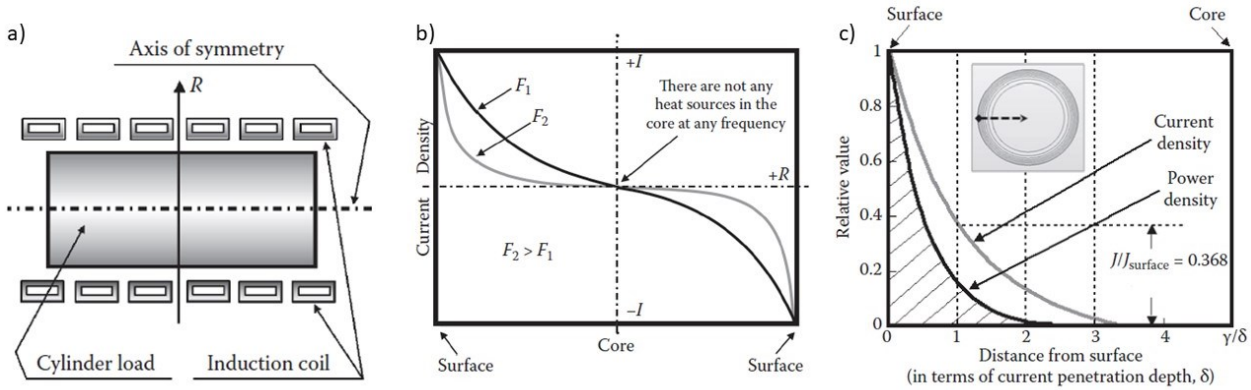


Figure 2.12 a) Bar positioned in the middle of a multiturn coil, b) Eddy current density distribution along the radius of the cylinder presented in a) at two different frequencies, and c) current and power density profiles owing to skin effect. Adapted from [104] with permission of Taylor and Francis; permission conveyed through Copyright Clearance Center, Inc.

The current distribution in a configuration as the one shown on Figure 2.12 a) is estimated using Eq. 2.26 [104].

$$J_y = J_{surf} e^{\frac{-y}{\delta}} \quad \text{Eq. 2.26}$$

Where J_y (A/m^2) is the current density at distance *y* from the surface, J_{surf} (A/m^2) is the current density at the workpiece surface, y (m) is the distance from the surface towards the core and δ (m) is the penetration depth. The penetration depth can be expressed as follows [104]:

$$\delta = 503 \sqrt{\frac{\sigma}{\mu_{rf}}} \quad \text{Eq. 2.27}$$

In Eq.2.27 *f* is the frequency. As such, the degree of the "skin effect" on a workpiece is a function of the material properties (σ and μ_r), frequency, metallic piece and coil geometries. The "skin effect" will be more pronounced on a workpiece when high frequencies are used or when the size of the of the body is large compared to the δ [104].

2.4.5.2. Proximity Effect

When an inductor carries an AC source, it develops an EMF. The electromagnetic field of the coil will in turn generate eddy currents of the same magnitude and opposite direction within the conductor in comparison to the AC source [103,104,107]. The coil current and the eddy currents induced on the workpiece will concentrate in the areas facing each other, as a result of the proximity effect [104], as shown in Figure 2.13 a).

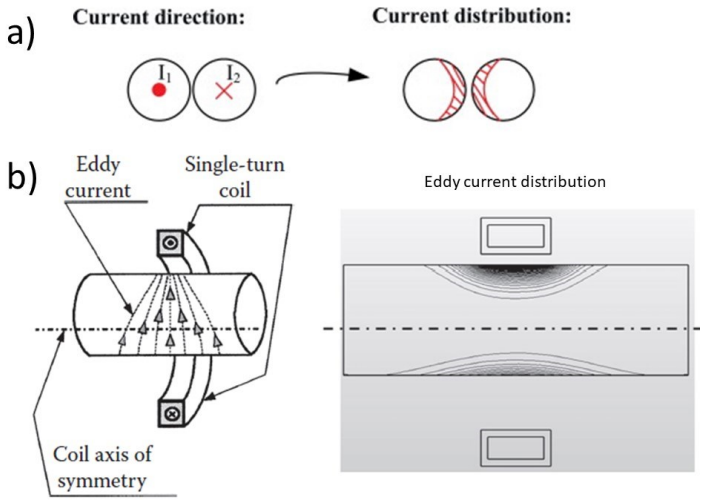


Figure 2.13 a) Proximity effect current distribution within two wires having opposite current directions, and b) proximity effect in single-turn coil with nonsymmetrical positioning of the workpiece. Adapted from [104] with permission of Taylor and Francis; permission conveyed through Copyright Clearance Center, Inc.

The proximity effect is also related to the geometry of the setup. In Figure 2.13 b) the bar is asymmetrically positioned in the middle of a single-turn coil. For this configuration, the eddy current density is higher in the area where the coil-to-bar air gap is smaller [103,104]. This will lead to an intense heating of this area in comparison to the opposite side of the

bar where the air gap is larger [103,104]. This effect is independent of the coil shape, and it is only related to the relative distance between the workpiece and the coil. The proximity effect is extensively used for heating selective areas (e.g. selective hardening, stress relieving or tempering). However, an inappropriate configuration can result in the appearance of hot and cold spots, overheating and potential melting, if not treated carefully [103,104].

2.4.5.3. Electromagnetic Ring Effect

The ring effect is one of the most relevant electromagnetic phenomena [103,104]. It is exclusive of single and multiturn coils, and it causes currents to concentrate at the inside surface of the induction coil [103,104], as shown in Figure 2.14. The ring effect plays a positive role when a metallic workpiece is placed in the middle of the coil because the coil-to-workpiece coupling is maximized, as presented in Figure 2.14 b). It is worth mentioning that while the ring effect and the proximity effect have a resemblance, the proximity effect does not require a ring or a multiturn coil. This effect in combination with the skin and proximity effects are responsible for the eddy current distribution shown in Figure 2.14 [103,104].

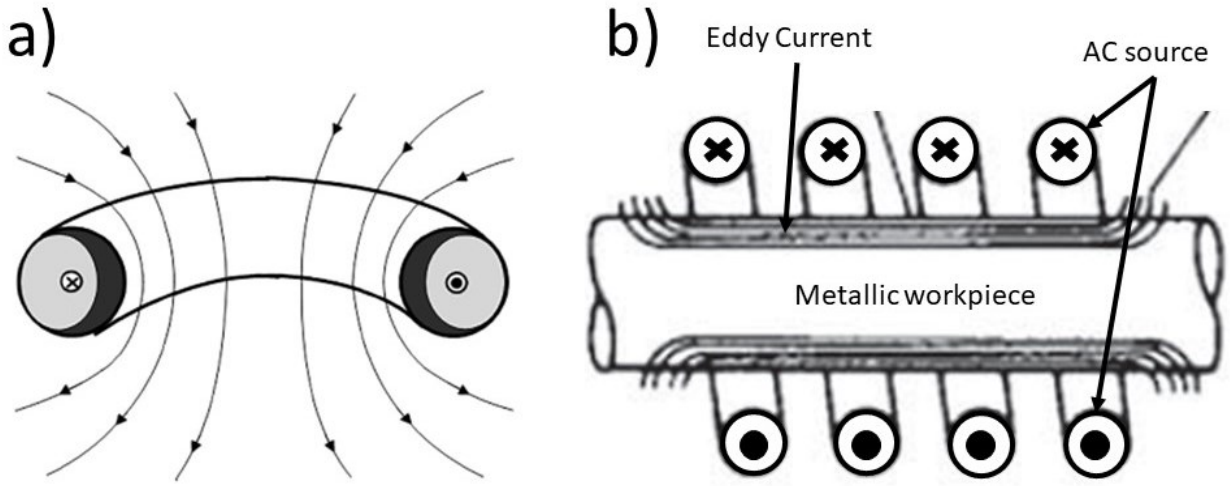


Figure 2.14 a) Ring effect in a round conductor, and b) eddy current distribution on a cylindrical geometry positioned in the middle of a multiturn coil due to the ring effect. Adapted from [104] with permission of Taylor and Francis; permission conveyed through Copyright Clearance Center, Inc.

Chapter 3 - Description of the Research Objectives

In the CS process, the substrate, the coating, and the particle impact temperatures are controlled by the gas stagnation temperature used as a spray parameter. The substrate temperature typically reaches half the gas stagnation temperature by the end of the spray time [30,55]. In the literature, the coating temperature is not commonly reported, but it is reasonable to assume that the coating reaches a similar temperature as the substrate. Lastly the particle impact temperature heavily relies on the powder injection location inside the nozzle (upstream or downstream) and the gas stagnation temperature [18,64,68]. In most of the studies dedicated to evaluate the influence of the particle impact temperature on the CS process, the gas stagnation conditions and the particle impact temperature are two intertwined variables. This is because the powder is fed in the upstream section of the nozzle, and any changes in the gas stagnation conditions have a simultaneous impact on the particle impact velocity and temperature. To decouple these two variables, it would be required to have a powder preheated unit to increase the initial particle temperature before its injection inside the nozzle, and feeding the powder in the diverging section of the nozzle would also be needed. Doing this is difficult, and for these reasons, the influence of the particle impact temperature on the CS deposition process is far from being completely understood. For these reasons, the purpose of this study is to establish how the initial substrate, coating, and particle impact temperatures can influence the overall performance of the CS process by decoupling these three variables from the general spray parameters, namely the gas stagnation temperature. To fulfill the purpose of this work, the objectives presented in Table 3.1 are identified. A detailed description of each objective as well as the tasks required to complete each one is provided in the following sections.

Table 3.1 Research objectives, a brief description of the tasks done to fulfill the objectives, and the material combination used.

Objectives	Description of the Tasks to Complete the Objective	Material Combination
Evaluate the role of the initial substrate temperature on the CS process.	• Evaluate the Particle/Substrate Deformation at the Interface and the Adhesion Strength at a Single-particle Level • Measure the Substrate Time-temperature History • Measure the Deposition Efficiency and Coating Thickness • Measure the Coating Mechanical Properties	• Soft-on-hard
Characterize the influence of the coating temperature on the CS process	• Predict the Coating Eddy Current Density Distribution • Measure the Coating Time-temperature History • Measure the Deposition Efficiency and Coating Thickness • Measure the Coating Mechanical Properties	• Soft-on-hard • Hard-on-hard
Assess the importance of the particle impact temperature on the CS process	• Decouple the Initial Particle Temperature from the Gas Stagnation Temperature • Predict the Particle Impact Temperature • Characterize the CS Deposition Process as a Function of the Particle Impact Temperature	• Hard-on-hard
Enhance the CS process performance based on the findings of the previous objectives		• Soft-on-hard • Hard-on-hard

3.1 Evaluate the Role of the Initial Substrate Temperature on the CS Deposition Process

In the literature, increasing the initial substrate temperature is proposed as a factor that could potentially play a significant role on the CS process performance [31,45,55,126]. However, the results are contradictory based on the results of different characterization techniques, as presented in Chapter 2. In this work, the soft-on-hard material combination will be used to study the influence of the initial substrate temperature on the CS deposition process. Pure aluminum is used as the soft powder, and Ti64 is used as the hard substrate. For this material combination, without a higher initial substrate temperature, the overall adhesion strength would be very limited. By increasing the initial substrate temperature metallic bond formation should, in theory, be accelerated, facilitating the evaluation of the role of the initial substrate temperature on the adhesion coating strength. A detailed explanation to support this particular material combination and selection is provided in Chapter 4.

3.1.1. Evaluate the Particle/Substrate Deformation Behavior and the Adhesion Strength at a Single-particle Level

As a first step to properly characterize the influence of the initial substrate temperature on the CS deposition process, particularly at the coating/substrate interface, individual pure aluminum particles are deposited on Ti64 substrates at different temperatures (25, 200,400 and 600°C). It has been shown that the number of deposited particles increases as the initial substrate temperature does too, but the mechanisms explaining this behavior are still unclear. This is mainly caused by the fact that cross-sectional images of individual particles are used to explain the role of the initial substrate temperature. The main drawback from this approach is that little to no information can be extracted from the cross-sectional images that can help quantify the role of the initial substrate temperature on the adhesion strength and bonded area of the deposited particles. Therefore, in this

work, a different approach is used to better understand the influence of the initial substrate temperature on the deposition of individual particles. To fully characterize the effect of the initial substrate temperature, particles are deposited, mechanically removed from the substrate surface. To do so, the following steps are followed:

1. Single-particle test samples are produced at different initial substrate temperatures (25, 200,400 and 600°C).
2. Particles are mechanically removed from the substrate using two approaches: a non-monitored and a monitored adhesion strength procedure. In the non-monitored procedure, the particle/substrate interfacial deformation is investigated by removing individual particles from the substrate using a thermally cured elastomeric adhesive. In the monitored procedure (single-splat adhesion strength testing), the force required to remove a particle from the substrate is recorded and the single-splat adhesion strength can be calculated. From the monitored procedure, the remaining particle bonded area is also calculated.
3. A finite element model is also carried out to better understand the particle/substrate deformation behavior.

This characterization procedure will better explain the mechanisms that promote a higher number of deposited particles as the initial substrate temperature increases. Additionally, the remaining particle bonded area and the single-splat adhesion strength are obtained as a function of the initial substrate temperature. The single-particle impact model has a complementary purpose as it aims to provide a greater understanding of the ongoing processes during the impact itself as opposed to after deposition is completed. The finite element model is used to better understand the particle/substrate deformation behavior and deposition mechanisms as a function of the initial substrate temperature.

3.1.2. Measure the Substrate Time-temperature History

One of the many reasons why the influence of the initial substrate temperature on the CS process is still a matter of debate is due to the lack of a substrate time-temperature history during the deposition process. Because of that, in this work, the substrate temperature is monitored using infrared thermometers during the spray time. The substrate time-temperature history is measured for the following initial substrate temperatures: 25, 200, 400 and 600 °C.

3.1.3. Measure the Deposition Efficiency and Coating Thickness

The deposition efficiency and coating thickness is quantified as a function of the initial substrate temperature. These measurements in combination with the substrate time-temperature history are used to provide a general understanding of the effect of the initial substrate temperature on the overall deposition process. Coatings are sprayed on substrates at initial substrate temperatures of 25 and 400 °C.

3.1.4. Measure the Coating Mechanical Properties

The influence of the initial substrate temperature on the coating micro-hardness and adhesion strength is also measured. For the adhesion strength testing, the characterization procedure is split in three steps, as follows:

1. A finite element model is carried out to point out the relevant bonding mechanisms (metallic or mechanical) taking place at the coating/substrate interface.
2. Adhesion strength samples are produced at different initial substrate temperatures (25 and 400 °C)
3. Fractured surfaces of the coating/substrate interface adhesion strength are examined using scanning electron microscope to the effect of the initial substrate temperature.

The soft-on-hard material combination is used to study the effect of the initial substrate temperature on the coating adhesion strength. Because of that, the formation of anchor points at the coating/substrate interface is expected to be unlikely. In the past, a finite element model has proven to be an extremely powerful tool to accurately predict the adhesion strength of CS coatings due to mechanical anchoring. However, this model cannot predict the metallic bond contribution on the overall adhesion strength. Therefore, the finite element model is used to estimate the mechanical contribution, if any, on the overall coating adhesion strength. In this way, if the coating adhesion strength increases during the experimental evaluation, the improvement can unequivocally be attributed to the enhanced metallic bond formation. This thorough procedure is expected to provide insight in the mechanisms enhancing the coating adhesion strength.

3.2 Characterize the Influence of the Coating Temperature on the CS Process.

Once the influence of the initial substrate temperature on the CS process is fully understood and properly characterized, the role of the coating temperature is evaluated. To thoroughly characterize the influence of the coating temperature on the CS deposition process, two powders are used: pure aluminum and In718, as soft and hard powders, respectively. These powders are chosen to fully characterize the influence of the coating temperature in the CS process for materials having opposite mechanical properties and deposition behaviors. Ti64 is selected as the substrate material for the deposition of both powders for consistency purposes as it is also used as a material pair for the deposition of the soft powder. A detailed explanation to support the material selection is provided in Chapter 4.

3.2.1. Predict the Coating Eddy Current Density Distribution

In the CS field, laser systems have become the "default" method to increase the coating temperature [50,53,60–62]. This is because the first reports of the use of a laser were produced more than 10 years ago. It has been recently demonstrated that, for the copper-on-steel combination, the effect of the laser spot is limited to up to three mm in coating thickness, and the local coating heating lasts less than five seconds [127]. Therefore, to achieve larger heating zones and longer heat treatment periods, it is likely that the laser power must be increased. However, this approach increases the risk of local melting of the coating top surface and oxidation. In addition, the use of a laser requires the enforcement of safety precautions and international standards and regulations. Not only that, but also the use of lasers often requires complex and large setups raising the operational costs. Therefore, as an alternative to avoid these problems and limitations, in this study, the use of an induction heating system is proposed to increase the coating temperature over longer duration periods than what is achieved through the use of laser.

The induction heating process is commonly used as a heating process for metallic parts and complex geometries [103,104,107]. Because of that, information of the use of induction heating systems on relatively thin metallic pieces, such as cold-spray coatings (in the order of ≤100 up to 1000 μm), is extremely limited. For this reason, it is still unclear if eddy currents may form within a metallic pieces of a thickness typical of a cold-spray coating. To answer this question, as a first approximation, a finite element model is used to predict the potential development of an eddy current density distribution within 100-μm pure aluminum and In718 coatings. The following parameters are studied for the coating:

1. The induction heating parameters
2. The coating geometry

The finite element model is developed to better understand the effect of the IH parameters and coating geometry on the potential eddy current formation. This model is also used to better explain the experimental results.

3.2.2. Measure the Coating Time-temperature History

The coating time-temperature history has not been reported in previous studies focused on the influence of the coating temperature on the CS deposition process. Therefore, in this work, the time-temperature history is monitored during the deposition of In718-on-Ti64 (hard-on-hard material combination). Two coating temperatures are investigated, 25 and 600 °C. The coating time-temperature history is measured during the deposition of a nozzle pass over the coated area.

3.2.3. Measure the Deposition Efficiency and Coating Thickness

The deposition efficiency, the coating thickness and porosity values are also measured during the deposition of pure aluminum and In718 coatings. The use of two dissimilar powders and the deposition efficiencies as a function of the coating temperature is expected to provide enough evidence to obtain a general conclusion of the influence of the coating temperature on the CS process. A detailed description of the different coating temperatures evaluated for the pure aluminum and In718 coatings is provided in sections 5.2 and 5.5 (Chapter 5), respectively.

3.2.4. Measure the Coating Mechanical Properties

Previous studies have barely evaluated the as-sprayed mechanical coating properties, only micro-hardness values, as a function of the coating temperatures [60–62]. Therefore, the efforts in that regard are taken a bit further in comparison to other studies. For the soft-on-hard material combination, micro-hardness testing, adhesion and tensile strength testing are used as characterization techniques to explain the influence of the coating

temperatures on the as-sprayed mechanical properties. Micro-hardness testing is used as a first approximation to evaluate if the coatings have experienced an *in-situ* heat treatment effect during the spray time. Subsequently, the coating adhesion strength is used to evaluate if the metallic bond formation at the interface is accelerated by the continuous heating of the coating. Finally, the tensile strength is used to assess if the characteristic brittle behavior of the cold-sprayed coatings persists even under the influence of a potential eddy current density distribution. For the hard-on-hard material combination, micro-hardness testing is used, as a first approximation, to quantify the level of plastic deformation experienced by the particles, but also as method to visually assess the cohesion of the as-produced coatings.

3.3 Assess the Importance of the Particle Impact Temperature on the Performance of the CS Process

The particle impact temperature is believed to be a crucial factor in the CS process performance because it is said to reduce the critical velocity [14,15,18]. However, it is still unclear what the role of the particle impact temperature on the overall coating quality is. A few studies have reported that higher particle impact temperatures result in lower porosity values [18,64–66], at the same time others have shown that the porosity increases as the particle impact temperatures do as well [70–72]. The author of this work believes that this discrepancy arises because upstream injection is used. This causes the gas stagnation temperature, and thus, the gas velocity (and particle velocity) and the particle impact temperature to become intertwined variables. Therefore, the results make it difficult to draw any conclusions. To study the influence of the particle impact temperature on the CS process, the hard-on-hard material combination is used. In718 powder is deposited on Ti64 substrates. In718 is chosen as the feedstock powder material due to its high mechanical properties up to temperatures in the 650 °C range. This is because if a transitional behavior from a hard to a softer material is observed, it can easily be attributed

to the relatively high particle impact temperatures experienced by the material. A detailed explanation to support this material choice is provided in Chapter 4

3.3.1. Decouple the Initial Particle Temperature from the Gas Stagnation Temperature

To decouple and to independently increase the initial particle temperature from gas stagnation temperature, in this work, controlled powder preheating units are used. Not only that but also, the powder particle is fed in the downstream section of the nozzle (diverging section). By doing so, constant spray parameters (particle impact velocity) can be used while having full and independent control of the initial particle temperature. In consequence, the particles will experience similar impact velocities, while the particle impact temperature is independently changed. Three different initial particle temperatures are tested: 25, 400 and 750 °C. These particle temperatures are used in combination with two sets of spray parameters.

3.3.2. Predict the Particle Impact Temperature

In the CS process, the particles are characterized by their relatively low particle impact temperature and relatively high velocities once they exit the nozzle. Because of these reasons, the use of classical optical pyrometry is not possible, making any particle impact temperature measurement a technical challenge or an extremely lengthy process. Recently, a computational fluid dynamics model has been developed and extensively validated using both a Cold-Spray meter and a high-speed infra-red camera [18,63]. The computational fluid dynamic model has been shown to be able to accurately predict the particle impact velocity and temperature. Therefore, in this work, the same extensively validated computational fluid dynamics model is used to predict the propellant gas flow characteristics inside a nozzle. From the resolved flow, the particle impact temperature is obtained. Because the gas velocity and temperature are needed to obtain the particle

impact temperature, the particle impact velocity is also estimated using the computational fluid dynamics model.

3.3.3. Characterize the CS Deposition Process as a Function of the Particle Impact Temperature

To completely determine the influence of the particle impact temperature on the overall coating quality, the deposition efficiency, coating porosity values, and micro-hardness values are used. These three characterization techniques in combination with fully controlled (independent of the gas stagnation temperature) particle impact temperatures are expected to provide enough information to fully explain the effect of the particle impact temperature on the coating deposition process. Three initial particle temperatures are explored: 25, 400, and 750 °C. Decoupling the initial particle temperature from the gas stagnation temperature, it is expected to finally answer the question of why some coatings exhibit higher porosity values even when the particle impact temperature increases.

3.4 Enhance the CS Process Performance Based on the Findings of the Previous Objectives

Based on the effect of each individual (substrate, coating, and particle) temperature, it is believed that increasing two or more of these temperatures, as controllable deposition parameters, can enhance the CS process performance. Enhancing the CS process performance means producing a better coating in comparison to coatings in which the gas stagnation temperature controls the substrate, the coating, and the particle impact temperatures. It is also expected that by having control of the initial substrate, coating, and particle impact temperatures (independent values from the gas stagnation temperature), the as-sprayed coating mechanical properties can be tailored and selectively chosen based on the application and requirements.

Chapter 4 - Research methodology

In the present section, the experimental methodology to achieve the objectives set in Chapter 3 will be outlined. This chapter focuses more specifically on the feedstock and substrate materials, the CS and induction heating systems, controlled powder preheating unit, and various analysis techniques to characterize the powder and the coating properties.

4.1 Feedstock Material

In this study, Ti64 is chosen as the substrate material, while pure aluminum and In718 are used as the feedstock powder materials. An in-depth description of the substrate and feedstock powder materials is presented in the following sections:

4.1.1. Substrate Material

In this work, a hard substrate is used in combination with soft and hard powders. This type of substrate is selected to assess the influence of the substrate and coating temperatures on the metallic bond formation on the overall coating adhesion strength. For the soft/hard material combination specifically, the creation of anchor points due to the particle impact is restricted, as demonstrated in Figure 4.1 a), because the substrate deformation is limited. Additionally, for this material pair, the breakage of the native oxide layer is difficult, producing extremely localized metallic bonding at the interface producing an extremely low, if any, overall coating adhesion strength. To accurately assess the effect of the substrate and the coating temperatures, the hard material (in this case the substrate) must also be able of retaining its properties from 25°C to at least 650 °C. This strict requirement is needed to avoid a potential loss of strength that could produce a transitional behavior from a hard to a much softer substrate in comparison to its as-received state at room temperature, as shown in Figure 4.1 b). Another strict requirement is that the substrate native oxide layer must not significantly grow by increasing the

temperature from 25 to 650 °C. For the hard-on-hard material combination, the same hard substrate material is used for consistency purposes and to facilitate the comparison results between material combinations.

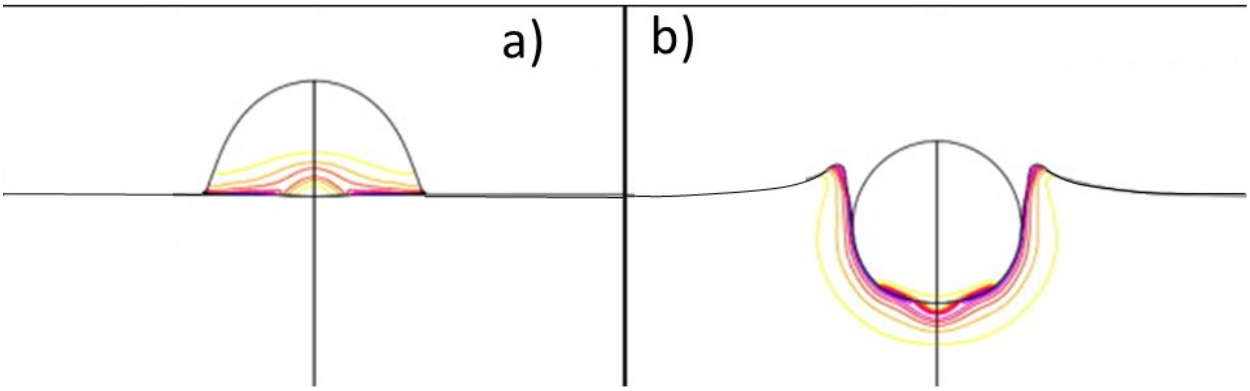


Figure 4.1 Particle/substrate interfacial deformation for a) the soft-on-hard material and b) hard material deformation under significant thermal softening upon impact. Reprinted from [41] with permission of Elsevier; permission conveyed through Copyright Clearance Center, Inc.

Therefore, the chosen substrate material is commercially available Ti64 (Titanium Industries, Inc. Montreal, QC, Canada). This alloy is characterized for its high hardness value and high mechanical properties from 25 up to 650 °C avoiding a potential loss in strength due to the preheating temperatures. Additionally, for the soft-on-hard material combination, the high hardness values at different temperatures are used to restrict particle penetration on the substrate (as shown in Figure 4.1 b)), while putting in evidence the accelerated metallic bond formation at the coating/substrate during the testing procedure. Ti64 is also chosen due to its oxidation resistance at elevated temperatures (up to 650 °C). This property restricts the native oxide layer growth as temperature increases facilitating the study of the influence of the initial substrate temperature on the coating adhesion strength without being hindered by the formation of a thick oxide layer. A Ti64 substrate is also used for the study of the hard-on-hard material combination.

Two substrate geometries and dimensions are used in this work. The rectangular Ti64 coupons have a size of 25.0 x 115.0 x 3.2 mm (W x L x T) and the cylindrical Ti64 coupons have a size of 25.4 x 45 mm (Ø x T). For the soft-on-hard material combination, the rectangular and cylindrical coupons are used, while for the hard-on-hard only the cylindrical geometry is used. Three different surface preparation methods are used: Mirror-polished surface, grit-blasted surface, and ground. The first two surface preparation methods are used in the soft-on-hard material combination to investigate if the preparation methodology has an influence on the overall coating deposition process. For the hard-on-hard material combination a ground surface is used as it has been reported that the surface preparation method has little to no influence on the overall deposition process, which is supported by the results for the soft-on-hard material combination [30,36,37]. For the mirror-polished surface preparation, the standard metallographic sample preparation is used and polishing suspensions of 9, 3 and 0.04 µm (Anamet, Quebec, QC, Canada) are used. The grit-blasted surface is achieved using Ebony Grit EG 20 (Opta Minerals, Waterdown, ON, Canada). This grit is mainly composed of iron oxide and silicon oxide. The respective arithmetic average roughness (Ra) are provided in the results section in Chapter 5.

4.1.2. Feedstock Powder Material

Two powders are used in this work: pure aluminum and In718. For the soft-on-hard material combination, pure aluminum is chosen due to its low hardness and relatively high ductility. Because of that, particle deformation upon impact with the substrate should be maximized, while the substrate deformation should be limited. Therefore, the influence of the substrate and coating temperature on the adhesion strength by favoring metallic bond formation becomes more evident. Pure aluminum is also chosen because it is one of the easiest materials to spray using the CS process, and thus, many studies in the field have been dedicated to understand the cold-spray deposition of aluminum coatings

[14,58,77–82]. Therefore, the influence of the substrate and coating temperatures on the CS process can be compared with previous studies. The gas-atomized pure aluminum powder (SST-A5001) (99.8% Al, Centerline (Windsor) Limited, Windsor, ON, Canada) is characterized by an irregular morphology, as presented in Figure 4.2 a). The 10th, 50th, and 90th size percentiles of the particle size distribution are 11.3, 25.8, and 60.3 µm, respectively.

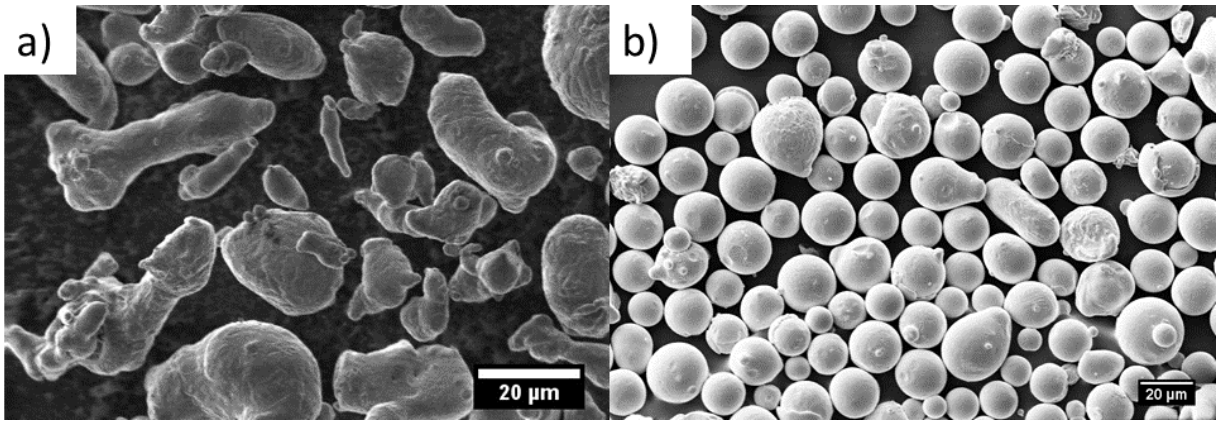


Figure 4.2 Feedstock powder materials used in this work. a) Pure aluminum and in b) Inconel 718.

To study the influence of the coating and particle impact temperatures, the hard-on-hard material combination is used. Because of that, an extremely hard powder that is capable of retaining its properties from 25°C to at least 650 °C is needed. This is because if a transitional behavior from a hard to a softer material is observed, it can be attributed to the relatively high coating and particle impact temperatures experienced by the material.

For the previous reasons, Inconel 718 is chosen because of its extremely good mechanical properties at a wide range of temperatures, from cryogenic temperatures up to 650 °C. In the as-received state, after the aging process, this alloy has limited plastic deformation due to its high yield strength (more than 1000 MPa) and it does not show significant thermal softening unless the material reaches higher temperatures than 650 °C. The commercially available gas-atomized In718 powder (TrueFrom718, Praxair Surface

Technologies, Indianapolis, IN, USA) is characterized by its spherical shape and smooth surface, as presented in Figure 4.2 b). The chemical composition (weight percentage) is Ni-19Cr-18Fe-Nb-5Ta-3Mo-1Ti. The powder particle size range is between 10 to 45 µm, with an average particle size of approximately 30 µm, according to the manufacturer's data sheet.

4.2 Experimental Equipment

4.2.1. Cold Spray System

A commercially available low-pressure CS system (SST-EPX, Centerline (Windsor) Limited, Windsor, ON, Canada) is used to produce all the samples in this work. The maximum operating pressure and temperature of the system are 3.45 MPa and 550 °C, respectively. The system is presented on Figure 4.3.

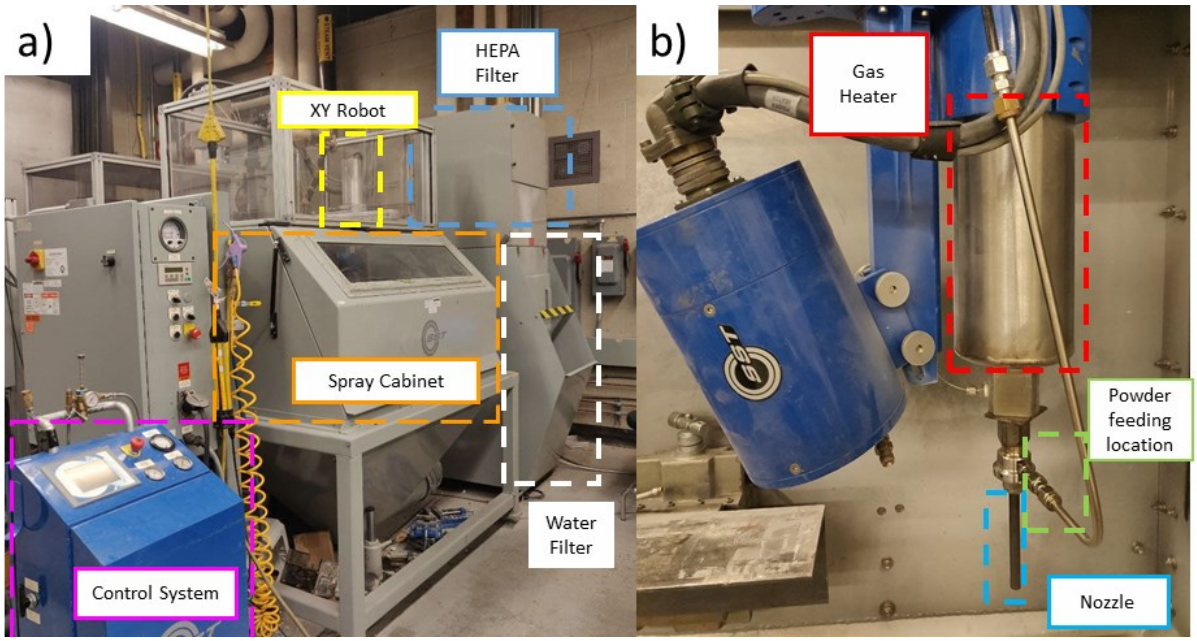


Figure 4.3 SST-EPX cold spray system. a) Overview of the of the spraying system, and b) interior of the safety cabinet.

The system is composed of a spray cabinet, control system, filtration system (HEPA and water filters), a gas heater, a nozzle, an XY-robot, and a commercially available controlled powder preheating unit. Gas pressure is regulated prior to its injection into the control system. For this work, nitrogen and helium will be used as the propellant gases. Once the gas is injected into the control system, the temperature of the gas is increased by the heater mounted to the robotic arm, presented on Figure 4.3 b). The temperature of the gas heater is controlled by a proportional–integral–derivative controller with feedback coming from a thermocouple at the nozzle inlet. The spraying process takes place inside the spray cabinet where the nozzle moves driven by the XY-robot controlled by an external computer. The pure aluminum powder is deposited using a PBI nozzle to avoid powder deposition at the inner walls of the nozzle during the spraying time when using relatively high stagnation parameters, as in this work. To produce In718 coatings, a WC-Co nozzle is selected. The PBI nozzle is switched to WC-Co nozzle to avoid erosion of the inner nozzle walls during the feeding of the hard In718 powder. Both nozzles have a throat diameter of 2 mm, and an exit diameter of 6.3 mm, and diverging length of 120 mm.

4.2.2. Powder Feeding

Powder is fed into the nozzle using a commercially available rotary powder feeder (AT-1200 Rotary, Thermach Inc., Appleton, WI, USA). The amount of powder fed into the nozzle is controlled using a perforated wheel that turns at a constant angular velocity. The amount of powder will be a function of the angular velocity and the number of holes perforated on the wheel. Nitrogen will be used as the carrier gas to deliver the powder from the powder feeder to the nozzle.

4.2.3. Controlled Powder Preheating Units

In this study, two controlled powder preheating units are used to increase the initial particle temperature prior to being fed into the nozzle diverging section, as shown in

Figure 4.4. The commercially available powder-preheating unit shown in b) (Centerline (Windsor) Limited, Windsor, ON, Canada) can increase the initial particle temperature up to 500 °C. This unit consists of a stainless steel coiled tube, and its temperature is increased by a heater radiating onto the coiled tube surface. The powder-preheating unit includes two built-in thermocouples, one at the inlet and the other at the outlet of the coiled tube, to control the tube wall temperature. The unit is assumed to reach a steady state temperature when the wall temperature difference between the inlet and outlet was less than 2 °C. Due to the extensive length of the heating tube, it is assumed that by the time the gas and the particles exit the powder-preheating unit, these reach the tube wall temperature. The configuration used to feed powder in the downstream section of the nozzle using this powder preheating unit is shown in Figure 4.4 b).

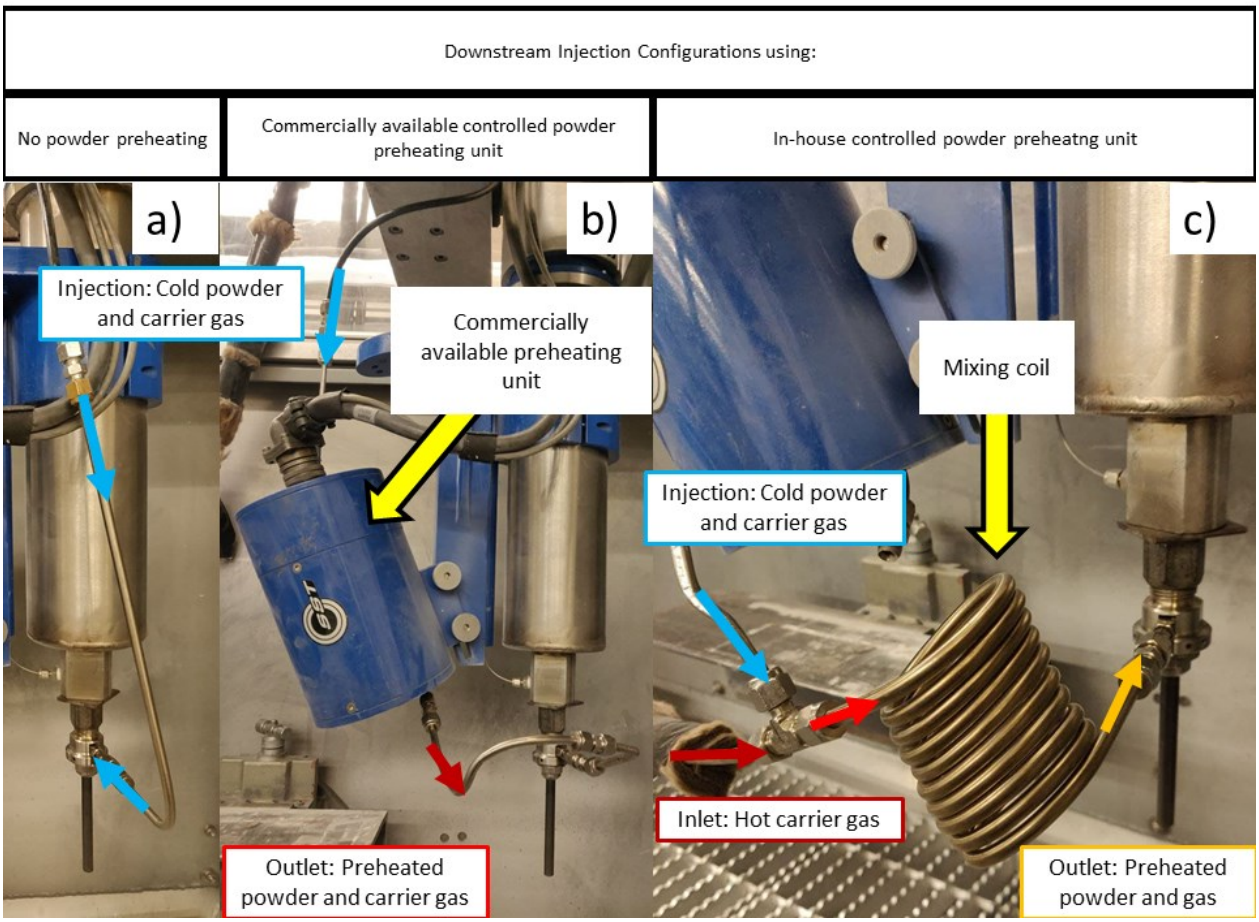


Figure 4.4 Downstream injection configurations using: a) no powder preheating, b) a commercially available controlled powder preheating unit, and c) an in-house controlled powder preheating unit. The insulation around the mixing coil in c) has been removed to provide a detailed perspective of the in-house controlled powder preheating unit.

To increase the initial particle temperature above 500 °C, an in-house powder preheater unit is used. The configuration used to feed powder in the downstream section of the nozzle using this powder preheating unit is shown in Figure 4.4 c). This preheating unit consists of a mixing T and a stainless steel coil in which hot (T_{hot}) and cold (T_{cold}) gases are brought together and mixed to reach a mixed gas temperature (T_{mixed}). The hot gas temperature is heated prior to its injection and its temperature is measured before entering the coil. The cold flow carries the powder into the in-house powder preheating

unit. The mixing coil is perfectly insulated from the exterior to avoid any potential heat loss to the environment. The mixing coil is long enough to ensure equilibrium between the gas and the particles at a temperature equal to T_{mixed}. A detailed image of the in-house preheater is presented in Figure 4.5.

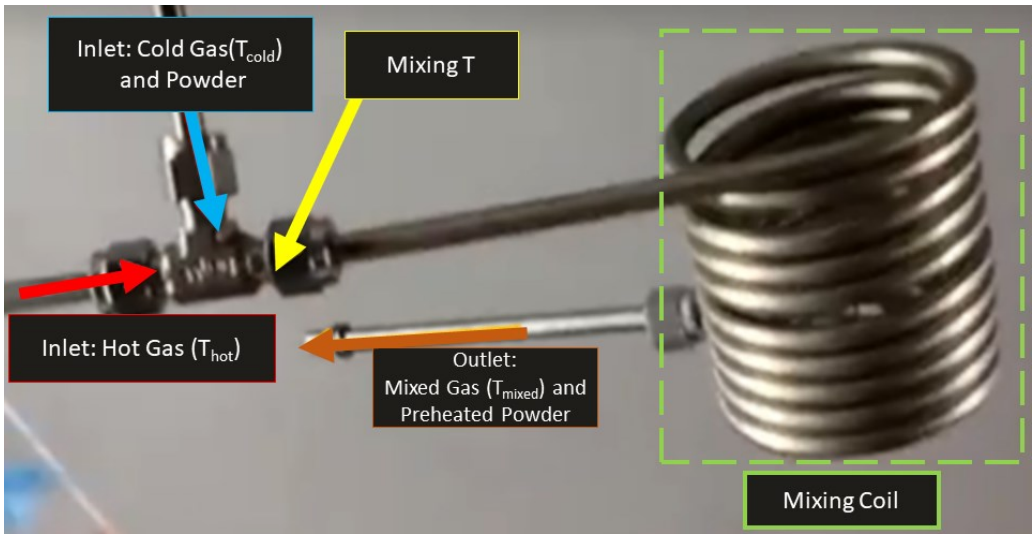


Figure 4.5 In-house powder preheater. Hot and cold gases are brought together and mixed inside a stainless steel coil. The insulation around the mixing coil has been removed to provide a detailed perspective of the in-house controlled powder preheating unit.

4.2.4. Induction Heating System

A 3kW induction heating system (Tucker Induction Sys. Inc. Shelby Township, MI, USA) is coupled to the CS process. The induction heating is used to preheat the substrate and the coating. The induction heater is positioned behind the spray cabinet, as show in in Figure 4.6 a). The induction coil is placed inside the spray cabinet through two perforated holes that allow its connection to the induction heating system located behind the spray cabinet (Figure 4.6 b)). The induction coil is made out of copper tubing with an outer diameter of 6.3 mm, and an inner diameter of 5.0 mm. The coil is composed of a total of four and half turns with an internal diameter of 42.0 mm, and an external diameter of 110.0 mm. Prior to the deposition process, the copper coil is covered with commercially available epoxy

resin, as presented in Figure 4.6 c). This is done to avoid material deposition and alter the electrical resistivity of the copper coil. The resin is also used to extend the coil life as the continuous bombardment of particles can erode the copper tubing and produce water leakage. Once the coil is covered with epoxy resin, it is placed inside the spray cabinet as presented in Figure 4.6 d). Once the deposition process is completed, the coil must be re-covered in epoxy resin, as the heat from the gas being decelerated by the gas damages and removes epoxy resin from the coil (Figure 4.6 e)). The rectangular and cylindrical substrate configurations when the induction heating system is used are presented respectively in Figure 4.6 f) and g).

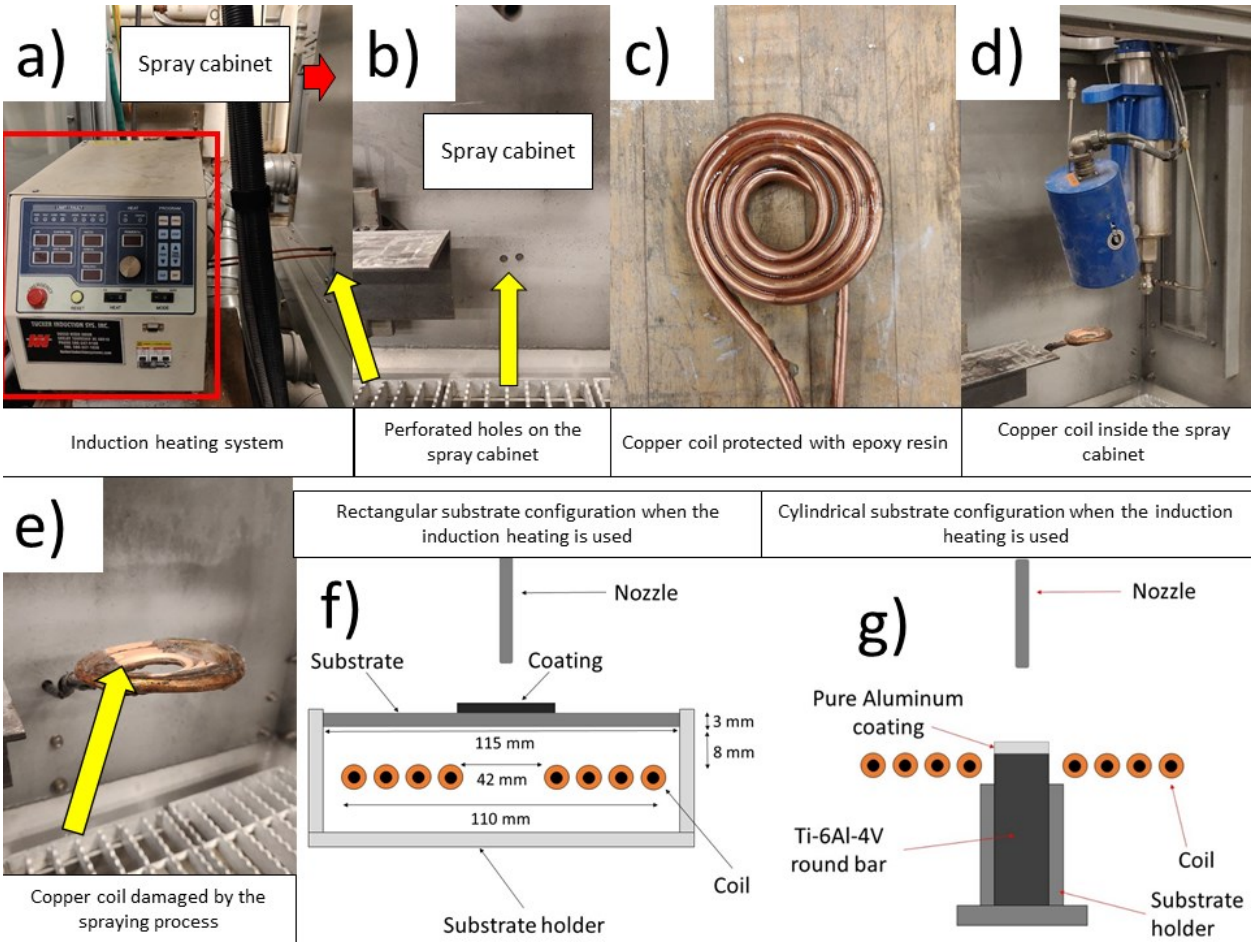


Figure 4.6 Induction heating system setup. In a) Induction heating system positioned behind the spray cabinet, in b) perforated holes that allow the copper coil connection to the induction heating system located behind the spray cabinet, in c) the copper coil covered in epoxy resin, in d) copper coil inside the spray cabinet, in e) zoomed-in image of the copper coil after the spraying process. Cross- sectional schematic view of the rectangular and cylindrical substrate configurations in f) and g), respectively.

4.2.5. Sample Preparation for Optical and Scanning Electron Microscope

After the spraying process, the samples are prepared for analysis using standard metallographic sample preparation procedures. The samples are first sectioned using a precision cut-off saw (Secotom-10, Struers, Mississauga, ON, Canada). Once the sample has the adequate size, the coupons are mounted using a phenolic plastic powder (LaboPress-3, Struers, Mississauga, ON, Canada). The mounted samples are then

mechanically ground and polished (TegraPol-31, Struers, Mississauga, ON, Canada). These equipment are shown in Figure 4.7.

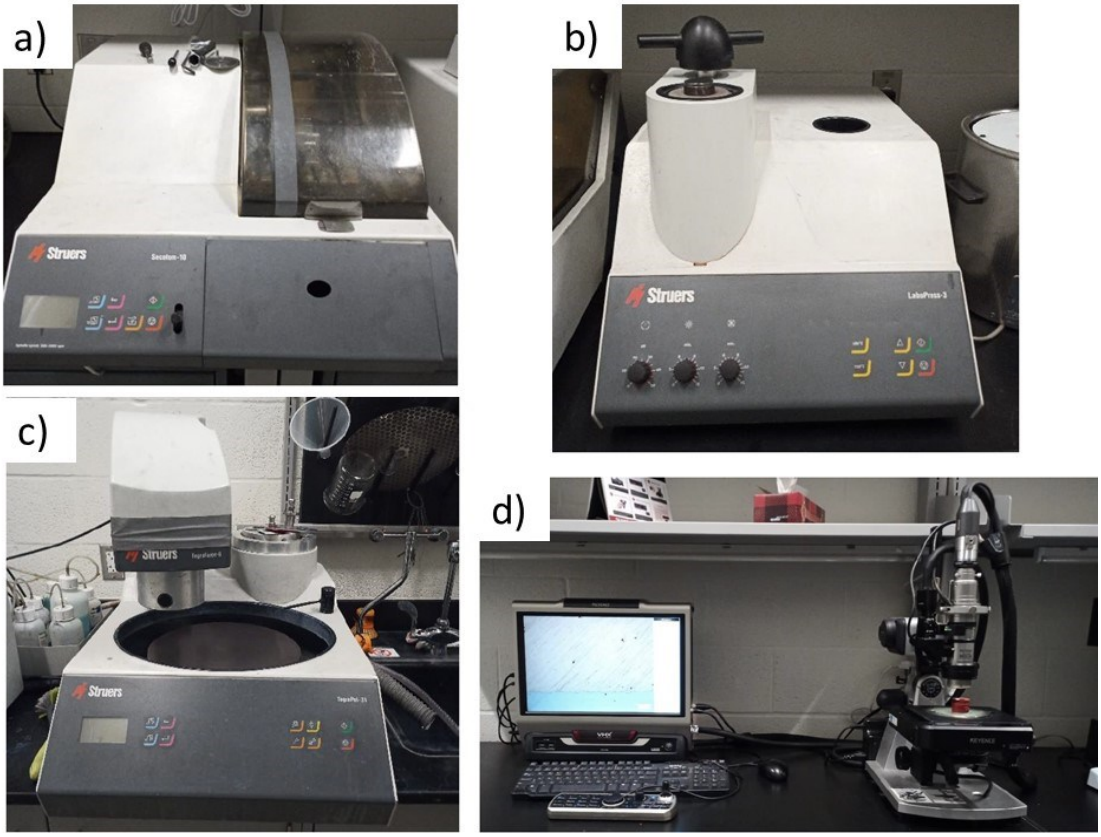


Figure 4.7 a) Secotom-10 precision cut-off saw, b) LaboPress-3 mounting machine, c) TegraPol-31 grinding and polishing machine and d) VHX-2000E optical microscope.

An optical microscope (Figure 4.7 d)) (VHX-2000E, Keyence, Canada) is used to get an overall assessment of the state of the coatings. The microscope is capable of providing a maximum magnification of 1000X through a digital camera mounted to an automated XY stage. The microscope is controlled using a computer that is able to move the stage and focus the sample. This microscope can produce 2D images and 3D compositions. The images taken with this microscope are used to calculate the porosity of the coatings.

4.2.6. Scanning Electron Microscope

To investigate the microstructure of the coatings, a scanning electron microscope (SEM) is used. The SEM (EVO-10MA, Carl Zeiss AG, Oberkochen, Germany), presented in Figure 4.8, is equipped with a tungsten source from which electrons are extracted and then accelerated to produce the images. The SEM can generate images using the secondary electron (SE) or the back-scattered electron (BSE) detectors. The SEM is also capable of performing other microscopy analyses using the energy dispersive X-ray spectrometer (EDS), electron backscatter diffraction (BSE) detectors. X-ray computed tomography (CT) is also available on the SEM.

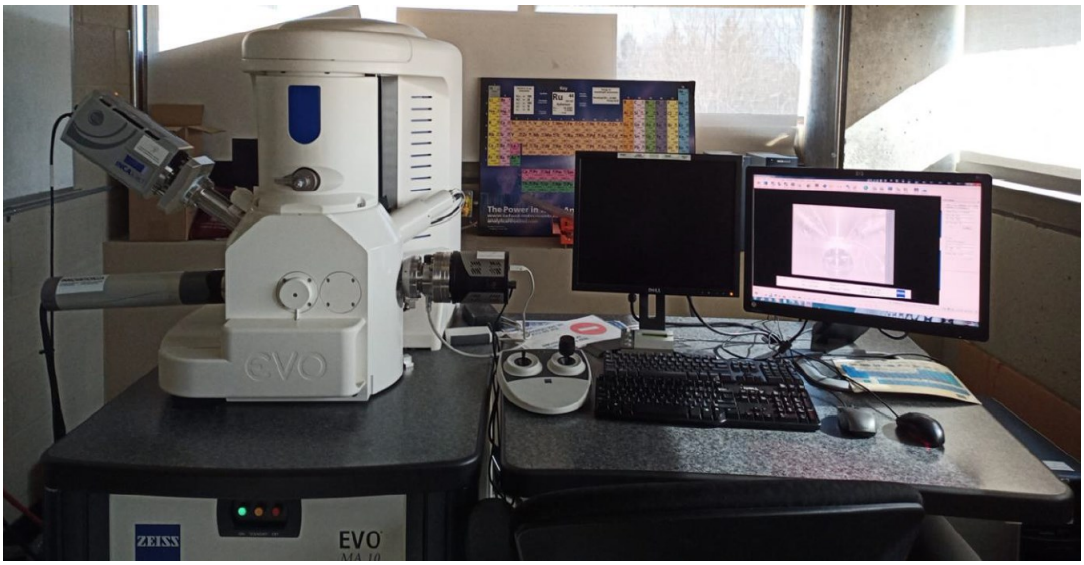


Figure 4.8 EVO-10MA scanning electron microscope.

4.2.7. Micro-hardness Testing

To quantify the influence of the initial substrate, coating, and particle impact temperatures, the coatings micro-hardness values are measured. To do so, a Duramin-10 (Struers, Mississauga, ON, Canada) is used. This equipment has range loading values from 0.05 kgf to 2 kgf. For this study, the coating micro-hardness is measured using a load of 0.3 kgf. The loading time is 10 seconds. The micro-hardness is measured from the

interface with the substrate up to the top of the coating every 50 μm. To avoid the effect of the stress field, the distance between two consecutive indentations is kept at 3 times the indentation size. This testing strategy follows the procedure reported by previous studies [13,128]. To properly characterize the sample, the testing procedure is repeated twice in different regions of a cross-section and in two different cross-sections. All the values are then averaged.

4.2.8. Splat Adhesion Strength Testing

To quantify the influence of the initial substrate temperature on the adhesion strength of individual pure aluminum particles on hard Ti64 substrates, a Micro-Combi Scratch Tester (Anton Paar, Graz, Austria) equipped with a light optical microscope (LOM) is used, as presented in Figure 4.9. A stylus with a semicircular cross section and a diameter of 100 μm is used to shear a particle. A normal force (F_n) of 100 mN is applied on the stylus to ensure that contact is maintained with the substrate. To calculate the adhesion strength of a particle, the tangential force (F_t) exerted on the stylus as a function of the scratch length and the projected area of the particle are used.

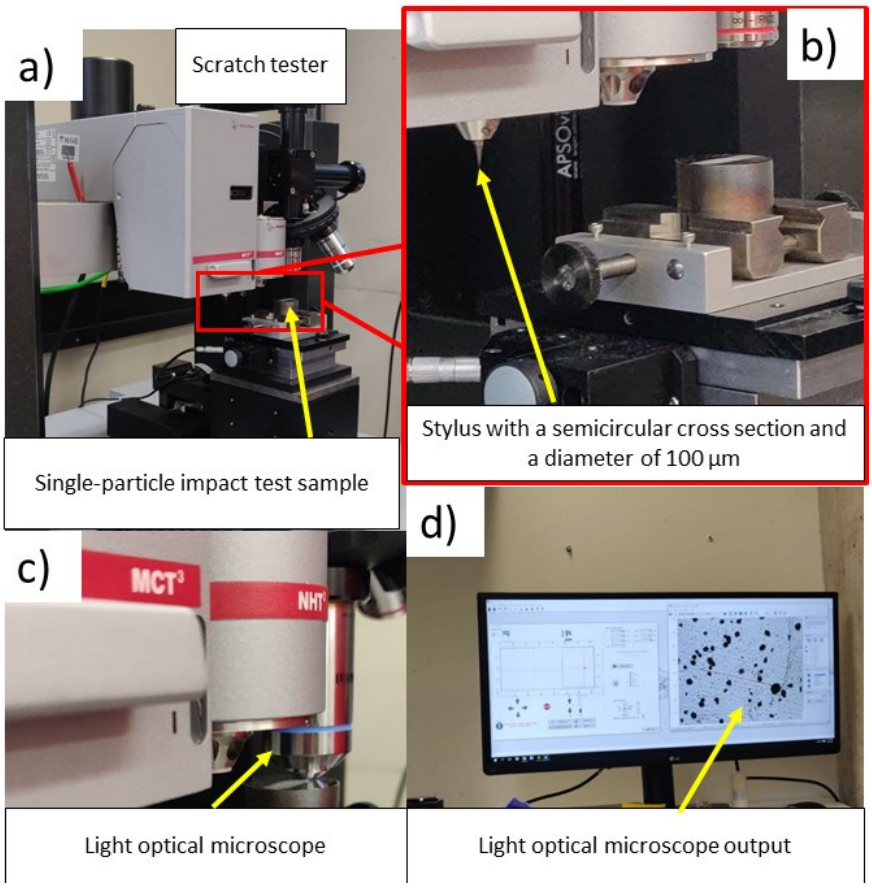


Figure 4.9 Micro-combi scratch tester. In a) overall setup of the equipment, in b) zoom-in image of the testing zone, in c) light-optical microscope objective, and in d) the output of the light-optical microscope objective.

4.2.9. Particle Distribution

The pure aluminum powder size distribution is characterized using a laser diffraction particle analyzer (Microtrac 3550, Nikkiso, Japan). To obtain the particle distribution, a sample of the powder is first left for 12 hours in a solution to remove any possible agglomeration of the particles that could exist. The samples are then vibrated and mixed in an aqueous solution inside the equipment. Finally, the solution is passed through to the dynamic analyzer, and the data is subsequently retrieved.

4.2.10. Tensile Strength

To assess the influence of the coating temperatures on the mechanical properties of the as-produced samples, the soft-on-hard material combination is used and the tensile strength of the pure aluminum coatings is measured following the ASTM-E8 standard. The sample thickness is 1.50 mm and three testing samples are produced. The samples are deposited using the Ti64 rectangular coupons and the spray setup presented in Figure 4.6 f). Once the samples are sprayed, the coatings are machined to the adequate geometry and tested in a universal testing system (Instron 4202, Norwood, MA, USA).

4.2.11. Adhesion Strength

The influence of the substrate and coating temperature on the coating adhesion strength is quantified using the soft-on-hard material combination. The adhesion strength of the pure aluminum coatings is obtained following the ASTM-633C standard. Therefore, round cylindrical Ti64 coupons are used. The cylindrical coupons are positioned in the middle of the coil as shown in Figure 4.6 g). Once the coatings are sprayed on the Ti64 coupons, the coatings are machined down to the adequate thickness (400 μm). After the machining process, the coatings are glued to a counter coupon using FM-1000 glue. The samples are then cured for 5 hours at 190 ºC. After the curing process, the samples are pulled in a universal testing machine.

4.2.12. Deposition Efficiency

To quantify the role of the initial substrate, coating, and particle impact temperatures on the coating production process, the deposition efficiency is measured. To do so, a constant feed rate is used and the substrate weight is measured before and after the spraying process. The DE is calculated from the ratio between the mass gained and the total powder into the nozzle, as presented by Eq. 4.1:

$$DE(\%) = \frac{Mass\ of\ the\ Substrate\ After\ the\ Coating\ Process}{Initial\ Masss\ of\ the\ Substrate} \times 100 \quad \text{Eq. 4.1}$$

4.2.13. Other Relevant Tools and Equipment

Image J

To quantify the porosity of the coatings, the open source Image J software is used. The porosity measurements are performed four times in different spots of a cross section. The contrast method is used to quantify the value.

Surface Roughness Meter

To measure the surface roughness of the substrate, a profilometer equipped with a 5 µm diamond stylus (Phase II, SRG-4000, NJ, USA) is used. The profilometer is capable of measuring values of Ra, Rz, Rq, and Rt. The resolution of this equipment is 0.001 µm.

Non-contact Infrared Thermometers

The substrate and coating temperatures are monitored using a RAYGPRSF non-contact infrared thermometer (Raytek, Santa Cruz, CA, USA), which has a working temperature range from -18 to 538 °C. For the production of samples with substrate and coating temperatures above 550 °C, a non-contact infrared thermometer OptCT3MH2SF (Optris, Portsmouth, NW, USA) is used. This infrared thermometer has a working range from 200 up to 1500 °C. Due to the different temperature working ranges, two infrared thermometers are required to accurately measure the time-temperature history during the spray time.

To calibrate the infrared thermometers, the substrate is heated from 25 to 300 °C, and the substrate time-temperature history is recorded using a thermocouple, as shown in Figure 4.10. Then, using an infrared thermometer with an emissivity value, such as 0.40, the

substrate time-temperature history is recorded. If the temperature difference is larger than 5 °C, the process is repeated with a different emissivity value in an iterative manner. The infrared thermometer is set to be calibrated once the temperature difference is less than 5 °C. For the RAYGPRSF non-contact infrared thermometer, it is found that an emissivity of 0.65 produces a similar substrate time-temperature history as the thermocouple. This process is also performed for the non-contact infrared thermometer OptCT3MH2SF and the Inconel 718 coating.

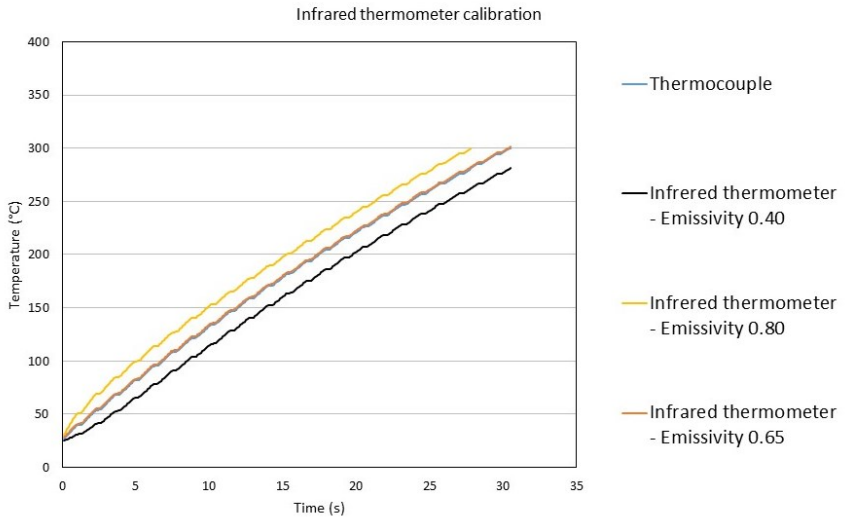


Figure 4.10 Calibration of the RAYGPRSF non-contact infrared thermometer for a Ti64 substrate in the 25 to 300 °C range.

4.3 Numerical Model Structure

4.3.1. Electromagnetic Model: Eddy Current Density Distribution

Studies using induction heating systems to increase the coating temperature during the spray time have not been reported, and thus, it is still unclear if eddy currents may form within a 100 µm coating to heat the latter. Consequently, in this work, Ansys Maxwell 2019 is used to predict the potential development of an eddy current density distribution within 100 µm pure aluminum and In718 coatings.

The eddy current density distribution within the coating geometries are predicted using a frequency-dependent 3D model. In this model, the resulting magnetic field (H) is calculated at a given frequency due to an AC source. The frequency-dependent 3D model has an adaptive mesh solution. This means excessive mesh operations are not required and over-defined meshes can lead to extensive computational times and time consuming calculations. The adaptive mesh tool refines after each iteration the regions where the resulting magnetic field is stronger, while the rest of the volume uses a coarser mesh to minimize the computational time. A 3-node adaptive uniform mesh is used. At least 1 million elements are used for all the simulations. As a convergence criterion, the energy error percentage must be less than 0.02% and the delta energy percentage between last and second-to-last pass must be less than 0.02%. A maximum number of 30 iterations for the solution is set. For none of the geometries, the maximum number is reached.

The default and only boundary condition is the "natural" boundary condition which is automatically applied on all surfaces of the problem space. In other words, there are no discontinuities in the magnetic field due to magnetic insulators. From the resulting magnetic field (H), the eddy current density distribution for any metallic piece can be predicted, as demonstrated in Chapter 2 (Section 2.4.1).

To accurately predict the eddy current density distribution produced by the electromagnetic field, the copper coil, the substrate and the coating are drawn using the computer aided design (CAD) tool available in Ansys Maxwell 19, as presented in Figure 4.11. The substrate, coating and coil position and dimensions used in the electromagnetic model are identical to the information provided in section 4.4.1 "Feedstock Substrate Material" and section 4.2.4 "Induction Heating System". To predict the eddy current density distribution within 100-µm pure aluminum and In718 coatings, the geometries presented in Figure 4.11 c) and d) are used. A 100-µm coating size is selected because it is the thickness of the first deposited layer produced by one nozzle pass over the substrate

when these two powders are sprayed. For the rectangular configuration, the coating dimensions are 14 x 25 x 0.10 mm (L x W x T), while for the cylindrical configuration, the coating dimensions are 25 x 0.10 mm (Ø x T). These dimensions are identical to the size of the experimentally produced coatings.

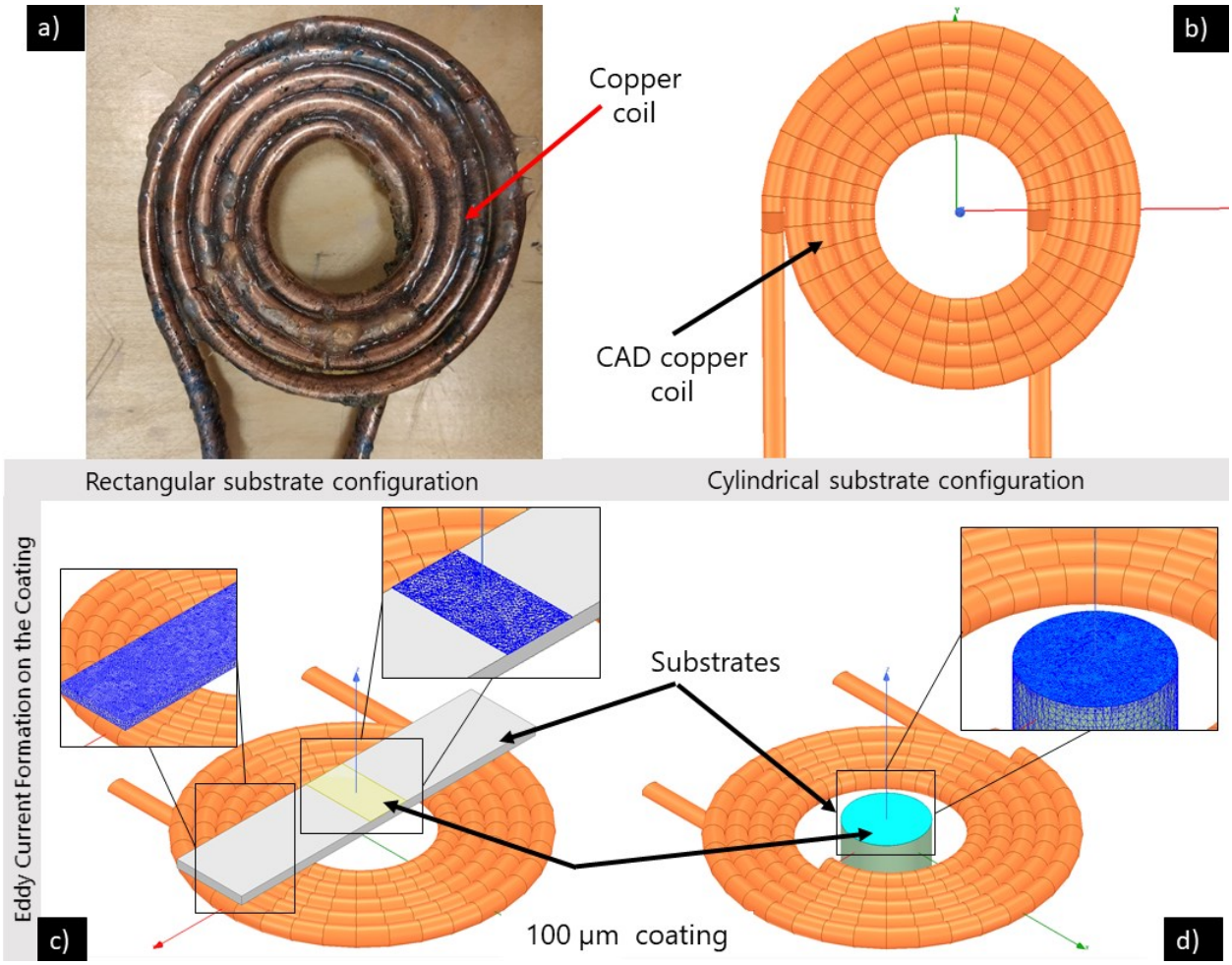


Figure 4.11 Computer aided designed geometries used to predict the eddy current density distribution within a 100 µm coating. The copper coil used in the experimental section of this work is presented in a) and in b) the CAD copper coil used for the electromagnetic simulations. Substrates with a 100 µm coating on top of the rectangular and cylindrical substrates are presented in c) and d), respectively.

As demonstrated in Chapter 2 (Section 2.4.1), to estimate the eddy currents inside a metal due to an electromagnetic field, the Maxwell Equations and the constitutive relationships between the electric displacement field (D), the electric field (E), the magnetic field (H) and the magnetic flux density (B) are required. The Maxwell-Àmpere equation (Eq. 4.2), which after mathematical manipulation can be re-written as Eq. 4.6 for a conductor in which eddy currents occur, is used to calculate H and from there the eddy currents density distribution can be obtained.

$$J = \nabla \times H \quad \text{Eq. 4.2}$$

$$\frac{\partial B}{\partial t} + \nabla \times E = 0 \quad \text{Eq. 4.3}$$

$$\nabla \cdot D = \varphi_{freecharge} \quad \text{Eq. 4.4}$$

$$\nabla \cdot B = 0 \quad \text{Eq. 4.5}$$

$$\nabla \times \left(\frac{1}{\sigma + j\omega\varepsilon_r\varepsilon_{vac}} + \nabla \times H\right) = -j\omega\mu_r H \quad \text{Eq. 4.6}$$

Table 4.1 presents the current and frequency values used in this work to predict the eddy current density distribution within the coatings. The current and frequency values presented in Table 4.1 are chosen as these are typical values used in industrial environments and commercial induction heating systems.

Table 4.1 AC source boundary conditions

AC source boundary conditions	Set 1	Set 2	Set 3	Set 4	Set 5
Current (A)	58	62	100	58	58
Frequency (kHz)	192	192	192	250	300

In these electromagnetic models, the relative permeability and electrical conductivities are needed as material properties. Ti64, pure aluminum, In718, and copper electromagnetic properties used to predict the eddy current density distribution within the substrate and the coating are presented in Table 4.2.

Table 4.2 Material properties of the different materials used in the electromagnetic models [73,76,99].

Material properties	Copper	Ti64	Aluminum	In718
Conductivity (S/m)	58,000,000	588,325	40,000,000	826,446
Magnetic permeability (μ_r)	0.999991	1.0005	1.00021	1.0011

A frequency-dependent solver is used to calculate the eddy current density distribution within the coating. This solver follows the steps presented in Figure 4.12 to calculate a solution to Eq. 4.6 and the Maxwell equations under specific boundary conditions, frequencies, current values, and material properties:

1. The model is initialized with the material properties and the specified boundary conditions.
2. A solution is calculated, called adaptive solution, as an approximate solution.
3. The convergence criteria are checked (delta energy and energy error percentages).
4. If the adaptive solution does not fulfil the convergence criteria, then the mesh is refined and the solution is iterated and a new solution is calculated.
5. If the maximum number of passes is reached or the convergence criteria are fulfilled, then the adaptive solution becomes the final solution and the magnetic and electric fields are calculated.
6. From the magnetic and electric field, other parameters and quantities are calculated, such as the eddy current density distribution.

7. If more than one frequency is evaluated, then the solver proceeds to the next one. If only one frequency is analyzed, then the solver stops.

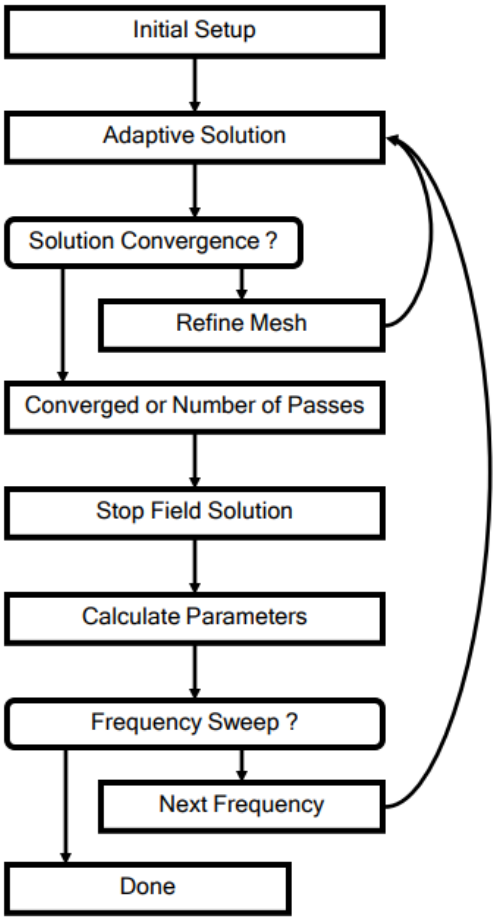


Figure 4.12 Ansys Maxwell frequency-dependent solution steps.

4.3.2. Single-Particle Impact and Adhesion Strength Bonding Simulation

A single-particle impact model and an adhesion strength finite element model are carried out to further understand the influence of the initial substrate temperature on the CS deposition process. The single-particle impact model is carried out to gain further understanding of the impact process and to access data that cannot be obtained experimentally due to the challenging time scales. Additionally, the finite element model is used to better understand the deformation behavior at particle/substrate interface and

deposition mechanisms as a function of initial substrate temperature. The single-particle impact finite element model is carried out using the soft-on-hard material combination. A detailed description of the geometries and boundary conditions used in the single-particle impact model is provided in Chapter 5 (section 5.2).

Previous studies have outlined the procedure to carry out a finite element model capable of predicting with extremely good accuracy the adhesion strength of CS coatings due to mechanical anchoring [36,38]. Following the outlined procedure by previous studies, a similar model is used to predict the mechanical anchoring contribution on the overall coating adhesion strength of aluminum coatings on TI64 substrates as a function of the initial substrate temperature. This model has a complementary purpose and it aims to provide further support of the experimental coating adhesion strength evaluation. Due to the selected material combination used to evaluate the influence of the initial substrate temperature on the adhesion strength (Al-on-Ti64), the mechanical contribution on the overall adhesion strength is likely to be non-significant (even at higher initial substrate temperatures). Therefore, if an improvement on the overall adhesion is observed during the experimental procedure, the results can be attributed to the enhanced metallic bonding. This can unequivocally be concluded because the finite element model is capable of predicting with extremely good accuracy the adhesion strength of CS coatings due to mechanical anchoring, but it lacks the ability to estimate the metallic bond contribution strength. A detailed description of the geometries and boundary conditions used in the adhesion strength finite element model is provided in Chapter 5 (section 5.3).

These finite element models are carried out using the commercially available software Abaqus/Explicit. The single-particle impact and the adhesion strength models are solved using non-linear analyses. In this type of analyses, the solution is found by specifying the loading as a function of time and incrementing time to obtain the nonlinear response. Abaqus/Explicit breaks the simulation into a number of time increments and finds the

approximate equilibrium configuration at the end of each time increment. The time increments are not arbitrarily selected, the stability limit is used for the time incrimination, which dictates the maximum time increment used by the explicit solver. An approximation of the stability limit is described by Eq.4.7

$$\Delta t_{stable} = \frac{L_{small}}{W} \text{ Eq. 4.7}$$

Where L_{small} is the smallest element dimension used in the meshing process and W is the wave speed of the material, defined as follows:

$$W = \sqrt{\frac{E_{young}}{\rho}} \text{ Eq. 4.8}$$

In Eq. 4.8, E_{young} is the material young modulus.

Materials can experience a change in volume and shape as a consequence of an arbitrary load. The hydrostatic and deviatory behaviors are related to the change in volume and shape, respectively. To model the hydrostatic response to an arbitrary load, an equation of state (EOS) is used. The energy conservation equation (Eq. 4.9) describes that the change in internal energy per unit mass E_m (left side of the equation) is equal to the rate at which work is being produced by stresses (first and second term right hand side) plus the rate at which heat is being added (third term on the right hand side), such that:

$$\rho \frac{\partial E_m}{\partial t} = (p - p_{bv}) \frac{1}{\rho} \frac{\partial \rho}{\partial t} + S : \dot{e} + \rho \dot{Q} \text{ Eq. 4.9}$$

Where p is the pressure stress, p_{bv} pressure stress due to the bulk viscosity (resistance to deformation), $\dot{e}$ is the deviatoric part of strain rate, S is the deviatoric stress tensor, and $\dot{Q}$ is the heat rate per unit mass. An EOS as a function of the density and the E_m can be defined such that:

$$p = f(\rho, E_m) \text{ Eq. 4.10}$$

In this work, the Mie-Grüneisen equation of state is used to model the hydrostatic deformation in the single-particle impact model as well as for the adhesion strength model. The EOS can be written as follows:

$$p - p_H = \rho\Gamma(E_m - E_H) \quad \text{Eq. 4.11}$$

In Equation 4.11, p_H and E_H are the Hugoniot pressure and specific energy per unit mass, respectively, and Γ is the Mie- Grüneisen constant defined as:

$$\Gamma = \frac{\Gamma_0 \rho_{ref}}{\rho} \quad \text{Eq. 4.12}$$

Where ρ_{ref} is the density at a reference state and Γ_0 is a material constant.

The Hugoniot pressure becomes only a function of density, as shown by Eq. 4.13, and is generally defined from fitting experimental data.

$$p_H = \frac{\rho_{ref} c_{ref}^2 \beta}{(1-s\beta)^2} \quad \text{Eq. 4.13}$$

Where c_{ref} is the speed of sound at the reference state, s is the Hugoniot slope, and $= 1 - \frac{\rho_{\text{ref}}}{\rho}$. The Hugoniot energy, E_H, is related to the Hugoniot pressure as follows:

$$E_H = \frac{p_H \beta}{2\rho_{ref}} \quad \text{Eq. 4.14}$$

Using the Eq.4.13 and Eq.4.14, the Mie-Grüneisen EOS can be re-written as follows:

$$p = \frac{\rho_{ref} c_{ref}^2 \beta}{(1-s\beta)^2}\left(1 - \frac{\Gamma_0 \beta}{2}\right) + \Gamma_0 \rho_{ref} E_m \quad \text{Eq. 4.15}$$

To use the Mie-Grüneisen EOS is Abaqus/Explicit, the material dependent constants (c_{ref}, ρ_{ref}, Γ_0) are required as input parameters to model the hydrodynamic stress.

The deviatory response is predicted using a linear isotropic elastic model. The deviatoric behavior is governed by the following relationship:

$$S = 2G_e e^{dev} \quad \text{Eq. 4.16}$$

S is the deviatory stress, G_e is the elastic shear modulus and e^{dev} is the deviatoric elastic strain. The linear isotropic relationship presented in Eq. 4.16 is used to predict the deviatoric stress in the single-particle impact and the adhesion strength models.

The Johnson-Cook (JC) model is used for the plastic response of the single-particle impact and adhesion strength numerical models. This plasticity model is ideal for problems in which rate-dependent effects and kinematic hardening are expected. Using the Johnson-Cook model, the yield stress can be calculated as follows:

$$\sigma_y = \left[A + B\bar{\varepsilon}^{\,n}_{plastic}\right]\left[1 + CIn\left(\frac{\dot{\varepsilon}_{plastic}}{\dot{\varepsilon}_{JCref}}\right)\right]\left[1 - \left(\frac{T - T_{ref}}{T_{melting} - T_{JCref}}\right)^m\right] \quad \text{Eq. 4.17}$$

Where A, B, and C are Johnson-Cook material constants, n is the strain hardening constant, m is the thermal softening power coefficient, $\bar{\varepsilon}_{plastic}$ is the equivalent plastic strain, $\dot{\varepsilon}_{plastic}$ is plastic strain rate, $\dot{\varepsilon}_{JCref}$ is strain rate at which the Johnson-Cook parameters were obtained, T_{JCref} is the reference temperature at which Johnson-Cook parameters were obtained, and T is the absolute current temperature. This plasticity model has limitations at very high strain rates (>x$10^7\ s^{-1}$) and it has been shown that the Preston-Tonks-Wallace (PTW) predicts more accurately the CS process particle/substrate deformation. However, PTW material model parameters are limited and not readily available for materials like Ti64 and In718. On the other hand, the JC materials constants for aluminum, TI64 and In718 can be found in the literature. For that reason, the JC plasticity model is used.

4.3.3. Computational Fluid Dynamic Model: Gas and particle interaction

To experimentally measure the particle impact temperature has been demonstrated to be a technically challenging and time-consuming process [63]. This is caused by the relatively

low temperatures and high velocities experienced by the particles which cause the use of classical optical pyrometry impossible. For these reasons, a computational fluid dynamics (CFD) model has been recently developed, allowing the estimation of the particle impact temperature. The CFD model has been able to accurately predict the particle impact temperature based on experimental data obtained using high-speed, high-definition infrared imaging technique and a cold spray meter [63]. In this work, the extensively validated CFD model is also used to predict the particles impact temperature. A detailed description of the geometries and boundary conditions used in the CFD model is provided in Chapter 5 (section 5.5).

The extensively validated model is carried out using the commercially available Ansys Fluent, solving the mass, momentum and energy conservation equations. The compressible flow is solved assuming that the flow follows the ideal gas law described by Eq. 4.18.

$$\rho_{gas} = \frac{P_{op}+P_{local}}{\frac{R}{M_w}T} \quad \text{Eq. 4.18}$$

Where P_{op} is the operating pressure, defined as atmospheric pressure, P_{local} is the local static pressure relative to the atmospheric pressure, and M_w is the molecular weight. The temperature is computed from the energy equation.

The mass conservation is presented in Eq. 4.19

$$\frac{\partial \rho}{\partial t} + \nabla \cdot (\rho \vec{v}) = S_m \quad \text{Eq. 4.19}$$

Where S_m is the mass added to the continuous phase from the dispersed second phase, i.e. powder particles injected inside the flow. It has been shown that the effect of the particles on the gas phase and the particle-particle interactions are not significant because of the low volume fraction of the powder particles with respect of the gas flow (volume fraction <10%). Therefore, the S_m in Eq. 4.19 can be neglected.

Conservation of momentum is presented by Eq. 4.20

$$\frac{\partial}{\partial t}(\rho\vec{v}) + \nabla\cdot(\rho\vec{v}\vec{v}) = -\nabla P + \nabla\cdot(\bar{\bar{\tau}}) + p\vec{g} + \vec{F} \quad \text{Eq. 4.20}$$

where P is the pressure, $p\vec{g}$ and $\vec{F}$ are the gravitational and external body forces (like lift force or external body force), respectively. Gravitational and body forces are also considered to be negligible. $\bar{\bar{\tau}}$ is the stress tensor and it is described by Eq. 4.21

$$\bar{\bar{\tau}} = \mu\left[(\nabla\vec{v} + \nabla\vec{v}^T) - \frac{2}{3}\nabla\cdot\vec{v}I\right] \quad \text{Eq. 4.21}$$

Where μ is the molecular viscosity, I is the unit tensor, and the second term on the right hand side is the effect of volume dilation.

The energy equation is given by Eq. 4.22:

$$\frac{\partial(\rho En)}{\partial t} + \nabla\cdot(\vec{v}[\rho En + P]) = \nabla\cdot\left(k_{eff}\nabla T - \sum_j h_{s_j}\vec{J}_j + \left[\bar{\bar{\tau}}_{eff}\cdot\vec{v}\right]\right) + S_h \quad \text{Eq. 4.22}$$

The first three terms on the right-hand side of Eq. 4.22 represent energy transfer due to conduction, species diffusion, and viscous dissipation, respectively. $\vec{J}_j$ is the diffusion flux of species, k_{eff} is the effective conductivity ($k_{eff} = \frac{1}{Pr}C_p\mu_{eff}$ in which P_r is the Prandtl number). S_h are the source terms to take into account heat from chemical reactions, which are null in the CS process as there no chemical reactions. The energy term, En, is comprised of multiple terms to consider internal energy and kinetic energy, as shown by Eq. 4.23:

$$En = h_s - \frac{P}{\rho} + \frac{v^2}{2} \quad \text{Eq. 4.23}$$

Where h_s is the sensible enthalpy and it is defined as follows for ideal gases:

$$h_s = \sum_j Y_j\ h_j \quad \text{Eq. 4.24}$$

And where Y_j is the mass fraction of the species j and h_j is defined as:

$$h_j = \int_{T_{ref}}^{T} C_{pj} dT \quad \text{Eq. 4.25}$$

Where T_{ref} = 298.15 K. In Eq. 4.22, the $\bar{\bar{\tau}}_{eff} \cdot \vec{v}$ term describes the thermal energy created by viscous shear in the flow. Compressible flows typically exhibit important viscous dissipation; therefore, this term must be considered when the energy equation is solved.

Turbulence is the three-dimensional unsteady random motion observed in fluids at moderate to high Reynolds numbers. Turbulence is, in principle, described by the Navier-Stokes equations, but in most situations it is not feasible to resolve the wide range of scales in time and space by Direct Numerical Simulation (DNS) as the CPU requirements would by far exceed the available computing power. For this reason, averaging procedures have to be applied to the Navier-Stokes equations to filter out all, or at least, parts of the turbulent spectrum. The most widely applied averaging procedure is Reynolds-averaging (which, for all practical purposes is time-averaging) of the equations, resulting in the Reynolds-Averaged Navier-Stokes (RANS) equations. By this process, all turbulent structures are eliminated from the flow and a smooth variation of the averaged velocity and pressure fields can be obtained. However, the averaging process introduces additional unknown terms into the transport equations (Reynolds Stresses and Fluxes) that need to be provided by suitable turbulence models (turbulence closures).

RANS models offer an economic approach for computing complex turbulent flows. One of the most well-known RANS models is the κ-ϵ. This turbulence model is based on the transport equations for the turbulence kinetic energy (κ) and its dissipation rate (ϵ). Previous studies have demonstrated that the most accurate model to evaluate the turbulent nature of a flow in the CS process is the renormalized group (RNG) κ-ϵ model [63,129]. For that reason, in this work, the RNG-derived κ-ε model is used and this model is described by the following equations:

$$\frac{\partial}{\partial t}(\rho K) + \frac{\partial}{\partial x_i}(\rho K u_i) = \frac{\partial}{\partial x_j}\left(\alpha_K \mu_{eff} \frac{\partial K}{\partial x_j}\right) + G_K + G_b - \rho - Y_M + S_K \quad \text{Eq. 4.26}$$

and

$$\frac{\partial}{\partial t}(\rho \epsilon) + \frac{\partial}{\partial x_i}(\rho \epsilon u_i) = \frac{\partial}{\partial x_j}\left(\alpha_\epsilon \mu_{eff} \frac{\partial \epsilon}{\partial x_j}\right) + C_{1\epsilon}\frac{\epsilon}{k}(G_K + C_{3\epsilon}G_b) - C_{2\epsilon}\rho\left(\frac{\epsilon^2}{k}\right) - R_\epsilon + S_\epsilon \quad \text{Eq. 4.27}$$

In these equations, G_K represents the generation of turbulence kinetic energy due to the mean velocity gradients, while G_b is the generation of turbulence kinetic energy due to buoyancy. Y_M represents the contribution of the fluctuating dilatation in compressible turbulence to the overall dissipation rate. The quantities α_k and α_ϵ are the inverse effective Prandtl numbers for κ and ϵ, respectively. Any potential additional user-defined source terms are taken into account by S_K and S_ϵ. The model constants $C_{1\epsilon}$ =1.42 and $C_{2\epsilon}$ = 1.68. $C_{3\epsilon}$ is the degree to which ϵ is affected by the buoyancy and it can be calculated $C_{3\epsilon} = \tanh\left|\frac{\nu}{u}\right|$. ν is the component of the flow velocity parallel to the gravitational vector and u is the component of the flow velocity perpendicular to the gravitational vector. In this way, $C_{3\epsilon}$ will become 1 for buoyant shear layers for which the main flow direction is aligned with the direction of gravity. For buoyant shear layers that are perpendicular to the gravitational vector, $C_{3\epsilon}$ will become zero. Part of the RNG procedure is to generate a differential equation for turbulent viscosity as shown below:

$$d\left(\frac{\rho^2 K}{\sqrt{\epsilon\mu}}\right) = 1.72\,\frac{\hat{\nu}}{\sqrt{\hat{\nu}^3 - 1 + C_{\nu x}}}\,d\hat{\nu} \quad \text{Eq. 4.28}$$

Where $\hat{\nu} = \frac{\mu_{eff}}{\mu}$ and $C_{\nu x} \approx 100$. Equation 4.28 provides a description of how the effective turbulent transport varies with the effective Reynolds number in order to better handle low-Reynolds number and near-wall flows.

To calculate the flow properties in the converging/diverging nozzle model, a pressure-based solver is used. The coupled algorithm solves the momentum and pressure-based

continuity equations together. The full implicit coupling is achieved through an implicit discretization of the pressure gradient terms in the momentum equations, and an implicit discretization of the face mass flux. Using the coupled approach offers some advantages over the non-coupled or segregated approach, such as SIMPLE algorithm. The coupled scheme obtains a robust and efficient single phase implementation for steady-state flows, with superior performance compared to the segregated solution schemes. This pressure-based coupled algorithm offers a good alternative to the density-based and pressure-based segregated algorithm. The governing equations controlling the flow properties is presented in Figure 4.13.

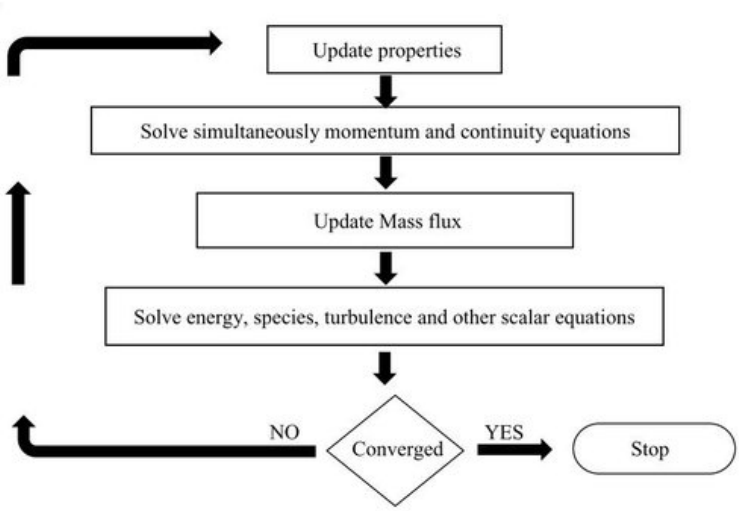


Figure 4.13 Illustration of the Coupled algorithm approach used by Ansys Fluent to solve the governing flow equations.

The steps are the following:

1. The flow properties (density, viscosity, specific heat, turbulent viscosity) are updated based on the initialization or the most recent solution.
2. The momentum and pressure-based continuity equations are solved simultaneously, in a coupled manner.

3. The mass flux is updated and with that the next set of equations is solved.
4. The energy, species, turbulence and other scalar equations are solved in a non-segregated manner.
5. The solution convergence is verified. If the solution has reached its convergence criteria, then solving algorithm stops. Otherwise, the steps are repeated until the solution has converged.

Chapter 5 - Results

This chapter is composed of five different sections. This is done to present the results obtained for the influence of the substrate, coating, and particle impact temperature on the CS deposition process for the two material combinations in a structured way. A detailed breakdown of each section and its relationship with each objective is presented in Table 5.1 The five sections of this Chapter address the objectives presented in Chapter 3.

Table 5.1 Objectives and specific section addressing each objectives

Objectives	Description of the Tasks to Complete Objective	Section Addressing Each Task to Complete Objective
Evaluate the role of the initial substrate temperature on the CS process.	1. Evaluate the Particle/Substrate Deformation at the Interface and the Adhesion Strength at a Single-particle Level 2. Measure the Substrate Time-temperature History 3. Measure the Deposition Efficiency and Coating Thickness 4. Measure the Coating Mechanical Properties	1. Section 5.2 and 5.4 2. Section 5.2 3. Section 5.2 4. Section 5.2 and 5.3
Characterize the influence of the coating temperature on the CS process	1. Predict the Coating Eddy Current Density Distribution 2. Measure the Coating Time-temperature History 3. Measure the Deposition Efficiency and Coating Thickness 4. Measure the Coating Mechanical Properties	1. Section 5.1 2. Section 5.5 3. Section 5.2 and Section 5.5 4. Section 5.3 and Section 5.5

Assess the importance of the particle impact temperature on the CS process	1. 2. 3.	Decouple the Initial Particle Temperature from the Gas Stagnation Temperature Predict the Particle Impact Temperature Characterize the CS Deposition Process as a Function of the Particle Impact Temperature	1. Section 5.5 2. Section 5.5 3. Section 5.5
Enhance the CS process performance based on the findings of the previous objectives			1. Section 5.2, Section 5.3 and Section 5.5

5.1 Induction Heating System Evaluation

Two studies have used the induction heating process as a method to increase the initial substrate temperature [49,126]. However, increasing the coating temperature using an induction heating system has never been investigated. In consequence, it is still uncertain if an eddy current density distribution may form within 100-µm pure aluminum and In718 coatings. Therefore, coatings matching the experimental size and dimensions are modeled to predict if an eddy current density distribution might develop within the consolidated material.

To determine the potential development of eddy currents within cold-sprayed coatings, 100-µm aluminum and In718 coatings are modeled. The eddy current density distribution, at the amplitude (or peak value) of the sinusoidal AC source, for 100-µm coatings is presented in Figure 5.1. The predicted eddy current density distribution for a 100-µm pure aluminum coating changes as a function of the coating shape, as shown in Figure 5.1 c) and d). This difference is attributed to the different geometry configuration, and thus, the different surface area exposed to the magnetic field, as has been previously discussed in Chapter 2. For the rectangular substrate configuration, it can be seen that the lowest eddy

current density values are located in the middle of the coating, as presented in Figure 5.1 c). This is because the magnitude of the magnetic field quickly decays towards the center having its lowest value in the middle of the coil. For the cylindrical substrate configuration, the pure aluminum coating exhibits a non-uniform eddy current density distribution, as presented in Figure 5.1 d). This result is caused by the coating and the first inner turn of the coil that have the smallest coil-to-coating air gap. Therefore, the magnetic field concentrates in that area resulting in a higher eddy current density distribution. This non-uniform distribution could potentially lead to an uneven heating pattern, especially for materials with low thermal conductivity such as Ti64 and In718. This result demonstrates the importance of having a good coil design to avoid the potential development of hot spots that could create a detrimental heating pattern on the substrate. For future studies, the coil shape should be optimized to avoid potential hot spots and an uneven density distribution, especially if material with low thermal conductivity are to be sprayed. These results also suggest that the current coil shape is potentially more efficient in creating an eddy current density distribution for the coating modeled under a rectangular substrate configuration.

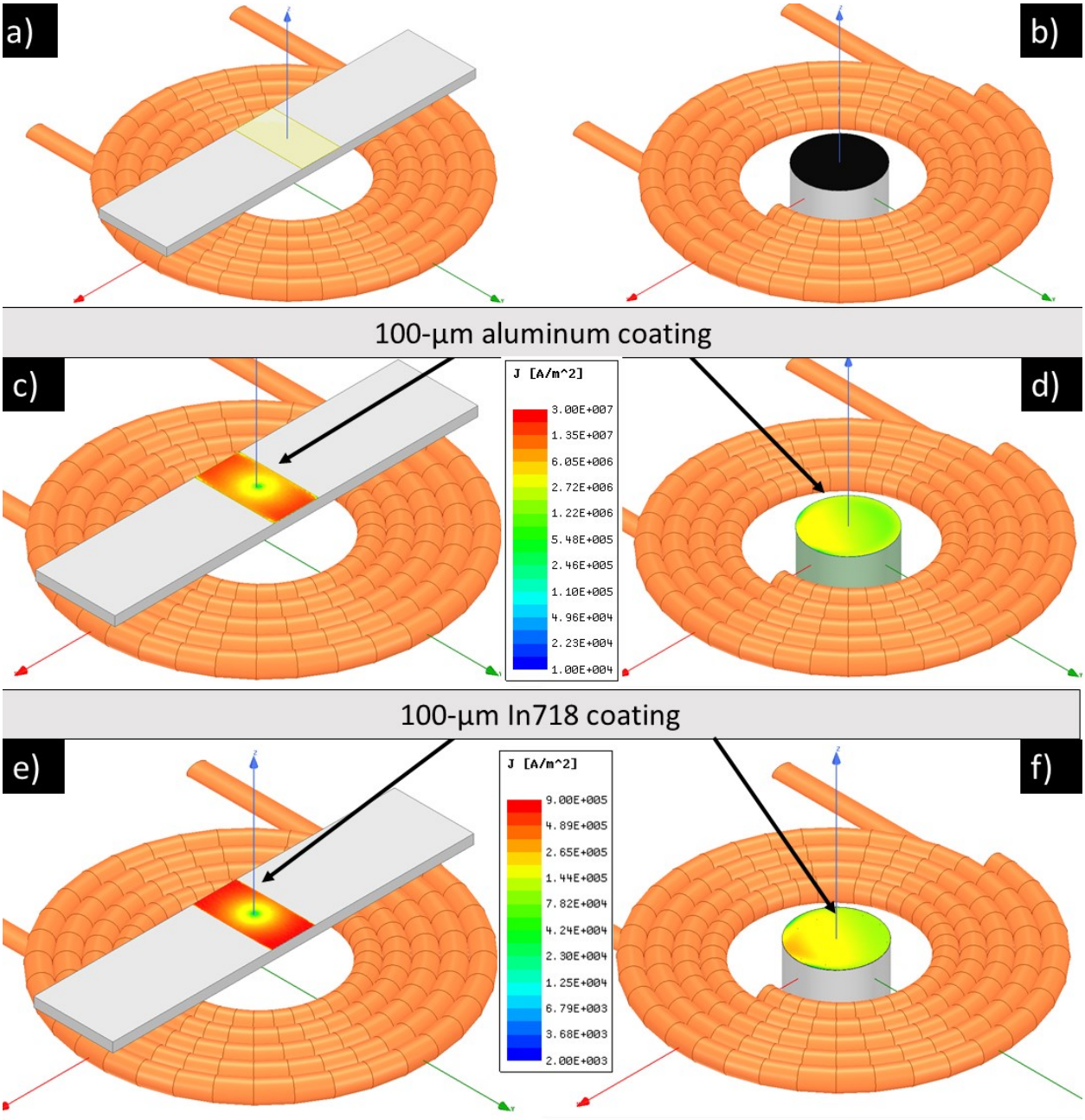


Figure 5.1 Finite element electromagnetic model of the Ti64 substrates and 100 µm coating. Isometric view a) the rectangular substrate configuration, and in b) of the cylindrical substrate configuration. c) to f) eddy current density distribution in a 100 µm coating. In c) and d), the coating is modeled as pure aluminum, while in e) and f) In718 is used as the coating material. The IH parameters were 58 A and 192 kHz. All the values are shown at the peak values of the sinusoidal AC source.

The eddy current density distribution for a 100μm In718 coating produced on top of rectangular and cylindrical substrates is also presented in Figure 5.1 e) and f), respectively. The predicted values are significantly lower in comparison to the values exhibited by pure aluminum. As presented in Chapter 2, the eddy currents are controlled by the electrical conductivity of a material ($J_{eddy} = \sigma E$). Thus, this difference is caused by the low electrical conductivity of In718 in comparison to pure aluminum. The electrical conductivity for aluminum is almost 50 times larger than the value for In718, as presented in Table 4.2. Using the rectangular substrate configuration, 58 A and 192 kHz as IH parameters (values used in Figure 5.1), and the aluminum coating result in a maximum eddy current density value of 1.59×10^7 J/m^2. If the same substrate configuration were to be used, an AC source of 1000 A would be required to produce a maximum value of 1.25×10^7 J/m^2 (same order of magnitude) in an In718 coating. This is approximately 17 times the initial current required to produce a peak value of 1.59×10^7 in an aluminum coating. The 1000 A source is obtained by assuming that the frequency is kept constant, as this parameter has less influence over the eddy current density distribution as will be shown in the following paragraph. The non-uniform eddy current density distribution is also present in the cylindrical configuration. Due to the constant heat generation of the eddy current density distribution and the low thermal conductivity of In718, the non-uniform distribution might lead to a more prominent uneven heating pattern as the heat cannot be re-distributed fast enough within the coating in comparison to pure aluminum.

In Chapter 2, it was mentioned that the current and frequency are the most relevant set of parameters in the IH process. In Figure 5.2, the effect of these is explored for a 100 μm pure aluminum coating. In Figure 5.2 b), c) and d), the role of the AC source on the eddy current density distribution is investigated. It can be seen that using higher current values increases the eddy current density distribution within the pure aluminum coating. The maximum value for the case presented in Figure 5.2 b) is 1.59×10^7 J/m^2. By almost

doubling the current (Figure 5.2 d)), the peak eddy current value is increased by approximately 70% ($2.76x10^7$ J/m^2). On the other hand, comparing Figure 5.2 b) and Figure 5.2 f), and their respective peak eddy current values, the effect of frequency is less prominent. For the case presented in Figure 5.2 f), the maximum eddy current value is approximately $1.96x10^7$ J/m^2. This is equivalent to an approximate increase of 25% in comparison to the baseline case presented in Figure 5.2 b).

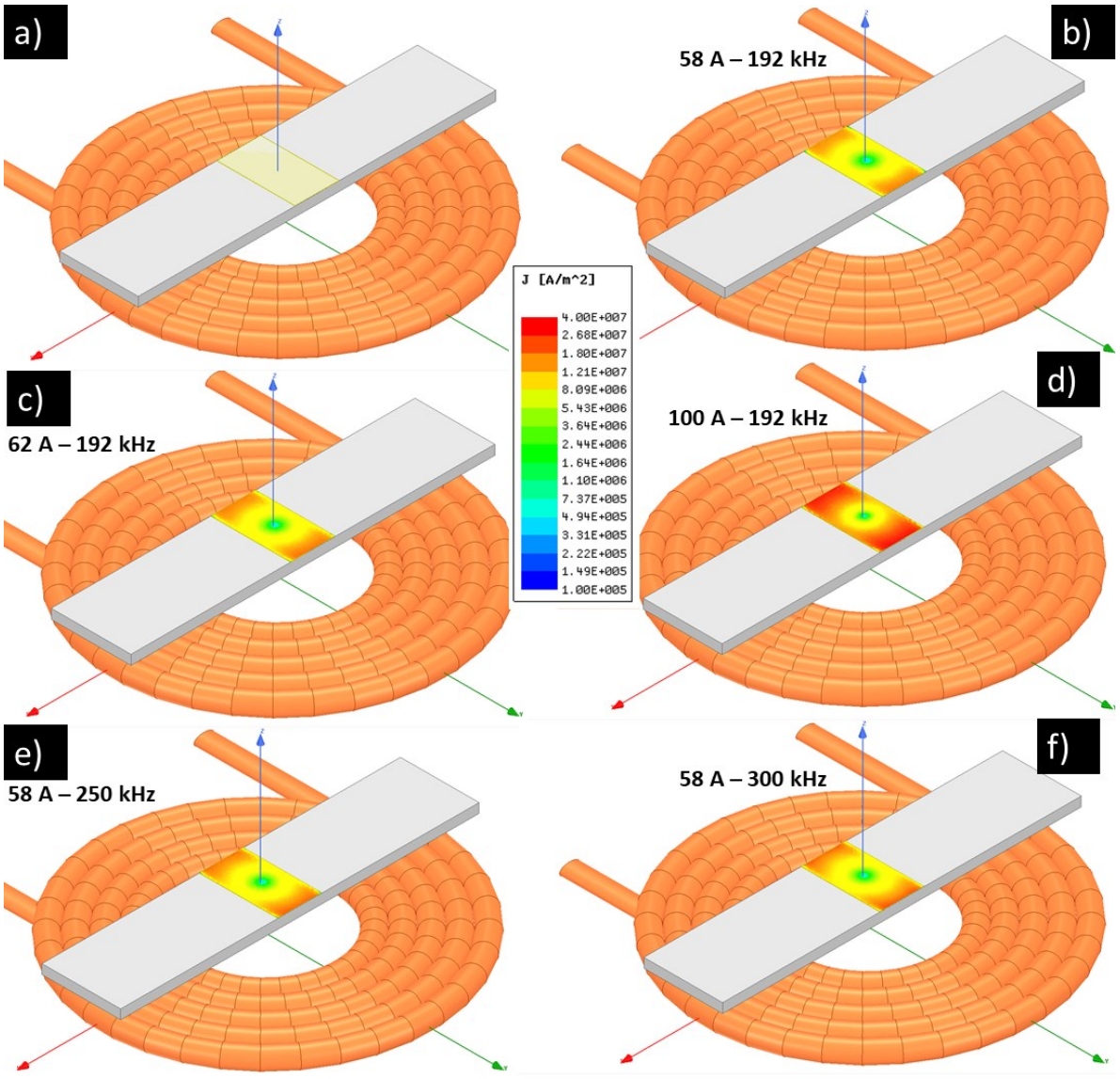


Figure 5.2 Finite element electromagnetic model of the Ti64 substrates and 100 µm pure aluminum coating using different IH parameters.

5.2 Influence of the Substrate and Coating Temperatures on the CS process using the Soft-on-Hard Material Combination – Part I

In this section, the influence of the substrate and coating temperatures on the CS process is investigated using the soft-on-hard material combination. To have independent control of the substrate and coating temperatures from the gas stagnation temperature, an induction heating system is used.

In this section, the following tasks are carried out to evaluate the role of the initial substrate temperature on the CS deposition process:

- Evaluate the Particle/Substrate Deformation at the Interface at a Single-particle level.
- Measure the Substrate Time-temperature History.
- Measure the Deposition Efficiency and Coating Thickness.

To characterize the influence of the coating temperature on the CS deposition process, the following tasks are completed:

- Predict the Coating Eddy Current Density Distribution.
- Measure the Deposition Efficiency and Coating Thickness.

To demonstrate how the CS process can be modified based on the previous findings, samples are produced using different combinations of substrate and coating temperatures.

The detailed evaluation of the individual and combined effect of the substrate and coating temperatures on the CS deposition process using the soft-on-hard material combination is presented in the form of a published peer-reviewed paper (Reprinted from [30] with permission of Springer; permission conveyed through Copyright Clearance Center, Inc.) as follows.

J Therm Spray Tech
https://doi.org/10.1007/s11666-020-01005-w



PEER REVIEWED

Hybrid Additive Manufacturing Technology: Induction Heating Cold Spray—Part I: Fundamentals of Deposition Process

R. Ortiz-Fernandez[1] · B. Jodoin[1]

Submitted: 28 September 2019 / in revised form: 30 January 2020
© ASM International 2020

Abstract The prevention of delamination of soft and ductile materials from hard substrates is a challenge when using the cold spray process. As a potential solution to this issue, a tunable hybrid additive manufacturing process was developed by coupling induction heating and cold spray processes. Pure aluminum was used as the soft feedstock powder, while Ti-6Al-4V was used for the hard substrate. The effects of induction heating and of the substrate initial temperature on the deposition process were evaluated. Single-particle impact tests suggested metallic bond formation at the particle/substrate region as the bonding mechanism. Deposition efficiency, coating thickness and porosity levels were evaluated to characterize the induction heating and initial substrate temperature effects. The deposition efficiency and the coating thickness were doubled with the hybrid additive manufacturing process compared to the traditional cold spray process. Moreover, the presence of eddy currents in the coating (in situ induction heating of the coating) was confirmed by an electromagnetic analysis which modeled the interaction between the coating and the electromagnetic field. Findings demonstrated that substrate preheating has little influence on the overall deposition process and coating quality compared to in situ induction heating effects.

Keywords additive manufacturing · cold spray · in-situ heating · substrate temperature

✉ R. Ortiz-Fernandez

[1] Cold Spray Research Laboratory, University of Ottawa, Ottawa, ON, Canada

Introduction

Cold spray (CS) is the most recent thermal spray process developed for coating production. It was introduced by Papyrin et al. in the mid-1980s (Ref 1). The main advantage of this material deposition process over other thermal spray processes is the solid-state aspect, as feedstock powder melting is avoided. As such, deposits with low oxide content can be consolidated (Ref 1-4). In CS, the feedstock material is injected in the spray gun in micron-size powder form. These powders are accelerated to high impact velocities by a supersonic gas stream inside a de Laval nozzle. Once the particles exit the nozzle and impact the substrate, approximately 90% of the their kinetic energy is converted into thermal energy, while the rest is transformed into elastic and plastic deformation at high strain rates (Ref 1-4). Bonding can take place once the particles and the substrate enter into intimate contact, combined with high interfacial pressure. Intimate contact is assumed to be reached when the particle/substrate respective native surface oxides are broken and removed after the impact (Ref 1-4).

Substrate surface temperature has been proposed as one factor enhancing CS coating bonding and quality (Ref 1-4). Many efforts to determine the effects of substrate preheating on the CS deposition process have been conducted. However, the breadth of results does not allow generalizing conclusions. Many authors have reported an increase in the number of deposited particles in single-particle tests ("wipe tests") as the substrate temperature increases (Ref 5-8). In terms of deposition efficiency (DE), the reported results are contradictory. On one hand, a significant increase has been reported for nickel, titanium, diamond/Ni60 and copper/alumina (Ref 7, 9-12). On the other hand, no significant change in DE for pure aluminum, copper,

Published online: 03 March 2020

iron, iron-based, tin, zinc and metallic glass coatings has been reported (Ref 13-15).

Many traditional methods have been used to preheat the substrate such as ceramic heaters, heating cartridges and flame torches (Ref 6, 7, 16). However, they have proven to be slow or inefficient when converting the input power into heat. Furthermore, all of them failed to maintain the desired temperature when exposed to the process supersonic flow (Ref 13-15). Additionally, complex configurations or intricate shapes cannot be heated easily. On the most innovative end, lasers have been used to preheat the substrates (Ref 9-12, 17). However, due to safety precautions and international standards and regulations, the use of lasers can lead to complex and large setups. Moreover, the costs associated with the use of lasers can be prohibitive.

The use of induction heaters as a preheating method in the CS literature is scarce and limited. Ernst et al. (Ref 5) used an induction heating system solely to increase the temperature of the substrate material and to heat by conduction an Al_2O_3 interlayer. The purpose of this study was to investigate the best route to successfully deposit copper coatings on an Al_2O_3 interlayer by focusing on the thermal activation of the ceramic surface. Arabgol et al. (Ref 18) used induction heating to preheat the substrate material and to investigate its effects on the deposition of copper and titanium coatings. In both cases, the induction heater parameters, inductor's shape and relative distance to the substrate are unknown and not investigated. More importantly, the interaction of the magnetic field caused by the induction heater with the coating remained unexplored.

An induction heating system is based on Faraday's law. An alternating voltage is applied at the inductor's end and as a result an AC current flows throughout the inductor (or coil). Subsequently, a time-variable electromagnetic field (EMF) of the same frequency as the AC current is formed. This EMF induces eddy currents of the same frequency as the AC current on any metallic piece located near the inductor (Ref 19, 20). Consequently, the metallic piece temperature rises due to the formation of eddy currents. Even though induction heating is a well-known process, its effects to maintain a substrate at a desired temperature when exposed to a supersonic gas stream have not been studied in detail. Also, the possibility of achieving in situ coating heat treatment during the deposition process remains to be explored. Additionally, many of the disadvantages shown by traditional heating methods, such as ceramic heaters, heating cartridges and flame torches, can be avoided by tuning the frequency and amplitude of the current, by minimizing the distance between the metal piece and the coil, or by changing the inductor's shape (Ref 19, 20). Moreover, an induction heater is an inexpensive simple equipment that can be coupled to any spray setup.

The objective of this study is to investigate the effects of the interaction of an EMF and cold-sprayed coatings produced by means of a hybrid induction heating CS system. Additionally, the effect of substrate temperature on the coating production is also evaluated.

The study was divided in two parts. The first part focuses on determining the most significant interaction affecting the coating production process. To do so, different induction heater conditions ("On" and "Off") were used *while spraying*, and the substrate surface temperature was monitored during the deposition process. Single-particle impact tests were performed to observe particle deformation and try to infer bonding mechanisms. Various induction heating conditions and initial substrate temperatures were tested to decouple the two parameters. Finally, an electromagnetic model was used to understand the interaction between the EMF caused by the induction heater and the layers deposited.

The second part of the study will address the effects of in situ induction heating and the initial substrate surface temperature on the coating mechanical properties. The latter were investigated evaluating the micro-hardness, the adhesion and tensile strengths of the coatings. To gain further knowledge, fracture surfaces of the adhesion and tensile strength tests were investigated using SEM. Adhesion strength samples were produced using different combinations of parameters (induction heating conditions and substrate temperatures) to better understand the adhesion process.

The study was carried out using a soft powder/hard substrate combination; thus, the findings are limited to such material combination. The selected substrate material was Ti-6Al-4V (Ti64) due to its high hardness level. Consequently, the formation of anchor points promoting particle mechanical adhesion to the substrate is reduced. Pure aluminum powder was selected due to its low hardness. This would minimize the particle penetration on the substrate and reduce mechanical adhesion contribution. Single-particle impact analysis was performed to understand the deformation and deposition mechanisms as a function of substrate temperature. A finite element (FE) model was also used to better understand the particle/substrate deformation behavior. In addition, deposition efficiency, coating thickness, and porosity level were evaluated to assess the effects of induction heating and substrate temperature on the coating formation process. Moreover, a FE model of the electromagnetic field was used to investigate the presence of eddy currents within the coatings.

Experimental Procedure

Substrate and Feedstock Material

25.0 mm × 115.0 mm × 3.2 mm Ti64 coupons were used as the substrate material. Gas-atomized commercially

available pure aluminum powder (SST-A5001) (99.8% Al, Centerline (Windsor) Limited, Windsor, ON, Canada) was used to produce the coatings. The powder irregular morphology is shown in Fig. 1. Laser diffraction (Microtrac model S3500, Montgomeryville, PA, USA) was used to determine the feedstock particle size distribution despite the non-spherical morphology. The resulting 10th, 50th, and 90th size percentiles were found to be 11.3, 25.8 and 60.3 μm, respectively.

Two different surface preparation methods were used. A substrate mirror finish surface was obtained by grinding the substrates' surface with water as a lubricant. To polish the surface, abrasive suspensions of 9, 3 and 0.04 μm, were subsequently used. A grit-blasted substrate surface finish was also used. Commercially available Ebony Grit EG 20 (Opta Minerals, Waterdown, ON, Canada) mainly composed of iron oxide and silicon oxide was used to prepare the surface. The substrates' arithmetic average roughness (Ra) was measured using a profilometer equipped with a diamond stylus (PHASE II, SRG-4000, NJ, USA). Surface roughnesses of 0.25 ± 0.04 μm and 2.66 ± 0.32 μm were obtained for the polished and the grit-blasted surfaces, respectively. Prior to the deposition process, all samples were cleaned and degreased in an ethanol ultrasonic bath for 3 min.

Cold Spray Deposition

The aluminum coatings were produced using a commercially available system (SST-EP, Centerline (Windsor) Limited (Windsor, ON, Canada)). A polymer de Laval nozzle with a 2.0 mm throat diameter and a 6.4 mm exit diameter was used. The pure aluminum powder was injected using a commercially available powder feeder (AT-1200 Rotary, Thermach Inc., Appleton, WI, USA). The spray parameters used are presented in Table 1.

Induction Heating Parameters for Coating Production

The substrate coupons were preheated to 200, 400 and 600 °C prior to the start of the spraying process using an induction heater (Tucker Induction Sys. Inc., Shelby Township, MI, USA). For these cases, the induction system was maintained "On" during the spray process. To gain further knowledge of the induction heating effects *while spraying* on the coating quality, an additional set of coatings was also sprayed on a preheated substrate at 400 °C. However, for this case, the induction heater was turned "Off" as the spraying process was initiated. A schematic of the spray setup used is presented in Fig. 2. The copper planar round inductor had an outer diameter of 110.0 mm and an inner diameter of 42.0 mm. The coil had a total of four turns. The outer and inner diameter of the copper tubing used on the coil was 6.3 and 5.0 mm, respectively. The substrates were positioned 8 mm above the induction coil and were thermally insulated on the sides and bottom.

The induction heater parameters used during the deposition can be found in Table 2.

Substrate Surface Temperature Measurement

To investigate the substrates' surface temperature evolution due to the induction heating and its interaction with the supersonic gas stream during the spraying process, the substrates' surface temperature was monitored locally before and during the spray through non-contact infrared sensors. A RAYGPRSF infrared thermometer (Raytek, Santa Cruz, CA, USA), which has a working temperature

Table 1 Cold spray deposition parameters

Parameters	Values
Stagnation temperature, °C	500
Stagnation pressure, MPa	3.45
Carrier gas	Nitrogen
Traverse speed, mm/s	120
Powder feed rate, g/min	4.5
Standoff distance, mm	15
Number of passes	5
Step size, mm	1

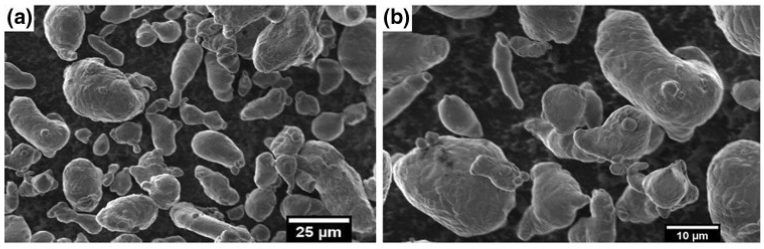


Fig. 1 Scanning electron microscope (SEM) image of the as-received aluminum powder. (a) Low magnification (b) high magnification

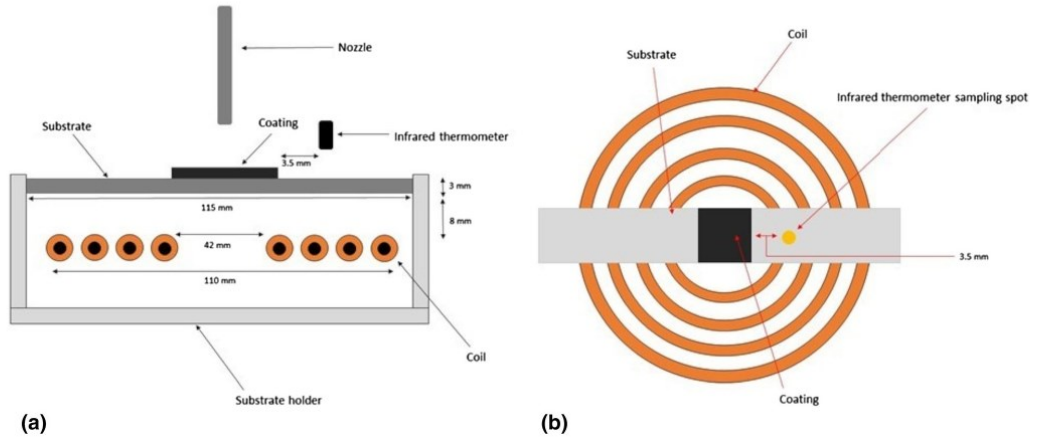


Fig. 2 Schematic of the setup used during the deposition process. (a) Cross section and (b) top view

Table 2 Induction heater parameters

Parameters	Parameters 1	Parameters 2
Current, A	58	43
Frequency, kHz	192	198

range from − 18 to 538 °C, was used to monitor the temperature for cases where the substrate temperature was below 500 °C. An OptCT3MH2SF (Optris, Portsmouth, NW, USA) infrared thermometer was used to monitor the substrates' temperature above 500 °C. The substrates' surface temperatures were measured at a position 3.5 mm away from the location where coatings were sprayed, as presented in Fig. 2(b). The induction heater parameters used during the substrates' surface temperature measurements can be found in Table 2. Parameters 1 produce a faster heating rate than Parameters 2.

Single-Particle Impact Test

Single-particle impact test samples ("wipe tests") were sprayed on mirror finish Ti64 rectangular substrates set at initial surface temperatures of 25, 200, 400 and 600 °C using the induction heater prior to the start of the spraying process. The parameters labeled as Parameters 1 in Table 2 were used to achieve the desired substrate temperatures in the production of these samples. As the spraying process was initiated, the induction heater was turned "Off." The powder feed rate was adjusted to obtain individual particles deposited on the mirror finish substrate.

Sample Characterization

The as-received powder, the single-particle samples, and the coatings' microstructure were investigated using a scanning electron microscope (SEM) (EVO MA-10, Carl Zeiss AG, Oberkochen, Germany) equipped with secondary (SE) and back-scattering electron (BSE) detectors as well as x-ray energy-dispersive spectroscopy (EDX) and an 3D digital microscope (VHX-2000E, Keyence Corporation, Osaka, Japan). Four coating cross sections were used to evaluate the porosity level of each coating as a function of the initial substrate temperature. The cross sections were stitched together using the VHX-2000 software at a magnification of 200x. The ImageJ software was used to quantify the porosity level of the deposits through contrast of the images. The coating thickness values were obtained by measuring the perpendicular distance from the substrate interface with the coating to the top region of the coating. The measurements were only performed in the middle region of the coating. Four cross sections were used to evaluate the coating thickness. On each cross section, the coating thickness was measured at ten different locations. The resultant values are an average of the measured thicknesses on the four cross sections.

Single-Particle Impact Morphologies and Adhesion Mechanisms on Ti64 Substrates

A schematic of the setup used to investigate the interface region and analyze the particles morphology after impact and their adhesion mechanisms on the Ti64 substrates is presented in Fig. 3(a). FM-1000 glue (Couch Sales LLC, Hilton Head Island, SC, USA) was used. After the curing

process, the produced samples were pulled. Once pulled, the particle and the substrate side, in Fig. 3(b) and (c), respectively, were investigated using SEM.

Particle Velocity

The particles' velocity was measured using a Cold Spray Meter (CSM) eVOLUTION (Tecnar Automation Ltd., St. Bruno, Canada). It uses a continuous 2.4 W (λ = 810 nm) laser with a dual-split photomask in order to perform in-flight measurement on individual particles. As a result, the CSM can provide a precise measurement of the in-flight particles velocity. The particles' velocity was measured at a point 15 mm downstream from the center of the nozzle exit. The measurements were done over a 10-min period to obtain a representative range of velocities.

Numerical Models

A 2D axisymmetric finite element (FE) model was used to investigate the impact behavior of the pure aluminum particles for the various initial substrate temperatures tested. The commercially available software, Abaqus/Explicit, was used to carry out these investigations.

In the CS literature, the possibility of producing an in situ heat treatment due to the formation eddy currents within the coating as the material is sprayed has never been explored before. To investigate this possibility, an electromagnetic model was used to predict the interaction between the EMF and a pure aluminum coating. To carry out this analysis, the commercially available software, Ansys Maxwell 19.2, was used.

Particle Impact Modeling

To simulate the particle deformation behavior upon impact with the substrate, a 2D axisymmetric Lagrangian model was used (Ref 21-24). The particle and the substrate region closest to the impact zone used a fine mesh size. The latter was selected to be 1/50 of the particles' average size (Ref 21, 22, 25). The substrate mesh used far from the impact zone was coarser to minimize computational time. The average size at this region was 1/25 of the particles' average size. A 4-node-coupled temperature–displacement (CAX4RT) mesh type was assigned to the substrate and the particle. In order to avoid excessive distortion at the impact region, an adaptive mesh was used for the particle and the substrate. The pure aluminum particles were assumed spherical for simplicity with a diameter of 25 µm, in accordance with the feedstock particle size distribution. The single-particle impact model has a complementary purpose as it aims to provide a greater understanding of the ongoing processes during the impact and to access data that cannot be obtained experimentally due to the challenging time scales.

The initial substrate temperatures were set to 25, 200, 400 and 600 °C, to match the experiments performed. The particle's temperature was initialized for all the cases at 348 K as used before by Nastic et al. (Ref 26) for the same powder and identical CS parameters. The particle velocity was set to the average particle velocity measured using the CSM.

The elastic response of the particles and the substrates during the simulations was modeled by the linear Us-Up Hugoniot form of Mie–Grüneisen (Eq 1). In order to model the plastic behavior, the Johnson–Cook equation (Ref 27, 28) (Eq 2) was used.

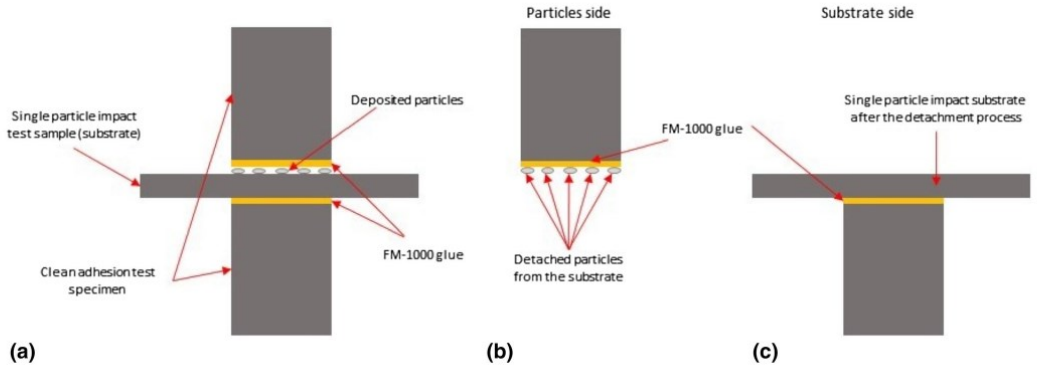


Fig. 3 Schematic of the separation process used to investigate the particle/substrate region of single-particle impact test samples. (a) Setup used for the removal process, (b) particle side obtained after the pulling process and (c) resulting substrate side after the particle detachment process

$$p = \frac{\rho_0 c_0^2 \eta}{(1 - s\eta)^2}\left(1 - \frac{\Gamma_0 \eta}{2}\right) + \Gamma_0 \rho_0 E_m, \quad \eta = 1 - \frac{\rho_0}{\rho} \tag{Eq 1}$$

$$\sigma_{eq} = \left[A + B\varepsilon_p^n\right]\left[1 + CIn\left(\frac{\dot{\varepsilon}_p}{\dot{\varepsilon}_{ref}}\right)\right]\left[1 - \left(\frac{T - T_{ref}}{T_m - T_{ref}}\right)^m\right] \tag{Eq 2}$$

where for the elastic response p is the hydrodynamic stress, ρ_0 is the initial density, ρ is the actual density, c_0 is the material speed of sound, Γ_0 is the Mie–Grïneisen's constant, E_m is the energy per unit mass. A, B, C, n are the Johnson–Cook parameters, $\dot{\varepsilon}_p$ is the plastic strain rate,ε_p is the equivalent plastic strain,$\dot{\varepsilon}_{ref}$ is the strain rate at which the Johnson–Cook parameters were obtained, T_m is the melting temperature, T_{ref} is the transition temperature, and T is the absolute temperature. Table 3 summarizes the properties used in the simulation.

Eddy Current Modeling

To investigate the substrate and coating interactions with the EMF, the commercially available Ansys Maxwell 19.2 software was used. A frequency-dependent 3D model was used to compute the eddy current field caused by the application of AC current in an inductor (coil). The coating and substrate region that were more affected by the magnetic field used a finer mesh, while the rest of the volume used a coarser mesh to minimize the computational time. The coating's initial mesh was 1/30 of the coating thickness. The substrate's initial mesh was 1/30 of the substrate thickness. A 3-node adaptive uniform mesh was used. These parameters were selected based on a mesh analysis which helped provide an adequate solution without compromising the computational time.

Table 3 Material properties used in the model (Ref 27, 29-31)

Properties	Aluminum	Ti64
Density (ρ_0), kg/m^3	2700	4510
Specific heat (C_p), J/kgK	910	600
Thermal conductivity (κ), W/mK	237	6.80
Melting temperature (T_m), K	934	1923
Shear modulus (G), GPa	26	45
Young modulus (E), GPa	69	115
A, MPa	148.40	3500
B, MPa	345.5	331
C	0.001	0.012
n	0.183	0.34
m	0.895	0.80
$\dot{\varepsilon}_{ref}$	1.00	1.00
T_{ref}, K	300	300
Grïneisen constant (Γ_0)	2.14	1.25
Speed of sound, m/s	5292	4950
Hugoniot slope, s	1.40	7

The model was used to investigate the presence and effect of eddy currents within a thin paramagnetic coating. The potential formation of eddy currents in the coating would indicate the possibility of producing an in situ heat treatment during the deposition process, potentially enhancing the deposition process as a hybrid manufacturing method. For this case, the substrate dimensions were 115 × 25 × 3.2 mm as the rectangular coupons used in the experimental section. The coating size was 14 × 25 × 0.15 mm. These dimensions were taken from the produced coatings. The coating thickness was reduced to investigate the possible presence of eddy currents on the coating from the production of the first deposited layer. The substrate and the coating were placed in the middle of the inductor. The coil geometry and dimensions replicate the experimental setup. The distance between the copper planar coil and the substrate was 8 mm as in the experimental section. A schematic of the model geometry is presented in Fig. 4.

The model assumes a sinusoidal function for the current. To evaluate the formation of eddy currents, the model uses Eq 3 to estimate the response of the metal to an alternating magnetic field. Using the previous equation and a simplified version of Ampere's law (Eq 4), the current density can be calculated on any given material.

$$\nabla \times \left(\frac{1}{\sigma + j\omega\varepsilon_r\varepsilon_0} + \nabla \times H\right) = -j\omega\mu_r H \tag{Eq 3}$$

$$\nabla \times H = J \tag{Eq 4}$$

where H is the magnetizing field due to current excitation, J is the current density, j ω is the angular frequency of the current, μ_r is the relative permeability, σ is the electrical conductivity of the material, ε_r is the relative permittivity, also called dielectric constant and ε_0 is vacuum

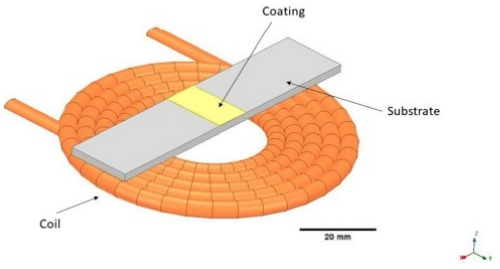


Fig. 4 Schematic of the model used to predict the eddy current distribution on the pure aluminum coating

Table 4 Material properties used in the model (Ref 4, 32, 33)

Properties	Aluminum	Ti64	Copper
Relative permeability (μ_r),	1.00021	1.0005	0.999991
Electrical conductivity (σ), S/m	40,000,000	588,325	58,000,000
Current, A	N/A	N/A	58
Frequency, kHz	N/A	N/A	192

permittivity. The material properties used are summarized in Table 4.

Results and Discussion

Particle Impact Simulation

The effect of substrate temperature on the particle and substrate deformation is analyzed through modeling to access data that cannot be measured experimentally, namely the equivalent plastic strain (PEEQ). PEEQ has been used widely to quantify the plastic deformation occurring in cold spray substrates and particles. Additionally, it has been proposed as a good indicator of the strain required to remove the native oxide layer and promote bonding (Ref 17, 34-37).

Cross-sectional images from the particle impact simulations at different initial substrate temperatures are presented in Fig. 5. These images were taken at the point of maximum particle deformation before the particle "bouncing-off" process started. The maximum PEEQ values of the particles impacting a substrate at 25, 200, 400 and 600 °C as initial surface temperatures were 6.75, 6.69, 6.69 and 6.51, respectively. Contrary to the large values observed on the particles, the substrate maximum PEEK values reached less than 0.50 for all cases. While the large PEEK values observed for the particles could suggest an adequate oxide removal process occurring at their surfaces, the small values observed for the substrates clearly indicate a lack of deformation, and potentially a poor oxide removal process. This drastic difference in PEEQ values is attributed to the dissimilarity in hardness and strength between the particles and the substrates. It is observed that regardless of the substrate temperature, all particles showed a similar deformation level. Additionally, it is evident that the substrates remained flat and no particle penetration is observed.

Single-Particle Impact Tests

The deposition behavior of single particles impacting substrates at different initial substrate surface temperatures is presented in Fig. 6. As the substrate surface temperature increased, the number of craters left by bouncing-off particles decreased to the point where no craters are visible at the highest initial substrate temperature (Fig. 6d). Additionally, in the case of the substrate initially at 25 °C (Fig. 6a), only small particles successfully deposited, whereas for higher initial substrate surface temperatures (Fig. 6b, c, and d), particles of all sizes have been successfully deposited.

At initial substrate surface temperature of 25 °C, only the smallest particles deposited as they exited the nozzle at higher velocities than larger particles (Ref 3, 25, 37-43), thus reaching the critical velocity required for adequate plastic deformation and adhesion (Ref 1, 3). As such, only a few particles deposited and many large craters are visible on the substrate surface. When the substrate initial temperature is increased, more particles adhere and particles of larger sizes start to adhere. Consequently, it is concluded that the critical velocity required to achieve bonding decreases. The proposed critical velocity equations available in the literature are a function of the particle diameter, the particle temperature and the particle material, among many other parameters (Ref 24, 32, 39, 44, 45), but the substrate temperature is not considered one of them. Despite this omission, experimental data (Ref 5-8) have shown the importance of the substrate temperature for the production of the coating first layer. Therefore, the critical velocity required to cause the particles to adhere to the substrate must also be substrate temperature dependent for the first layer deposited and for the case of single impact particles.

The single-particle samples were glued and pulled to investigate the particle/substrate interface. Figure 7 presents the substrate side after the detachment process. The substrates show almost no sign of deformation at any of the initial surface temperatures as predicted by the modeling results. This behavior was also confirmed by high magnification cross-sectional images of the single splat tests. Thermal softening and its effects on Ti64 have been widely studied for various strain rates. Similarly to other metals, it exhibits a significant drop in stress required to achieve similar levels of deformation with temperature (Ref 46-49). Thus, the lack of substrate deformation is attributed to the softer nature of the particles. Even though the substrates have softened, the pure aluminum particles are not hard enough to cause significant contact pressure at the impact region that would allow them to deform the substrate.

Despite the additional available thermal energy and a thermally softened substrate, no trace of metallic bonded areas is visible at the scale used to observe the substrates surface. This further suggests that not enough contact pressure was exerted on the substrate by the particles to allow large intimate contact zones. Additionally, as

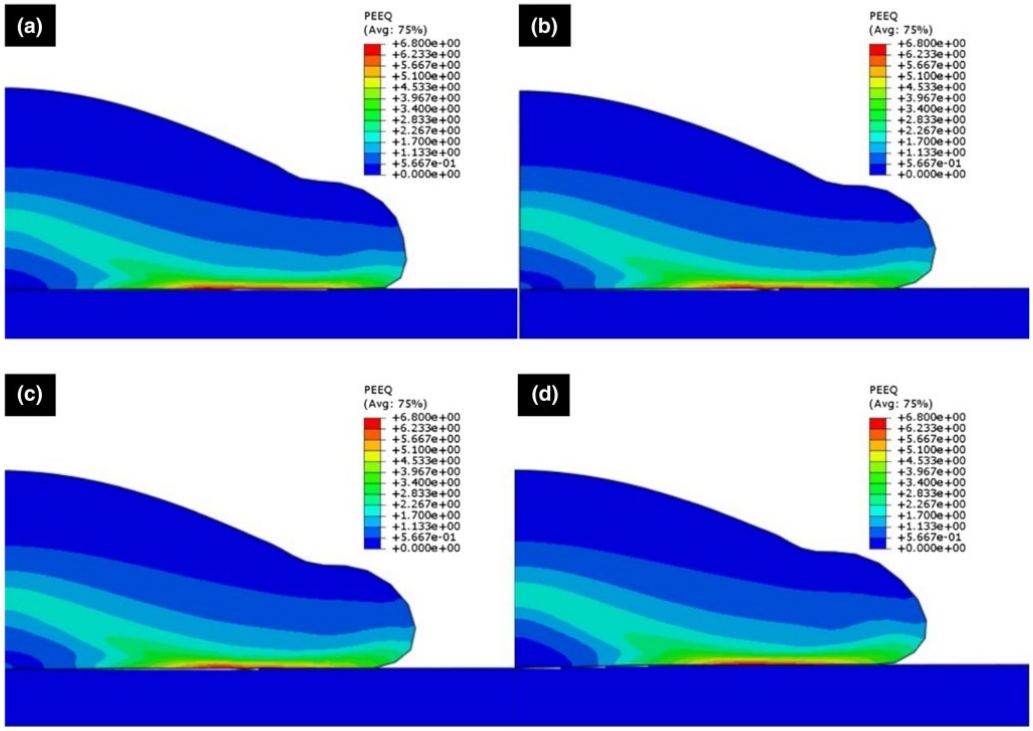


Fig. 5 Finite element analysis (FEA) cross-sectional images of the particles after impact at different substrate temperatures. The substrate initial temperatures were: (a) 25 °C, (b) 200 °C, (c) 400 °C and (d) 600 °C

suggested by the model, the native oxide layer on the substrate/particle might not have been removed sufficiently in order to drive the formation of large visible characteristic features of metallic bonding.

The particles detached from the substrates after the pulling process were also examined through SEM and are shown in Fig. 8. It is observed that all particles experienced similar levels of severe plastic deformation, as predicted by the model, even though they impacted substrates preheated at different initial surface temperatures. As observed on the substrate sides, the particles presented no visible characteristic features of metallic bonding at the scale used to observe them, indicating that the conditions to produce large easily visible bonded areas were not met at the individual particle level. Mechanical bonding is unlikely to be a bonding mechanism since the substrates remained flat after the deposition process. Therefore, the deposited particles must have bonded to the substrate due to the formation of nano-sized metallic bonded areas.

The modeling and experimental results have failed to provide insightful details that could help explaining the higher occurrence of particle deposition on the substrate during the single-particle impact tests as the substrate temperature increased. On the modeling side, it is hypothesized that this issue is related to the model capabilities. Further investigation must be conducted on the development of a model that can predict particle bonding during the impact process, so the effects of substrate temperature on the single-particle deposition process can be better understood. From the experimental perspective, nano-sized bonded areas can only be observed using high-resolution and precise microscopy tools, such as TEM or HRSEM. Consequently, a dedicated thorough investigation will be conducted to fully understand the relationship between the metallic bond formation and substrate preheating in single-particle impact tests in another work.

Substrate Surface Temperature Evolution Under Spray Conditions: Effect of Induction Heating

The temperature evolution obtained on polished substrates at the sampling point shown in Fig. 2(b) is presented in

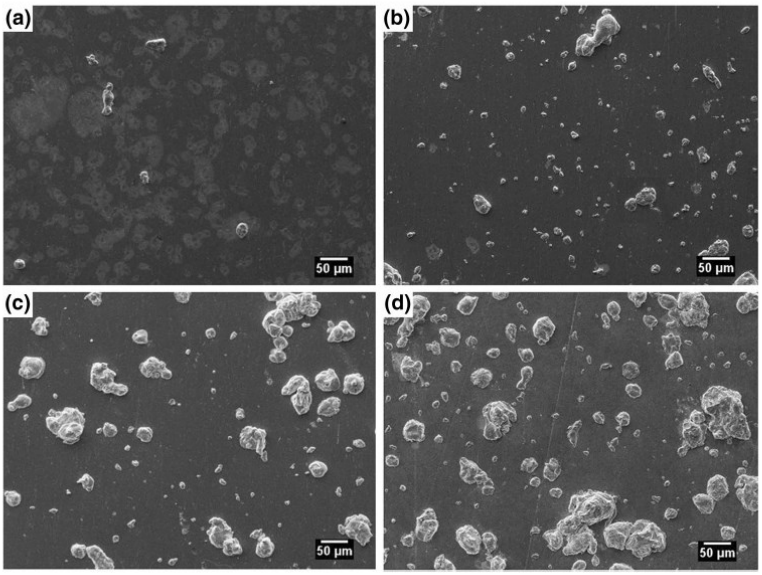


Fig. 6 Scanning electron microscope (SEM) images of the single-particle samples at various surface initial temperatures: (a) 25 °C, (b) 200 °C, (c) 400 °C and (d) 600 °C

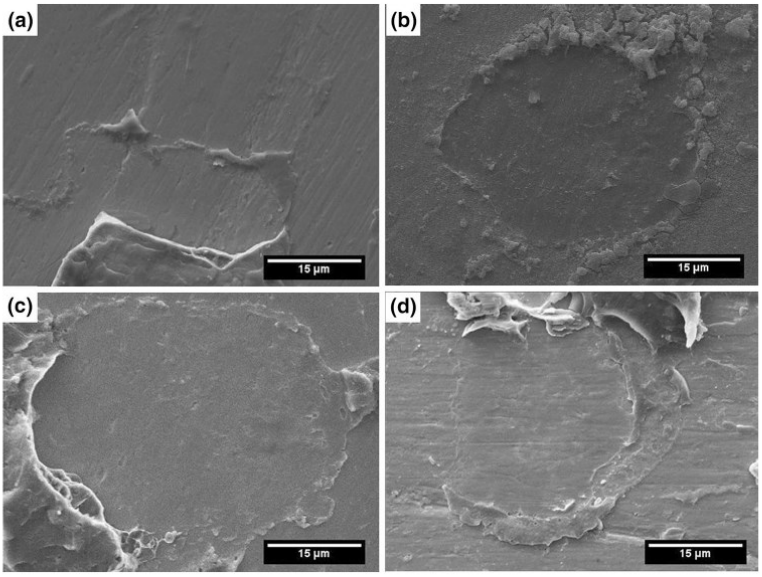


Fig. 7 Scanning electron microscope (SEM) images of substrate side after the particle removal process. The initial surface temperatures were: (a) 25 °C, (b) 200 °C, (c) 400 °C and (d) 600 °C. Glue remnants are present at the periphery (confirmed by EDX analysis)

Fig. 9. For all the spray conditions, the spraying time process took approximately 44 s. The infrared thermometer and the substrate were fixed at all times. Thus, the resulting curves are an outcome of the temperature evolution at the surface of the substrate right underneath the sampling spot while the coatings were deposited. The temperature evolution measured at 25 °C as initial surface temperature (curve a) in Fig. 9 exhibits an increasing trend, with some noticeable fluctuations, attributed to the nozzle scanning pattern. This overall increase in temperature is caused by the convective heat transfer between the impinging gas stream and the substrate combined with conduction heat

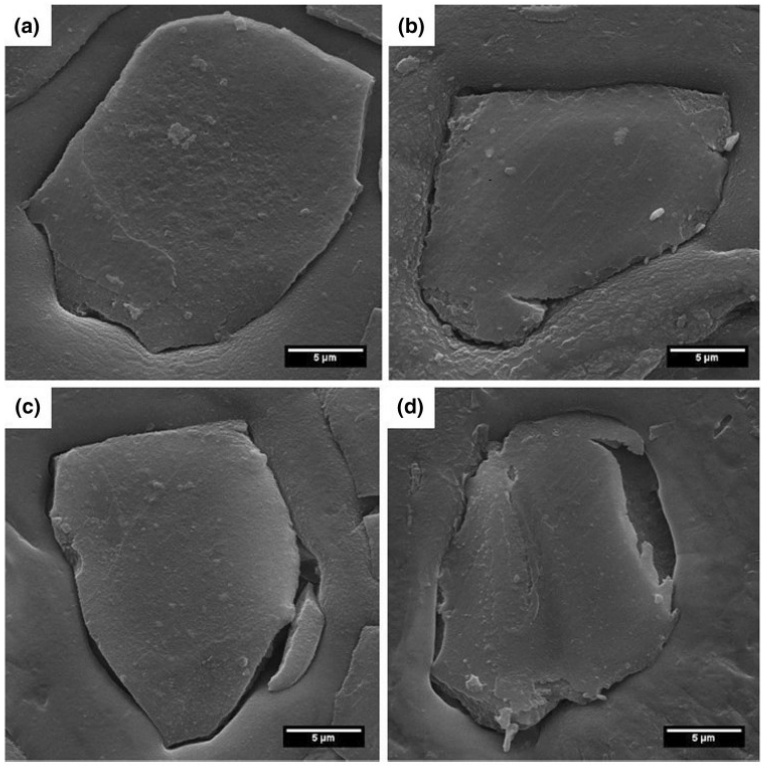


Fig. 8 Scanning electron microscope (SEM) images of particle side after the detachment process. The particles were sprayed on a substrate at initial surface temperature of: (a) 25 °C, (b) 200 °C, (c) 400 °C, (d) 600 °C

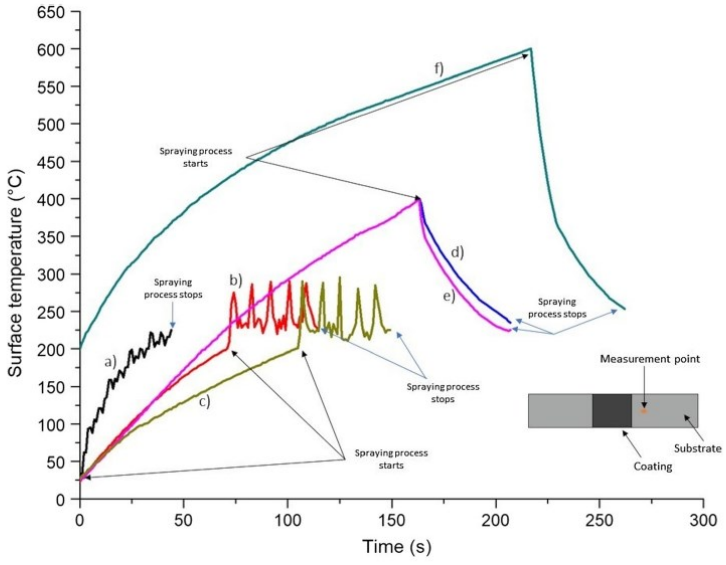


Fig. 9 Substrate surface temperature evolution at the measurement point during the spray process. The spraying process was initiated when the substrate surface temperature reached: (a) 25 °C, (b) and (c) 200 °C, (d, e) 400 °C and (f) 600 °C. The induction heater was maintained "On" in curves (b), (c), (d) and (f) during the deposition process, while it was turned "Off" in curve (e) once the spraying process started. Parameters 1 were used to preheat the substrates and during the deposition process in curves (b), (d) and (f). The substrate in curve (c) was preheated using Parameters 2

transfer through the substrate. In theory, the gas flow should decelerate on the substrate and bring the gas back to the stagnation temperature (Ref 39, 50-53). However, the process is not isentropic as it is far from being reversible so there are losses contributing to a stagnation gas temperature lower than the initial temperature. As such, the increasing temperature at the sampling point seems to start reaching a "steady-state" temperature at around 225 °C, lower than the initial gas temperature (500 °C). Nevertheless, this value is in agreement with the "steady-state" temperatures reported by Legoux et al. (Ref 15) under similar conditions.

Two preheating rates were used to heat the substrate to 200 °C as initial surface temperature prior to beginning the spraying process. In Fig. 9 Parameters 1 were used for curve (b), while Parameters 2 were used for curve (c). For both curves, the induction heater was maintained "On" during the spray time. The difference in the heating rate is noticeable as curve (b) reached 200 °C faster than curve (c). However, it is observed that once the spray starts, the curves are very similar. Five passes were carried out during the spraying process, and thus five peaks are visible. These peaks are a consequence of the nozzle location being instantaneously closer to the temperature sampling point. The measured temperatures at these peaks show good agreement with the results obtained by Legoux et al. (Ref 15). Despite the fact that Parameters 1 preheated the substrate at a faster rate than Parameters 2, once the spraying process started, the substrate heating due to the gas stream became dominant over the induction heating. Consequently, both curves point to a temperature around 225 °C between the peaks and at the end of the spraying process.

Parameters 1 were used to preheat the substrate surface to 400 °C, and two cases were analyzed. In Fig. 9 curve (d), the induction heater was maintained "On" during the spray process while the induction heater was turned "Off" for curve (e). Because the initial surface temperature was above the "steady-state" temperature, these two curves exhibit a cooling process behavior. Curve (e) exhibits a slightly larger cooling rate than curve (d), which is attributed to the absence of eddy currents in the substrate. Nevertheless, the cooling rate caused by the gas stream was dominant over the heating rate of the induction heater.

Finally, curve (f) in Fig. 9 represents the substrate temperature evolution at the sampling location for the case of 600 °C as the initial substrate surface temperature, with the induction heater maintained "On" during the spraying process. This curve shows the largest cooling rate among the different substrate surface temperature conditions. This is expected due to the large temperature difference between the gas stream and the substrate surface temperature. As in previous cases, the cooling rate from the gas stream is dominant over the heating rate caused by the induction heater.

As other preheating methods, induction heating failed in retaining the initial substrate surface temperature when the supersonic gas stream interacted with the substrate as the convective heat transfer caused by the gas stream was dominant over the induction heating rate. Consequently, independently of the initial substrate temperature, the latter is brought to the "steady-state" temperature value around 225 °C. The average surface temperature during the spray time for curves (a), (b), (c), (d), (e) and (f) was 161, 244, 233, 296, 277 and 349 °C, respectively.

Coatings Characterization

The DE of the sprayed coatings for the various cases is presented in Fig. 10. It becomes evident that for the same initial substrate surface temperature, the DE is barely affected by the surface preparation, in accordance with results found in the literature (Ref 4, 6, 24, 26). The prepared surface only interacts with the first layer of deposited particles. Once these have adhered to the substrate, the incoming particles do not interact any more with the substrate, but with the previously deposited layer. Consequently, the surface preparation does not affect much the subsequent layers for such low Ra values. Furthermore, both surface preparations yielded very similar surface roughness, thus limited impact was predictable.

Contrary to what has been reported on the substrate preheating literature where minimum to no increase in DE was observed for pure aluminum coatings (Ref 12, 15), the deposition efficiency seems to be drastically affected by the initial substrate surface temperature. An increase in DE from 52% at room temperature to 65% at 200 °C was observed. When the initial substrate temperature was increased to 400 °C, the DE was 77% and reached 95% at 600 °C.

However, contrary to the drastic increase in DE observed for the cases mentioned previously for which the induction heater was maintained "On," the DE did not increase when the induction heater was turned "Off" prior to the start of the spray process. The coatings sprayed on preheated substrates at 400 °C as the initial substrate temperature but with the induction heater turned "Off" prior to the spray start resulted in a DE of 52%, as shown in Fig. 10. This value is almost identical to the case where no substrate preheating was used, in accordance with the literature where minimal or no effect on DE has been observed when substrate preheating was used (Ref 13-16, 18). This follows the findings reported in the literature that the beneficial effect of preheating is only limited to the first deposited layer.

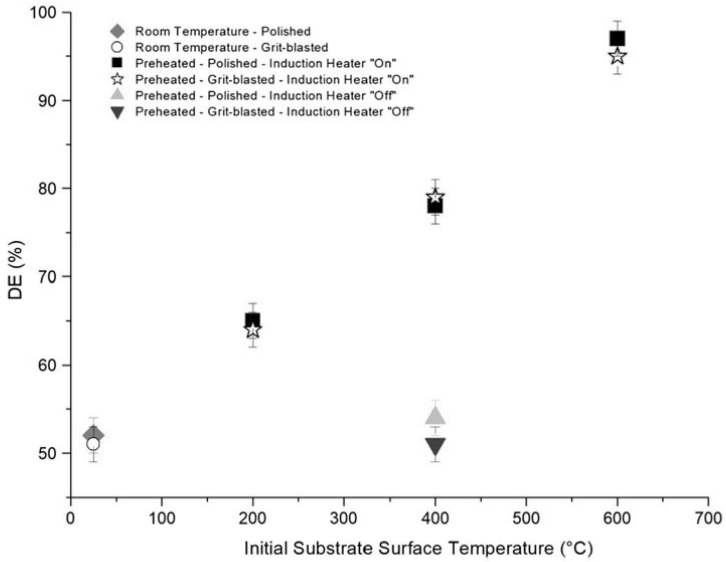


Fig. 10 Deposition efficiency of pure aluminum on Ti64 substrates at different initial substrate temperatures with the induction heater "On" and "Off." Parameters 1 were used for all cases

As shown in the previous section, the difference in initial substrate temperature between all the cases does not explain the linear increase trend in DE, especially when the average temperature of curves (d) and (e) in Fig. 9 is compared (296 and 277 °C). Both curves experienced a similar evolution and their average temperature difference is less than 20 °C, but the resultant DE is drastically different. Therefore, maintaining the induction heater "On" must cause the positive effect on the coating deposition process.

To explain the observed DE increasing trend when the induction heating is kept "On," the interactions between the coating, the substrate and the magnetic field generated by the induction heater must be considered. While the coating is deposited, the magnetic field interacts not only with the substrate but with the coating as well. Two possible consequences arise from these interactions. First, due to the supply of thermal energy to the substrate by the formation of eddy currents, the substrate cools down at a lower rate compared to the cases where there is no induction heating in use. Thus, the substrate is able to transfer more heat to the coating, making it softer. However, this hypothesis is unlikely to produce the increase in DE because a very similar substrate temperature time-history is observed in both cases when the heater is kept "On" and "Off." Second, even though pure aluminum is a paramagnetic material, it still interacts with the magnetic field (Ref 19, 20). Therefore, eddy currents will also form in the coating, contributing to locally heating it up. From the single-particle impact test, it has been observed that as the initial substrate temperature increases, the number of deposited particles also increases (Ref 5-7). Thus, it is plausible to assume that the deposited layer at 600 °C resulting from the first nozzle pass is thicker than the one at lower initial substrate surface temperatures. For that reason, the eddy current formation on the first layer of a coating deposited at an initial surface temperature of 600 °C will be larger than at lower temperatures, allowing the coating to reach/retain a locally higher temperature for longer time. Thus, the incoming particles should impact a softer coating at all times, decreasing the critical velocity and promoting more deformation of the already deposited particles and adhesion.

Figure 11 presents cross-sectional images of the coatings sprayed at different initial substrate temperatures and the induction heater maintained "On" during the deposition process. The measured porosity was less than 0.1% for all the different cases. Significant increases in the resultant coatings thicknesses are observed as a function of initial surface temperature condition. It is also evident that the surface preparation has no effect on the resulting coatings because similar thicknesses are produced for both surface preparations, for each initial substrate surface temperature.

The resultant coating thicknesses after the deposition of five layers of material for all the different initial surface temperatures, induction heater conditions and surface preparation are summarized in Table 5.

Cross-sectional images of the coatings produced at initial substrate temperatures of 25 and 400 °C with the heater

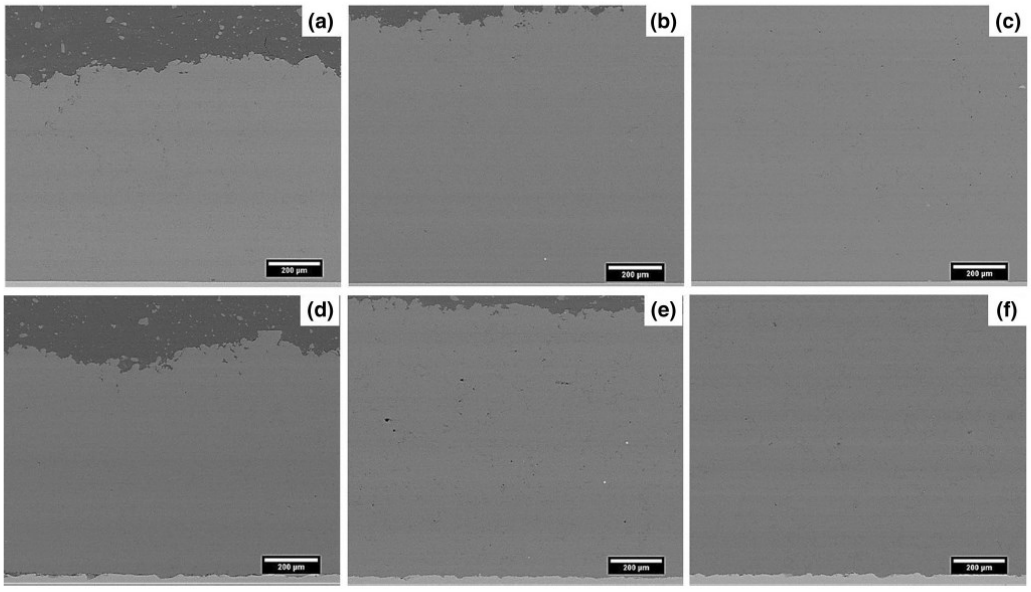


Fig. 11 Back-scattered cross-sectional images of the cold-sprayed coatings: (a) and (d) at 200 °C, (b) and (e) at 400 °C, and (c) and (f) at 600 °C. The induction heater was "On" during the deposition process for all the cases. The surface preparation for (a), (b) and (c) was a polished finish, while for (d), (e) and (f) they were grit-blasted. Parameters 1 were used for all cases. From the bottom to the top, the light gray on the images is the substrate

Table 5 Resultant coating thicknesses for all the different spray conditions after five passes

Induction heater status	Induction heater "On"		Induction heater "Off"	
Surface preparation Initial surface temperature, °C	Polished Thickness, µm	Grit-blasted Thickness, µm	Polished Thickness, µm	Grit-blasted Thickness, µm
25	N/A	N/A	673 ± 11	654 ± 18
200	862 ± 4	848 ± 21	N/A	N/A
400	1027 ± 10	1011 ± 8	698 ± 15	650 ± 12
600	1258 ± 4	1200 ± 15	N/A	N/A

"Off" during the deposition process are presented in Fig. 12. The coatings do not show any significant porosity difference, with mean porosity values less than 0.2%. No significant difference in resultant coating thickness was observed between the coatings. This is further confirmed by the values presented in Table 5. When the spraying process is carried out at 400 °C as the initial substrate surface temperature and the induction heater is turned "Off" prior to spraying, the cooling rate caused by the gas stream is assumed to be larger than the conduction rate from the substrate to the coating. Thus, most of the thermal energy is quickly removed during the first nozzle pass hindering any positive effect on the coating build up and final thickness.

Electromagnetic Modeling

Figure 13 presents the predicted current density distribution in the aluminum coating caused by the magnetic field. The coating experiences a predominantly high current density distribution at the substrate edge, while the center experiences a lower current density. The current density distribution in a metal piece is a function of the metal properties, induction heater parameters, the distance between the inductor and the metal piece, and the coil's shape. Therefore, for this particular setup, the coating experiences the highest current density at the region where the magnetic field flux lines converge (Ref 33, 54). Also, as the magnetic field flux lines distribute across the metal

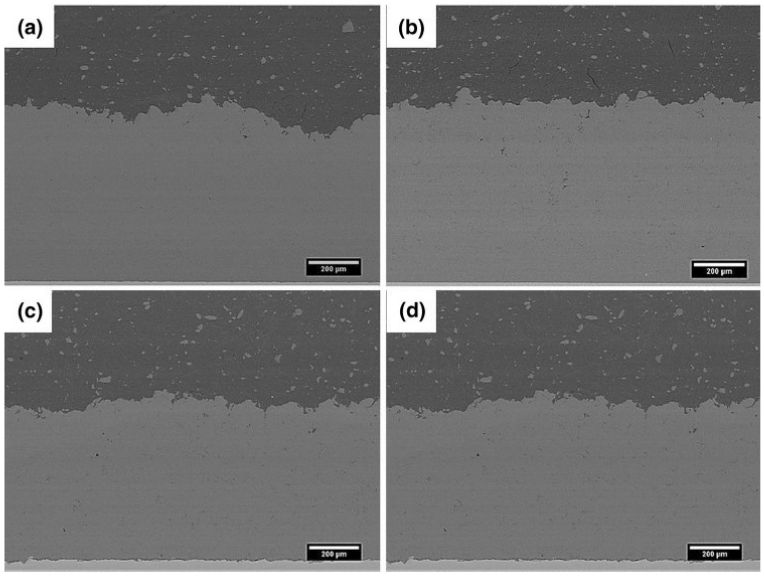


Fig. 12 Back-scattered cross-sectional images of the cold-sprayed coatings (a) and (c) at 25 °C and (b) and (d) at 400 °C as the initial substrate surface temperature and induction heater turned "Off" during the spraying process. Surface preparation for (a) and (b) is polished while (c) and (d) were grit-blasted. Parameters 1 were used to preheat the substrate in (b) and (d). Light gray on the images is the substrate

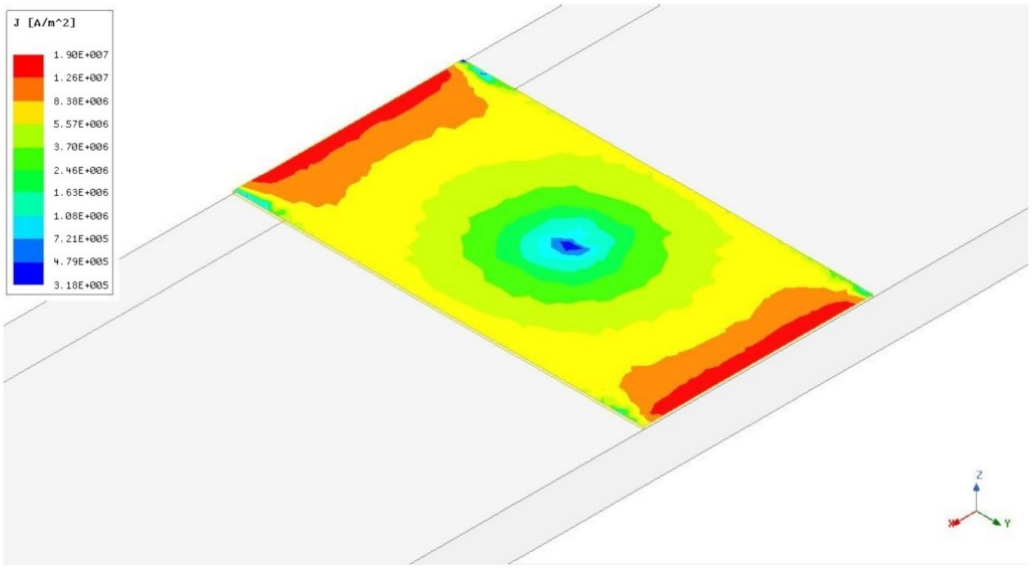


Fig. 13 Electromagnetic finite element analysis (FEA) current density distribution on the surface of a 150 µm pure aluminum coating as consequence of the interaction with the EMF

coating, the current density decays to the center because of the penetration depth effect (Ref 19, 20).

The presence of a current density within such a thin deposit makes plausible the assumption that, when the induction heater is maintained "On," the deposited layers are in situ heated and thermally softened. Thus, the incoming particles are deposited on a softer coating, decreasing the critical velocity required for deposition,

increasing the deposition efficiency, and minimizing the plastic deformation of the incoming particles upon impact while maximizing the impingement effect on the already deposited particles. Moreover, as more layers are sprayed, more material is exposed to EMF generating eddy currents within the newly deposited layers.

Conclusion

Induction heating and substrate preheating effects on Ti64 substrates and cold-sprayed pure aluminum coatings were investigated using a hybrid deposition process. Single-particle impact tests ("wipe tests") were used to help elucidate the adhesion mechanisms on the substrate. Mechanical bonding was discarded as an important adhesion mechanism because the substrates did not exhibit any visible signs of deformation, and this conclusion was supported by modeling results. However, no observable characteristic features of metallic bonding were found at the particle/substrate interface suggesting that a more thorough investigation should be conducted using high-resolution microscopy tools to bring insightful and conclusive evidence of the effects of substrate preheated temperature on metallic bond formation.

Induction heating could not maintain the initial substrate surface temperature as the gas stream interacted with the substrate due to the large convective heat transfer rate over the substrate. Consequently, the initial substrate surface temperature was quickly brought to a steady-state temperature value around 225 °C for all (RT, 200, 400, 600 °C) initial substrate temperatures.

Finally, it was found that the presence of an electromagnetic field drastically enhanced the deposition efficiency by in situ heating the coating. These important improvements were attributed to the formation of eddy currents within the coating, as suggested by modeling results. Consequently, the incoming particles deposit on a softer coating, decreasing the critical velocity required for deposition, and increasing the deposition efficiency. In addition, it was concluded that substrate preheating had no effect on the deposition efficiency, but it promoted the in situ heating effect on the coatings.

As an in situ heating of the coating was observed during the deposition of the coatings, it is of great interest to investigate its effect on the coating properties. Thus, Part II of this study is dedicated to evaluate the role on the in situ heating effect the coating properties such as micro-hardness, adhesion and tensile strength.

References

1. A.N. Papyrin, V.K. Kosarev, S. Klinkov, A. Alkimov, and V. Fomin, *Cold Spray Technology*, 1st ed., A.N. Papyrin, Ed., Elsevier, Oxford, 2007,
2. A. Moridi, S.M. Hassani-Gangaraj, M. Guagliano, and M. Dao, Cold Spray Coating: Review of Material Systems and Future Perspectives, *Surf. Eng.*, 2014, **30**(6), p 369-395
3. J. Villafuerte, Ed., *Modern Cold Spray: Materials, Process, and Applications*, Springer, Cham, 2015
4. J.R. Davis, Ed., *Handbook of Thermal Spray Technology*, 1st ed., ASM International, Cleveland, 2004
5. K.R. Ernst, J. Braeutigam, F. Gaertner, and T. Klassen, Effect of Substrate Temperature on Cold-Gas-Sprayed Coatings on Ceramic Substrates, *J. Therm. Spray Technol.*, 2013, **22**(2-3), p 422-432
6. W. Sun, A.W.Y. Tan, A. Bhowmik, I. Marinescu, X. Song, W. Zhai, F. Li, and E. Liu, Deposition Characteristics of Cold Sprayed Inconel 718 Particles on Inconel 718 Substrates with Different Surface Conditions, *Mater. Sci. Eng. A*, 2018, **720**, p 75-84
7. S. Yin, X. Suo, Y. Xie, W. Li, R. Lupoi, and H. Liao, Effect of Substrate Temperature on Interfacial Bonding for Cold Spray of Ni onto Cu, *J. Mater. Sci.*, 2015, **50**(22), p 7448-7457
8. S. Yin, X. Suo, Z. Guo, H. Liao, and X. Wang, Deposition Features of Cold Sprayed Copper Particles on Preheated Substrate, *Surf. Coat. Technol.*, 2015, **268**, p 252-256
9. M. Bray, A. Cockburn, and W. O'Neill, The Laser-Assisted Cold Spray Process and Deposit Characterisation, *Surf. Coat. Technol.*, 2009, **203**(19), p 2851-2857
10. J. Yao, L. Yang, B. Li, and Z. Li, Beneficial Effects of Laser Irradiation on the Deposition Process of Diamond/Ni60 Composite Coating with Cold Spray, *Appl. Surf. Sci.*, 2015, **330**, p 300-308
11. M. Kulmala and P. Vuoristo, Influence of Process Conditions in Laser-Assisted Low-Pressure Cold Spraying, *Surf. Coat. Technol.*, 2008, **202**(18), p 4503-4508
12. D.K. Christoulis, S. Guetta, E. Irissou, V. Guipont, M.H. Berger, M. Jeandin, J.G. Legoux, C. Moreau, S. Costil, M. Boustie, Y. Ichikawa, and K. Ogawa, Cold-Spraying Coupled to Nano-Pulsed Nd-YaG Laser Surface Pre-treatment, *J. Therm. Spray Technol.*, 2010, **19**(5), p 1062-1073
13. Y. Watanabe, C. Yoshida, K. Atsumi, M. Yamada, and M. Fukumoto, Influence of Substrate Temperature on Adhesion Strength of Cold-Sprayed Coatings, *J. Therm. Spray Technol.*, 2014, **24**(1-2), p 86-91
14. A. List, F. Gärtner, T. Schmidt, and T. Klassen, Impact Conditions for Cold Spraying of Hard Metallic Glasses, *J. Therm. Spray Technol.*, 2012, **21**(3-4), p 531-540
15. C. Legoux, J.G. Irissou, and E. Moreau, Effect of Substrate Temperature on the Formation Mechanism of Cold-Sprayed Aluminum, Zinc and Tin Coatings, *J. Therm. Spray Technol.*, 2007, **16**(5-6), p 619-626
16. Y. Xie, M.P. Planche, R. Raoelison, H. Liao, X. Suo, and P. Hervé, Effect of Substrate Preheating on Adhesive Strength of SS 316L Cold Spray Coatings, *J. Therm. Spray Technol.*, 2016, **25**(1-2), p 123-130
17. X.K. Suo, M. Yu, W.Y. Li, M.P. Planche, and H.L. Liao, Effect of Substrate Preheating on Bonding Strength of Cold-Sprayed Mg Coatings, *J. Therm. Spray Technol.*, 2012, **21**(5), p 1091-1098
18. Z. Arabgol, M. Villa Vidaller, H. Assadi, F. Gartner, and T. Klassen, Influence of Thermal Properties and Temperature of Substrate on the Quality of Cold-Sprayed Deposits, *Acta Mater.*, 2017, **127**, p 287-301

19. V. Rudnev, D. Loveless, and R.L. Cook, *Handbook of Induction Heating*, 2nd ed., CRC Press, Boca Raton, 2017
20. R.E. Haimbaugh, *Practical Induction Heat Treating*, 1st ed., ASM International, Cleveland, 2001
21. W.Y. Li, C. Zhang, C.J. Li, and H. Liao, Modeling Aspects of High Velocity Impact of Particles in Cold Spraying by Explicit Finite Element Analysis, *J. Therm. Spray Technol.*, 2009, **18**(5-6), p 921
22. W.Y. Li, H. Liao, C.J. Li, G. Li, C. Coddet, and X. Wang, On High Velocity Impact of Micro-Sized Metallic Particles in Cold Spraying, *Appl. Surf. Sci.*, 2006, **253**(5), p 2852-2862
23. T. Hussain, D.G. McCartney, P.H. Shipway, and D. Zhang, Bonding Mechanisms in Cold Spraying: The Contributions of Metallurgical and Mechanical Components, *J. Therm. Spray Technol.*, 2009, **18**(3), p 364-379
24. T. Schmidt, F. Gärtner, H. Assadi, and H. Kreye, Development of a Generalized Parameter Window for Cold Spray Deposition, *Acta Mater.*, 2006, **54**(3), p 729-742
25. H. Assadi, F. Gärtner, T. Stoltenhoff, and H. Kreye, Bonding Mechanism in Cold Gas Spraying, *Acta Mater.*, 2003, **51**(15), p 4379-4394
26. A. Nastic, M. Vijay, A. Tieu, S. Rahmati, and B. Jodoin, Experimental and Numerical Study of the Influence of Substrate Surface Preparation on Adhesion Mechanisms of Aluminum Cold Spray Coatings on 300 M Steel Substrates, *J. Therm. Spray Technol.*, 2017, **26**(7), p 1461-1483
27. G.R. Johnson and W.H. Cook, A Constitutive Model and Data for Metals Subjected to Large Strains, High Strain Rates, and High Temperatures, *7th Int. Symp. Ballist.*, 1983, **21**, p 541-547
28. G.R. Johnson and W.H. Cook, Fracture Characteristics of Three Metals Subjected to Various Strains, Strain Rates, Temperatures and Pressures, *Eng. Fract. Mech.*, 1985, **21**(1), p 31-48
29. F.P. Incropera, A.S. Lavine, T.L. Bergman, and D.P. DeWitt, *Fundamentals of Heat and Mass Transfer*, 2nd ed., Wiley, New York, 2007
30. W.D. Callister, *Fundamentals of Materials Science and Engineering*, 5th ed., Wiley, New York, 2001
31. D. Steinberg, *Equation of State and Strength Properties of Selected Materials*, Lawrence Livermore National Laboratory, Livermore, 1996
32. W.J. Zhang, B.V. Reddy, and S.C. Deevi, Physical Properties of TiAl-Base Alloys, *Scr. Mater.*, 2001, **45**(6), p 645-651
33. J.D. Jackson, *Classical Electrodynamics*, 3rd ed., Wiley, New York, 1999
34. K.H. Kim, W. Li, and X. Guo, Detection of Oxygen at the Interface and Its Effect on Strain, Stress, and Temperature at the Interface Between Cold Sprayed Aluminum and Steel Substrate, *Appl. Surf. Sci.*, 2015, **357**(B), p 1720-1726
35. Y. Cormier, P. Dupuis, B. Jodoin, and A. Ghaei, Finite Element Analysis and Failure Mode Characterization of Pyramidal Fin Arrays Produced by Masked Cold Gas Dynamic Spray, *J. Therm. Spray Technol.*, 2015, **24**(8), p 1549-1565
36. M. Grujicic, J.R. Saylor, D.E. Beasley, W.S. DeRosset, and D. Helfritch, Computational Analysis of the Interfacial Bonding Between Feed-Powder Particles and the Substrate in the COld-Gas Dynamic-Spray Process, *Appl. Surf. Sci.*, 2003, **219**(3-4), p 211-227
37. D.L. Gilmore, R.C. Dykhuizen, R.A. Neiser, T.J. Roemer, and M.F. Smith, Particle Velocity and Deposition Efficiency in the Cold Spray Process, *J. Therm. Spray Technol.*, 1999, **8**(4), p 576-582
38. F. Raletz, M. Vardelle, and G. Ezo'o, Critical Particle Velocity Under Cold Spray Conditions, *Surf. Coatings Technol.*, 2006, **201**(5), p 1942-1947
39. T. Schmidt, H. Assadi, F. Gärtner, H. Richter, T. Stoltenhoff, H. Kreye, and T. Klassen, From Particle Acceleration to Impact and Bonding in Cold Spraying, *J. Therm. Spray Technol.*, 2009, **18**(5-6), p 794-808
40. M. Grujicic, C.L. Zhao, C. Tong, W.S. DeRosset, and D. Helfritch, Analysis of the Impact Velocity of Powder Particles in the Cold-Gas Dynamic-Spray Process, *Mater. Sci. Eng. A*, 2004, **368**(1-2), p 222-230
41. X.J. Ning, J.H. Jang, and H.J. Kim, The Effects of Powder Properties on In-Flight Particle Velocity and Deposition Process During Low Pressure Cold Spray Process, *Appl. Surf. Sci.*, 2007, **253**(18), p 7449-7455
42. C.J. Li, W.Y. Li, and H. Liao, Examination of the Critical Velocity for Deposition of Particles in Cold Spraying, *J. Therm. Spray Technol.*, 2006, **15**(2), p 212-222
43. B. Jodoin, L. Ajdelsztajn, E. Sansoucy, A. Zúñiga, P. Richer, and E.J. Lavernia, Effect of Particle Size, Morphology, and Hardness on Cold Gas Dynamic Sprayed Aluminum Alloy Coatings, *Surf. Coatings Technol.*, 2006, **201**(6), p 3422-3429
44. C. Li, S. He, Y. Fan, H. Engelhardt, S. Jia, W. Xuan, X. Li, Y. Zhong, and Z. Ren, Enhanced Diffusivity in Ni-Al System by Alternating Magnetic Field, *Appl. Phys. Lett.*, 2017, **110**(7), p 074102
45. H. Assadi, T. Schmidt, H. Richter, J.O. Kliemann, K. Binder, F. Gärtner, T. Klassen, and H. Kreye, On Parameter Selection in Cold Spraying, *J. Therm. Spray Technol.*, 2011, **20**(6), p 1161-1176
46. Q. Bai, J. Lin, T.A. Dean, D.S. Balint, T. Gao, and Z. Zhang, Modelling of Dominant Softening Mechanisms for Ti-6Al-4V in Steady State Hot Forming Conditions, *Mater. Sci. Eng. A*, 2013, **559**, p 352-358
47. W.-S. Lee and C.-F. Lin, Plastic Deformation and Fracture Behaviour of Ti-6Al-4V Alloy Loaded with High Strain Rate Under Various Temperatures, *Mater. Sci. Eng. A*, 1998, **241**(1-2), p 48-59
48. N. Kotkunde, A.D. Deole, A.K. Gupta, and S.K. Singh, Comparative Study of Constitutive Modeling for Ti-6Al-4V Alloy at Low Strain Rates and Elevated Temperatures, *Mater. Des.*, 2014, **55**, p 999-1005
49. W.S. Lee and M.T. Lin, The Effects of Strain Rate and Temperature on the Compressive Deformation Behaviour of Ti-6Al-4V Alloy, *J. Mater. Process. Technol.*, 1997, **71**(2), p 235-246
50. V.F. Kosarev, S.V. Klinkov, A.P. Alkhimov, and A.N. Papyrin, On Some Aspects of Gas Dynamics of the Cold Spray Process, *J. Therm. Spray Technol.*, 2003, **12**(2), p 265-281
51. S. Yin, M. Meyer, W. Li, H. Liao, and R. Lupoi, Gas Flow, Particle Acceleration, and Heat Transfer in Cold Spray: A Review, *J. Therm. Spray Technol.*, 2016, **25**(5), p 847-896
52. J. Pattison, S. Celotto, A. Khan, and W. O'Neill, Standoff Distance and Bow Shock Phenomena in the Cold Spray Process, *Surf. Coatings Technol.*, 2008, **202**(8), p 1443-1454
53. R.C. Dykhuizen and M.F. Smith, Gas Dynamic Principles of Cold Spray, *J. Therm. Spray Technol.*, 1998, **7**(2), p 205-212
54. R.K. Wangsness, *Electromagnetic Fields*, 2nd ed., Wiley, New York, 1979

Publisher's Note Springer Nature remains neutral with regard to jurisdictional claims in published maps and institutional affiliations.

5.3 Influence of the Substrate and Coating Temperatures on the CS process using the Soft-on-Hard Material Combination – Part II

In this section, the influence of the initial substrate and coating temperatures on the CS process are investigated using the soft-on-hard material combination. To have independent control of the substrate and coating temperatures from the gas stagnation temperature, an induction heating system is used.

In this section, the following task is carried out to evaluate the role of the initial substrate temperature on the CS deposition process:

- Measure the Coating Mechanical Properties (micro-hardness and adhesion strength testing).

To characterize the influence of the coating temperature on the CS deposition process, the following task is completed:

- Measure the Coating Mechanical Properties (micro-hardness, adhesion and tensile strength testing).

To demonstrate that the mechanical properties of the cold-sprayed coatings can be modified based on the previous findings, samples are produced using different combinations of substrate and coating temperatures, and the coating mechanical properties are characterized.

The detailed evaluation of the individual and combined effect of the substrate and coating temperatures on the coating mechanical properties of cold-sprayed coatings using the soft-on-hard material combination is presented in the form of a published peer-reviewed paper (Reprinted from [130] with permission of Springer; permission conveyed through Copyright Clearance Center, Inc.).

J Therm Spray Tech
https://doi.org/10.1007/s11666-020-01006-9



PEER REVIEWED

Hybrid Additive Manufacturing Technology: Induction Heating Cold Spray—Part II: Coating Mechanical Properties

R. Ortiz-Fernandez[1] · B. Jodoin[1]

Submitted: 28 September 2019 / in revised form: 30 January 2020
© ASM International 2020

Abstract Delamination of soft and ductile materials from hard substrates is a challenge when using the cold spray process. Additionally, the as-sprayed coatings often exhibit a significant reduction in ductility and a brittle behavior upon fracture. As a potential solution to these problems, a tunable hybrid additive manufacturing process was developed by coupling induction heating and the cold spray process. Pure aluminum was used as the soft feedstock powder, while Ti-6Al-4V was used as the hard substrate. In situ induction heating and substrate preheating temperature effects on the coating's properties were evaluated: micro-hardness, adhesion and tensile strength were assessed and compared to traditional cold spray coating's properties. A reduction of up to 20% was found in the coating's micro-hardness produced by the hybrid process. Additionally, the adhesion strength was drastically increased when using the hybrid process while tensile strength reached almost 3 times the total elongation of the specimens produced using the traditional cold spray process. These results open up the possibility of using this hybrid technique as an additive manufacturing process for bulk parts and coating production.

Keywords additive manufacturing · cold spray · in situ heating · substrate temperature

✉ R. Ortiz-Fernandez

[1] Cold Spray Research Laboratory, University of Ottawa, Ottawa, ON, Canada

Introduction

Among the many thermal spray processes, cold spray (CS) is characterized by the deposition of particles in a solid state. In CS, particles are injected in a de Laval nozzle and accelerated to high speed velocities by the supersonic gas stream (Ref 1-4). Upon impact, the particles' kinetic energy is converted into heat (approximately 90%) and the rest is transformed into elastic and plastic deformation under high strain rates (Ref 1-4). Particles bond to the substrate once they enter into intimate contact with it and when high interfacial contact pressures are reached. Intimate contact can only be achieved when the particles and substrate respective native oxide surfaces are broken and removed following the impact (Ref 1-4).

Substrate preheating has been suggested as a way to improve CS coating properties (Ref 1-4). Despite the efforts and extent of results, it becomes difficult to generalize any conclusions. The authors have reported that the coating hardness does not change with substrate temperature (Ref 6, 7), while decreases in coating hardness have also been reported (Ref 7, 8). In terms of adhesion strength, an increase for different materials has been reported in some of the studies (Ref 5, 6, 9-13). Interestingly, the coatings' mechanical properties have not been investigated extensively. The scarce data have shown an increase in the coating strength when the substrate is preheated (Ref 7, 9).

Many preheating methods have been used such as ceramic heaters, heating cartridges and flame torches (Ref 5, 9, 14). The use of induction heaters (IH) as a preheating method is scarce and limited (Ref 7, 15). An induction heater produces a time-variable electromagnetic field (EMF) when an AC current flows throughout the inductor (or coil). The resulting EMF induces eddy currents on any metallic piece located near the inductor. As a consequence,

Published online: 03 March 2020

the temperature rises on any metallic piece due to the formation of eddy currents within the material (Ref 16, 17).

Induction heaters are commonly found in the case hardening industry for gears, bars and other industrial components (Ref 16, 17). In recent years, the use of induction heaters has been extended to new horizons. Induction sintering is a technique where metallic, ceramic or composite powders are compressed and then heated. As a result, powders are sintered homogenously due to the formation of large current densities within the compressed powder and/or due to an indirect source of radiative heat transfer from a graphite die (Ref 18-28). However, a drawback from this process is the requirement of a vacuum environment to avoid oxidation due to the very high temperatures reached by the compressed powder and to increase the radiative heat transfer between the graphite die and the compressed powder.

The purpose of the current study is to investigate the possible in situ effects of an EMF on cold-sprayed coatings produced by means of a hybrid induction heating CS system. Additionally, the effect of the initial substrate temperature on the coating production is also evaluated separately. In Part I of this study, the single-particle impact tests ("wipe tests") revealed an increase in the number of deposited particles as the initial substrate surface temperature was increased. Nevertheless, the effect of the initial substrate surface temperature was limited to the first deposited layer; as it was found that this surface temperature was quickly brought to a "steady-state" value around 225 °C, no matter its initial value. By keeping the induction heater "On" *while spraying*, a considerable increase in DE was observed. These results suggested the possibility of in situ heating the coating *while spraying*. The increase in DE was more prominent as the initial substrate surface temperature was increased. As a result, it was concluded that substrate preheating promotes the in situ heating effect on the deposit. Similar results have also been reported by Dalaee et al. (Ref 29) which coupled an IH to a directed energy deposition (DED) process. Finally, the presence of eddy currents in the pure aluminum coating was confirmed by an electromagnetic model which predicted their formation within the material.

In the second part of this work, the efforts are focused on assessing the effects of the in situ induction heating and the initial substrate surface temperature on the properties of the deposits. As in Part I, pure aluminum and Ti-6Al-4V (Ti64) were used as a soft powder/hard substrate material combination, respectively. By selecting this pair, the mechanical adhesion contribution to overall coating adhesion strength was reduced and the adhesion mechanism should be limited to metallic bond formation, as observed in Part I. Micro-hardness, adhesion and tensile strengths were also investigated in this part of the study. Finite element (FE) modeling simulating adhesion tests were used to point out the relevant bonding mechanisms occurring in the deposited coatings. Lastly, fractured surfaces of the adhesion and tensile strength samples were investigated to gain additional insight of the ongoing processes occurring during deposition using the hybrid spray process.

Experimental Procedure

Substrate and Feedstock Material

Ti64 coupons were used as the substrate material for the production of the coatings used for the micro-hardness evaluation and tensile samples. The coupons' dimensions were 25.0 mm × 115.0 mm × 3.2 mm. A 25.4-mm-diameter bar of commercially available Ti64 (Titanium Industries, Inc., Montreal, QC, Canada) was used as the substrate to perform adhesion strength samples. The substrate chemical composition provided by the supplier is Ti—balance, Al—5.94%, V—4%.

Commercially available gas-atomized pure aluminum powder (SST-A5001) (99.8% Al, Centerline (Windsor) Limited, Windsor, ON, Canada) was used to produce the coatings. The irregular morphology powder can be seen in Fig. 1. Despite the powder being non-spherical, laser diffraction (Microtrac model S3500, Montgomeryville, PA, USA) was used to determine the particle size distribution.

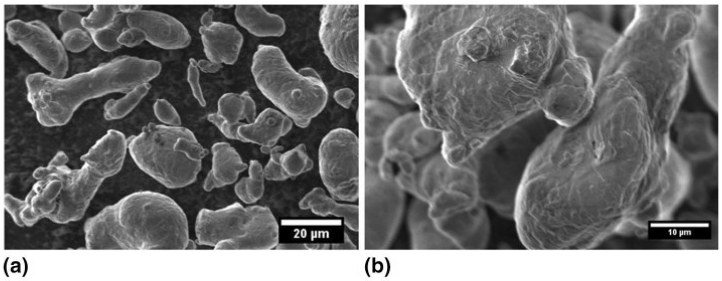


Fig. 1 Scanning electron microscope (SEM) image of the as-received aluminum powder. (a) Low magnification, (b) high magnification

Table 1 Cold spray deposition parameters

Parameters	Values
Stagnation temperature (°C)	500
Stagnation pressure (MPa)	3.45
Carrier gas	Nitrogen
Traverse speed (mm/s)	120
Powder feed rate (g/min)	4.5
Standoff distance (mm)	15
Number of passes	5
Step size (mm)	1

The resulting 10^{th}, 50^{th} and 90^{th} size percentiles were found to be 11.3 μm, 25.8 μm and 60.3 μm, respectively.

Polished and grit-blasted surfaces were used as substrate preparation methods. More information about the steps followed to obtain these can be found in Part I of this study. A profilometer equipped with a diamond stylus (PHASE II, SRG-4000, NJ, USA) was used to measure the substrates' arithmetic average roughness (Ra). Surface roughnesses of 0.25 ± 0.04 μm and 2.66 ± 0.32 μm were obtained for the polished and the grit-blasted surfaces, respectively. All samples were cleaned and degreased in an ethanol ultrasonic bath for 3 min prior to the deposition process.

Cold Spray Deposition

A commercially available system (SST-EP, Centerline (Windsor) Limited (Windsor, ON, Canada)) equipped with a polymer De Laval nozzle with a 2.0 mm throat diameter and a 6.4 mm exit diameter was used to produce the pure aluminum coatings. The powder was injected in the divergent section of the nozzle using a commercially available powder feeder (AT-1200 Rotary, Thermach Inc., Appleton, WI, USA). The spray parameters used are presented in Table 1.

Induction Heating Parameters for Coating Production

The Ti64 rectangular coupons and round bar were preheated to 200, 400 and 600 °C prior to the start of the spraying process using an induction heater (Tucker Induction Sys. Inc., Shelby Township, MI, USA). During the deposition of the pure aluminum coatings for all these cases, the induction heater was kept "On." To decouple the effects of substrate temperature and an electromagnetic field on the coating properties an additional set of coatings were also sprayed on a preheated substrate at 400 °C. However, for this case the induction heater was turned "Off" *while spraying*. The spraying setup used for the production of the samples on the rectangular coupons can be found in Fig. 2.

The induction heater parameters used during the deposition of the pure aluminum coating on the rectangular coupons are given in Table 2.

Sample Characterization

The as-received powder and the fractured surfaces were investigated using a scanning electron microscope (SEM) (EVO MA-10, Carl Zeiss AG, Oberkochen, Germany). Micro-hardness values were obtained using a Duramin-10 (Struers Aps, Denmark) equipped with a Vickers indenter using a load of 0.3 kg. Indentations were performed every 50 μm from the bottom to the top region of the coatings. This process was performed twice at different locations in a cross section. Two cross sections were tested for each condition. Indentations on the substrates were performed every 50 μm from the coating interface to the middle of the substrate thickness.

Coating Adhesion Strength Evaluation

Adhesion strength tests were performed in compliance with the ASTM C-633 standard test method for adhesion/cohesion strength of thermal spray coatings (Ref 30). The adhesion substrate samples were polished to a mirror finish before the deposition process. As per the standard, the coatings were deposited and then machined off using a lathe to a thickness of 400 μm. A 25.4-mm-diameter round bar made of Ti64 was used as substrate material. Because of the difference in shape between the rectangular coupons used for the coating production and the round bar, the induction heating setup to produce the adhesion test samples was modified. A schematic of the induction heating configuration used is presented in Fig. 3.

The Ti64 round bar was positioned in the middle of the coil. The heating rate caused by the formation of eddy currents in the substrate material is geometry dependent (Ref 16, 17). Thus, the induction heater parameters were modified in order to match the heating rate used on the rectangular coupons. The parameters used to preheat the bars are presented in Table 3. Parameters 3 produce a heating rate identical to Parameters 1 on the adhesion test substrates, while Parameters 4 produce a faster preheating rate than Parameters 3.

The induction heater conditions and the initial surface temperatures used to produce the various adhesion samples are presented in Table 4. For the samples labeled as Group 1 and Group 2, a total of three adhesion test samples were produced for each condition. For Group 3 and Group 4, a total of nine samples were tested for each set, three for each initial substrate surface temperature. The labels Group 1 to

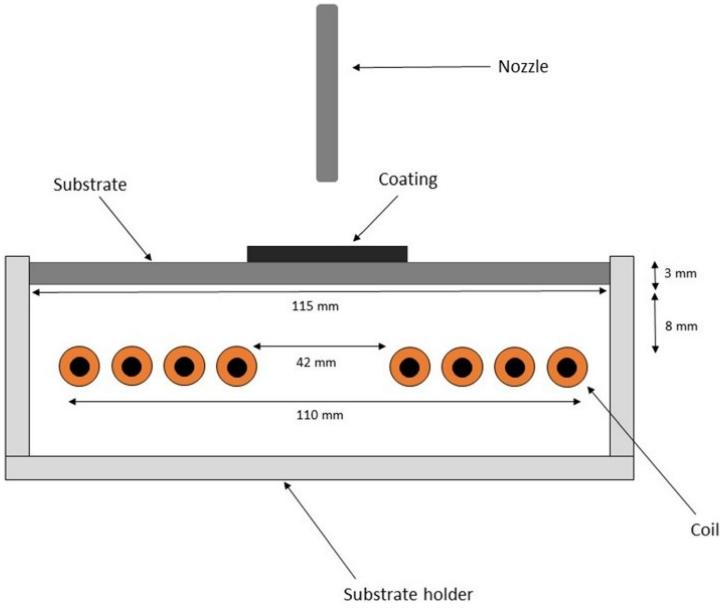


Fig. 2 Cross-sectional schematic of the setup used for the production of coating on rectangular coupons

Table 2 Induction heater parameters

Parameters	Parameters 1	Parameters 2
Current (A)	58	43
Frequency (kHz)	192	198

Group 4 will be used from this section forward to simplify the naming process.

Mechanical Testing

Tensile test samples were produced to investigate the coatings' mechanical properties. The samples were produced in compliance with the ASTM E8 (Ref 31) standard test method for sub-size specimens of metallic materials. The samples thickness was 1.50 mm. The samples were produced using the Ti64 rectangular coupons and the spray setup presented in Fig. 2. The induction heater conditions and the initial surface temperature used for the production of the tensile samples are presented in Table 5. Three tensile samples were produced for each condition. The label designated to each set of samples will be used from this section forward to simplify the naming process.

Adhesion Strength Modeling

2D FE Lagrangian models have been used to accurately predict the adhesion strength of CS coatings due to mechanical anchoring (Ref 32, 33). Thus, a similar model was used to predict the mechanical contribution on the overall coatings' adhesion strength. FE analysis was carried on using Abaqus/Explicit. Cross-sectional images were taken at the coating/substrate interfaces with an optical microscope, as illustrated in Fig. 4(a). To capture all the interface features, the cross-sectional images were taken at $\times 1000$ magnification. These were subsequently processed by an in-house python script which based on the contrast produces a digitalized profile of the cross-sectional image, as shown in Fig. 4(b). The digitalized interface was then exported into Abaqus/Explicit. To prevent the possible influence of stress concentration for the determination of the overall average stress, the coating/substrate thickness was ten times the greatest peak to valley distance in the profile. Once exported into Abaqus/Explicit, a 4-node plane strain (CPE4R) mesh was used on the substrate and the coating as presented in Fig. 4(c). This mesh was selected following the standard procedure described in the literature which is adequate for all different surface roughnesses (Ref 32, 33). Finally, the boundary conditions were assigned as exhibited in Fig. 4(d). The bottom of the substrate was fixed. The substrate/coating side walls were set as x-symmetric. Finally, the top part of the coating was

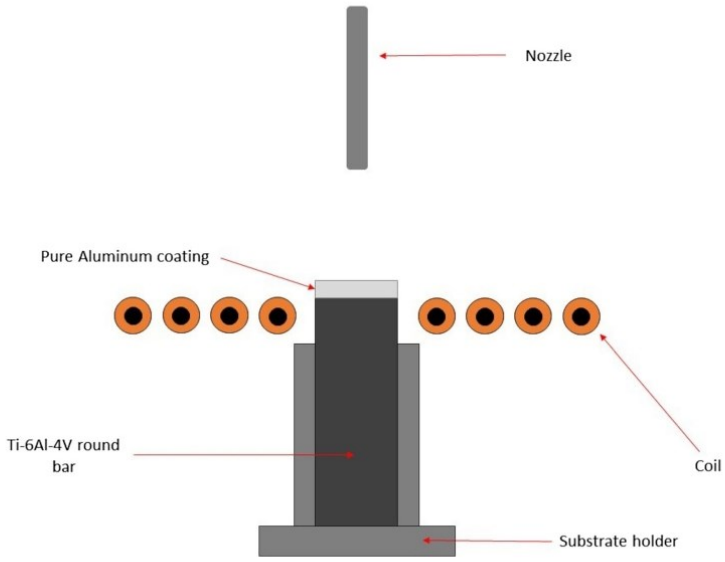


Fig. 3 Cross-sectional view of the setup used for producing the adhesion strength samples

Table 3 Induction heater parameters used for preheating the Ti64 round bar

Parameters	Parameters 3	Parameters 4
Current (A)	50	68
Frequency (kHz)	198	193

assigned a uniform displacement equivalent 0.02 mm/s as per the ASTM-C633 standard.

A friction coefficient of 0.5 was assigned in this interaction (Ref 32, 33). The coating and the substrate were initialized at room temperature. The elastic response of the particles and the substrates during the simulations were modeled by the linear Us-Up Hugoniot form of Mie–

Table 4 Deposition conditions used to produce the adhesion strength samples

Induction heater conditions	Initial surface temperature (°C)	Label
No preheating of the adhesion substrates	25	Group 1
Preheating of the adhesion substrates using Parameters 3. The induction heater was turned "Off" during the deposition process.	400	Group 2
Preheating of the adhesion substrates using Parameters 3. The induction heater was maintained "On" during the deposition process.	200, 400 and 600	Group 3
Preheating of the adhesion substrates using Parameters 4. The induction heater was maintained "On" during the deposition process.	200, 400 and 600	Group 4

Table 5 Deposition conditions used on the production of the tensile test samples

Induction heater condition	Initial surface temperature (°C)	Label
No preheating	25	CS
Preheating using Parameters 1. The induction heater was maintained "On" during the deposition process.	600	CS + IH

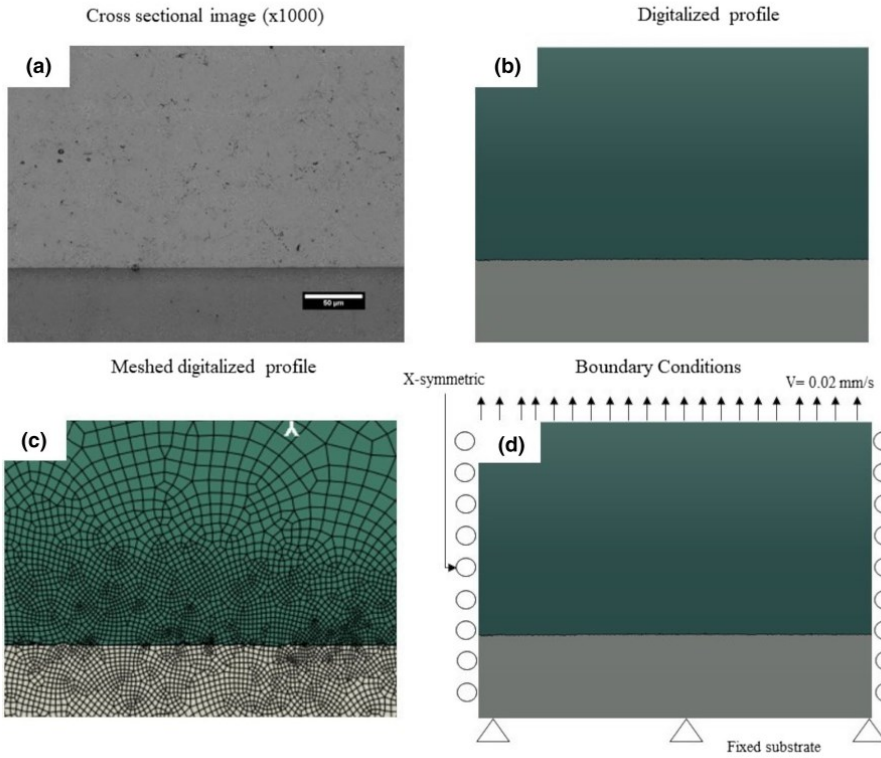


Fig. 4 Adhesion strength modeling process. To develop the simulation, steps are (a) to take a cross-sectional image of the interface. (b) Digitalize the image. (c) Export the digitalized image into Abaqus/Explicit and mesh it. (d) Assign boundary conditions to the model

Grüneisen (Eq 1). In order to model the plastic behavior, the Johnson–Cook equation (Ref 34, 35) (Eq 2) was used.

$$p = \frac{\rho_0 c_0^2 \eta}{(1 - s\eta)^2}\left(1 - \frac{\Gamma_0 \eta}{2}\right) + \Gamma_0 \rho_0 E_m, \quad \eta = 1 - \frac{\rho_0}{\rho} \tag{Eq 1}$$

$$\sigma_{eq} = \left[A + B\varepsilon_p^n\right]\left[1 + C\ln\left(\frac{\dot{\varepsilon_p}}{\dot{\varepsilon_{ref}}}\right)\right]\left[1 - \left(\frac{T - T_{ref}}{T_m - T_{ref}}\right)^m\right] \tag{Eq 2}$$

where for the elastic response p is the hydrodynamic stress, ρ_0 is the initial density,ρ is the actual density, c_0 is the material speed of sound,Γ_0 is the Mie–Grüneisen's constant, E_m is the energy per unit mass. A, B, C, n are the Johnson–Cook parameters, $\dot{\varepsilon_p}$ is the plastic strain rate, ε_p is the equivalent plastic strain, $\dot{\varepsilon_{ref}}$ is the strain rate at which the Johnson–Cook parameters were obtained, T_m is the melting temperature, T_{ref} is the transition temperature, and T is the absolute temperature. The material properties used in these simulations can be found in Table 6.

The adhesion strength value was obtained by averaging the y-direction stresses (S22) on the elements located at the bottom of the substrate, which follows the procedure used in the literature (Ref 32, 33). Five cross-sectional images per substrate temperature were analyzed to obtain the average adhesion strength of the sample.

Results and Discussion

Coating Micro-hardness

The aluminum powder micro-hardness was 20 ± 5 HV. The substrates' micro-hardness was measured in the as-received state and after the deposition process for all the

different temperatures. The substrates micro-hardness was 342 ± 5 HV in the as-received state. For the different initial substrate temperatures, the mean substrate micro-hardness after the spraying process was 343 ± 6 HV. This indicates that the substrate did not experience changes in hardness due to the preheating and (hybrid) deposition processes.

In CS, the as-sprayed coating hardness is a good indicator of the level of plastic deformation experienced by the sprayed particles (Ref 4, 39-42). Figure 5 presents the average coating micro-hardness as a function of the initial substrate temperature. The coatings' micro-hardness was evaluated using the produced samples in the first part of this work.

Table 6 Material properties used in the model (Ref 33, 36-38)

Properties	Aluminum	Ti64
Density (ρ_0), kg/m^3	2700	4510
Specific heat (C_p), J/kgK	910	600
Thermal conductivity (κ), W/mK	237	6.80
Melting temperature (T_m), K	934	1923
Shear modulus (G), GPa	26	45
Young modulus (E), GPa	69	115
A (MPa)	148.40	3500
B (MPa)	345.5	331
C	0.001	0.012
n	0.183	0.34
m	0.895	0.80
$\dot{\varepsilon}_{ref}$	1.00	1.00
T_{ref} (K)	300	300
Grüneisen constant (Γ_0)	2.14	1.25
Speed of sound (m/s)	5292	4950
Hugoniot slope (s)	1.40	7

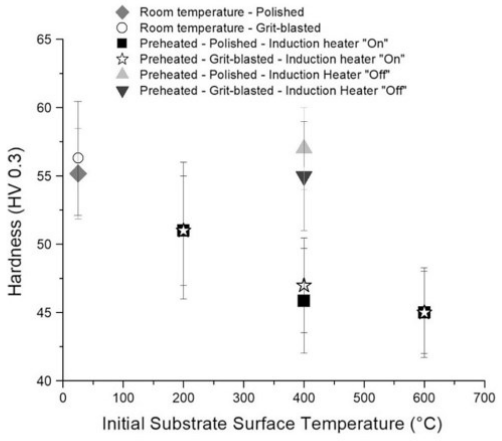


Fig. 5 Pure aluminum coating hardness at different initial substrate surface temperatures. Parameters 1 were used to preheat the substrates to the initial surface temperature

As can be observed, the surface preparation (polished and grit-blasted) had no effect on the coatings' micro-hardness, since only the first layer of the deposited particles interacts with the prepared surfaces. The coatings deposited on polished and grit-blasted substrates at 25 °C presented the hardest values at 55 ± 4 and 56 ± 5 HV, respectively. Upon impact, particles plastically deform and experience cold working, so they strain hardened. Additionally, the successive impact of the incoming high velocity particles further contributes to this hardening effect on the previously deposited particles. As a result, metallic coatings are always harder than the as-received powder.

A reduction of the coating hardness is observed when the initial surface temperature is increased and the induction heater is maintained "On" during the spraying process. At 200 °C, the average coating hardness on polished and grit-blasted substrates was 51 ± 4 and 51 ± 5 HV, respectively. At 400 °C, the measured micro-hardness was 47 ± 4 and 48 ± 3 HV. Finally, at 600 °C the coatings' micro-hardness was further reduced to an average value of 45 ± 5 and 46 ± 4 HV. Conversely, the micro-hardness of the coatings sprayed at 400 °C as the initial substrate temperature and the induction heater turned "Off" showed an average value of 57 ± 3 and 55 ± 4 HV, similar to the one produced at room temperature. This suggests that the deposited particles experienced similar plastic deformation as in the 25 °C case. Additionally, this similitude shows that the initial surface temperature has no effect on the coating hardness, potentially because the additional available thermal energy is quickly removed by the gas stream, as shown in Part I (Ref 5, 6).

The coating micro-hardness reduction is attributed to an in situ heat treatment occurring within the pure aluminum coating during the hybrid spraying process when the induction heating is kept "On." In Part I, it has been shown that eddy currents are present in the coatings since the early stages of the deposition process. Thus, during the spray time, the deposited layers are continuously warmed up by the localized heat source generated by the eddy currents and by the heat conducted from the bottom of the coating to the newly deposited layers. Consequently, the incoming particles impact a thermally softened coating, thus deforming the already deposited layer more easily while experiencing less cold working. Long and extensive post-heat treatments ranging from 1 to 36 h have been used to release stress and soften coatings (Ref 7, 42-45). However, in the current study, the spraying time is short (approximately 44 s), suggesting a unique fast in situ heating effect.

Adhesion Strength Tests

The coatings' adhesion strength was evaluated to gain further knowledge of the effects of in situ induction heating and the initial substrate temperature. Experimental values as well as values predicted by the FE model are presented in Fig. 6

The FEA results are represented by the white squares in Fig. 6. The cross-sectional images at room temperature displayed delamination. Thus, the adhesion value was set to zero. For the rest of the modeled cases, an overall average value of 6 ± 2 MPa was obtained. In the past, FEA has accurately predicted the mechanical bonding of the coating (Ref 32, 33). However, despite the increase in substrate temperature, all the interface cross sections showed a similar substrate deformation level. Cross-sectional images of the produced coating can be found in Part I of this work. Consequently, the FEA model predicted a similar adhesion strength for all initial substrate temperatures. It is important to note that the model is unable to predict metallic bonding contribution. Because all the experimental results show adhesion strengths considerably larger than the predicted values, it can be concluded that the coatings must adhere to the substrate by the additional formation of localized metallic bonds.

Group 1 (circular symbol) in Fig. 6 represents the samples produced at 25 °C as initial surface temperature. These samples failed in adhesion during the process of machining to the adequate thickness. Therefore, the adhesion strength was considered to be zero.

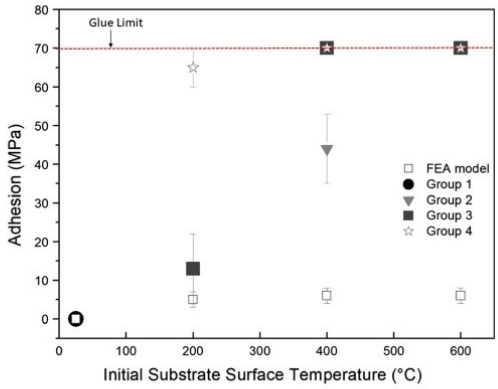


Fig. 6 Adhesion values at different initial surface temperatures. The white squares represent the FEA results. Group 1: 25 °C as initial surface temperature. Group 2: 400 °C as initial surface temperature, heater "Off'. Groups 3 and 4: 200 °C, 400 °C and 600 °C, heater "On'. Groups 2 and 3 were preheated using Parameters 3, while Group 4 used Parameters 4

Group 2 (triangular symbol) in Fig. 6 presents the samples preheated at 400 °C using Parameters 3, with the induction heater turned "Off" during the deposition process. These samples showed an adhesion strength of 44 ± 9 MPa. These samples exhibited an adhesion/cohesion failure combination. The increase in adhesion compared to the previous case is attributed to the higher initial substrate temperature, even though the surface temperature quickly drops in time. When the initial substrate temperature is increased, the substrate material is thermally softened, resulting in a more efficient oxide removal process as it deforms more easily. As such, the substrate and the particles can enter into intimate contact. Moreover, due to the higher initial surface temperature, additional thermal energy is available to help the metallic bond formation at the particle/substrate region. This result shows good accordance with the literature (Ref 5-7, 9, 11-13).

Group 3 (black square symbols) presents the adhesion values of the samples preheated at different initial surface temperatures using Parameters 3, with the induction heater "On" during the deposition process. The samples sprayed at 200 °C as the initial surface temperature showed a strength value of 13 ± 10 MPa. These samples failed at the substrate/coating interface (adhesion). At 400 °C and 600 °C values larger than 70 MPa are extrapolated as the glue limit was reached. As the limit was reached and the glue failed, it caused the coating to fail in an adhesion/cohesion combination. It is interesting to note that the adhesion samples sprayed at 400 °C as the initial surface temperature exhibited a far superior adhesion strength compared to the values obtained in Group 2 sprayed under similar conditions, but with the induction heating turned "Off" during the spray. In the CS literature, it has been proposed that the adhesion depends solely on the mechanisms that occur during the first deposited layer (Ref 32, 33, 46, 47). However, this suggests that the adhesion quality is not only a function of the particle/substrate contact, but an additional contribution caused by the interaction of the interface with the EMF must be considered. During the deposition process, the higher initial surface temperature promotes an intimate contact between the substrate and the particle enhancing adhesion (Ref 5-7, 9, 10), but, if sufficiently close contact is reached, the eddy currents must contribute in some form to the increased coating adhesion strength.

Group 4 (star symbols) in Fig. 6 shows the adhesion values of the samples preheated at different initial surface temperatures using Parameters 4, with the induction heater "On" during the deposition process. At 200 °C, the adhesion was increased to an average value of 65 ± 5 MPa. As in previous cases, an adhesion/cohesion failure mode occurred. The samples at 400 and 600 °C reached the glue limit. After the testing procedure, only a

few small pits created by the glue fracture were present. The sprayed samples at 200 °C exhibited an adhesion strength almost five times larger than the samples sprayed under similar conditions in Group 3. This implies that the adhesion strength can be tuned and modified by increasing the eddy current density in the material, which ultimately is reflected on a higher heating rate, without necessarily preheating the substrate to 400 or 600 °C. The results from Groups 3 and 4 further suggest that the hybrid deposition process causes in situ heat treatment of the coating.

Adhesion Strength Fracture Analysis

To gain further knowledge from the adhesion test samples, the coating/substrate interfaces were investigated. Figure 7 presents the fracture surface on the substrate side of samples of Groups 2 and 3. It can be observed that the substrate in Fig. 7(a) and (b) remained flat and no sign of deformation was present, as it was also observed in Part I of this work. However, scattered small areas of cup and cone features are observed in Fig. 7(a). The few necking features on the substrate are consequences of metallic bond formation at the particle/substrate interface during the deposition process. Also, these elements suggest a successful oxide removal process and an intimate contact between the two metal surfaces upon the particle impact. Lastly, these morphologies explain the drastic increase in adhesion strength observed from 25 to 400 °C as the initial surface temperature.

Figure 7(b) presents similar cup and cone features, but these are larger and less scattered. These larger necking areas explain the pronounced increase in adhesion strength

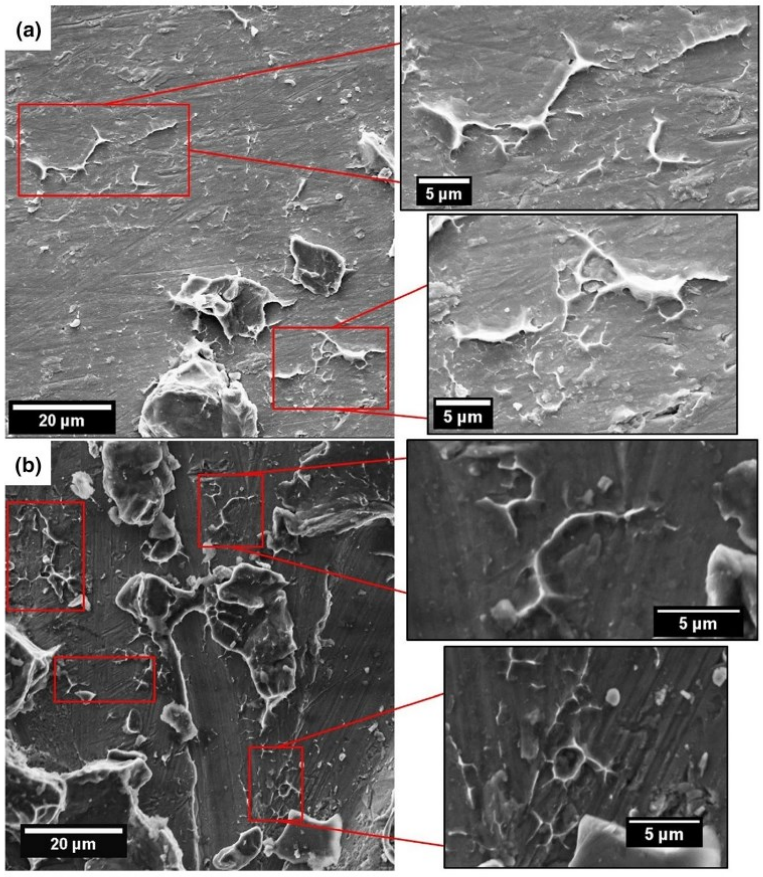


Fig. 7 Scanning electron microscope (SEM) image of the substrate side after adhesion testing process. In (a) initial surface temperature at 400 °C and induction heater "Off" during the deposition process (Group 2) and in (b) at 400 °C and induction heater maintained "On" during the deposition process (Group 3). The red squares show necking features (Color figure online)

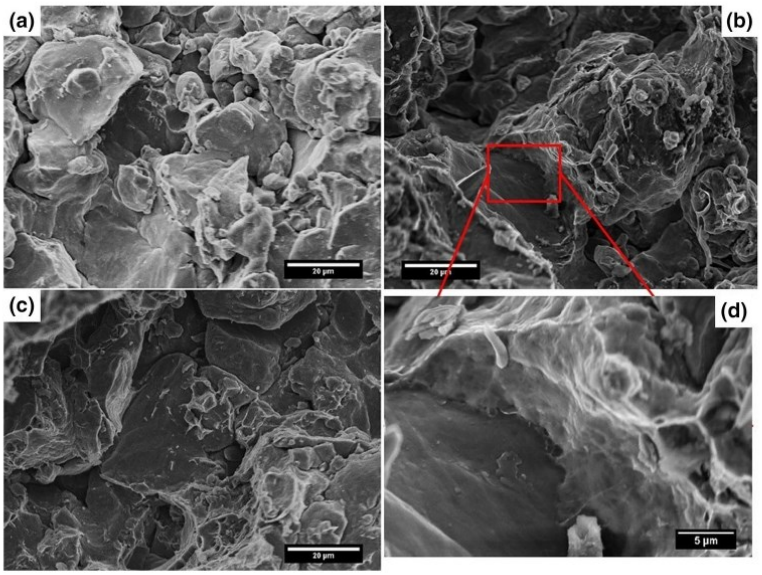


Fig. 8 Scanning electron microscope (SEM) images of the fractured coating after adhesion strength test. (a) Sample from Group 2, (b) sample from Group 3 and (c) sample from Group 4. All the samples were sprayed at an initial surface temperature of 400 °C. The induction heater was turned "Off" for (a), while it was maintained "On" for b) and (c). Parameters 3 and 4 were used for (b) and (c), respectively. (d) Presents a zoomed-in image of the red square in (b) (Color figure online)

observed in Fig. 6. Therefore, maintaining the induction heater "On" during the deposition process must produce an additional beneficial effect on the regions where the particle reached intimate contact with the substrate.

Figure 8 presents the coatings' fracture surface of an adhesion test sample from Groups 2, 3 and 4. Even though the coatings were deposited at a similar initial surface temperature, the surfaces present different morphologies from each other. Figure 8(a) presents the characteristic inter–particle fracture pattern of the CS process. Additionally, little to no signs of metallic bonds at the particle/particle interface are observed. This result was expected, because most of the available thermal energy was quickly removed by the gas stream as it moved over the substrate, as presented in Part I. As a consequence, the higher initial surface temperature had only an effect on the first deposited layer, but a minimal effect on the subsequent deposited layers.

Figure 8(b) and (c) shows a combination of inter-particle/intra-particle fracture. Even though the coatings were deposited at a similar initial substrate surface temperature, the inter-particle interfaces showed necking features at these regions. Furthermore, some inter-particle boundaries are no longer clearly distinguishable. Because of that, some regions seem to have fractured at the intra-particle region as shown in Fig. 8(b). Since these are not present in Fig. 8(a), it can be concluded that they must have formed because of the interaction of the aluminum particles with the EMF. This is further confirmed by Fig. 8(b) and (d) where two particles exhibit sintered-like features.

In situ Sintering Mechanism

Induction sintering is a process that has been widely studied in the literature. As a first step, this technique cold presses powders at a pressure which ranges from 10 to 300 MPa before the heating step. The heating stage can be carried out without applying any pressure or while maintaining the pressure used during the compressing stage. Once the green is formed, the heating stage is carried out using an induction heater. In most of the studies, this step ranges from 1 to 3 min (Ref 18-28). In CS, the particles and the substrate experience local contact pressures upon impact above the pressure range used in induction sintering at the particle/substrate and particle/particle interface region (Ref 32, 48-50). If the required pressures to reach intimate contact and the native oxide layer is removed, particles will bond and form a coating (an equivalent of green obtained in the first step of the induction sintering process). The spraying process in the current study occurred within the induction sintering time frame used in the literature. Therefore, based on these similitudes, an analogy can be drawn between induction sintering and the current hybrid process.

Figure 9 presents a schematic of multiple particle impact and their interaction with the EMF. In the

conducted tests, the spraying process acts as an equivalent step to the pressing stage used in induction sintering. While powder is compacted, eddy currents are formed within the coating due to their interaction with the EMF. Due to a non-uniform contact at the particle/particle and particle/substrate regions, high-resistivity bridges are created producing peak temperature values at these locations. These peak values have been shown to exceed the maximum temperature of the consolidated body by 2 or 3 orders of magnitude (Ref 51, 52). Interestingly, the theoretical high temperatures at the high-resistivity bridges might not be the sole reason promoting the formation of the metallic bonds. The formation of metallic bonds is also well known to be enhanced at nano-sized grain regions (Ref 53-56) and by the presence of an alternating magnetic field (Ref 57-61). It is interesting to note that in the CS literature the formation of nano-sized grains has been reported at particle/particle and particle/substrate regions (Ref 62-65) as a result of the intensive plastic deformation taking place at these zones during the impact process. Thus, a potential combination of the formation of nano-sized grains at these zones, the mass transfer that has been shown to be accelerated under an alternating magnetic field and the localized high temperatures promoting the formation of metallic bonds at these bridges, as it is shown in Fig. 7(b) and 8(b), (c) and (d), may all be involved in the enhanced process features.

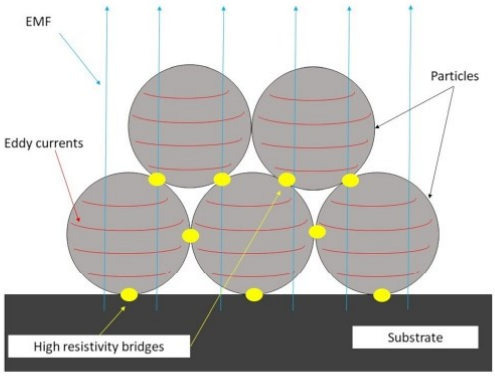


Fig. 9 Schematic of the interaction of the particles and the substrate with the EMF

Table 7 Tensile properties of the produced samples

Samples	Average UTS (MPa)	Average strain
CS	60 ± 17	0.008 ± 0.001
CS + IH	71 ± 14	0.023 ± 0.002

Tensile Strength Test

Tensile testing results are presented in Table 7. The samples showed similar UTS, with the sample produced by the hybrid process presenting a slightly larger UTS, but their behaviors were different. The CS samples presented a brittle behavior since they were barely strained before reaching the breaking point. This is a characteristic of CS coatings, and it shows good agreement with results available in the literature for CS aluminum coatings (Ref 66, 67). Conversely, the CS + IH samples were able to reach over 2% total elongation. This is a unique result, as extensive post-heat treatments have been required to significantly increase the ductility of CS coatings. It is hypothesized that the in situ sintering process was able to considerably increase the ductility of the cold-sprayed coatings.

The fracture surfaces of the tensile samples are presented in Fig. 10. The CS tensile sample clearly shows inter-particle fracture, characteristics of the CS process. No signs of necking features or cup and cone are visible. Thus, the samples in CS failed in a decohesive manner.

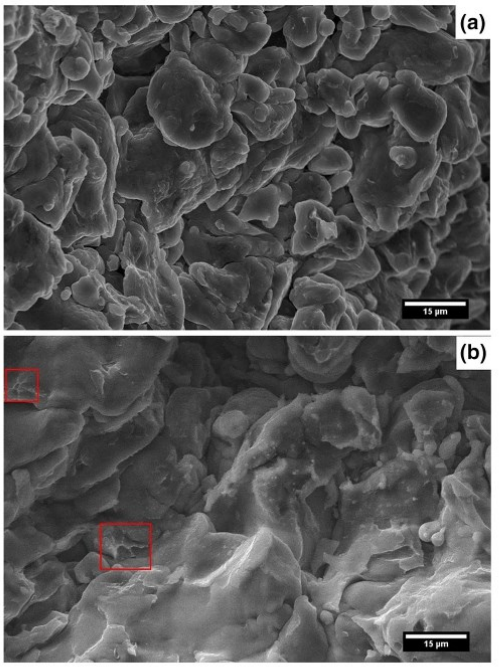


Fig. 10 Scanning electron microscope (SEM) image of the fracture region of the tensile samples. (a) CS sample, (b) CS + IH sample. In the red squares, characteristic features of metallic bonding are observable

A unique topography and different morphology compared to the CS sample is observable for the hybrid CS + IH sample. Firstly, the inter-particle regions are no longer distinguishable. Instead, melted-like features are visible at the inter-particle regions. Secondly, cups and cones are seen on some particles. Interestingly, the appearance of the necking and melted-like features coincided with the regions proposed as high-resistivity bridges. Therefore, these must be a consequence of the very localized high temperatures at the inter-particle region. As a result, a mixed inter-/intra-particle fracture mode was obtained for the first time in the literature without the need of a post-heat treatment process.

Conclusion

The effects of in situ induction heating during the hybrid spray process and substrate preheating on the coating properties were investigated. Pure aluminum was deposited on Ti64 substrates using an induction-assisted hybrid cold spray process. Micro-hardness, adhesion and tensile strengths of the coatings produced were evaluated. The pure aluminum deposits produced by the traditional cold spray process exhibited an average value of 55 and 56 HV for polished and grit-blasted substrates, respectively. It was found that the pure aluminum coatings did not exhibit a significant change in hardness when using a preheated substrate (400 °C). However, keeping the induction heater "On" *while spraying* produced a 20% hardness reduction in comparison with the traditional cold-sprayed coatings.

The adhesion strength of the samples deposited using cold spray with no substrate preheating was zero, as they delaminated during the machining process. However, by increasing the initial substrate temperature (to 400 °C) the adhesion strength was increased to 44 MPa. The adhesion strength of samples produced using the hybrid technique was found to be higher than 70 MPa, as they reached glue failure. Additionally, it was observed that adhesion strength of the deposits produced by the hybrid process are a function of the induction heating parameters.

Adhesion strength fracture surfaces revealed that in situ heating produced a sintering-like effect at the coating/substrate and inter-particle regions. This in situ heating process promoted adhesion at the coating/substrate interface and increased the cohesion between the particles. In Part I of this work, the possibility of an in situ heating process was suggested by the modeling results which predicted the presence of eddy currents on the coating.

Finally, a comparison of tensile properties of the coatings was performed. The cold-sprayed samples exhibited the characteristic brittle behavior. The latter was accompanied by an inter-particle fracture at the neck of the samples. The samples produced using the hybrid process showed almost three times the total elongation obtained by the traditional cold spray process and exhibited an intra-particular fracture with melted-like features visible at the inter-particle regions. These results open up the possibility of using this hybrid technique as an additive manufacturing process for bulk parts and coating production.

Acknowledgements The authors would like to thank Dr. Michel Nganbe for facilitating the use of his induction heater for the production of this work. R. Ortiz-Fernandez would also like to thank the technical officers: Leo Denner, Stanley Weedmark, Paul Burberry and Jacques Audet, for their advice during the development of the setup for the tests and always responsive help to machine the samples presented in this paper.

References

1. A.N. Papyrin, V.K. Kosarev, S. Klinkov, A. Alkimov, and V. Fomin, *Cold Spray Technology*, 1st ed., A.N. Papyrin, Ed., Elsevier, Oxford, 2007,
2. A. Moridi, S.M. Hassani-Gangaraj, M. Guagliano, and M. Dao, Cold Spray Coating: Review of Material Systems and Future Perspectives, *Surf. Eng.*, 2014, **30**(6), p 369-395
3. J. Villafuerte, Ed., *Modern Cold Spray: Materials, Process, and Applications*, Springer, Berlin, 2015
4. J.R. Davis, Ed., *Handbook of Thermal Spray Technology*, 1st ed., ASM International, Cleveland, 2004
5. Y. Xie, M.P. Planche, R. Raoelison, H. Liao, X. Suo, and P. Hervé, Effect of Substrate Preheating on Adhesive Strength of SS 316L Cold Spray Coatings, *J. Therm. Spray Technol.*, 2016, **25**(1–2), p 123-130
6. X.K. Suo, M. Yu, W.Y. Li, M.P. Planche, and H.L. Liao, Effect of Substrate Preheating on Bonding Strength of Cold-Sprayed Mg Coatings, *J. Therm. Spray Technol.*, 2012, **21**(5), p 1091-1098
7. K.R. Ernst, J. Braeutigam, F. Gaertner, and T. Klassen, Effect of Substrate Temperature on Cold-Gas-Sprayed Coatings on Ceramic Substrates, *J. Therm. Spray Technol.*, 2013, **22**(2–3), p 422-432
8. S. Yin, X. Suo, Z. Guo, H. Liao, and X. Wang, Deposition Features of Cold Sprayed Copper Particles on Preheated Substrate, *Surf. Coat. Technol.*, 2015, **268**, p 252-256
9. W. Sun, A.W.Y. Tan, A. Bhowmik, I. Marinescu, X. Song, W. Zhai, F. Li, and E. Liu, Deposition Characteristics of Cold Sprayed Inconel 718 Particles on Inconel 718 Substrates with Different Surface Conditions, *Mater. Sci. Eng., A*, 2018, **720**, p 75-84
10. D.K. Christoulis, S. Guetta, E. Irissou, V. Guipont, M.H. Berger, M. Jeandin, J.G. Legoux, C. Moreau, S. Costil, M. Boustie, Y. Ichikawa, and K. Ogawa, Cold-Spraying Coupled to Nano-Pulsed Nd-YaG Laser Surface Pre-treatment, *J. Therm. Spray Technol.*, 2010, **19**(5), p 1062-1073
11. Y. Watanabe, C. Yoshida, K. Atsumi, M. Yamada, and M. Fukumoto, Influence of Substrate Temperature on Adhesion Strength of Cold-Sprayed Coatings, *J. Therm. Spray Technol.*, 2014, **24**(1–2), p 86-91
12. R. Drehmann, T. Grund, T. Lampke, B. Wielage, K. Manygoats, T. Schucknecht, and D. Rafaja, Splat Formation and Adhesion Mechanisms of Cold Gas-Sprayed Al Coatings on Al_2O_3 Substrate, *J. Therm. Spray Technol.*, 2014, **23**(1–2), p 68-75
13. R. Drehmann, T. Grund, T. Lampke, B. Wielage, K. Manygoats, T. Schucknecht, and D. Rafaja, Essential Factors Influencing the

Bonding Strength of Cold-Sprayed Aluminum Coatings on Ceramic Substrates, *J. Therm. Spray Technol.*, 2018, **27**(3), p 446-455
14. S. Yin, X. Suo, Y. Xie, W. Li, R. Lupoi, and H. Liao, Effect of Substrate Temperature on Interfacial Bonding for Cold Spray of Ni onto Cu, *J. Mater. Sci.*, 2015, **50**(22), p 7448-7457
15. Z. Arabgol, M. Villa Vidaller, H. Assadi, F. Gartner, and T. Klassen, Influence of Thermal Properties and Temperature of Substrate on the Quality of Cold-Sprayed Deposits, *Acta Mater.*, 2017, **127**, p 287-301
16. V. Rudnev, D. Loveless, and R.L. Cook, *Handbook of Induction Heating*, 2nd ed., CRC Press, Boca Raton, 2017
17. R.E. Haimbaugh, *Practical Induction Heat Treating*, 1st ed., ASM International, Cleveland, 2001
18. A.D. LaLonde, T. Ikeda, and G.J. Snyder, Rapid Consolidation of Powdered Materials by Induction Hot Pressing, *Rev. Sci. Instrum.*, 2011, **82**(2), p 025104
19. H.C. Kim, D.K. Kim, K. Do Woo, I.Y. Ko, and I.J. Shon, Consolidation of Binderless WC-TiC by High Frequency Induction Heating Sintering, *Int. J. Refract. Met. Hard Mater.*, 2008, **26**(1), p 48-54
20. H.C. Kim, I.J. Shon, and Z.A. Munir, Rapid Sintering of Ultra-Fine WC-10 Wt% Co by High-Frequency Induction Heating, *J. Mater. Sci.*, 2005, **40**(11), p 2849-2854
21. I.J. Shon, I.K. Jeong, I.Y. Ko, J.M. Doh, and K. Do Woo, Sintering Behavior and Mechanical Properties of WC-10Co, WC-10Ni and WC-10Fe Hard Materials Produced by High-Frequency Induction Heated Sintering, *Ceram. Int.*, 2009, **35**(1), p 339-344
22. K.A.-R. Khalil and S.W. Kim, High-Frequency Induction Heating Sintering of Hydroxyapatite-(Zro2 + 3%Mol Y2o3) Bioceramics, *Mater. Sci. Forum*, 2007, **534–536**, p 1033-1036
23. S.W. Kim and K.A.R. Khalil, High-Frequency Induction Heat Sintering of Mechanically Alloyed Alumina–Yttria-Stabilized Zirconia Nano-Bioceramics, *J. Am. Ceram. Soc.*, 2006, **89**(4), p 1280-1285
24. E.A. Olevsky and D.V. Dudina, *Field-Assisted Sintering: Science and Applications*, Springer, Berlin, 2018
25. A. Guyon, D. Bouvard, J.M. Chaix, and C.P. Carry, Densification and Microstructure Changes of Micron Size Nickel Powder During Direct Induction Sintering, *Powder Metall.*, 2014, **57**(1), p 54-60
26. D.V. Dudina, K. Georgarakis, Y. Li, M. Aljerf, A. LeMoulec, A.R. Yavari, and A. Inoue, A Magnesium Alloy Matrix Composite Reinforced with Metallic Glass, *Compos. Sci. Technol.*, 2009, **69**(15–16), p 2734-2736
27. K.A. Khalil and A.A. Almajid, Effect of High-Frequency Induction Heat Sintering Conditions on the Microstructure and Mechanical Properties of Nanostructured Magnesium/Hydroxyapatite Nanocomposites, *Mater. Des.*, 2012, **36**, p 56-68
28. H.C. Kim, D.Y. Oh, and I.J. Shon, Sintering of Nanophase WC-15vol.%Co Hard Metals by Rapid Sintering Process, *Int. J. Refract. Met. Hard Mater.*, 2004, **22**(4–5), p 197-203
29. M.T. Dalaee, L. Gloor, C. Leinenbach, and K. Wegener, Experimental and Numerical Study of the Influence of Induction Heating Process on Build Rates Induction Heating-assisted Laser Direct Metal Deposition (IH-DMD), *Surf. Coatings Technol.*, 2019, **384**, p 125275
30. "Standard Test Method for Adhesion or Cohesion Strength of Thermal Spray Coatings", C633-13, ASTM International, 2017.
31. "Standard Test Methods for Tension Testing of Metallic Materials", E8/E8M-16a, ASTM International, 2016.
32. A. Nastic, M. Vijay, A. Tieu, S. Rahmati, and B. Jodoin, Experimental and Numerical Study of the Influence of Substrate Surface Preparation on Adhesion Mechanisms of Aluminum Cold Spray Coatings on 300 M Steel Substrates, *J. Therm. Spray Technol.*, 2017, **26**(7), p 1461-1483
33. R. Fernandez, D. MacDonald, A. Nastić, B. Jodoin, A. Tieu, and M. Vijay, Enhancement and Prediction of Adhesion Strength of Copper Cold Spray Coatings on Steel Substrates for Nuclear Fuel Repository, *J. Therm. Spray Technol.*, 2016, **25**(8), p 1577-1587
34. G.R. Johnson and W.H. Cook, A Constitutive Model and Data for Metals Subjected to Large Strains, High Strain Rates, and High Temperatures, *7th Int. Symp. Ballist.*, 1983, **21**, p 541-547
35. G.R. Johnson and W.H. Cook, Fracture Characteristics of Three Metals Subjected to Various Strains, Strain Rates, Temperatures and Pressures, *Eng. Fract. Mech.*, 1985, **21**(1), p 31-48
36. F.P. Incropera, A.S. Lavine, T.L. Bergman, and D.P. DeWitt, *Fundamentals of Heat and Mass Transfer*, 2nd ed., Wiley, New York, 2007
37. W.D. Callister, *Fundamentals of Materials Science and Engineering*, 5th ed., Wiley, New York, 2001
38. D. Steinberg, *Equation of State and Strength Properties of Selected Materials*, Lawrence Livermore National Laboratory, Livermore, 1996
39. B. Jodoin, L. Ajdelsztajn, E. Sansoucy, A. Zúñiga, P. Richer, and E.J. Lavernia, Effect of Particle Size, Morphology, and Hardness on Cold Gas Dynamic Sprayed Aluminum Alloy Coatings, *Surf. Coat. Technol.*, 2006, **201**(6), p 3422-3429
40. D. MacDonald, S. Rahmati, B. Jodoin, and W. Birtch, An Economical Approach to Cold Spray Using In-Line Nitrogen-Helium Blending, *J. Therm. Spray Technol.*, 2019, **28**(1–2), p 161-173
41. K. Balani, T. Laha, A. Agarwal, J. Karthikeyan, and N. Munroe, Effect of Carrier Gases on Microstructural and Electrochemical Behavior of Cold-Sprayed 1100 Aluminum Coating, *Surf. Coatings Technol.*, 2005, **195**(2–3), p 272-279
42. T. Stoltenhoff, C. Borchers, F. Gärtner, and H. Kreye, Microstructures and Key Properties of Cold-Sprayed and Thermally Sprayed Copper Coatings, *Surf. Coatings Technol.*, 2006, **200**(16–17), p 4947-4960
43. W.Y. Li, C.J. Li, and H. Liao, Effect of Annealing Treatment on the Microstructure and Properties of Cold-Sprayed Cu Coating, *J. Therm. Spray Technol.*, 2006, **15**(2), p 206-211
44. X.M. Meng, J.B. Zhang, W. Han, J. Zhao, and Y.L. Liang, Influence of Annealing Treatment on the Microstructure and Mechanical Performance of Cold Sprayed 304 Stainless Steel Coating, *Appl. Surf. Sci.*, 2011, **258**(2), p 700-704
45. P. Vo, E. Irissou, J.G. Legoux, and S. Yue, Mechanical and Microstructural Characterization of Cold-Sprayed Ti-6Al-4V After Heat Treatment, *J. Therm. Spray Technol.*, 2013, **22**(6), p 954-964
46. T. Hussain, D.G. McCartney, P.H. Shipway, and D. Zhang, Bonding Mechanisms in Cold Spraying: The Contributions of Metallurgical and Mechanical Components, *J. Therm. Spray Technol.*, 2009, **18**(3), p 364-379
47. T. Samson, D. MacDonald, R. Fernández, and B. Jodoin, Effect of Pulsed Waterjet Surface Preparation on the Adhesion Strength of Cold Gas Dynamic Sprayed Aluminum Coatings, *J. Therm. Spray Technol.*, 2015, **24**(6), p 984-993
48. T. Schmidt, F. Gärtner, H. Assadi, and H. Kreye, Development of a Generalized Parameter Window for Cold Spray Deposition, *Acta Mater.*, 2006, **54**(3), p 729-742
49. R. Fernandez and B. Jodoin, Cold Spray Aluminum-Alumina Cermet Coatings: Effect of Alumina Morphology, *J. Therm. Spray Technol.*, 2019, **27**(4), p 603-623
50. X. Wang, F. Feng, M.A. Klecka, M.D. Mordasky, J.K. Garofano, T. El-Wardany, A. Nardi, and V.K. Champagne, Characterization and Modeling of the Bonding Process in Cold Spray Additive Manufacturing, *Addit. Manuf.*, 2015, **8**, p 149-162
51. E.A. Olevsky and L. Froyen, Impact of Thermal Diffusion on Densification during SPS, *J. Am. Ceram. Soc.*, 2009, **92**, p 122-132

52. A.V. Kuz'Mov, E.A. Olevskii, and E.V. Aleksandrova, Effect of Micrononuniform Heating of Powder in Field-Assisted Sintering on Shrinkage Kinetics, *Powder Metall. Met. Ceram.*, 2013, **51**(11–12), p 657-665
53. H. Mehrer, *Diffusion in Solids—Fundamentals, Methods, Materials, Diffusion-Controlled Processes*, Springer, New York, 2007
54. S. Schumacher, R. Birringer, R. Strauß, and H. Gleiter, Diffusion of Silver in Nanocrystalline Copper Between 303 and 373 K, *Acta Metall.*, 1989, **37**(9), p 2485-2488
55. H. Horvarth, J. Birringer, and R. Gleiter, Diffusion in Nanocrystalline Material, *Solid State Commun.*, 1987, **62**(5), p 319-322
56. R. Birringer, Nanocrystalline Materials, *Mater. Sci. Eng. A*, 1989, **117**, p 33-43
57. C. Li, S. He, Y. Fan, H. Engelhardt, S. Jia, W. Xuan, X. Li, Y. Zhong, and Z. Ren, Enhanced Diffusivity in Ni-Al System by Alternating Magnetic Field, *Appl. Phys. Lett.*, 2017, **110**(7), p 074102
58. X. Liu, J. Cui, Y. Guo, X. Wu, and J. Zhang, Phase Formation and Growth in Al-Mg Couple with an Electromagnetic Field, *Mater. Lett.*, 2004, **58**(9), p 1520-1523
59. X. Liu, J. Cui, X. Wu, Y. Guo, and J. Zhang, Phase Growth in Diffusion Couples under an Low Frequency Alternating Magnetic Field, *Scr. Mater.*, 2005, **52**(1), p 79-82
60. H. Fujii and S. Tsurekawa, Diffusion of Carbon in Iron under Magnetic Fields, *Phys. Rev. B—Condens. Matter Mater. Phys.*, 2011, **83**(5), p 054412
61. D. Li, Q. Wang, G. Li, T. Liu, and J. He, Evolution of Coating Layers during Pack Alumetizing Process Induced by High Magnetic Fields, *Mater. Lett.*, 2009, **63**(11), p 890-892
62. C. Borchers, R. Gärtner, T. Stoltenhoff, and H. Kreye, Microstructural Bonding Features of Cold Sprayed Face Centered Cubic Metals, *J. Appl. Phys.*, 2004, **96**(8), p 4288-4292
63. C. Borchers, F. Gärtner, T. Stoltenhoff, and H. Kreye, Formation of Persistent Dislocation Loops by Ultra-High Strain-Rate Deformation during Cold Spraying, *Acta Mater.*, 2005, **53**(10), p 2991-3000
64. P.C. King, S.H. Zahiri, and M. Jahedi, Microstructural Refinement within a Cold-Sprayed Copper Particle, *Metall. Mater. Trans. A*, 2009, **40**(9), p 2115-2123
65. X.T. Luo, C.X. Li, F.L. Shang, G.J. Yang, Y.Y. Wang, and C.J. Li, High Velocity Impact Induced Microstructure Evolution during Deposition of Cold Spray Coatings: A Review, *Surf. Coatings Technol.*, 2014, **254**, p 11-20
66. R. Huang, M. Sone, W. Ma, and H. Fukanuma, The Effects of Heat Treatment on the Mechanical Properties of Cold-Sprayed Coatings, *Surf. Coatings Technol.*, 2015, **261**, p 278-288
67. T.H.V. Steenkiste, J.R. Smith, and R.E. Teets, Aluminum Coatings via Kinetic Spray with Relatively Large Powder Particles, *Surf. Coatings Technol.*, 2002, **154**(2–3), p 237-252

Publisher's Note Springer Nature remains neutral with regard to jurisdictional claims in published maps and institutional affiliations.

5.4 Influence of the Initial Substrate Temperature on the CS process at the Single-Particle Level using the Soft-on-Hard Material Combination

In this section, the influence of the initial substrate temperature on the CS process at the single-particle level is further investigated using the soft-on-hard material combination. In the first two studies, the importance of the initial substrate temperature is investigated. However, the mechanisms leading to a superior adhesion strength are still unclear as the characterization methodology used did not allow the proper identification of the adhesion mechanisms. The use of transmission electron microscopy (TEM) could potentially be used to investigate the mechanisms leading to a superior adhesion strength. However, the use of this technique is complex and time-consuming. Additionally, TEM would only allow the investigation of extremely localized regions at the interface, and any conclusions would be based on the investigation of a few locations. Therefore, a third study focused on a macroscopic monitored approach: the deposition and removal of single pure aluminum particles from the Ti64 substrates. To have independent control of the substrate temperature from the gas stagnation temperature, an induction heating system is used. To limit the number of samples to analyze (as many particles have to be evaluated for statistical significance of each case to be studied) two initial substrate temperatures are evaluated: 25 and 600 °C.

In this section, the following task is carried out to evaluate the role of the initial substrate temperature on the CS deposition process:

- Evaluate the Particle/Substrate Deformation at the Interface and the Adhesion Strength at a Single-particle Level.

The detailed evaluation of the effect of the initial substrate temperature on the CS deposition process at the single-particle level using the soft-on-hard material combination is presented in the form of a published peer-reviewed paper as follows

(Reprinted from [42] with permission of Springer; permission conveyed through Copyright Clearance Center, Inc.).

J Therm Spray Tech
https://doi.org/10.1007/s11666-020-01148-w



PEER REVIEWED

The Role of Substrate Preheating on the Adhesion Strength of Cold-Sprayed Soft Particles on Hard Substrates

R. Ortiz-Fernandez[1] · S. Imbriglio[2] · R. Chromik[2] · B. Jodoin[1]

Submitted: 3 September 2020 / in revised form: 7 December 2020 / Accepted: 17 December 2020
© ASM International 2021

Abstract Induction heating cold spray has recently been proposed as a new hybrid additive manufacturing technique and a possible solution to avoid the delamination of soft material coatings from hard substrates. This process relies on the combined contributions of substrate preheating and in situ coating heating as a result of the alternating electromagnetic field applied that generates eddy currents. However, fundamental studies at the micron-scale explaining the role of substrate preheating on the adhesion strength of the soft/hard (particle/substrate) material combination are scarce. Therefore, this study focuses on investigating the role of substrate preheating in induction heating cold spray on bond formation and adhesion strength at the individual particle level by removing sprayed single soft particles (pure aluminum) from hard substrates (Ti-6Al-4V) using the splat adhesion test. Substrate preheating improved the splat adhesion strength by 30% and the bonded area sixfold. In addition, due to an increase in the splat adhesion energy, the failure mode changed from brittle to a more ductile type of failure when the initial substrate surface temperature was increased from 25 to 600 °C. These results are attributed to a combined effect of a more effective oxide removal on the substrate surface due to enhanced localized deformation, and a local heat treatment process in the vicinity of the particle/substrate interface that induces recovery, and, possibly, static recrystallization.

✉ R. Ortiz-Fernandez

[1] Cold Spray Research Laboratory, University of Ottawa, Ottawa, ON, Canada

[2] Department of Mining and Materials Engineering, McGill University, Montreal, QC, Canada

Keywords cold spray · induction heating · soft/hard combination · substrate preheating

Introduction

Cold spray (CS) has gained popularity as a coating process over the last decade due to its high deposition rates, low oxide content deposits, and prevention of undesirable phase transformations. In CS, the micron-size feedstock powder is accelerated to high velocities, ranging from 300 to 1200 m/s, using a de Laval nozzle (Ref 1-4). Upon impact with the substrate, the kinetic energy of the particles is mainly transformed into heat, with the remaining energy converted into elastic and plastic deformation (Ref 5). To achieve metallic bonding, the native oxide layer of the particles/substrate must be broken upon impact and high interfacial pressures must be reached in order to achieve intimate interatomic contact (Ref 6). Additionally, particles may also adhere to the substrate if they mechanically anchor through interfacial deformation due to the impact.

Among the different particle/substrate material combinations, the soft/hard pair is of special interest because substrate deformation is typically limited (Ref 7-9). Consequently, for this combination, the contribution of substrate deformation on mechanical anchoring is generally negligible. Furthermore, the limited substrate deformation restricts the native oxide layer removal process resulting in reduced metallic bonding and frequent delamination of the coating (Ref 7, 10).

To mitigate this problem, the use of substrates with a high surface roughness has been suggested and shown to improve the adhesion of soft particles on hard substrates by artificially creating anchoring points before the spraying

Published online: 18 January 2021

process. Consequently, the mechanical contribution to the overall adhesion strength increases (Ref 10-12).

Substrate preheating has also been suggested to facilitate and enhance adhesion. According to different studies, an increase in adhesion strength is expected with an increase in substrate temperature (Ref 7, 13-20), unless a thick oxide layer is formed on the substrate during preheating, which ultimately hinders adhesion (Ref 13, 14). Nevertheless, micron-scale fundamental studies on the effect of substrate preheating on single-particle adhesion strength are limited and mainly focused on materials with similar strength (Ref 20, 21).

Recently, a new hybrid additive manufacturing technique has been proposed as an alternative solution for the consolidation of soft feedstock powder (pure aluminum) onto a hard substrate (Ti-6Al-4V) (Ref 7, 9). In this process, induction heating is coupled with the CS processes resulting in in situ heating of the coating during the spraying process due to the formation of eddy currents on the deposited material. By this hybrid technique, adhesion strength can be increased and tailored by varying the induction heating parameters and initial substrate temperature (Ref 7). While the observation of individually removed particles from the substrate from single-impact tests ruled out mechanical anchoring as the adhesion mechanism, the results did not provide any additional information to understand the observed enhanced adhesion strength of the coatings. Furthermore, the method used did not provide any quantifiable data regarding the bond strength of the individual particles. It was concluded that a more thorough investigation should be conducted to further understand the fundamental role of substrate preheating on the coating adhesion strength.

Consequently, the objective of this study is to investigate the role of substrate temperature on the adhesion strength of the soft/hard material combination at the first-deposited layer level. By doing so, any potential contribution due to the tamping of subsequent particles is avoided, while the role of substrate temperature can be isolated. To that end, single-particle impact tests ("wipe tests") were produced using the hybrid induction heating cold spray process with two initial substrate surface temperatures (25 and 600 °C). To further investigate the results reported in the literature (Ref 7, 9), pure aluminum and Ti-6Al-4V were used as feedstock powder and substrate materials. The resulting samples were tested by removing individual particles from the substrate using the splat adhesion test introduced by Chromik et al. (Ref 22). The failed interfaces (particle/substrate) were analyzed through scanning electron microscopy to understand the bonding mechanisms and the influence of the initial substrate surface temperature.

Experimental Procedure

Substrate and Feedstock Material

A 25.4-mm-diameter commercially available α-β Ti-6Al-4V (Ti64) (Titanium Industries, Inc., Montreal, QC, Canada) bar was used as the substrate to produce the single-particle samples. The manufacturer's data sheet indicated that the composition of the bar by weight percentage was Ti—balance, Al—5.94%, V—4%.

Gas atomized pure aluminum (ST-A5001, 99.8% Al) (Centerline (Windsor) Limited, Windsor, ON, Canada) was used as the feedstock material. This powder was characterized by its irregular morphology, as shown in Fig. 1. Despite the irregular shape of the feedstock material, laser diffraction (Microtrac model S3500, Montgomeryville, PA, USA) was used to obtain an approximate particle size distribution. The resulting 10th, 50th, and 90th size percentiles are 11.3, 25.8, and 60.3 μm, respectively. Before the spraying process, the as-received powder was sieved to reduce the particle size distribution to 25 ± 5 μm.

The substrates were polished before conducting the single-particle impact test. The mirror substrate surface finish was achieved following the polishing steps previously reported for Ti64 (Ref 7, 9). After the surface preparation, the arithmetic average roughness (Ra) was obtained using a profilometer equipped with a diamond stylus (Phase II, SRG-400, NJ, USA). The measurements were performed on two samples before performing the single-particle impact test on them. The Ra was measured ten times on each mirror polished surface at different locations of the substrate top surface. The resulting average surface Ra was 0.23 ± 0.05 μm. Before the deposition process, the substrates were cleaned and degreased in an ethanol ultrasonic bath for 3 min.

Cold Spray Deposition Parameters

A commercially available cold spray system (SST-EPX, Centerline (Windsor) Limited, Windsor, ON, Canada) was used to perform the single-particle impact tests. A polymer de Laval nozzle with a 2.0 mm throat diameter and 6.4 mm exit diameter was used. The pure aluminum feedstock powder was injected radially in the downstream section of the nozzle using a rotary powder feeder (AT-1200 Rotary, Thermach Inc., Appleton, WI, USA). The cold spray parameters used to perform the wipe tests are found in Table 1.

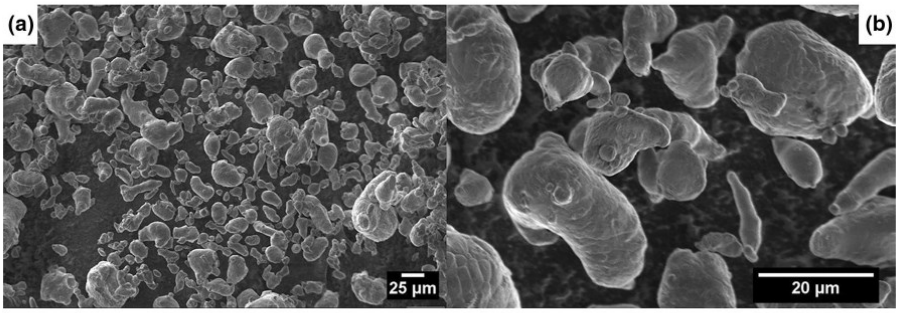


Fig. 1 Scanning electron microscope (SEM) images of the pure aluminum feedstock powder. (a) Low magnification and (b) high magnification

Table 1 Cold spray deposition parameters

General deposition parameters	Values
Propellant gas	Nitrogen
Stagnation temperature (°C)	500
Stagnation pressure (MPa)	3.45
Traverse speed (mm/s)	120
Standoff distance (mm)	15
Number of passes	1

Induction Heater Parameters for Substrate Preheating

The Ti64 bar was preheated to 600 °C prior to the start of the spraying process using an induction heater (Tucker Induction Sys. Inc., Shelby Township, MI, USA). Once the substrate surface reached the desired temperature, the induction heater was turned "Off." The copper planar round coil had an outer diameter of 110.0 mm and an inner diameter of 42.0 mm, as presented in Fig. 2(b). The coil had a total of four turns. The inner and outer diameter of the coil tubing were 5.0 and 6.3 mm, respectively. The Ti64 bar was positioned in the middle of the inductor (coil) as suggested in the literature (Ref 7) and presented in Fig. 2. The induction heating parameters used to preheat the Ti64 bar were 193 kHz and 68 A.

Substrate Surface Temperature Measurement

The substrate surface temperature was monitored locally during the preheating process and the production of the single-particle impact tests. To do so, a RAYGPRSF infrared thermometer (Raytek,Santa Cruz, CA, USA), which has a working temperature range from -18 to 538 °C, was used to monitor the temperature during the production of the single-particle impact test produced at 25 °C as the initial surface temperature. For the production of the sample at 600 °C, a non-contact infrared thermometer OptCT3MH2SF (Optris, Portsmouth, NW, USA) was used. The substrate surface temperature was measured 4 mm away from the location where single particles were sprayed, as presented in Fig. 2(b).

Single-particle Impact Test

Single-particle impact tests were produced on the Ti64 bar substrate at an initial substrate surface temperature of 25 and 600 °C. For the case at 600 °C, the induction heater was used as the preheating method. It was turned "off" as the cold spray gun passed over the substrate to minimize temperature changes on the substrate surface. To obtain individual particles, the powder feeding rate was adjusted to minimize deposition. Figure 2 presents a schematic of the setup used to produce these samples.

Sample Characterization

To observe the interfacial region and particles' cross sections, the single-particle impact tests were sectioned using a precision cutoff saw (Secotom-10, Struers, Mississauga, ON, Canada). The samples were then mechanically ground and polished (TegraPol-31, Struers, Mississauga, ON, Canada). A scanning electron microscope (SEM) (EVO MA-10, Carl Zeiss AG, Oberkochen, Germany) equipped with secondary (SE) and backscattering electron (BSE) detectors was used to investigate the as-received powder, the cross section of the single-particle impact tests, and the particle/substrate interface after the splat adhesion test.

Splat Adhesion Test

To perform the splat adhesion test, a Micro-Combi Scratch Tester (Anton Paar, Graz, Austria) equipped with a light optical microscope (LOM) was used. A stylus with a

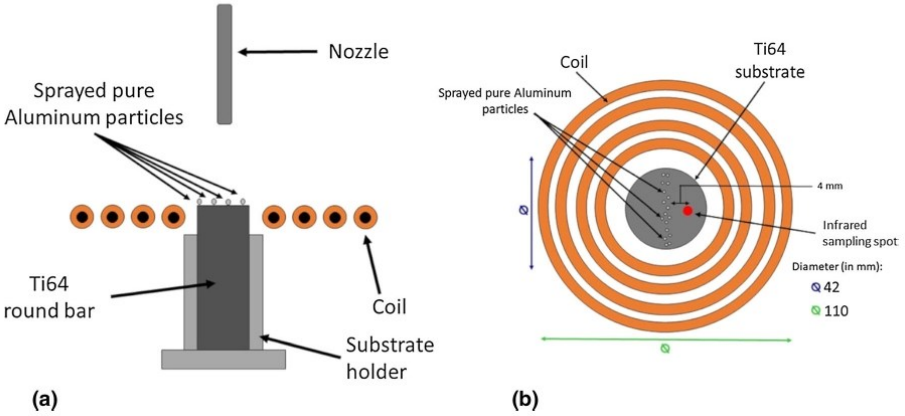


Fig. 2 Schematic of the setup used for the production of the single-particle impact tests. (a) Cross section and (b) top view

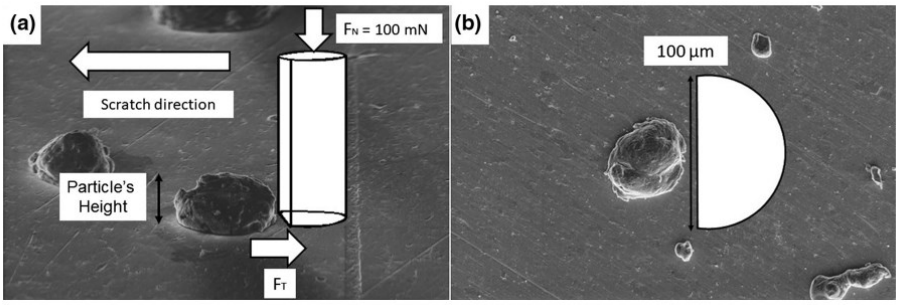


Fig. 3 Schematic of the splat adhesion testing. (a) Side view and (b) top view of the testing procedure. In (a), F_t represents the tangential force exerted on the stylus by the particle, while F_n indicates the normal force applied on the tip of the stylus

semicircular cross section and a diameter of 100 µm was used to shear individual particles, as shown in Fig. 3.

A normal force (F_n) of 100 mN was applied on the stylus to ensure that contact was maintained with the substrate. The scratch length used during the testing procedure was 150 µm, and the substrate holder moved at a constant speed of 150 µm/min. The output of the splat adhesion test is the tangential force (F_t) exerted on the stylus as a function of the scratch length. A minimum of 25 particle splats were tested for each initial substrate surface temperature (25 and 600 °C). During the testing procedure, a baseline F_t due to friction along the scratch length with the substrate and a peak F_t due to the removal process are recorded. From the recorded F_t during the testing procedure, the splat adhesion strength was quantified using Eq. 1 (Ref 22). The projected splat area and the remaining bonded area after the testing procedure were measured using an image processing software (ImageJ) and the LOM images, as previously performed in the literature (Ref 20, 22-24).

$$\text{Splat Adhesion Strength (MPa)} = \frac{F_{t\,\text{peak}}\,(\text{mN}) - F_{t\,\text{baseline}}\,(\text{mN})}{\text{Projected splat area}\,(\mu\text{m}^2)} * 1000 \quad \text{(Eq 1)}$$

The tangential force as a function of the scratch length and the projected splat area were also used to calculate the splat adhesion energy using Eq 2 (Ref 22-24).

$$\text{Splat Adhesion Energy}\left(\frac{\text{kJ}}{\text{m}^2}\right) = \frac{\int_{\text{Contact}}^{\text{Failure}}\left[F_t(x) - F_{t(\text{baseline})}\right]\text{d}x[\text{mN}\cdot\mu\text{m}]}{\text{Projected splat area}\,(\mu\text{m}^2)} \quad \text{(Eq 2)}$$

The splat adhesion energy was used to distinguish between a brittle and a more ductile type of failure (Ref 22, 23). For both initial substrate surface temperatures, the splat adhesion energy was calculated up to the initial peak

drop of the tangential force plot, as this location represented the subsequent splat failure (Ref 23).

The splat adhesion testing procedure was limited to particles having an approximate powder diameter prior to deposition of 25 ± 5 μm, as previously investigated for an identical feedstock powder and substrate material combination (Ref 9). This range was selected as it is a representative value of the powder size. In the past, the equivalent powder diameter has been used to calculate the particle size of the tested particles prior to their impact. Finally, only particles displaying a spherical-like morphology upon impact were tested, as presented in Fig. 3(b), and as previously investigated (Ref 9).

As a micromechanical testing procedure, the splat adhesion test provides quantifiable data regarding the adhesion or bond strength of cold-sprayed particles to substrates. The measured splat adhesion strength values range from zero up to the theoretical shear strength of the splat material. High splat adhesion strength values, near the theoretical shear strength, indicate high adhesion or significant metallic bonding between the particle and the substrate. In this scenario, a sheared particle after the testing procedure is expected rather than failure at the particle/substrate interface. On the other hand, low adhesion strength values suggest that limited adhesion or metallic bonding has been reached at the particle/substrate interface. Thus, failure across the interface is anticipated. To take advantage of this testing procedure, post-characterization of the tested particles is required to properly interpret the results and understand the failure mechanisms as a function of the initial substrate surface temperature. Due to the different scales between an individual splat and a coating, the splat adhesion strength values may not be completely representative with respect to a full coating. However, this testing procedure becomes a powerful tool to assess and compare the adhesion or bond strength of the particles as a function of different spray parameters.

Results and Discussion

Single-Particle Deposition

Figure 4 presents cross-sectional SEM images of pure aluminum single-particle deposition on Ti64 substrates at the two different initial surface temperatures (25 and 600 °C). Substrate deformation is similar independently of its initial temperature. In both cases, the substrate remains flat, and no visible indentation is observable, as previously reported (Ref 7, 9). Additionally, this confirms that for these two materials, the mechanical contribution to the overall splat adhesion strength is negligible. While the substrate deformation behavior observed in Fig. 4(a) was expected due to a large dissimilarity between powder and substrate strength (Ref 8), the substrate deformation observed in Fig. 4(b) was not expected. Ti64 yield strength is sensitive to both temperature and strain rate (Ref 25). However, at relatively high temperatures, the thermal softening becomes dominant over the strain rate effect (Ref 25). Thus, it is possible that for the case at 25 °C, despite the local increase in temperature at the substrate surface (due to the particle impact), the latter still suffered a local increase in yield strength as a result of the high strain rate deformation caused by the particle impact (Ref 25-28). Ultimately, this restricted deformation and close contact at the vicinity of the two metal surfaces. Conversely, at 600 °C, the relatively high substrate surface temperature in combination with a local increase in temperature due to the particle impact possibly reduced the effect of strain rate hardening, allowing more localized plastic deformation at the substrate surface. However, despite the increase in temperature (due to preheating and the impact process), the flow stress was not likely reduced enough to produce an indentation on the substrate upon the particle impact. Finally, the lack of substrate deformation might also be caused by the soft nature of the particles, which are not hard enough to impose sufficient contact pressure on the substrate to deform it (Ref 8).

The particles in Fig. 4 presented a similar deformation regardless of the initial substrate surface temperature. In both cases, the particle deformation was restrained to the region in contact with the substrate, where a flattened bottom can be observed as a result of the deformation experienced during the impact, as predicted by Bae et al. (Ref 8). Interestingly, two different contact behaviors are visible on the flattened bottom of the particles. The particle deposited at 25 °C (as the initial substrate surface temperature) exhibits a non-uniform contact with the substrate with visible gaps (as shown by the arrows in Fig. 4a), while at 600 °C, no gaps are visible at the interface. As such, different adhesion strength behaviors are expected due to this difference at the interface.

Splat Adhesion Testing Post-Characterization

To gain knowledge about the different adhesion behaviors during the splat adhesion tests, the top view image of a particle before the testing procedure, the resulting F_t exerted on the stylus as a function of the scratch length, and the top view image of the particle remnants after the testing procedure were investigated. Based on their failure mechanism and morphology after the testing process, the particles were categorized, and four different failure cases were identified. The first three pertain to the tested particles deposited at 25 °C as the initial substrate surface temperature, while at 600 °C, only the fourth type was observed.

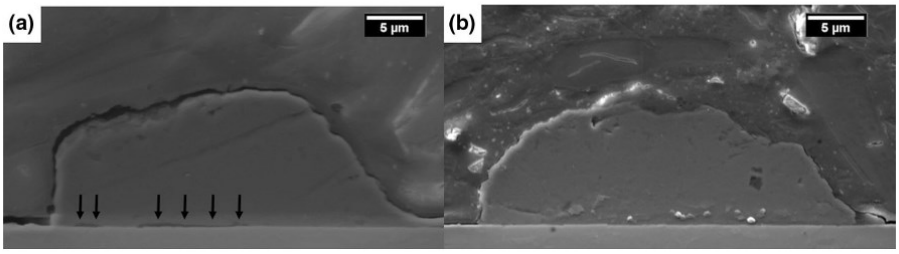


Fig. 4 Scanning electron microscope (SEM) images of individual pure aluminum particles deposited on Ti64 substrate at initial surface temperature of (a) 25 °C and (b) 600 °C. The black arrows in (a) indicate the visible gaps and uneven contact at the particle/substrate interface

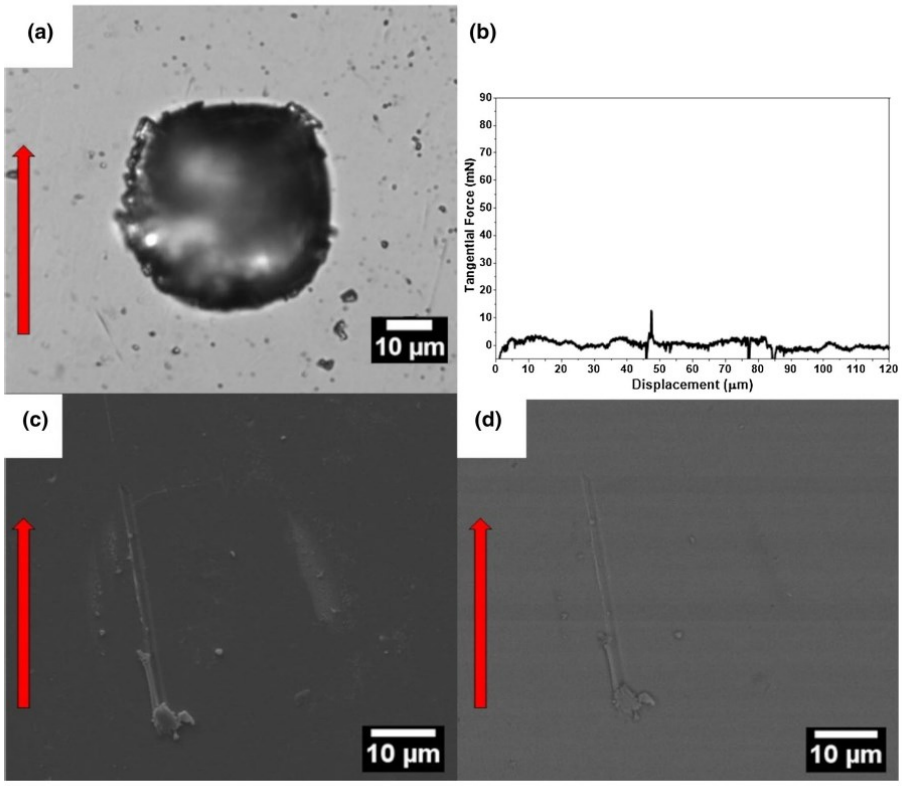


Fig. 5 Failure Case 1. (a) LOM image of the particle before the testing process, (b) tangential force (F_t) as a function of the displacement of the particle, (c) and (d) SE and BSE images of the tested area. The light gray contrast in (d) represents the Ti64 substrate. Red arrows indicate the scratch direction (Color figure online)

Figure 5 presents the first type of failure, labeled as Case 1. Particles exhibiting Case 1 behavior are characterized by the lack of distinguishable peak in the tangential force (F_t). This case was displayed by 20% of the tested particles at 25 °C as the initial substrate surface temperature. A top view image of an as-deposited particle that exhibited Case 1 behavior during the test is presented in Fig. 5(a). In this image, jetting-like features that are visible at the periphery of the particle, which according to authors in the literature, are indicators of "successful bonding" (Ref 5, 29, 30). However, from the tangential force (Fig. 5b), no distinguishable peak is present across the

distance traveled by the stylus. The splat adhesion strength and energy for particles exhibiting Case 1 failure were approximately 3 ± 5 MPa and $0.01 \pm 0.010 \times 10^{-9}$ kJ/m^2, respectively. The relatively low splat adhesion strength value suggests "poor" bonding (Ref 20, 24). This behavior is observed in Fig. 5(c) and (d), where minor evidence of bonding on the substrate is present after the testing procedure. As a reference, splat adhesion energy is two orders of magnitude below the common values reported for well-adhered cold-sprayed splats (Ref 22-24). Therefore, for this soft/hard material combination, the existence of particle jetting features at the level observed is not necessarily a sign of "successful bonding," contrary to what has been suggested by the literature (Ref 5, 29, 30).

Figure 6 presents a particle that failed according to the second kind of failure, labeled Case 2. This case is characterized by a distinguishable peak followed by a sudden drop in the tangential force when the splat is removed. This type of failure was observed in 35% of the total number of tested particles deposited on the substrate with an initial surface temperature of 25 °C. An as-deposited particle that exhibited the second type of failure during the removal process is presented in Fig. 6(a). From the top view image, the tested particle shows similar jetting features at its periphery as the particle presented in Case 1. Thus, top view examination of as-deposited particles does not allow predicting/distinguishing Case 2 from Case 1 behavior. In this case, the distinct peak in the tangential force is located at approximately 45 µm from the start of the testing procedure, as presented in Fig. 6(b). This peak is caused by the splat adhesion strength which opposes resistance to the displacement of the stylus. Once crack propagation takes place at the splat/substrate interface upon reaching maximum tangential force, the force quickly drops due to the lack of well-bonded areas. This is followed by the splat delamination from the substrate. The previous sequence of events (also presented in Fig. 6b) was inferred based on the size of the tested particle, the tangential force curve, and

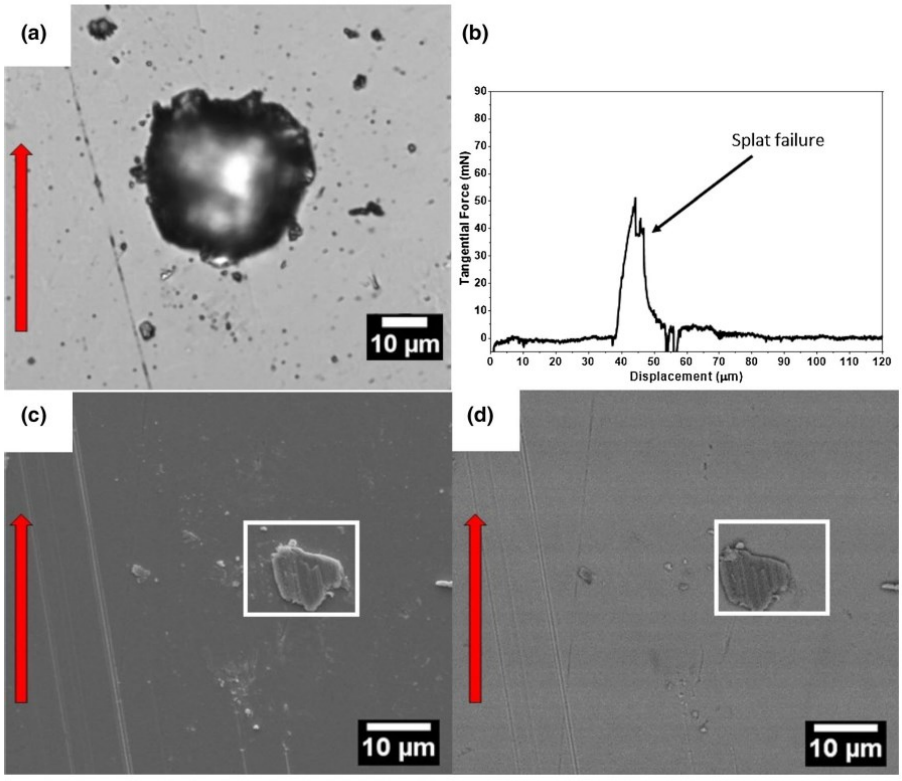


Fig. 6 Failure Case 2. (a) LOM image of the particle before the testing process, (b) tangential force (F_t) as a function of the displacement of the particle, (c) and (d) SE and BSE images of the tested area. The light and dark gray contrast in (d) represent the Ti64 substrate and the remnant of the pure aluminum particle, respectively. Red arrows indicate the scratch direction (Color figure online)

previous results in the literature (Ref 20, 23). The splat adhesion strength and energy for particles exhibiting Case 2 failure were 29 ± 10 MPa and 0.16 ± 0.08 × 10^{-9} kJ/m^2. Figure 6(c) and (d) presents the tested zone after the removal process. From these images, only a small remnant of the pure aluminum particle is observed which suggests that only in this region, the conditions for bonding were fulfilled. The presence of this particle remnant after the testing procedure suggests that as the bonded area increases, the splat adhesion strength is also increased. It is also interesting to note that jetting zones do not match the well-bonded zones, as also observed for Case 1.

A particle that failed following the third failure type, labeled Case 3, is presented in Fig. 7. This type of failure is characterized by a peak followed by a slow decrease in the tangential force. Case 3 was present in 45% of the tested particles deposited at 25 °C as the initial substrate surface temperature. As in previous cases, the particle exhibits jetting at the periphery (Fig. 7a), but its behavior upon testing was different compared to previous cases. Figure 7(b) shows that once the maximum tangential force is reached, a gradual decrease is present (from 52 to 57 µm approximately) followed by an abrupt decrease (from 58 to 60 µm approximately). This behavior indicates a brittle shearing failure of the particle (Ref 20, 23). The first gradual decrease in the tangential force is caused by the constant contact of the tip of the stylus with the sheared particle. Once a part of the tip of the stylus (100 µm diameter) leaves the sheared particle, the force quickly decreases as one part of the tip is no longer in "complete" contact with particle. Eventually, the totality of the tip of the stylus leaves the sheared particle, and the tangential force comes back to the baseline value. This failure process and the information provided in Fig. 7(b) were inferred based on the size of the tested particle, the tangential force curve, and previous results in the literature (Ref 20, 23). The SE and BSE images (Fig. 7c, d, respectively), confirmed the failure mechanism previously suggested as the

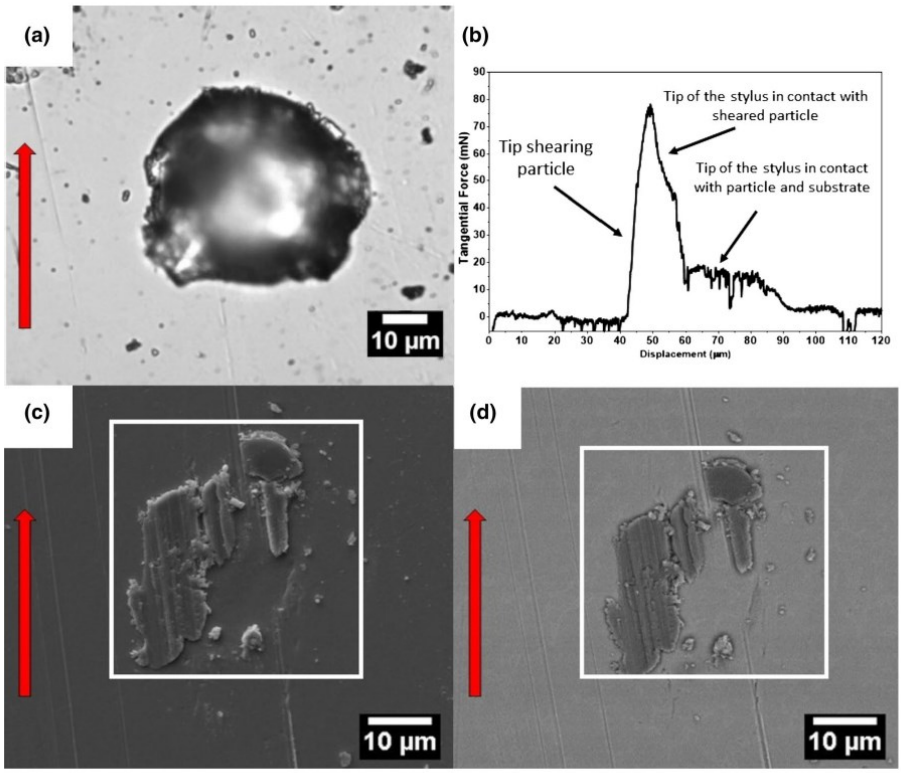


Fig. 7 Failure Case 3. (a) LOM image of the particle before the testing process, (b) tangential force (F_t) as a function of the displacement of the particle, (c) and (d) SE and BSE images of the tested area. The light and dark gray contrast in (d) represent the Ti64 substrate and the remnant of the pure aluminum particle, respectively. Red arrows indicate the scratch direction (Color figure online)

remaining particle was not delaminated during the testing procedure. Instead, a sheared particle can be seen. Among the three cases observed at an initial substrate temperature of 25 °C, Case 3 exhibited the highest splat adhesion strength and energy value (61 ± 7 MPa and $0.28 \pm 0.15 \times 10^{-9}$ kJ/m^2), which is related to its larger bonded area and the previously suggested failure mechanism. It is also interesting to note that even though the particle was sheared off during the testing, the entire bottom of the particle did not reach intimate contact with the substrate, as there are regions where the substrate can be seen, and particle remnants are not present. This behavior is likely caused by an uneven oxide removal process occurring during the impact. Thus, localized bonding is likely to have occurred only at the zones where successful breakage of the native oxide layer took place. As such, particles exhibiting Case 3 experienced a more successful oxide removal process compared to Cases 2 and 1. These differences in the bonding area and the successful breakage of the native oxide layer will be discussed in section "Overall Effect of Substrate Preheating on Splat Adhesion Strength".

The fourth type of failure was exclusively exhibited by the particles deposited on a substrate at an initial surface temperature of 600 °C. A top view image of a Case 4 particle is presented in Fig. 8(a). The particle does not present significant signs of jetting, which according to the literature would indicate "poor" bonding (Ref 5, 29, 30). However, the tangential force (F_t) in Fig. 8(b) displayed a continuous ascending curve, which according to previous studies indicates ductile shearing failure of the particle, followed by a descending trend once the tip of the stylus has cut through the particle (Ref 20, 23). The previous failure mechanism and the information provided in Fig. 8(b) were inferred based on the size of the tested particle, the tangential force curve, and previous results in the literature (Ref 20, 23). The suggested behavior is confirmed by the SE and BSE images in Fig. 8(c) and (d), where a sheared particle can be seen as a result of the testing process. Interestingly, from the BSE image (Fig. 8d), a continuous trace of pure aluminum (or particle "footprint") over the substrate can be seen. Because it has been shown that particle penetration at the substrate interface is limited (Fig. 4b), the particle "footprint" left as the stylus cut through the particle is attributed to enhanced adhesion at the particle/substrate interface. This result further confirms that jetting does not always correlate with "successful" bonding, as it has also been suggested by other authors in the literature (Ref 6, 31, 32).

The area under the tangential force (F_t) curve, as the ones presented in Fig. 5–8(b), represents the energy required to remove a particle, and this has been used to classify the type of failure exhibited by the particles upon removal (Ref 22, 23). As such, small areas suggest a brittle type of failure, while larger areas indicate a more ductile behavior. In Fig. 8(b), it can be seen that the fourth case exhibited a larger area under the F_t curve (region from 55 to 85 μm approximately) compared to other cases. The splat adhesion energy for particles exhibiting Case 4 was $0.74 \pm 0.32 \times 10^{-9}$ kJ/m^2. The higher splat adhesion energy, compared to the other cases, suggests that Case 4 is characterized by a more ductile type of failure in comparison with Cases 1 to 3. This transition from a brittle to a ductile type of failure could be explained as a result of the larger bonded area (as will be shown in the next section), and a potential localized heat treatment process occurring at the vicinity of the particle/substrate interface which increases the splat adhesion strength (51 ± 15 MPa). As a result, the failure mechanism is not necessarily through crack propagation at interfacial porosities between the particle and the substrate (as in Case 3), but rather cohesion failure across the particle. Additionally, high dislocation densities near the particle/substrate region due to the impact process have been reported (Ref 33-39). Therefore, at the particle/substrate interface vicinity, ideal conditions are likely met to produce the first stage of the heat treatment process (recovery) and, possibly, static recrystallization (SRX) because heat is transferred to the particles from the surface at an initial substrate temperature of 600 °C. As a consequence, ductility is likely promoted at the vicinity of the interface, and the particle's brittle behavior is minimized. It is worth noting that recrystallization has been observed before for titanium splats deposited on preheated titanium substrates (Ref 21).

Overall Effect of Substrate Preheating on Splat Adhesion Strength

Different types of failure behaviors have been presented in the previous section. The overall effects of substrate preheating on the splat adhesion strength are now presented. The splat adhesion strength of the particles deposited at different initial substrate surface temperatures (25 and 600 °C) is presented in Fig. 9. It is important to note that the maximum testing strength was, in theory, limited to the bulk shear strength of the pure aluminum particles, which in some cases caused the particles to shear off of the substrate, as it has been shown in the previous section. Therefore, the splat adhesion strength value for the sample deposited at 600 °C might not necessarily be the maximum adhesion strength of the splats, because the particles were first sheared instead of being completely removed from the substrate surface. Thus, the adhesion strength of the 600 °C sample is possibly larger than the reported value.

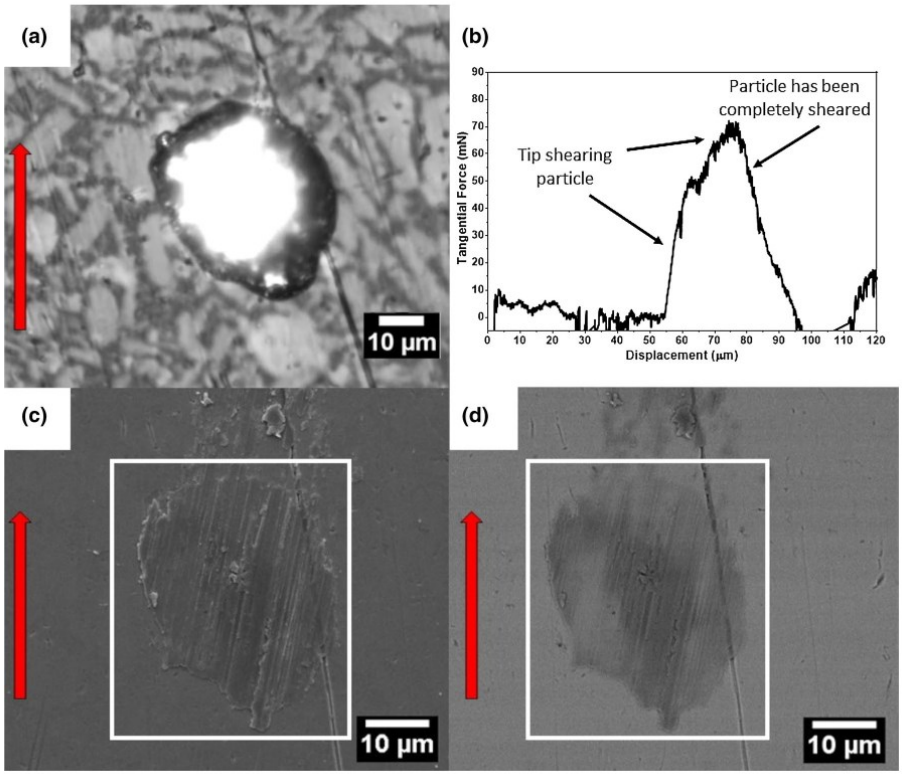


Fig. 8 Failure Case 4. (a) LOM image of the particle before the testing process, (b) tangential force (F_t) as a function of the displacement of the particle, (c) and (d) SE and BSE images of the tested area. The light and dark gray contrast in (d) represent the Ti64 substrate and the remnant of the pure aluminum particle, respectively. Red arrows indicate the scratch direction (Color figure online)

The mean splat adhesion strength for the substrate temperature at 25 °C was 38 MPa, as presented in Fig. 9. Additionally, a widespread of splat adhesion strength values is visible. This wide distribution is likely attributed to the significant difference in bonded areas between the particle and the substrate, as observed in Cases 1 to 3. It could also be explained by the different particle impact velocity and temperature due to different flight history, different native oxide layer thicknesses (particle and substrate), and/or the different particle microstructure, all of which have been shown to impede the bonding process (Ref 6, 33, 41-54).

The oxidation rate of Ti64 at 600 °C (Ref 55) predicts that in one minute (time required to preheat the bar and produce the single-particle impact tests), the native oxide layer thickness can increase by up to 59 nm (Ref 55). Nevertheless, higher splat adhesion strength values were obtained when 600 °C was used as the initial substrate surface temperature, as the mean was raised to 51 MPa (Fig. 9). Additionally, for this substrate temperature, a tighter and skewed (to higher values) distribution was obtained. This suggests that for this particular pair (Al on Ti64), the potentially thicker oxide layer and the previously listed variables did not likely restrict the bonding process to a similar extent as suggested for its counterpart at 25 °C. This behavior is potentially caused by the higher substrate surface temperature which has been shown to facilitate the native oxide layer removal process, and thus the bonding process (Ref 7, 13-20). Lastly, even though most of the particles at 600 °C were sheared during the testing procedure, the splat adhesion strength, in most cases, was below the bulk shear strength value for pure aluminum. This implies that the particles deposited at 600 °C do not necessarily exhibit the bulk properties of the pure aluminum, as also observed for other materials (Ref 56). This could potentially be caused by the non-uniform microstructure developed in the particle after the impact and subsequent heat treatment process due to higher substrate surface temperature.

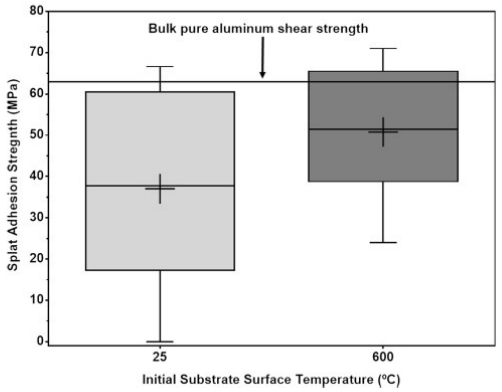


Fig. 9 Splat adhesion strength of the pure aluminum particles deposited on Ti64 substrate at different initial surface substrate temperatures (box and whisker plot with + representing the mean, the whiskers representing the 10-90%, and the box representing 25-50-75% of all tested particles). The black solid line indicates the bulk pure aluminum shear strength (Ref 40)

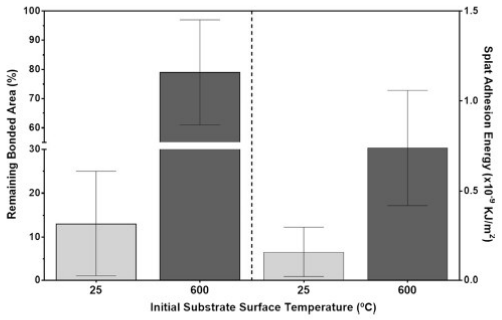


Fig. 10 Remaining bonded area (%) and splat adhesion energy on the left and right Y-axes, respectively. The bars in light and dark gray represent particles deposited at 25 and 600 °C as the initial surface substrate temperature, respectively

To further understand the role of higher substrate temperatures on the splat adhesion strength, the remaining bonded area (after the testing procedure) is presented in Fig. 10. The remaining bonded area at 25 and 600 °C was 13 and 80%, respectively. This drastic difference is likely caused by more regions of the substrate surface meeting the required conditions to experience sufficient deformation upon the particle impact, as higher temperatures have shown to reduce the maximum shear stress required to onset adiabatic shear instability (ASI) for Ti alloys (Ref 25, 28, 57). Ultimately, as the overall bonded area at the particle/substrate interface increased, the splat adhesion strength values were raised to higher values (as observed in Fig. 9) (Ref 58, 59) along with a change of failure mode.

Moreover, the particles deposited at 600 °C (as the initial substrate surface temperature) possibly experienced ideal conditions, namely high dislocation densities at the vicinity of the particle/substrate interface (Ref 36, 60-62), to start recovery and, possibly, static recrystallization (SRX) at the particle/substrate interface. This is due to heat conduction from the substrate to the particle after the deposition occurred, as observed before for the Ti/Ti pair (Ref 21). Thus, the strength of the bond is further enhanced, and ductility is developed at the vicinity of the interface. This can be observed in Fig. 10 where the splat adhesion energy required to produce failure was tripled at 600 °C. It is important to note that the initial surface temperature of the substrate is above the widely accepted convention ($0.4T_m = T_R$) to start recovery and recrystallization, as well as above the suggested recrystallization temperatures for pure aluminum for similar atomic compositions (Ref 63-65).

Conclusions

The role of substrate preheating on the adhesion strength of pure aluminum particles deposited on Ti64 substrates was investigated by the splat adhesion strength test. Four cases were observed during the testing procedure, with three cases (Cases 1, 2, and 3) solely identified for particles deposited at 25 °C as the initial substrate surface temperature and the other case (Case 4) identified solely for particles deposited at 600 °C. Case 1 exhibited poor adhesion, and no distinguishable peak in the tangential force curve was observed. Moreover, minor evidence of bonding at the particle/substrate interface was found after the testing procedure. Case 2 was characterized by a distinguishable peak in the tangential force curve in which only a few local regions of the particle reached intimate contact with the substrate. Case 3 was also characterized by a distinguishable peak in the tangential force curve, but in this case, the particles presented large bonded areas. These three cases showed a brittle behavior upon removal. For Case 4, most of the particles were sheared during the testing procedure, and they exhibited a more ductile behavior upon removal compared to Cases 1 to 3. The splat adhesion strength of the particles deposited at 600 °C increased by 35% in comparison with their counterpart at 25 °C. Additionally, the remaining bonded area and the splat adhesion energy were increased six- and threefold, respectively, when substrate preheating was used. This increase could be explained by the combined contribution of a softer substrate, more regions at the substrate surface possibly meeting the local conditions to experience enhanced deformation and/or ASI, and higher diffusion rates at the particle/substrate interface. All of this helped provide enough deformation to break the oxide layer, to increase and enlarge the bonding sites, and to strengthen the bonds. Moreover, the

possible development of a local heat treatment (recovery and, possibly, start of static recrystallization) at the particle/substrate interface is also believed to have helped increase the splat adhesion strength. Finally, the particles deposited at 600 °C exhibited a tighter range of splat adhesion strength values in comparison with the ones deposited at 25 °C, which suggests that substrate preheating can minimize the negative factors hindering the bonding process (and ultimately the splat adhesion strength) such as variability in particle impact velocity and temperature, particle native oxide layer, and particle microstructure.

Acknowledgments The authors would like to thank Dr. Michel Nganbe for facilitating the use of his induction heater for the production of this work.

References

1. A.N. Papyrin, Ed., *Cold Spray Technology*, Elsevier, Amsterdam, 2007
2. A. Moridi, S.M. Hassani-Gangaraj, M. Guagliano, and M. Dao, Cold Spray Coating: Review of Material Systems and Future Perspectives, *Surf. Eng.*, 2014, **30**(6), p 369-395
3. J. Villafuerte, Ed., *Modern Cold Spray: Materials, Process, and Applications*, Springer, Cham, 2015
4. J.R. Davis & Associates and ASM International, Eds., *Handbook of Thermal Spray Technology*, ASM International, Materials Park, OH, 2004
5. H. Assadi, F. Gärtner, T. Stoltenhoff, and H. Kreye, Bonding Mechanism in Cold Gas Spraying, *Acta Mater.*, 2003, **51**(15), p 4379-4394
6. S. Rahmati and B. Jodoin, Physically Based Finite Element Modeling Method to Predict Metallic Bonding in Cold Spray, *J. Therm. Spray Tech.*, 2020, **29**(4), p 611-629
7. R. Ortiz-Fernandez and B. Jodoin, Hybrid Additive Manufacturing Technology: Induction Heating Cold Spray—Part II: Coating Mechanical Properties, *J. Therm. Spray Tech.*, 2020, **29**(4), p 700-713
8. G. Bae, Y. Xiong, S. Kumar, K. Kang, and C. Lee, General Aspects of Interface Bonding in Kinetic Sprayed Coatings, *Acta Mater.*, 2008, **56**(17), p 4858-4868
9. R. Ortiz-Fernandez and B. Jodoin, Hybrid Additive Manufacturing Technology: Induction Heating Cold Spray—Part I: Fundamentals of Deposition Process, *J. Therm. Spray Tech.*, 2020, **29**(4), p 684-699
10. R. Fernández, D. MacDonald, A. Nastić, B. Jodoin, A. Tieu, and M. Vijay, Enhancement and Prediction of Adhesion Strength of Copper Cold Spray Coatings on Steel Substrates for Nuclear Fuel Repository, *J. Therm. Spray Tech.*, 2016, **25**(8), p 1577-1587
11. A. Nastic, M. Vijay, A. Tieu, S. Rahmati, and B. Jodoin, Experimental and Numerical Study of the Influence of Substrate Surface Preparation on Adhesion Mechanisms of Aluminum Cold Spray Coatings on 300 M Steel Substrates, *J. Therm. Spray Tech.*, 2017, **26**(7), p 1461-1483
12. T. Samson, D. MacDonald, R. Fernández, and B. Jodoin, Effect of Pulsed Waterjet Surface Preparation on the Adhesion Strength of Cold Gas Dynamic Sprayed Aluminum Coatings, *J. Therm. Spray Tech.*, 2015, **24**(6), p 984-993
13. X.K. Suo, M. Yu, W.Y. Li, M.P. Planche, and H.L. Liao, Effect of Substrate Preheating on Bonding Strength of Cold-Sprayed Mg Coatings, *J. Therm. Spray Tech.*, 2012, **21**(5), p 1091-1098
14. Y. Watanabe, C. Yoshida, K. Atsumi, M. Yamada, and M. Fukumoto, Influence of Substrate Temperature on Adhesion Strength of Cold-Sprayed Coatings, *J. Therm. Spray Tech.*, 2014, https://doi.org/10.1007/s11666-014-0165-3
15. Y. Xie, M.-P. Planche, R. Raoelison, H. Liao, X. Suo, and P. Hervé, Effect of Substrate Preheating on Adhesive Strength of SS 316L Cold Spray Coatings, *J. Therm. Spray Tech.*, 2016, **25**(1–2), p 123-130
16. D.K. Christoulis, S. Guetta, E. Irissou, V. Guipont, M.H. Berger, M. Jeandin, J.-G. Legoux, C. Moreau, S. Costil, M. Boustie, Y. Ichikawa, and K. Ogawa, Cold-Spraying Coupled to Nano-Pulsed Nd-YaG Laser Surface Pre-Treatment, *J. Therm Spray Tech.*, 2010, **19**(5), p 1062-1073
17. R. Drehmann, T. Grund, T. Lampke, B. Wielage, K. Manygoats, T. Schucknecht, and D. Rafaja, Splat Formation and Adhesion Mechanisms of Cold Gas-Sprayed Al Coatings on Al2O3 Substrates, *J. Therm Spray Tech.*, 2014, **23**(1–2), p 68-75
18. R. Drehmann, T. Grund, T. Lampke, B. Wielage, C. Wüstefeld, M. Motylenko, and D. Rafaja, Essential Factors Influencing the Bonding Strength of Cold-Sprayed Aluminum Coatings on Ceramic Substrates, *J. Therm Spray Tech.*, 2018, **27**(3), p 446-455
19. W. Sun, A.W.Y. Tan, A. Bhowmik, I. Marinescu, X. Song, W. Zhai, F. Li, and E. Liu, Deposition Characteristics of Cold Sprayed Inconel 718 Particles on Inconel 718 Substrates with Different Surface Conditions, *Mater. Sci. Eng. A*, 2018, **720**, p 75-84
20. D. Goldbaum, J.M. Shockley, R.R. Chromik, A. Rezaeian, S. Yue, J.-G. Legoux, and E. Irissou, The Effect of Deposition Conditions on Adhesion Strength of Ti and Ti6Al4V Cold Spray Splats, *J. Therm Spray Tech.*, 2012, **21**(2), p 288-303
21. D. Goldbaum, R.R. Chromik, N. Brodusch, and R. Gauvin, Microstructure and Mechanical Properties of Ti Cold-Spray Splats Determined by Electron Channeling Contrast Imaging and Nanoindentation Mapping, *Microsc. Microanal.*, 2015, **21**(3), p 570-581
22. R.R. Chromik, D. Goldbaum, J.M. Shockley, S. Yue, E. Irissou, J.-G. Legoux, and N.X. Randall, Modified Ball Bond Shear Test for Determination of Adhesion Strength of Cold Spray Splats, *Surf. Coat. Technol.*, 2010, **205**(5), p 1409-1414
23. S.I. Imbriglio, V.N.V. Munagala, T. Schmitt, R. Gauvin, J.E. Klemberg-Sapieha, and R.R. Chromik, Failure Dynamics of Spherical and Irregular Shaped Ti Splats Deposited on Sapphire by Cold Spray, *Surf. Topogr. Metrol. Prop.*, 2019, **7**(4), p 045002
24. X. Chu, R. Chakrabarty, H. Che, L. Shang, P. Vo, J. Song, and S. Yue, Investigation of the Feedstock Deposition Behavior in a Cold Sprayed 316L/Fe Composite Coating, *Surf. Coat. Technol.*, 2018, **337**, p 53-62
25. W.-S. Lee and C.-F. Lin, Plastic Deformation and Fracture Behaviour of Ti–6Al–4V Alloy Loaded with High Strain Rate under Various Temperatures, *Mater. Sci. Eng. A*, 1998, **241**(1–2), p 48-59
26. T. Mukai, K. Ishikawa, and K. Higashi, Influence of Strain Rate on the Mechanical Properties in Fine-Grained Aluminum Alloys, *Mater. Sci. Eng. A*, 1995, **204**(1–2), p 12-18
27. D.T. Casem, J.P. Ligda, B.E. Schuster, and S. Mims, High-Rate Mechanical Response of Aluminum Using Miniature Kolsky Bar Techniques, *Dynamic Behavior of Materials*, Vol 1, J. Kimberley, L. Lamberson, and S. Mates, Ed., Springer, Cham, 2018, p 147-153 https://doi.org/10.1007/978-3-319-62956-8_25
28. W.S. Lee and C.F. Lin, Adiabatic Shear Fracture of Titanium Alloy Subjected to High Strain Rate and High Temperature Loadings, *J. Phys. IV France*, 1997, **07**(C3), p C3-855-C3-860
29. M. Grujicic, C.L. Zhao, W.S. DeRosset, and D. Helfritch, Adiabatic Shear Instability Based Mechanism for Particles/Substrate

Bonding in the Cold-Gas Dynamic-Spray Process, *Mater. Des.*, 2004, **25**(8), p 681-688
30. T. Schmidt, F. Gärtner, H. Assadi, and H. Kreye, Development of a Generalized Parameter Window for Cold Spray Deposition, *Acta Mater.*, 2006, **54**(3), p 729-742
31. M. Hassani-Gangaraj, D. Veysset, V.K. Champagne, K.A. Nelson, and C.A. Schuh, Adiabatic Shear Instability Is Not Necessary for Adhesion in Cold Spray, *Acta Mater.*, 2018, **158**, p 430-439
32. R. Nikbakht, S.H. Seyedein, S. Kheirandish, H. Assadi, and B. Jodoin, Asymmetrical Bonding in Cold Spraying of Dissimilar Materials, *Appl. Surf. Sci.*, 2018, **444**, p 621-632
33. M. Hassani-Gangaraj, D. Veysset, K.A. Nelson, and C.A. Schuh, Impact-Bonding with Aluminum, Silver, and Gold Microparticles: Toward Understanding the Role of Native Oxide Layer, *Appl. Surf. Sci.*, 2019, **476**, p 528-532
34. C.K.S. Moy, J. Cairney, G. Ranzi, M. Jahedi, and S.P. Ringer, Investigating the Microstructure and Composition of Cold Gas-Dynamic Spray (CGDS) Ti Powder Deposited on Al 6063 Substrate, *Surf. Coat. Technol.*, 2010, **204**(23), p 3739-3749
35. K. Kim, M. Watanabe, J. Kawakita, and S. Kuroda, Grain Refinement in a Single Titanium Powder Particle Impacted at High Velocity, *Scr. Mater.*, 2008, **59**(7), p 768-771
36. C. Borchers, F. Gärtner, T. Stoltenhoff, and H. Kreye, Microstructural Bonding Features of Cold Sprayed Face Centered Cubic Metals, *J. Appl. Phys.*, 2004, **96**(8), p 4288-4292
37. M.R. Rokni, C.A. Widener, V.K. Champagne, and G.A. Crawford, Microstructure and Mechanical Properties of Cold Sprayed 7075 Deposition during Non-Isothermal Annealing, *Surf. Coat. Technol.*, 2015, **276**, p 305-315
38. D. Goldbaum, R.R. Chromik, S. Yue, E. Irissou, and J.-G. Legoux, Mechanical Property Mapping of Cold Sprayed Ti Splats and Coatings, *J. Therm. Spray Tech.*, 2011, **20**(3), p 486-496
39. V.N.V. Munagala, S.I. Imbriglio, and R.R. Chromik, The Influence of Powder Properties on the Adhesion Strength and Microstructural Evolution of Cold Sprayed Ti6Al4V Single Splats, *Mater. Lett.*, 2019, **244**, p 58-61
40. J.G. Kaufman, *Parametric Analyses of High-Temperature Data for Aluminum Alloys*, ASM International, Materials Park, Ohio, 2008
41. M. Hassani-Gangaraj, D. Veysset, K.A. Nelson, and C.A. Schuh, In-Situ Observations of Single Micro-Particle Impact Bonding, *Scr. Mater.*, 2018, **145**, p 9-13
42. C. Chen, Y. Xie, R. Huang, S. Deng, Z. Ren, and H. Liao, On the Role of Oxide Film's Cleaning Effect into the Metallurgical Bonding during Cold Spray, *Mater. Lett.*, 2018, **210**, p 199-202
43. Y. Ichikawa and K. Ogawa, Effect of Substrate Surface Oxide Film Thickness on Deposition Behavior and Deposition Efficiency in the Cold Spray Process, *J. Therm. Spray Tech.*, 2015, **24**(7), p 1269-1276
44. C.-J. Li, H.-T. Wang, Q. Zhang, G.-J. Yang, W.-Y. Li, and H.L. Liao, Influence of Spray Materials and Their Surface Oxidation on the Critical Velocity in Cold Spraying, *J. Therm. Spray Tech.*, 2010, **19**(1–2), p 95-101
45. K. Kim, W. Li, and X. Guo, Detection of Oxygen at the Interface and Its Effect on Strain, Stress, and Temperature at the Interface between Cold Sprayed Aluminum and Steel Substrate, *Appl. Surf. Sci.*, 2015, **357**, p 1720-1726
46. Y. Ichikawa, R. Tokoro, M. Tanno, and K. Ogawa, Elucidation of Cold-Spray Deposition Mechanism by Auger Electron Spectroscopic Evaluation of Bonding Interface Oxide Film, *Acta Mater.*, 2019, **164**, p 39-49
47. L. Ajdelsztajn, A. Zúñiga, B. Jodoin, and E.J. Lavernia, Cold-Spray Processing of a Nanocrystalline Al-Cu-Mg-Fe-Ni Alloy with Sc, *J. Therm. Spray Technol.*, 2006, **15**(2), p 184-190
48. B. Jodoin, L. Ajdelsztajn, E. Sansoucy, A. Zúñiga, P. Richer, and E.J. Lavernia, Effect of Particle Size, Morphology, and Hardness on Cold Gas Dynamic Sprayed Aluminum Alloy Coatings, *Surf. Coat. Technol.*, 2006, **201**(6), p 3422-3429
49. V.S. Bhattiprolu, K.W. Johnson, O.C. Ozdemir, and G.A. Crawford, Influence of Feedstock Powder and Cold Spray Processing Parameters on Microstructure and Mechanical Properties of Ti-6Al-4V Cold Spray Depositions, *Surf. Coat. Technol.*, 2018, **335**, p 1-12
50. T. Liu, W.A. Story, and L.N. Brewer, Effect of Heat Treatment on the Al-Cu Feedstock Powders for Cold Spray Deposition, *Metall. Mater. Trans. A*, 2019, **50**(7), p 3373-3387
51. T. Schmidt, H. Assadi, F. Gärtner, H. Richter, T. Stoltenhoff, H. Kreye, and T. Klassen, From Particle Acceleration to Impact and Bonding in Cold Spraying, *J. Therm. Spray Tech.*, 2009, **18**(5–6), p 794-808
52. S. Yin, M. Meyer, W. Li, H. Liao, and R. Lupoi, Gas Flow, Particle Acceleration, and Heat Transfer in Cold Spray: A Review, *J. Therm. Spray Tech.*, 2016, **25**(5), p 874-896
53. J. Pattison, S. Celotto, A. Khan, and W. O'Neill, Standoff Distance and Bow Shock Phenomena in the Cold Spray Process, *Surf. Coat. Technol.*, 2008, **202**(8), p 1443-1454
54. R.C. Dykhuizen and M.F. Smith, Gas Dynamic Principles of Cold Spray, *J. Therm. Spray Technol.*, 1998, **7**(2), p 205-212
55. H. Guleryuz and H. Cimenoglu, Oxidation of Ti–6Al–4V Alloy, *J. Alloys Compd.*, 2009, **472**(1–2), p 241-246
56. H. Assadi, I. Irkhin, H. Gutzmann, F. Gärtner, M. Schulze, M. Villa Vidaller, and T. Klassen, Determination of Plastic Constitutive Properties of Microparticles through Single Particle Compression, *Adv. Powder Technol.*, 2015, **26**(6), p 1544-1554
57. S.L. Semiatin and G.D. Lahoti, Deformation and Unstable Flow in Hot Forging of Ti-6Ai-2Sn-4Zr-2Mo-0.1Si, *MTA*, 1981, **12**(10), p 1705-1717
58. S.I. Imbriglio, N. Brodusch, M. Aghasibeig, R. Gauvin, and R.R. Chromik, Influence of Substrate Characteristics on Single Ti Splat Bonding to Ceramic Substrates by Cold Spray, *J. Therm. Spray Tech.*, 2018, **27**(6), p 1011-1024
59. S.I. Imbriglio, M. Hassani-Gangaraj, D. Veysset, M. Aghasibeig, R. Gauvin, K.A. Nelson, C.A. Schuh, and R.R. Chromik, Adhesion Strength of Titanium Particles to Alumina Substrates: A Combined Cold Spray and LIPIT Study, *Surf. Coat. Technol.*, 2019, **361**, p 403-412
60. P.C. King, S.H. Zahiri, and M. Jahedi, Microstructural Refinement within a Cold-Sprayed Copper Particle, *Metall. Mater. Trans. A*, 2009, **40**(9), p 2115-2123
61. C. Borchers, F. Gärtner, T. Stoltenhoff, and H. Kreye, Formation of Persistent Dislocation Loops by Ultra-High Strain-Rate Deformation during Cold Spraying, *Acta Mater.*, 2005, **53**(10), p 2991-3000
62. X.-T. Luo, C.-X. Li, F.-L. Shang, G.-J. Yang, Y.-Y. Wang, and C.-J. Li, High Velocity Impact Induced Microstructure Evolution during Deposition of Cold Spray Coatings: A Review, *Surf. Coat. Technol.*, 2014, **254**, p 11-20
63. N. Ravichandran and Y.V.R.K. Prasad, Dynamic Recrystallization during Hot Deformation of Aluminum: A Study Using Processing Maps, *MTA*, 1991, **22**(10), p 2339-2348
64. B. Bay and N. Hansen, Recrystallization in Commercially Pure Aluminum, *MTA*, 1984, **15**(2), p 287-297
65. R.A. Vandermeer and D. Juul Jensen, Microstructural Path and Temperature Dependence of Recrystallization in Commercial Aluminum, *Acta Materialia*, 2001, **49**(11), p 2083-2094

Publisher's Note Springer Nature remains neutral with regard to jurisdictional claims in published maps and institutional affiliations.

5.5 Influence of the Coating and Particle Impact Temperatures On the CS Process using the Hard-on-Hard Material Combination

In this section, the influence of the coating and particle impact temperatures on the CS process are investigated using the hard-on-hard material combination. To have independent control of the coating temperatures from the gas stagnation temperature, an induction heating system is used. The initial particle temperature is controlled using powder preheating units and feeding the powder in the diverging section of the nozzle. By doing so, the initial particle temperature is not a function of the gas stagnation temperature. In this section, the following tasks are carried out to evaluate the role of the coating temperature on the CS deposition process:

- Measure the Coating Time-temperature History.
- Measure the Deposition Efficiency and Coating Thickness.
- Measure the Coating Mechanical Properties.

To characterize the influence of the particle impact temperature on the CS deposition process, the following tasks are completed:

- Decouple the Initial Particle Temperature from the Gas Stagnation Temperature.
- Predict the Particle Impact Temperature.
- Characterize the CS Deposition Process as a Function of the Particle Impact Temperature.

To demonstrate that the CS process can be enhanced based on the previous findings, samples are produced using different combinations of coating and particle impact temperatures.

The detailed evaluation of the effect of the coating and particle temperatures on the CS deposition process using the hard-on-hard material combination is presented in the form of a manuscript that has been accepted for publication in a peer-reviewed journal.

Towards Efficient Cold Spraying of Inconel 718: Understanding the Influence of Coating and Particle Impact Temperatures

Abstract

The production of Inconel 718 coatings using the cold spray process is often challenging due to the limited plastic deformation of particles upon impact associated to its mechanical properties. This leads to the requirement of high spray parameters to achieve dense coating build-up that may result in high and complex residual stresses that can also affect negatively the substrate and lead to nozzle clogging. In this work, the role of the coating and particle impact temperatures is investigated while ensuring they are decoupled from the particle impact velocity. This allows starting exploring potential ways to produce a sound and quality Inconel 718 coating at reduced spray parameters. To decouple and evaluate the role of the particle impact temperature, three initial particle temperatures are studied: 25, 400 and 750 °C. The effect of the coating temperature on the deposition process is investigated by controlling this temperature independently of the gas stagnation temperature through the use of induction heating. Deposition efficiency, porosity, and micro-hardness are used to asses the coatings quality. The coating time-temperature history is measured to better understand its influence on the deposition of Inconel 718. In this work, enhanced understanding of the effect of both particle and coating temperatures on the coating process is obtained, and the findings allow the establishment of a potential approach to produce dense coatings using reduced spray parameters.

1. Introduction

Inconel 718 (In718) is a nickel-based superalloy characterized by its excellent mechanical properties from cryogenic temperatures up to 650 °C [1–4]. It also exhibits excellent performance in high corrosion

environments, and is resistant to oxidation at elevated temperatures [2–4]. These characteristics have made In718 a coating material of interest in the power generation and aerospace fields. Deposition of In718 coatings has been achieved using thermal spray processes such as high-velocity oxygen fuel (HVOF) [5–7] and atmospheric plasma spraying (APS) [8,9]. However, coatings produced by these techniques are usually characterized by a high level of oxide inclusions and porosities [5–7,9]. Additionally, the associated powder melting/solidification leads to undesirable phase transformations [5–9].

Cold Spray (CS) has emerged as an alternative method for the production of In718 coatings [9–26]. In CS, feedstock powder particles are injected into a converging/diverging nozzle and accelerated to high velocities by a supersonic gas flow prior to impacting and deforming onto the substrate [27,28]. During the solid-state deformation of the particles occurring at high strain rates, approximately 90% their kinetic energy is converted into heat while the remaining is transformed into elastic and plastic deformation [28]. Particles bond to the substrate if intimate oxide-free contacts are created at the interfaces allowing metallic bonds and by mechanically anchoring to the substrate [29,30].

It has been found that the exceptional mechanical properties of In718 hinder the production of dense CS In718 coatings by limiting plastic deformation upon impact [10,13,26]. As such, production of CS In718 coatings have required using a high operating gas pressure (up to 5 MPa) and temperature (up to 1000 °C) [9–26]. With these spray parameters, η (the non dimensional ratio of $V_{impact}/V_{critical}$) values ranging from 1.09 to 1.43 have been reported for the production of In718 coatings [10–12]. High operating gas temperatures increase the gas velocity, while high operating gas pressures increase the gas density, both leading to enhanced particle impact velocity [31–33]. Additionally, by feeding the powder into an elongated pre-chamber or converging region of the nozzle, an increase in the particle impact temperature is achieved as a result of the heat transfer with the hot slow gas [34,35]. Higher particle impact temperatures promote thermal softening facilitating plastic deformation upon their impact [35–37]. The combination of relatively high particle velocities and temperatures for the deposition of In718 coatings has shown promising results,

but porous coatings (≥ 1.5%) are still observed [10–12,14,16,19–22,26]. Furthermore, nozzle clogging near the throat area has been reported when operating at high gas temperatures [10,14,16,19], and substrate damage (bending) has been observed as a result of the high temperatures recovered at the substrate surface (stagnation) while spraying [9,16].

A potential alternative to avoid these issues resulting from using high operating gas temperatures is the use of reduced spray parameters. This approach has never been explored for the production of In718 coatings because studies have demonstrated that increasing the operating gas temperatures often leads to higher deposition efficiency values and a less porous coating due to the higher particle impact velocities and temperatures [10,19,26]. However, other studies have demonstrated that this is not always the case as higher DE values and more porous coatings have also been reported for materials such as aluminum, MCrAlY, and Al-12Si [38–40]. These contradictory results demonstrate that the influence of the particle impact temperature on the overall coating quality (DE and coating porosity values) has not yet been completely understood.

Few studies have been devoted to assess the role of the coating temperature on the CS deposition process [41–47] as maintaining a constant coating temperature becomes difficult due to heat exchanged with the impacting propellant gas [46,47]. In previous studies, the coating temperature has been raised using a laser system coupled to the CS process. In the laser-assisted CS process, increasing the coating temperature is mostly limited to the spot size of the laser which creates a very localized and instantaneous raise in temperature [41–45]. A detailed and validated model has shown that, for the copper-on-steel combination, the effect of the laser spot is limited to up to 3 mm in coating thickness, and the local coating heating lasts less than 5 seconds [48]. Recently, the induction heating (IH) and CS processes were coupled (IHCS) to allow a more uniform coating heating in the case of pure Aluminum [46,47]. However, the effect of the coating temperature on the deposition of In718 has not yet been reported.

The objective of the current study is to investigate the effect of both particle impact and coating temperatures on the deposition of In718 and explore the effect of using reduced spray parameters that could minimize the possibilities of nozzle clogging, deformed substrate due to high temperature and high residual stresses. The influence of particle impact velocity on the production of In718 coatings is also investigated. To properly characterize the effect of the particle temperature, this variable is decoupled from the gas stagnation temperature (and therefore particle impact velocity) by using controlled powder preheating. Additionally, the powder is fed in the diverging section of the nozzle to prevent heat exchange between the powder and the hot slow propellant gas that is otherwise unavoidable and impossible to control. Three initial particle temperatures (leading to three different particle impact temperatures) are evaluated: 25, 400, and 750 °C. The particle impact temperature and velocity are predicted using a validated three-dimensional computational fluid dynamics (CFD) model. The CS process is assisted by an IH system to investigate the role of the coating temperature on the production of In718 coatings and the coating time-temperature history is measured for the two initial temperatures: 25 and 600 °C. DE, coating porosity level, coating micro-hardness and thickness are evaluated to characterize the influence of the coating and particle impact temperatures on the CS deposition of In718 coatings.

2. Experimental Procedures

2.1. Feedstock and Substrate Materials

Commercially available gas-atomized In718 powder (TrueFrom718, Praxair Surface Technologies, Indianapolis, IN, USA) was used as the feedstock material. This powder is characterized by a spherical shape and smooth surface, as shown in Fig. 1. The chemical composition (weight percentage) is Ni-19Cr-18Fe-Nb-5Ta-3Mo-1Ti. The powder particle size ranges between 10 to 45 µm, with an average particle size of approximately 30 µm, according to the manufacturer's data sheet.

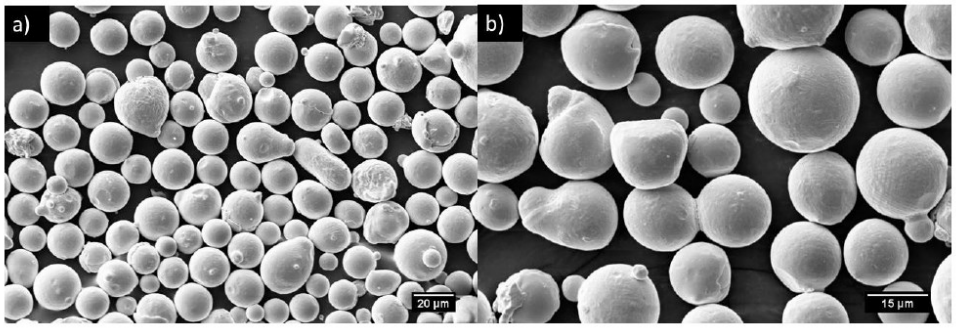


Fig. 1 Scanning electron microscope images of the In718 feedstock power. a) Lower magnification and b) higher magnification.

The substrate material was commercially available Ti-6Al-4V (Ti64) alloy bars of 25.4 mm in diameter (Titanium Industries, Inc., Montreal, QC, Canada). The bars were sectioned into 45 mm thick coupons. This substrate material was chosen because previous studies focused on evaluating the role of the substrate and coating temperatures on the CS process have used this substrate material removing one variable to consider when assessing the results [46,47,49]. Additionally, Ti64 also provides further understanding of the influence of the coating temperature on the deposition of the hard-on-hard (In17-on-Ti64) material combination. The manufacturer's data sheet indicated a composition by weight percentage of Ti – balance, Al – 5.94%, V – 4%. The coupons were ground with water as a lubricant prior to being coated. The resulting arithmetic average roughness (RA) after the grinding process was 0.45 ± 0.07 µm, measured using a profilometer equipped with a diamond stylus (Phase II, SRG-4000, NJ, USA). The substrates were cleaned and degreased in an ethanol ultrasonic bath for 3 minutes prior to the start of the deposition process.

2.2. Consolidation parameters

A commercially available CS system (SST-EPX, Centerline (Windsor) Limited, Windsor, ON, Canada) was used. This type of equipment was chosen because it allows controlling the particle temperature at the diverging section of the nozzle independently from the operating gas temperature, as the powder is fed downstream. To increase the initial particle temperature at the injection location, two powder-preheating

units were used. A commercially-available powder preheating unit (Centerline (Windsor) Limited, Windsor, ON, Canada) was used to increase the initial particle temperature to 400 °C prior to being fed into the nozzle diverging section. The powder-preheating unit consisted of a stainless steel coiled tube, and its temperature is increased by a heater radiating onto the coiled tube surface. The powder-preheating unit included two built-in thermocouples, one at the inlet and the other at the outlet of the coiled tube, to control the tube wall temperature. The unit was assumed to reach a steady state temperature when the wall temperature difference between the inlet and outlet was less than 2 °C. Due to the extensive length of the heating tube, it is assumed that by the time the gas and the particles exited the powder-preheating unit, these had reached the tube wall temperature.

To increase the initial particle temperature above 500 °C, an in-house powder preheater unit is used. This preheating unit consists of a mixing T and a stainless steel coil in which a heated gas and a cold gas with powder are brought together to reach a mixed gas temperature (T_{mixed}). The coil is perfectly insulated from the exterior to avoid any potential heat loss to the environment. The coil is long enough to ensure equilibrium between the gas and the particles at a temperature equal to T_{mixed}. The in-house powder preheating unit is presented in Fig. 2.

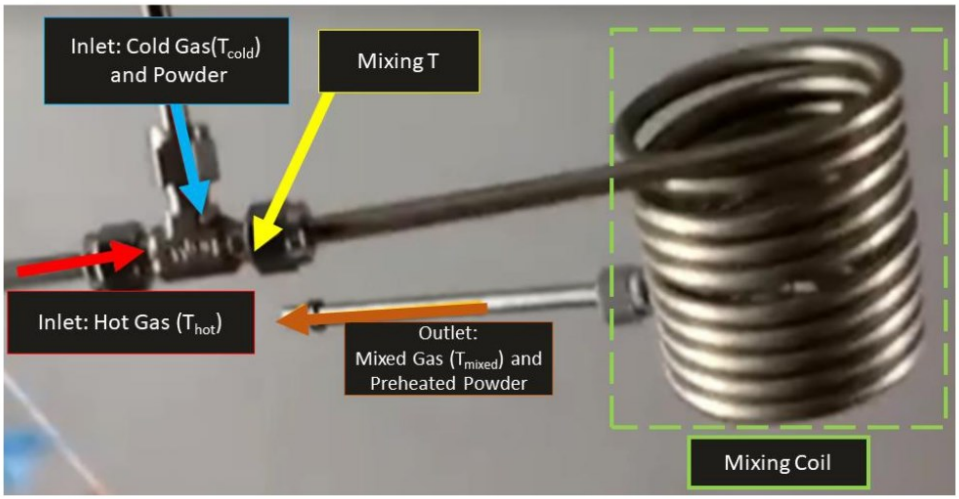


Fig. 2 Detailed view of the In-house powder preheater. Hot (T_{hot}) and cold (T_{cold}) gases are brought together and mixed inside a stainless steel coil. Powder is fed into the coil with the cold gas. The insulation around the mixing coil has been removed to provide a detailed perspective of the in-house controlled powder preheating unit.

A WC-Co nozzle (Ultilife, Centerline (Windsor) Limited, Windsor, ON, Canada) with a throat and exit diameters of 2 and 6.3 mm, respectively, was used. The nozzle diverging section has a 120 mm length. Table 1 presents the CS parameters used for the production of the samples, which are the maximum gas stagnation conditions that the system can reach.

Table 1 Cold Spray deposition parameters

General Deposition Parameters	**Values**	
Propellant Gas	Nitrogen	Helium
Stagnation Temperature (T_0) (°C)	500	500
Stagnation Pressure (P_0) (MPa)	3.45	2.06
Initial Powder Temperature (°C)	25, 400, and 750	
Traverse Speed (mm/s)	120	
Powder Feed rate (g/s)	1	

Stand-off distance (SOD) (mm)	15
Number of passes	5
Step Size (mm)	1

The IHCS system consisted of an induction heating system (Tucker Induction Sys. Inc., Shelby Township, MI, USA) coupled to the SST-EPX equipment [46,47]. The copper planar round coil had an outer and inner diameter of 110.0 mm and 42.0 mm respectively, as presented in Fig. 3 b). The coil had a total of four turns. The inner and outer diameters of the coil tubing were 5.0 and 6.3 mm, respectively. The substrates were positioned in the center of the IH coil, as presented in Fig. 3. The IH was kept "On" before and during the spraying process when IHCS was used. For the IHCS process, the initial substrate surface temperature was 600 °C, as a result of the eddy currents quickly heating up the substrate prior to the start of the spraying process. The IH parameters were 68 A and 193 kHz which are the highest IH parameters the system can reach for this specific substrate-coating configuration. For the cases in which the IH system was not coupled to the CS process, the initial substrate temperature was 25 °C. 25 and 600 °C as the initial substrate temperatures were selected for consistency purposes based on previous investigations of the influence of the substrate temperature on the CS deposition for the deposition of aluminum-on-Ti64 substrates [46,47,49].

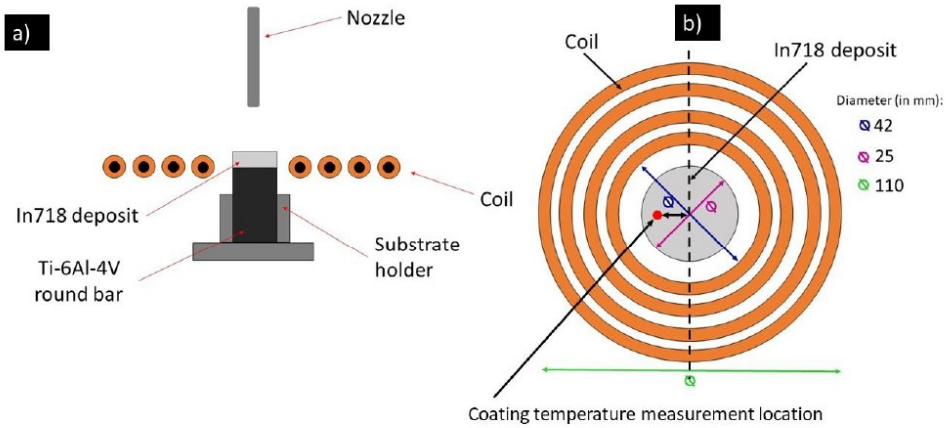


Fig. 3 Schematic of the IHCS setup. a) Cross section and b) top view.

To monitor the coating time-temperature history, a Ti64 substrate was first coated with a single-layer In718 coating using nitrogen as the propellant gas (500 °C and 3.45 MPa). Once the sample was prepared, it was set aside to let it cool down to room temperature before trials were performed using that pre-coated sample. Because the single-layer coating was thin (≤ 30 µm), it was assumed that during the deposition of this layer, the coating reached the initial substrate temperature. For that reason, as a first approximation, 25 and 600 °C were used as the initial coating temperature. The coating surface time-temperature history was monitored using two non-contact infrared thermometers. A RAYGPRSF (Raytek,Santa Cruz, CA, USA) non-contact infrared thermometer was used to measure the coating surface time-temperature history when the initial coating temperature was 25 °C. This infrared thermometer has a maximum working range of approximately 540 °C. For that reason, a second non-contact infrared thermometer was needed. The OptCT3MH2SF (Optris, Portsmouth, NW, USA) was used to measure the coating time-temperature history when the initial coating temperature was 600 °C. The OptCT3MH2SF has a working range of 200 up to 1500 °C. The infrared thermometers monitored the coating temperature-history 7.5 mm away from the middle of the bar top surface, as shown in Fig. 3 b).

Table 2 presents a summary of the samples produced in this work using different combinations of production methods and initial particle and coating temperatures.

Table 2 Designation of the produced deposits

Label	Initial Temperature (°C)	
	Particle	Coating
CS – N_2	25	25
CS – N_2 – PP_1	400	25
CS – N_2 – PP_2	750	25
CS – He	25	25
CS – He – PP_1	400	25
IHCS – N_2	25	600
IHCS – He	25	600
IHCS – He – PP_1	400	600
IHCS – N_2 – PP_2	750	600

CS, IHCS, N_2, He and PP stand for cold spray, induction heating cold spray, nitrogen, helium, and particle preheating, respectively. The first part of the label indicates the process used for the production of the sample, CS or IHCS. The second part of the label represents the propellant gas used during the spraying process (nitrogen or helium). The third part of the label represents the use of controlled particle preheating. PP_1 and PP_2 represents 400 and 750 °C, respectively, as the initial injection particle preheating temperature. If PP is not used on the labels, then the initial injection particle temperature was 25 °C [35].

2.3. Sample Characterization

To characterize the coatings, scanning electron microscopy (SEM) (EVO MA-10, Carl Zeiss AG, Oberkochen, Germany) was used. The cross-sectional images of the coatings were obtained under the detection of backscattered electrons (BSD). To quantify the densification/porosity level of the deposits, the ImageJ

software and the contrast imaging technique were used [46,47,50]. The coatings micro-hardness was obtained using a Duramin-10 tester (Struers Aps, Denmark) equipped with a Vickers indenter using a load of 0.3 kg. Indentations were performed every 50 µm, from the coating/substrate interface up to the top region of the coatings. This process was repeated twice at different locations in a cross-section, and the values were then averaged.

2.4. Computational Fluid Dynamics (CFD)

In the CS process, the particles exiting the nozzle are characterized by their relatively low particle temperature and relatively high velocities. For these reasons, the use of classical optical pyrometry is not possible, and thus, any particle temperature measurement becomes a technical challenge or an extremely lengthy process. Recently, a computational fluid dynamics model has been developed to predict the particle impact velocity and temperature. This model has also been extensively validated using a Cold Spray meter and high-speed infra-red camera [14,63]. The model has been shown to be able to accurately predict the particle impact velocity and temperature. Therefore, in this work, the same extensively validated CFD model is used to predict the particle impact temperature and velocity. The commercially available Ansys Fluent 16 software was used to carry out the CFD model.

The predicted average particle impact velocity and temperature are used to calculate η value. Assadi et al. [36] first defined η as shown by Eq. 1:

$$\eta = \frac{V_{impact}}{V_{critical}} \quad \text{Eq.1}$$

Where $V_{impatct}$ is the average particle impact velocity and $V_{critical}$ is the critical velocity. This parameter has proven to be a valuable tool for predicting the ability of producing CS coatings. The critical velocity values for In718 are taken from the data reported by Perez-Andrade et. al. [10]. In this work, η is used as valuable indicator of what to expect in terms of the deposition based on the different spray conditions.

The three-dimensional model comprised by the nozzle and the spray chamber/substrate geometries was split into different computational domains and grids to accurately capture all the flow features, as shown in Fig. 4. The meshing process was carried out using the built-in Ansys Meshing Module. The sweepable mesh was used where the nozzle geometries allowed, otherwise a tetragonal mesh was used. A grid dependency study was carried out in which five meshes were tested: less than 100,000 elements, ~200,000 elements, ~700,000 elements, ~900,000 elements, and more than 1,000,000 elements. The model comprised of ~900,000 elements provided adequate results without compromising the computational time.

CFD subdomain	Size (mm)
Throat diameter (Φ_{Throat})	2
Surrounding atmosphere ($\Phi_{Atmosphere}$)	60
Nozzle exit diameter (Φ_{Exit})	6.3
Stand-off distance (SOD)	15
Pre-chamber length (Pc_L)	10
Converging length (C_L)	10
Diverging length (D_L)	120

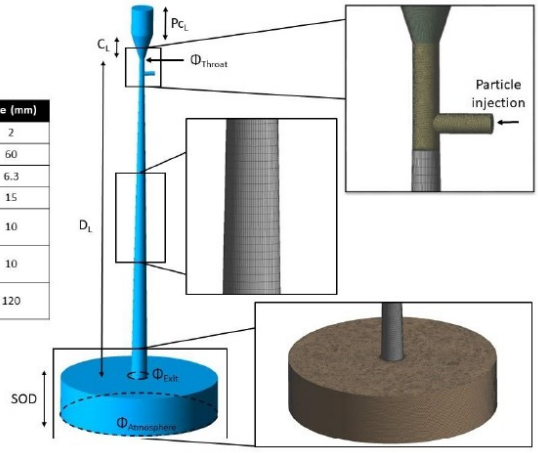


Fig. 4 Three-dimensional computational domain and meshing for the CS system.

The Reynolds-Average Navier-Stokes (RANS) equations were used along with the re-normalized k-ε turbulence model (RNG k-ε) to model the gas flow [35,51–53]. Convergence was assumed to be reached when the residuals decreased by at least four orders of magnitude. As an additional criterion for convergence, a mass imbalance of less than 1% between the gas inlet and the nozzle exit was required.

At the nozzle inlet, the stagnation pressure and temperature were specified using the values presented in Table 1. At the inlet of the powder feeding line, a gas mass flow rate boundary condition was fixed. The gas

mass flow rate at the powder feeding inlet was 0.00033 kg/s. Three gas temperatures at the powder feeding line inlet were modeled: 25, 400 and 750 ºC. Due to the long powder preheater tube length, it was assumed that by the time the particles were fed into the nozzle, their temperature had already reached the powder feeding gas temperature. The surrounding atmosphere at the end of the nozzle was set at room temperature and atmospheric pressure. A summary of the boundary conditions (BC) used in the CFD model is presented in Table 3.

Table 3 Numerical model boundary conditions

Location	Type of BC	Temperature (°C)		Pressure (MPa)	
		Nitrogen	Helium	Nitrogen	Helium
Main gas inlet	Pressure inlet	Stagnation conditions		Stagnation conditions	
Powder inlet	Mass inlet	25, 400, and 750	400	N/A	
Surrounding atmosphere	Pressure outlet	25	N/A	Atmospheric	N/A
Substrate	Wall	Adiabatic		N/A	

The fluid and particle properties used in this CFD model are presented in Table 4. The values presented in Table 4 were selected based on the data available in the literature [1,11,35,54–56] .

Table 4 Properties used in the CFD model

Properties	Nitrogen gas	Helium gas	In718 particles
Particle size distribution, average size (µm)	N/A	N/A	10–45, 30
Stagnation conditions	Available in Table 1		N/A
Density (kg/m^3)	Ideal gas		8190
Specific heat capacity (J/kgK)	1040.6	5192.6	435
Thermal conductivity (W/mK)	0.0242	0.152	11.4
Viscosity (kg/m-s)	Sutherland's law		N/A
Initial particle temperature at the injection location (°C)	N/A	N/A	25, 400, and 750

A particle size distribution of 10 to 45 µm with an average size of 30 µm was used, as presented in Table 4. These values were selected as they correspond to the powder size distribution used experimentally. The effect of the particles on the gas phase and the particle-particle interactions were neglected because of the low volume fraction of the powder particles with respect of the gas flow (volume fraction <10%) [51,57–59]. The different particle trajectories and their stochastic behavior inside the nozzle were taken into account by using the discrete random walk (DRW) model. The particles were injected in the divergent region of the nozzle, matching the injection location of the physical nozzle, as shown in Fig. 5. A minimum of 1000 particles were used to calculate the average particle impact velocity and temperature. An in-depth description of the validated computational model can be found elsewhere [35].

3. Results and Discussion

3.1. Particle Impact Temperature and Velocity

The predicted average particle impact velocity and temperature are presented in Table 5.

Table 5 Predicted average particle impact velocity and temperature, and average η for the In718 powder

Propellant gas - T_0 (°C) - P_0 (MPa) - Initial particle temperature (°C)	Particle Impact		Critical velocity (m/s) [10]	η
	Velocity (m/s)	Temperature (°C)		
N_2 – 500 – 3.45 – 25	604 ± 95	77 ± 25	802	0.75
N_2 – 500 – 3.45 – 400	590 ± 102	349 ± 29	702	0.85
N_2 – 500 – 3.45 – 750	590 ± 87	600 ± 66	598	0.98
He – 500 – 2.06 – 25	848 ± 168	139 ± 44	787	1.07
He – 500 – 2.06 – 400	845 ± 158	257 ± 49	739	1.14

Using nitrogen as the propellant gas accelerates the particles to an average V_{impact} of around 604 m/s. For this case, the average particle impact temperature is approximately 77 °C. At this temperature, $V_{critical}$ is approximately 800 m/s [10]. Thus, for the use of nitrogen as the propellant gas, an η equal to 0.75 was calculated. Consequently, minimal to no deposition is expected. The particle impact velocity for the cases in which the initial particle temperature was increased to 400 and 750 °C is on average 590 m/s. For these cases, the average particle impact temperatures are 349 and 600 °C, respectively. The difference between the initial and the impact temperatures is caused by heat exchanged between the relatively cold gas in the diverging section and the warm particles. The benefit from increasing the particle impact temperature is visible in Table 5 as the critical velocity is reduced by approximately 25% (598 m/s vs 802 m/s). Despite this reduction, η was 0.85 and 0.98 and thus minimal deposition is also expected.

The use of helium in combination with initial particle temperatures of 25 and 400 ºC lead to a predicted average particle impact velocity of approximately 850 m/s for both cases. The higher average particle impact velocity values are caused by the low molecular weight and high specific heat ratio of helium in comparison to nitrogen, resulting in considerably higher gas velocities [31,32,50,60–64]. The predicted average particle impact temperatures for the feeding gas temperatures of 25 and 400 ºC were 139 and 257 ºC, respectively. Based on the predicted values, particles are likely to deposit under these two spray conditions as their η is slightly above 1 (Table 6). In the literature, an η=1.5 has been used as a benchmark that ensures dense copper coatings [36], but a clear benchmark for the deposition of an In718 dense coating has not yet been established.

3.2. Coating Surface Time-Temperature History

In a previous work [46], measuring the substrate time-temperature history provided insightful information to better understand the influence of this temperature on the CS deposition process. For that reason, a similar approach is followed and the coating surface time-temperature history is monitored for two initial coating temperatures: 25 and 600 °C. Figure 5 presents the coating surface time-temperature history for one nozzle pass over the coating surface using nitrogen as a propellant gas.

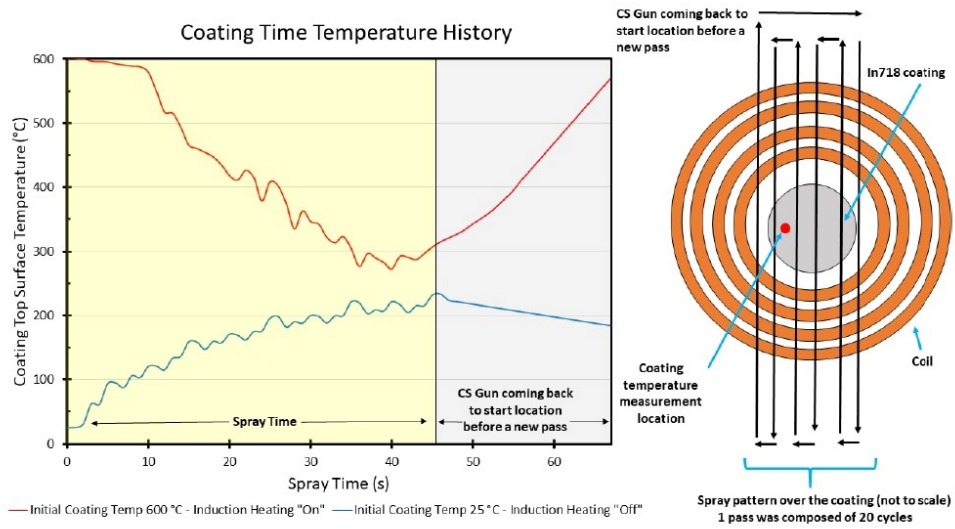


Fig. 5 Coating surface time-temperature history. Red curve: the induction heating system "On" during the spray time and initial coating temperature is 600 °C. Blue curve: induction heating system is kept "Off" during the spray time and initial coating temperature is 25 °C. A "pass" over the coating is completed by the time the nozzle has completed 20 cycles (cycle = 1 back and forth movement).

The blue curve in Fig. 5 represents the coating surface time-temperature history for the case in which the induction heating system is "Off" during the spray time. The coating surface temperature exhibited an increasing trend, with some noticeable fluctuations, attributed to the nozzle scanning pattern over the coating surface [46,47]. This trend is caused by the convective heat transfer between the impinging gas stream and the coating combined with conduction heat transfer through the coating thickness and substrate. The gas flow should decelerate on the coatings surface bringing the gas back to the stagnation conditions. However, losses associated with a non-isentropic and non-reversible process contribute to a lower stagnation gas temperature than the initial temperature. By the end of the nozzle pass, the coating heating rate tends to stabilize pointing to a "steady-state" coating temperature at around 225 °C, lower than the initial gas temperature (500 °C) [46,47]. This result suggests that the maximum temperature a coating could reach is about 50% of the stagnation temperature. The primary reason driving the use of high

stagnation temperatures for the deposition of In718 coatings is higher particle impact velocities and temperatures. By monitoring the coating surface time-temperature history, it can be concluded that another benefit of the use of high stagnation temperatures is inducing thermal softening on the already deposited coating layers. Using stagnation temperatures ranging 600 to 1000 °C could potentially increase the coating temperature to values between 300 and 500 °C favoring coating densification, reducing the critical velocity for deposition, and thus, increasing the DE.

The red curve presented in Fig. 5 represents the coating surface time-temperature history for the case in which the IH system is "On" during the spray time. The coating experienced a cooling effect because the initial temperature was above the "steady-state" temperature (225 °C), as expected based on previous results [46,47]. The fluctuations are also attributed to the nozzle scanning pattern over the coating surface and the relatively low thermal conductivity of In718. These fluctuations become more evident as the nozzle approaches the measurement location. During most of the spray time, the heat exchange between the gas stream and the coating surface was dominant over the heating rate of the induction heater. However, in the last few seconds, when the nozzle was about to leave the coating surface, it can be seen that the coating temperature started to ramp up. By the time the nozzle was about to start a new pass of the deposition process, the coating temperature had already reached about 95% of the initial coating temperature (600 °C). Based on the trend shown by the red curve, to achieve similar coating surface temperatures, the stagnation temperatures near the 1000 °C range would be needed to achieve a similar effect. The different coating surface time-temperature histories shown in Fig. 5 are expected to produce a significant difference in the deposition process because the particles will impact on average a softer coating in comparison to the case represented by the blue curve [46,47].

3.3. Effect of Particle Impact Temperature and Impact Velocity

Before investigating the influence of the coating temperature on the production of In718 coatings, the influence of the particle impact temperature and velocity are first investigated.

Using nitrogen as the propellant gas and three different initial particle temperatures: 25, 400 and 750 ºC (with an average predicted particle impact temperature of 77, 349 and 600 ºC, respectively) resulted in minimal deposition (DE less than 1%), as presented in Fig 6 a) – c) respectively. Increasing the particle impact temperature reduced the critical velocity, and thus, the η value increased from a minimum of 0.75 to a maximum of 0.98. For the three cases (CS – N_2, CS – N_2 – PP_1 and CS – N_2 – PP_2) only a first layer of particles was able to adhere to the substrate, most likely through mechanical interlocking with no subsequent layers being built. The particles of these single-layer coatings were well deformed as a consequence of the repeated impingement of the incoming non-adhering particles.

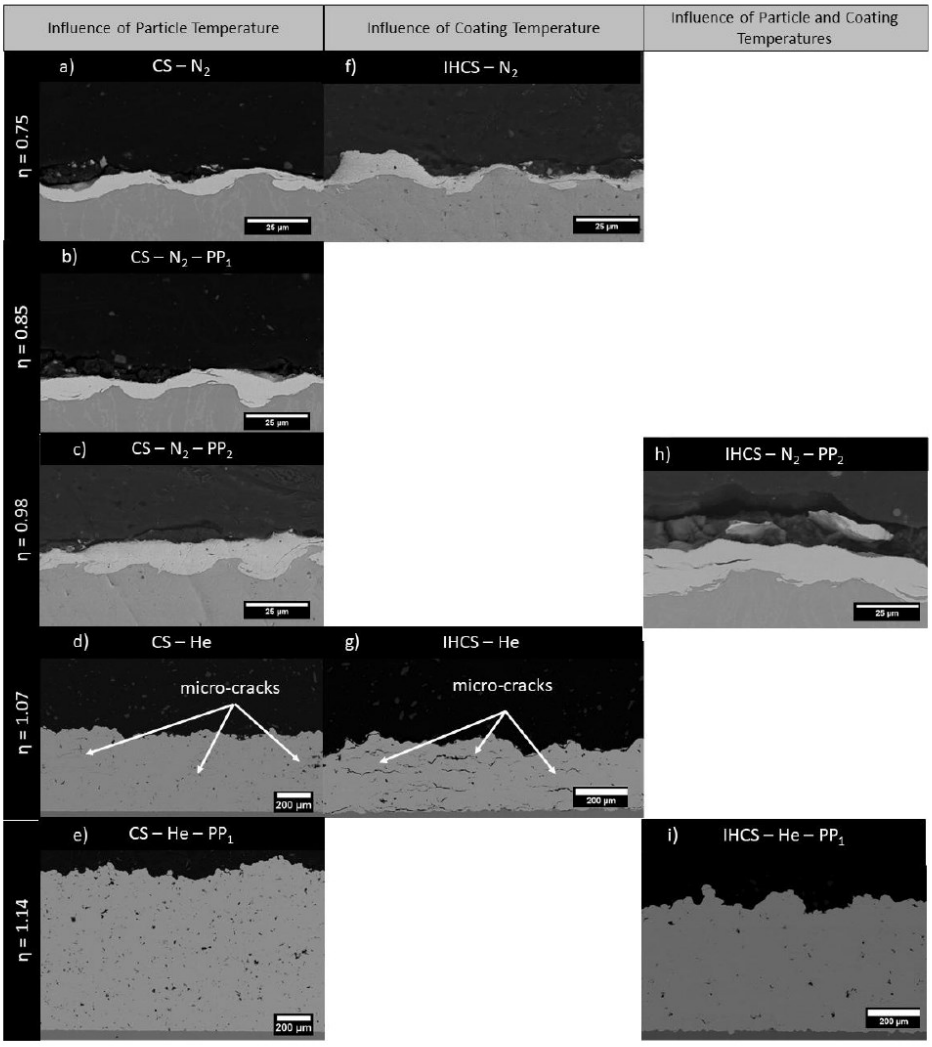


Fig. 6 Cross-sectional images of the different coatings produced in this study. CS, IHCS, N_2, He and PP stand for cold spray, induction heating cold spray, nitrogen, helium, and particle preheating, respectively. PP_1 and PP_2 represent 400 and 750 °C, respectively, as the initial injection particle preheating temperature. If PP is not used on the labels, then the initial injection particle temperature was 25 °C.

A drastic increase in coating thickness (Fig. 6 d)) was obtained when using helium, due to the higher η value (1.07) experienced by the impacting particles. The In718 particles had more kinetic energy prior to impact to break their native oxide layer, deform, and bond. The thick CS – He sample shows a relatively low porosity (<1%). While the particles reached significantly higher impact velocities (approximately 40 % higher in comparison to nitrogen), micro-cracks parallel to the substrate/coating interface and scattered across the coating cross-section were visible.

The CS – He – PP_1 sample (Fig. 6 e)) is significantly thicker than the sample without particle preheating. As predicted by η (Table 5), the higher particle impact temperature improved the DE, from 8 to 17%, as presented in Table 6, with the coating thickness increasing accordingly by about 50%. The increased particle impact temperature facilitated localized deformation (adiabatic shear instabilities) at the region close to the particle surface, and promoted the particles to meet the minimal conditions required for bonding [34,35]. However, the coating porosity level increased from <1 % to close to 2%. The latter is not something that could have been predicted for a higher η value. However, increasing the particle impact temperature has eliminated the presence of micro-cracks, as observed in Fig. 6 d) vs. Fig.6 e).

Table 6 Characteristics of In718 coatings. CS, IHCS, He and PP stand for cold spray, induction heating cold spray, nitrogen, helium, and particle preheating, respectively. PP_1 represents 400 as the initial injection particle preheating temperature. If PP is not used on the labels, then the initial injection particle temperature was 25 °C

Label	Thickness (µm)	Micro-hardness (HV)	DE(%)	Porosity (%)
CS – He	461 ± 21	469 ± 26	8.0± 0.4	<1
CS – He – PP_1	907 ± 28	460 ± 25	17.2 ± 0.5	~ 2
IHCS – He	230 ± 23	N/A*	4.1 ± 0.2	N/A*
IHCS – He – PP_1	508 ± 33	537 ± 28	10.4± 0.4	< 1

**The micro-hardness and porosity are not available (N/A) because the coating contained too many cracks.*

Even tough successful deposition was achieved using helium as the propellant gas (CS – He), additional micro-cracks appeared at the vicinity of the mark left by the indenter after completing the micro-hardness measurement, as shown in Fig. 7 a). The presence of cracks induced by micro-hardness testing have also been observed in as-sprayed In718 coatings when elevated spray parameters (800 °C and 3.5 MPa) were used [13]. The appearance of these cracks has been proposed as an indicator of weak inter-particle bonding, limited particle deformation and a low coating quality [13,65].

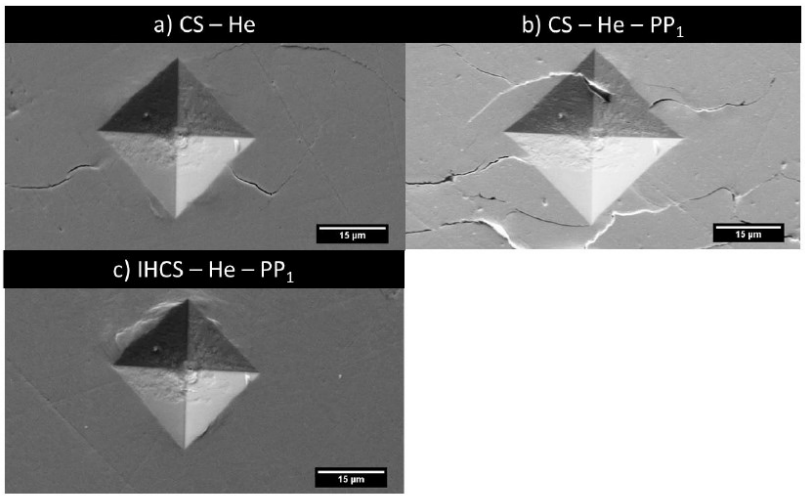


Fig. 7 SEM image of the mark left on the samples by the micro-hardness indenter. CS, IHCS, He and PP stand for cold spray, induction heating cold spray, helium, and particle preheating, respectively. PP_1 represents 400 °C as the initial injection particle preheating temperature. If PP is not used on the labels, then the initial injection particle temperature was 25 °C.

Even though the initial particle temperature was set to 400 °C (with a particle impact temperature of approximately 260 °C), superior inter-particle bonding was not achieved, as confirmed by the cracks that appeared in the vicinity of the indentation mark shown in Fig. 7 b), suggesting limited plastic deformation that lead to porosity and reduced cohesion [13,65]. Additionally, more cracks are visible in comparison to Fig. 7 a). The higher number of cracks is potentially caused by the numerous pores inside the coating (Fig.

6 e)). Porosities act as stress concentrators facilitating crack propagation through the weakest points of the coating (particle-to-particle interfaces). The similar micro-hardness values, available in Table 6, between the CS – He and CS – He – PP_1 coatings also support this observation.

To summarize the effect of particle impact temperature and velocity during the cold spraying process of spherical metallic powders, Fig. 8 (adapted from [40]) presents the DE and densification level % (100 – porosity level) values for pure aluminum as a function of the average particle impact velocity. The variation of particle impact temperature was not monitored or considered in that study [40].

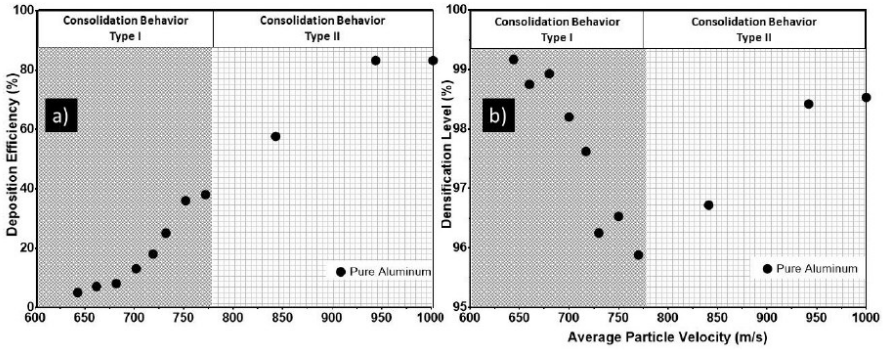


Fig. 8 a) Deposition efficiency and b) densification values of pure aluminum coatings as a function of the average particle impact velocity. The data points for spherical pure aluminum were taken and adapted from [40].

The first consolidation behavior (Type I) occurs in the region where low particle impact velocities result in lower DEs and higher densification (low porosity) values, as presented in Fig. 8 a) and b). In this zone, plastic deformation of the few adhering particles is promoted by the many particles impacting on and bouncing off the adhered particles. This closes the pores and densifies the consolidated material (impingement effect) [40]. As the average particle impact velocity increases, the DE increases. However, this reduces the impingement effect resulting in a reduced densification level of the consolidated material [40]. The second consolidation behavior (Type II) is characterized by a simultaneous increase in both DE and densification

level. In that region, the main densification mechanism is attributed to the extensive plastic deformation that the particles experience directly upon impact [40].

The previous trends have also been observed for spherical aluminum alloy, stainless steel, and CoNiCrAlY [50]. Therefore, it is likely that all spherical metallic powder materials display these two consolidation behaviors. The trends presented in Fig. 9 are shown schematically for, in theory, any feedstock powder material in Fig. 9 a) and b) (red curves).

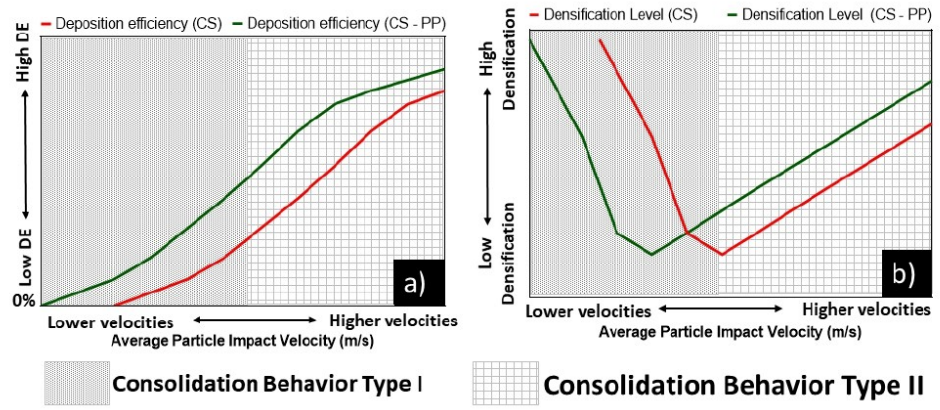


Fig. 9 Consolidation behavior as a function of the average particle impact velocity and particle preheating. In a) DE and in b) densification level as a function of the average particle impact velocity and particle preheating (higher particle impact temperature). The red curves represent the CS process, while the green line indicates the effect of particle preheating on the CS process (CS – PP).

Based on the estimated particle impact velocity and the η values presented in Table 5, the particles examined so far in the current work were likely sprayed in the "Consolidation Behavior Type I" region, further supported by the low DE values registered. Consequently, the densification process observed and reported in Table 6 must be controlled by the impingement effect [40,66].

Figure 9 a) and b) present the effect of particle preheating on the trends of DE and densification levels as a function of the average particle impact velocity (green curves). The DE curve (CS – PP) in Fig. 9 a) has been

shifted to the left from its original position (red curve). This shift occurs because higher particle impact temperatures reduce the critical velocity for deposition as particle deformation is facilitated [34–37,67–69]. A good example of this is demonstrated by Eq. 2 [36], which expresses the critical velocity of copper, only, as a function of the material properties and particle temperature:

$$V_{critical} = k_1\sqrt{c_p\left(T_m - T_p\right) + 16\,\frac{\sigma}{\rho_p}\left(\frac{T_m - T_p}{T_m - 293}\right)} \quad \text{(Eq. 2)}$$

In Eq. 2, k_1 is a particle size-dependent dimensionless fitting parameter, C_p is the specific heat of the particle material, T_m is the particle material melting temperature, T_p is the particle impact temperature, σ is the tensile strength of the particle material at 293 K, and ρ_p is the particle density. In the literature, this equation has been used to describe how the critical velocity behavior for other materials, and it is widely accepted that the critical velocity is a function of the particle temperature. Therefore, warmer particles are likely to deposit at lower velocities, producing higher DE values for a similar average particle impact velocity [34–37,67–69].

A common knowledge of the CS field is that increasing the particle impact temperature will improve the coating density (decrease the coating porosity). This has driven the use of elevated spray parameters in the CS field, and more particularly their use for the deposition of In718 [9–26]. However, in the "Consolidation Behavior Type I" region of Fig. 9 b) for a specific impact velocity, the densification level of a coating decreases (green curve) in comparison to particles at lower impact temperatures (red curve). In this zone, higher particle impact temperatures are enough to promote localized deformation (adiabatic shear instabilities) at the region close to the particle surface, but not enough to promote extensive deformation of the entire particles. This enhances particle bonding and leads to an increased DE, but reduces the impingement effect and the pores created due insufficient overall particle deformation are left open [40,66]. This behavior explains the increase in porosity (decrease in densification) for the CS – HE – PP sample with

respect to the CS – HE coating. An increase in the porosity levels have also been observed for the deposition of Al-Si and MCrAlY when the particle impact temperature increased [38,39].

In the "Type II" region of Fig. 9 b), the powder preheating curve (green curve) shows higher densification values with respect to the curve without powder preheating (red curve). The higher values for the green curve in Fig. 9 b) are caused by the combination of relatively higher particle impact temperatures and velocities, which both enhance plastic deformation, and thus, densification upon impact. In other words, the "Type II" region demonstrates why elevated spray parameters are commonly associated with the production of a less porous coating [10,14,19,21,40,70–77]. Ultimately, Fig. 9 b) unifies the very different results that have been reported for the effect of the particle impact temperature on the coating quality.

3.4. Effect of the Coating Temperature and Particle Impact Velocity

As a first step to investigate the effect of the coating (or already deposited layers) temperature on the CS deposition of In718, an initial coating temperature of 600 °C, an injection particle temperature of 25°C, and nitrogen as the propellant gas were used. This combination of spray parameters resulted in a thin coating similar to the one produced for an initial coating temperature of 25 °C, as shown in Fig. 6 f), and the DE was less than 1%. Based on the significant higher average coating temperature reported in Fig. 5 (red curve), these results were unexpected because, for aluminum, higher coating temperatures produced significant increases in DE and coating thickness [46]. In previous work, the drastic changes in DE were attributed to a reduction of the critical velocity as a result of the local heating process of the coating layers by the eddy current density distribution resulting from the induction heating [46]. As a result, the incoming particles impacted thermally softened coating layers. This promoted more particles to meet conditions for bonding, and thus, higher deposition rates were obtained [46]. However, while Fig. 5 confirms that the particles impacted a warmer (thus softer) coating, in Fig. 6 f) only a slight effect can be seen in comparison to Fig. 6 a). The slight difference is attributed to the higher initial substrate temperature, which had a limited effect

to only the first layer of deposited particles [47]. The samples presented in Fig. 6 a) and f) were produced using identical spray parameters and because of that η was 0.75. While the coating temperature at the end of the time-temperature history was relatively high (570 °C) (based on Fig. 5), this coating temperature was not high enough to produce an enhanced thermal softening that could promote a drastic reduction of the critical velocity. To potentially further reduce the critical velocity of In718, and based on its mechanical properties, coating temperatures beyond 650 °C are needed. Therefore, the induction heating parameters must be re-evaluated and assessed. It is likely that by increasing the current from the IH to higher values, a superior coating heating process can be achieved resulting in a more noticeable reduction of the critical velocity. Higher coating temperatures would promote particle entrapment in the coating upon impact, as observed for aluminum in a previous work [46].

To further investigate the influence of the coating temperature on the CS deposition process, the particle velocity was increased by using helium as the propellant gas, the initial coating temperature was set at 600 °C, and no powder preheating was used (η = 1.07). Despite having an identical η value (IHCS – He vs CS – He), which in theory should result in similar deposition behavior, the IHCS – He coating (Fig. 6 g)) was approximately 50% thinner than the one produced without the use of IH (Table 6). This indicates that the coating temperature can significantly influence the CS deposition process and that while the η value is traditionally a sound indicator to predict the deposition behavior, it does not include information about the substrate/coating temperatures and their effect on the overall coating quality. It is believed that the thinner coating is likely caused by the dissimilar deformation behavior between the thermally softened coating layers and the incoming hard particles. For the CS – He sample (Fig. 6 d)), hard particles were sprayed on relatively hard coating layers. By increasing the coating temperature (using the IH process), the incoming hard particles impacted warmer coating layers (the coating temperature can be estimated between 300 to 600 °C based on Fig. 5) compared to the case without using IH. However, the coating temperatures were likely not high enough to promote particle embedment and increase the DE during the spraying process.

Instead the relatively high coating temperatures restricted the particle deformation because their kinetic energy was mostly dissipated into deformation of the relatively softer counterpart, as first suggested by Bae et al [78]. It is believed that based on the mechanical properties of In718, coating temperatures above 650 °C would be needed to produce sufficient local coating deformation that would lead to particle embedment in a similar way than the one observed for aluminum [46,47]. With the current coating temperatures that can be achieved using the maximum parameters of the IH system, higher impact velocities would be required to penetrate into the already deposited coating layers, deform, and produce a similar coating thickness as the one obtained for the CS – He sample [78]. This transition in the deformation behavior between the coating layers and the incoming particles is likely to be more pronounced as the powder material strength increases. For that reason, this effect was likely not observed during the deposition of a soft powder (pure aluminum) [46].

In addition to the lower deposition rates, increasing the coating temperature also had a detrimental effect on the consolidated material as large cracks between layers can be observed in Fig. 6 g). To explain these cracks, it is important to first consider that the samples without coating heating had already exhibited weak inter-particle bonding, as shown in Fig. 7 a). Additionally, the coating experiences quick heating caused by the IH system (heating rate of ~11 to 12 °C/s) and rapid cooling (~12 °C or higher as this sample had helium as the propellant gas) due to heat exchange between the propellant gas during each nozzle pass over the coating surface (Fig. 5). In the CS process, the presence of thermal residual stresses is not significant due to the relatively low coating temperatures [79], and experimental values associated to thermal residual stresses are often below 100 MPa for Inconel 718 coatings [10,17,18]. However, knowing that thermal stresses become significant at coating temperatures above 400 °C [79–81], as in this work (Fig. 5), a theoretical value for these can be approximated to 1 GPa ($\sigma = E\alpha(T_i - T_f)$), if E =200 GPa, α=12.8 x10^{-6} , $T_i = 600\,°C$, and $T_f = 200\,°C$. While the theoretical value provides a first approximation of the maximum expected value, it has been shown that various stress-relaxation mechanisms operate within the coating

reducing the maximum tensile stress values [82], as reported by Barton [44]. Based on these conditions and the In718 low thermal conductivity and relatively high thermal expansion coefficient, tensile residual stresses are likely developed and these potentially overcame the cohesion strength of the coating creating defects such as the cracks shown in Fig. 6 g).

3.5. Effect of the Coating Temperature, Particle Impact Temperature and Impact Velocity

To further study the relationship between the coating temperature and the particle impact temperature and velocity, nitrogen was used as the propellant gas, the initial particle temperature was increased to 750 °C, and the initial coating temperature was set at 600 °C. Similarly, as for the IHCS – N_2 sample, the IHCS – N_2 – PP_2 sample was mainly composed of one or two particles at most, as shown in Fig. 6 h). Even though the critical velocity is likely a function of the coating temperature, for the current temperature values, the benefit of higher coating temperatures is not sufficient to obtain a significant build up.

To increase the particle impact velocity, helium was used. Additionally, to minimize powder/coating hardness differences while maximizing the coating quality and DE using the available maximum IH power output and spray parameters available on the commercial CS system used in this work, powder preheating was set at 400 °C. In Fig. 6 i), a representative cross-sectional image of the sample (IHCS – He – PP_1) produced using the IHCS, with helium as the propellant gas and powder preheating is presented. A crack-free coating was obtained with an average thickness of 508 µm (Table 6). The coating porosity was within or below the reported range of values obtained using high spray parameters [10,11,13–17,17,19,21–23,26] as well as lower compared to APS [8] and HVOF [5]. The samples presented in Fig. 6 e) and i) had an identical η value (1.14), but the coating quality was significantly different. While η is an excellent tool to estimate particle deposition, the equation to calculate η might be incomplete and terms should be added to account for the influence of the coating and substrate temperatures, as the results have suggested until this point.

Additionally, the IHCS – He – PP_1 sample (Fig. 7 c)) exhibited a superior inter-particle bonding in comparison to any of the other samples presented in Fig. 7, as no cracks appeared in the surrounding area of the mark left by the indenter after the micro-hardness testing procedure. The average micro-hardness was 537 HV (Table 6) showing good agreement with the reported micro-hardness values for cold-sprayed In718 coatings [13,16,17,19,22].

The IHCS – He – PP_1 sample shows the benefit of increasing both the particle and coating temperatures towards the production of a high quality coatings. Increasing the particle temperature reduces the potential temperature difference between the coating layers and the impacting particles. Consequently, the softer coating layers and particles were able to deform more similarly, even at low η values, enhancing the inter-particle bonding (as demonstrated by Fig. 7 c)). Additionally, the particles were still "hard" enough to produce significant peening on the thermally softened coating layers further increasing the coating cohesion strength and reducing the coating porosities. The higher coating temperatures produced by the IH system are also likely to have enhanced the coating cohesion strength by producing an in-situ heat treatment as temperatures between 300 and 600 °C are likely reached, as shown in Fig. 5. While some tensile residual stresses might still be present in the coating, due to the rapid cooling and heating caused by the propellant gas and IH heating rate, respectively, the coating cohesion strength was strong enough to avoid the development of internal coating cracks. A future study will be dedicated to evaluate the residual stresses inside the coating due to the rapid cooling and heating caused by the propellant gas and IH heating rate.

A summary of the effect of the coating temperature during the cold spraying process of spherical metallic powders is presented in Fig. 10 a) and b).

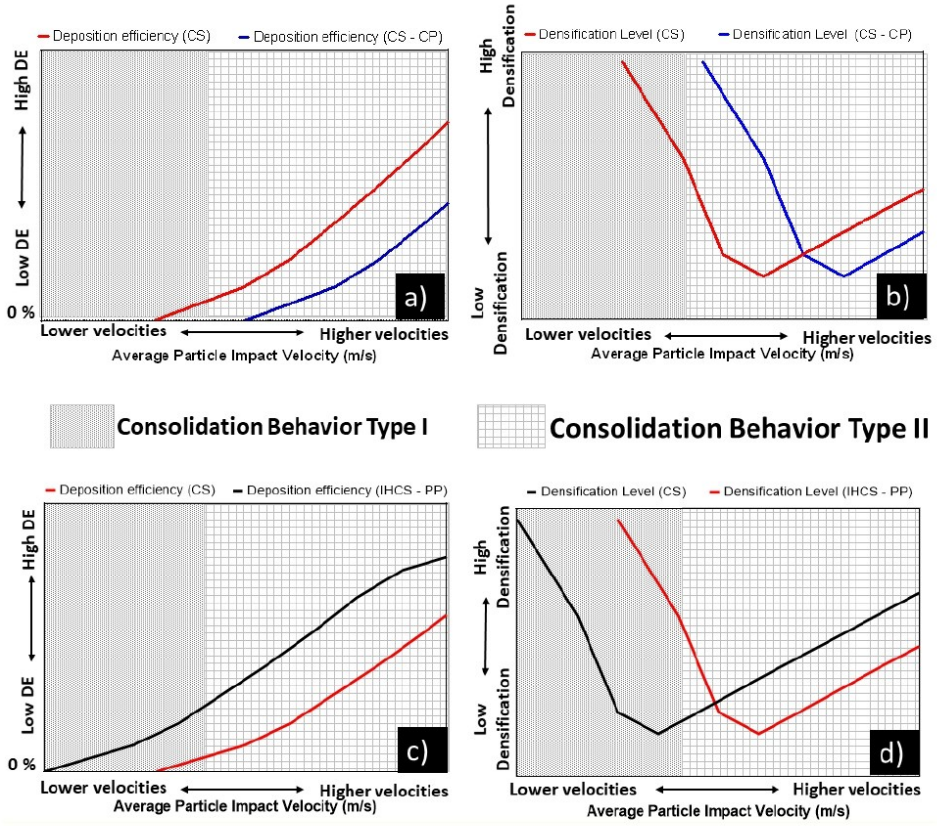


Fig.10 Consolidation behavior as a function of the average particle impact velocity, coating and particle temperatures. In a) and c), DE, and in b) and d) densification levels are presented. In a) and b), the effect of the and coating temperature as a function of the average particle impact velocity on the deposition process is presented. In c) and d), the combined effect of the coating and particle impact temperatures is also included. The red curves represent the CS process, while the blue curves (CS – CP) indicate the effect of the coating temperature on the CS process. CP stands for coating preheating. The black curve (CS – CP – PP) indicates the combined effect of coating and particle temperatures on the CS process.

The shifting of DE to the right (blue curve, CP stands for coating preheating) from its original position (red curve) in Fig. 10 a) is attributed to the coating layers acting as a soft material in comparison to the hard particles. This follows the behavior first suggested by Bae et. al, in which higher impact velocities are required to start depositing the particles when the hard-on-soft material combination is used [78]. In this

material combination, the soft material experiences most of the plastic deformation. However, due to the very limited plastic deformation that the particles may experience, the native oxide layer covering them is potentially not broken. While high-interfacial pressures might be reached at the particle/coating interface, it has been demonstrated that fresh and oxide free surfaces at these two surfaces are needed to ensure bonding. Therefore, for the hard-on-soft material combination, unless high coating temperatures promote enough coating deformation for particle embedment, increasing the coating temperature can lead to lower DE values. This hypothesis was experimentally observed because the DE of the IHCS – HE coating decreased by 50% in comparison to the CS – He sample.

In Figure 10 b), the "Type I" region is characterized by relatively low average particle velocities, as in this work. This region predicts an increase in the densification level when the coating temperature is increased (blue curve) in comparison to the CS process (red curve). In this zone, the impingement effect is maximized by dissimilar hardness of the coating and the particles. As a result, deformation on the coating layers is enhanced closing the remaining pores. An analogous effect has been reported by adding secondary hard particles to a soft powder matrix. The material mixture results in an "in-situ shot-peening" effect that densifies the coating during the deposition process [22,83–85]. Promoting the impingement effect on the thermally softened coating layers by the hard particles is unquestionably beneficial as the porosities are reduced. However, for this particular powder material, the by-product of using this approach is the creation of a relatively dense coating with cracks between layers (Fig. 6 g)). The relatively dense coating presented in Fig. 6 g) is obtained due to the repetitive impingement of the relatively hard particles on the soft coating layers promoting coating deformation and closing the remaining pores. The micro-cracks are potentially caused by the quick heating caused by the IH system and rapid cooling due to heat exchange between the propellant gas during each nozzle pass over the coating surface. These conditions and In718 low thermal conductivity and relatively high thermal expansion coefficient promote tensile residual stresses that overcome the cohesion strength of the coating.

To illustrate the combined influence of the coating and particle impact temperatures on the consolidation behavior of In718, Fig. 10 c) and d) are used. The curves labeled as CS – CP – PP (black lines, CP stands for coating preheating) are shifted to the left from the CS process curve (red curve) because increasing the coating and particle impact temperature (thus softening them both) reduces the critical velocity [34,35,46,86]. In Fig. 10 c) the CS – CP – PP curve illustrates higher DE values in comparison to the CS curve (red line), as observed experimentally and presented in Table 6. This demonstrates that the material strength (hardness) plays an important role when the coating temperature is increased. In a previous work focused on the deposition of aluminum, the material hardness difference between the coating layers and the sprayed particles, as in this work, was not observed because aluminum is an extremely soft and ductile material [46]. However, for In718, increasing the particle impact temperature reduced the particle strength. In consequence, the hardness difference between the particles and the coating layers was reduced. This favored a similar deformation behavior leading to the creation of fresh and oxide free surfaces between coating/particles promoting bonding. Once the hardness difference was reduced between the coating layers and the particles, a reduction in the critical velocity was obtained demonstrating the benefit of increasing the coating temperature. In the current work, the impingement effect controlled the densification of the coating. Thus, any increase in DE must come at the expense of increasing the pores inside the coating, as presented in Fig. 10 d) for the "Type I" region. Experimentally, the porosity level of the CS – He and the IHCS – He – PP_1 samples remained similar for both samples as the values were less than 1%. The similar porosity values are attributed to the resolution of the the contrast imaging technique used to calculate the porosity values.

In the "Type II" region of Fig. 10 d), the black curve (CS – CP – PP) illustrates a continuous increase in the densification of the coating in comparison to the CS curve (red one). This portion of Fig. 10 d) shows the benefit of coupling the IH and the CS process because a higher coating quality (cohesion strength) in combination with higher deposition rates can be achieved. This portion of Fig. 10 d) was not explored in

this work, but based on the extensive mapping reported in [50] for pure aluminum and DE and porosity values reported in [46], the predicted trend can be validated.

The need to use higher coating and particle impact temperatures would suggest that there is no benefit in the use of reduced spray parameters because a similar coating to the IHCS – He – PP_1 (Fig 6 i)) could potentially have been achieved using high spray parameters. However, the added benefit of decoupling the coating temperature from the gas stagnation temperature and fully controlling the coating temperature results in an improvement in the mechanical properties [47]. It has been demonstrated that the adhesion, cohesion, and tensile strength can be tailored and greatly enhanced by independently increasing the coating temperature during the spray process [47,49]. Tailoring the coating mechanical properties using high spray parameters is impossible, because these properties are intrinsically tied to the spray parameters used for the coating fabrication. Additionally, having independent control of the coating and particle impact temperatures eliminated the persistent nozzle clogging issue that has been reported for the deposition of In718 powders [10,14,16,19].

4. Conclusions

The effect of both particle and coating temperatures on the deposition of In718 and the exploration of the effect of using reduced spray parameters were studied. To ensure proper characterization, these temperatures were decoupled from the gas stagnation temperature (and consequently from impact velocity).

The influence of the particle impact temperature on the coating quality (DE and porosity levels) was linked to the particle impact velocity. For relatively low particle impact velocities, as in this work, higher particle impact temperatures increase the DE while also increasing the coating porosity. This is due to the fact that particle impingement is the main consolidation mechanism under these conditions. For high particle impact velocities, higher particle impact temperatures increase the DE and reduce the coating porosity values as

the particles deform appropriately at impact, and this is enhanced with superior particle impact temperatures.

Independently of the particle impact temperature, and as opposed to previous results when pure aluminum was used as feedstock powder, the coating temperatures achieved in this work were not large enough to drastically reduce the critical velocity for deposition when nitrogen (and low spray parameters) was used. Higher coating temperatures than the ones achieved would be needed to significantly reduce the In718 critical velocity and promote particle embedment into the coating.

Helium was used as propellant gas at reduced spray parameters (stagnation gas pressure and temperature). In the one hand, it was shown that solely elevating the coating temperature has a negative impact on the CS process. Elevating the coating temperature results in particle impact energy mostly dissipated into the deformation of the softer coating, while the hard particles experience reduced deformation generating weak inter-particle bonding and the formation of internal cracks. On the other hand, a simultaneous increase in the particle impact and coating temperatures reduced the hardness difference between the powder and the coating as well as the powder critical velocity. This produced an increase in the DE and enhanced the inter-particle bonding with coating porosity levels within or below reported values using higher CS parameters than the ones used in this work. Superior cohesion was also obtained due to the higher coating temperatures.

5. Acknowledgements

The authors would like to thank Dr. Michel Nganbe for facilitating the use of the induction heating system used in this work for the production of the samples.

6. References

[1] Special Metals, Inconel 718 Properties, n.d. https://www.specialmetals.com/documents/technical-bulletins/inconel/inconel-alloy-718.pdf (accessed July 28, 2020).

[2] R.C. Reed, The Superalloys: Fundamentals and Applications, Cambridge University Press, Cambridge, 2006. https://doi.org/10.1017/CBO9780511541285.

[3] E. Akca, A. Gürsel, A Review on Superalloys and IN718 Nickel-Based INCONEL Superalloy, PEN. 3 (2015). https://doi.org/10.21533/pen.v3i1.43.

[4] T.M. Pollock, S. Tin, Nickel-Based Superalloys for Advanced Turbine Engines: Chemistry, Microstructure and Properties, Journal of Propulsion and Power. 22 (2006) 361–374. https://doi.org/10.2514/1.18239.

[5] C. Lyphout, P. Nylén, L. Östergren, Relationships Between Process Parameters, Microstructure, and Adhesion Strength of HVOF Sprayed IN718 Coatings, J Therm Spray Tech. 20 (2011) 76–82. https://doi.org/10.1007/s11666-010-9543-7.

[6] C. Lyphout, P. Nylen, L.G. Östergren, Adhesion Strength of HVOF Sprayed IN718 Coatings, J Therm Spray Tech. 21 (2012) 86–95. https://doi.org/10.1007/s11666-011-9689-y.

[7] C. Lyphout, A. Fasth, P. Nylen, Mechanical Property of HVOF Inconel 718 Coating for Aeronautic Repair, J Therm Spray Tech. 23 (2014) 380–388. https://doi.org/10.1007/s11666-013-0007-8.

[8] C.S. Ramesh, D.S. Devaraj, R. Keshavamurthy, B.R. Sridhar, Slurry erosive wear behaviour of thermally sprayed Inconel-718 coatings by APS process, Wear. 271 (2011) 1365–1371. https://doi.org/10.1016/j.wear.2011.01.057.

[9] Z. Zhang, D.H.L. Seng, M. Lin, S.L. Teo, T.L. Meng, C.J.J. Lee, Z.-Q. Zhang, T. Ba, J. Guo, K. Sundaravadivelu, P.K. Aw, J. Pan, Cold spray deposition of Inconel 718 in comparison with atmospheric plasma spray deposition, Applied Surface Science. 535 (2021) 147704. https://doi.org/10.1016/j.apsusc.2020.147704.

[10] L.I. Pérez-Andrade, F. Gärtner, M. Villa-Vidaller, T. Klassen, J. Muñoz-Saldaña, J.M. Alvarado-Orozco, Optimization of Inconel 718 thick deposits by cold spray processing and annealing, Surface and Coatings Technology. 378 (2019) 124997. https://doi.org/10.1016/j.surfcoat.2019.124997.

[11] W. Sun, A.W.Y. Tan, A. Bhowmik, I. Marinescu, X. Song, W. Zhai, F. Li, E. Liu, Deposition characteristics of cold sprayed Inconel 718 particles on Inconel 718 substrates with different surface conditions, Materials Science and Engineering: A. 720 (2018) 75–84. https://doi.org/10.1016/j.msea.2018.02.059.

[12] W. Sun, A. Bhowmik, A.W.-Y. Tan, R. Li, F. Xue, I. Marinescu, E. Liu, Improving microstructural and mechanical characteristics of cold-sprayed Inconel 718 deposits via local induction heat treatment, Journal of Alloys and Compounds. 797 (2019) 1268–1279. https://doi.org/10.1016/j.jallcom.2019.05.099.

[13] D. Levasseur, S. Yue, M. Brochu, Pressureless sintering of cold sprayed Inconel 718 deposit, Materials Science and Engineering: A. 556 (2012) 343–350. https://doi.org/10.1016/j.msea.2012.06.097.

[14] W. Wong, E. Irissou, P. Vo, M. Sone, F. Bernier, J.-G. Legoux, H. Fukanuma, S. Yue, Cold Spray Forming of Inconel 718, J Therm Spray Tech. 22 (2013) 413–421. https://doi.org/10.1007/s11666-012-9827-1.

[15] R. Singh, K.-H. Rauwald, E. Wessel, G. Mauer, S. Schruefer, A. Barth, S. Wilson, R. Vassen, Effects of substrate roughness and spray-angle on deposition behavior of cold-sprayed Inconel 718, Surface and Coatings Technology. 319 (2017) 249–259. https://doi.org/10.1016/j.surfcoat.2017.03.072.

[16] R. Singh, S. Schruefer, S. Wilson, J. Gibmeier, R. Vassen, Influence of coating thickness on residual stress and adhesion-strength of cold-sprayed Inconel 718 coatings, Surface and Coatings Technology. 350 (2018) 64–73. https://doi.org/10.1016/j.surfcoat.2018.06.080.

[17] S. Bagherifard, G. Roscioli, M.V. Zuccoli, M. Hadi, G. D'Elia, A.G. Demir, B. Previtali, J. Kondás, M. Guagliano, Cold Spray Deposition of Freestanding Inconel Samples and Comparative Analysis with Selective Laser Melting, J Therm Spray Tech. 26 (2017) 1517–1526. https://doi.org/10.1007/s11666-017-0572-3.

[18] R. Vaßen, J. Fiebig, T. Kalfhaus, J. Gibmeier, A. Kostka, S. Schrüfer, Correlation of Microstructure and Properties of Cold Gas Sprayed INCONEL 718 Coatings, J Therm Spray Tech. (2020). https://doi.org/10.1007/s11666-020-00988-w.

[19] W. Ma, Y. Xie, C. Chen, H. Fukanuma, J. Wang, Z. Ren, R. Huang, Microstructural and mechanical properties of high-performance Inconel 718 alloy by cold spraying, Journal of Alloys and Compounds. 792 (2019) 456–467. https://doi.org/10.1016/j.jallcom.2019.04.045.

[20] S.Y. Kim, V. Luzin, M.L. Sesso, J. Thornton, S. Gulizia, The Effect of Low Temperature Range Heat Treatment on the Residual Stress of Cold Gas Dynamic Sprayed Inconel 718 Coatings via Neutron Diffraction, J Therm Spray Tech. 29 (2020) 1477–1497. https://doi.org/10.1007/s11666-020-01080-z.

[21] L. Perez, J. Colburn, L.N. Brewer, M. Renfro, T. McKechnie, Cold Spray Deposition of Heat-Treated Inconel 718 Powders, in: F. Azarmi, X. Chen, J. Cizek, C. Cojocaru, B. Jodoin, H. Koivuluoto, Y.C. Lau, R. Fernandez, O. Ozdemir, H. Salimi Jazi, F. Toma (Eds.), Virtual, 2021: pp. 171–176. https://doi.org/10.31399/asm.cp.itsc2021p0171.

[22] X.-T. Luo, M.-L. Yao, N. Ma, M. Takahashi, C.-J. Li, Deposition behavior, microstructure and mechanical properties of an in-situ micro-forging assisted cold spray enabled additively manufactured Inconel 718 alloy, Materials & Design. 155 (2018) 384–395. https://doi.org/10.1016/j.matdes.2018.06.024.

[23] M. Kazasidis, S. Yin, J. Cassidy, T. Volkov-Husović, M. Vlahović, S. Martinović, E. Kyriakopoulou, R. Lupoi, Microstructure and cavitation erosion performance of nickel-Inconel 718 composite coatings produced with cold spray, Surface and Coatings Technology. 382 (2020) 125195. https://doi.org/10.1016/j.surfcoat.2019.125195.

[24] W. Sun, A. Bhowmik, A.W.Y. Tan, F. Xue, I. Marinescu, F. Li, E. Liu, Strategy of incorporating Ni-based braze alloy in cold sprayed Inconel 718 coating, Surface and Coatings Technology. 358 (2019) 1006–1012. https://doi.org/10.1016/j.surfcoat.2018.12.050.

[25] W. Sun, A.W.-Y. Tan, D.J.Y. King, N.W. Khun, A. Bhowmik, I. Marinescu, E. Liu, Tribological behavior of cold sprayed Inconel 718 coatings at room and elevated temperatures, Surface and Coatings Technology. 385 (2020) 125386. https://doi.org/10.1016/j.surfcoat.2020.125386.

[26] G. Mauer, R. Singh, K.-H. Rauwald, S. Schrüfer, S. Wilson, R. Vaßen, Diagnostics of Cold-Sprayed Particle Velocities Approaching Critical Deposition Conditions, J Therm Spray Tech. 26 (2017) 1423–1433. https://doi.org/10.1007/s11666-017-0596-8.

[27] J. Villafuerte, ed., Modern cold spray: materials, process, and applications, Springer Verlag, Cham, 2015.

[28] H. Assadi, F. Gärtner, T. Stoltenhoff, H. Kreye, Bonding mechanism in cold gas spraying, Acta Materialia. 51 (2003) 4379–4394. https://doi.org/10.1016/S1359-6454(03)00274-X.

[29] S. Rahmati, B. Jodoin, Physically Based Finite Element Modeling Method to Predict Metallic Bonding in Cold Spray, J Therm Spray Tech. 29 (2020) 611–629. https://doi.org/10.1007/s11666-020-01000-1.

[30] S. Rahmati, R.G.A. Veiga, A. Zúñiga, B. Jodoin, A Numerical Approach to Study the Oxide Layer Effect on Adhesion in Cold Spray, J Therm Spray Tech. (2021). https://doi.org/10.1007/s11666-021-01245-4.

[31] D.L. Gilmore, R.C. Dykhuizen, R.A. Neiser, T.J. Roemer, M.F. Smith, Particle Velocity and Deposition Efficiency in the Cold Spray Process, Journal of Thermal Spray Technology. 8 (1999) 576–582. https://doi.org/10.1361/105996399770350278.

[32] R.C. Dykhuizen, M.F. Smith, Gas Dynamic Principles of Cold Spray, Journal of Thermal Spray Technology. 7 (1998) 205–212. https://doi.org/10.1361/105996398770350945.

[33] S. Yin, X. Suo, H. Liao, Z. Guo, X. Wang, Significant influence of carrier gas temperature during the cold spray process, Surface Engineering. 30 (2014) 443–450. https://doi.org/10.1179/1743294414Y.0000000276.

[34] T. Schmidt, F. Gaertner, H. Kreye, New Developments in Cold Spray Based on Higher Gas and Particle Temperatures, Journal of Thermal Spray Technology. 15 (2006) 488–494. https://doi.org/10.1361/105996306X147144.

[35] A. Nastic, B. Jodoin, D. Poirier, J.-G. Legoux, Particle temperature effect in cold spray: A study of soft particle deposition on hard substrate, Surface and Coatings Technology. 406 (2021) 126735. https://doi.org/10.1016/j.surfcoat.2020.126735.

[36] H. Assadi, T. Schmidt, H. Richter, J.-O. Kliemann, K. Binder, F. Gärtner, T. Klassen, H. Kreye, On Parameter Selection in Cold Spraying, J Therm Spray Tech. 20 (2011) 1161–1176. https://doi.org/10.1007/s11666-011-9662-9.

[37] T. Schmidt, F. Gärtner, H. Assadi, H. Kreye, Development of a generalized parameter window for cold spray deposition, Acta Materialia. 54 (2006) 729–742. https://doi.org/10.1016/j.actamat.2005.10.005.

[38] Y. Hao, J. Wang, X. Cui, J. Wu, T. Li, T. Xiong, Microstructure Characteristics and Mechanical Properties of Al-12Si Coatings on AZ31 Magnesium Alloy Produced by Cold Spray Technique, J Therm Spray Tech. 25 (2016) 1020–1028. https://doi.org/10.1007/s11666-016-0409-5.

[39] D.L. Guo, D. MacDonald, L. Zhao, B. Jodoin, Cold Spray MCrAlY Coatings on Single-Crystal Superalloy Using Nitrogen: Properties and Economics, J Therm Spray Tech. (2020). https://doi.org/10.1007/s11666-020-01058-x.

[40] R. Jenkins, S. Yin, B. Aldwell, M. Meyer, R. Lupoi, New insights into the in-process densification mechanism of cold spray Al coatings: Low deposition efficiency induced densification, Journal of Materials Science & Technology. 35 (2019) 427–431. https://doi.org/10.1016/j.jmst.2018.09.045.

[41] M. Bray, A. Cockburn, W. O'Neill, The Laser-assisted Cold Spray process and deposit characterisation, Surface and Coatings Technology. 203 (2009) 2851–2857. https://doi.org/10.1016/j.surfcoat.2009.02.135.

[42] J. Yao, L. Yang, B. Li, Z. Li, Beneficial effects of laser irradiation on the deposition process of diamond/Ni60 composite coating with cold spray, Applied Surface Science. 330 (2015) 300–308. https://doi.org/10.1016/j.apsusc.2015.01.029.

[43] D.J. Barton, V.S. Bhattiprolu, G.B. Thompson, L.N. Brewer, Laser assisted cold spray of AISI 4340 steel, Surface and Coatings Technology. 400 (2020) 126218. https://doi.org/10.1016/j.surfcoat.2020.126218.

[44] D.J. Barton, V.S. Bhattiprolu, B.C. Hornbuckle, C.M. Batali, K.A. Darling, G.B. Thompson, L.N. Brewer, Residual Stress Generation in Laser-Assisted Cold Spray Deposition of Oxide Dispersion Strengthened Fe91Ni8Zr1, J Therm Spray Tech. 29 (2020) 1550–1563. https://doi.org/10.1007/s11666-020-01079-6.

[45] D.J. Barton, B.C. Hornbuckle, K.A. Darling, L.N. Brewer, G.B. Thompson, Influence of surface temperature in the laser assisted cold spray deposition of sequential oxide dispersion strengthened layers: Microstructure and hardness, Materials Science and Engineering: A. 811 (2021) 141027. https://doi.org/10.1016/j.msea.2021.141027.

[46] R. Ortiz-Fernandez, B. Jodoin, Hybrid Additive Manufacturing Technology: Induction Heating Cold Spray—Part I: Fundamentals of Deposition Process, J Therm Spray Tech. 29 (2020) 684–699. https://doi.org/10.1007/s11666-020-01005-w.

[47] R. Ortiz-Fernandez, B. Jodoin, Hybrid Additive Manufacturing Technology: Induction Heating Cold Spray—Part II: Coating Mechanical Properties, J Therm Spray Tech. 29 (2020) 700–713. https://doi.org/10.1007/s11666-020-01006-9.

[48] M. Razavipour, J.-G. Legoux, D. Poirier, B. Guerreiro, J.D. Giallonardo, B. Jodoin, Artificial Neural Networks Approach for Hardness Prediction of Copper Cold Spray Laser Heat Treated Coatings, J Therm Spray Tech. 31 (2022) 525–544. https://doi.org/10.1007/s11666-021-01311-x.

[49] R. Ortiz-Fernandez, S. Imbriglio, R. Chromik, B. Jodoin, The Role of Substrate Preheating on the Adhesion Strength of Cold-Sprayed Soft Particles on Hard Substrates, J Therm Spray Tech. (2021). https://doi.org/10.1007/s11666-020-01148-w.

[50] D. MacDonald, S. Rahmati, B. Jodoin, W. Birtch, An Economical Approach to Cold Spray Using In-line Nitrogen–Helium Blending, J Therm Spray Tech. 28 (2019) 161–173. https://doi.org/10.1007/s11666-018-0813-0.

[51] R. Lupoi, W. O'Neill, Powder stream characteristics in cold spray nozzles, Surface and Coatings Technology. 206 (2011) 1069–1076. https://doi.org/10.1016/j.surfcoat.2011.07.061.

[52] B. Jodoin, Cold Spray Nozzle Mach Number Limitation, Journal of Thermal Spray Technology. 11 (2002) 496–507. https://doi.org/10.1361/105996302770348628.

[53] S. Yin, M. Meyer, W. Li, H. Liao, R. Lupoi, Gas Flow, Particle Acceleration, and Heat Transfer in Cold Spray: A review, J Therm Spray Tech. 25 (2016) 874–896. https://doi.org/10.1007/s11666-016-0406-8.

[54] T.L. Bergman, A. Lavine, F.P. Incropera, Fundamentals of heat and mass transfer., 2017. https://ebookcentral.proquest.com/lib/qut/detail.action?docID=5106220 (accessed September 20, 2021).

[55] Y.A. Çengel, M.A. Boles, Thermodynamics: an engineering approach, Seventh edition, McGraw-Hill, New York, NY, 2011.

[56] James Braun, Jorge Sousa, Guillermo Paniagua, Numerical Assessment of the Convective Heat Transfer in Rotating Detonation Combustors Using a Reduced-Order Model, Applied Sciences. 8 (2018).

[57] P. Liebersbach, A. Foelsche, V.K. Champagne, M. Siopis, A. Nardi, D.P. Schmidt, CFD Simulations of Feeder Tube Pressure Oscillations and Prediction of Clogging in Cold Spray Nozzles, J Therm Spray Tech. 29 (2020) 400–412. https://doi.org/10.1007/s11666-020-00992-0.

[58] H. Tabbara, S. Gu, D.G. McCartney, T.S. Price, P.H. Shipway, Study on Process Optimization of Cold Gas Spraying, J Therm Spray Tech. 20 (2011) 608–620. https://doi.org/10.1007/s11666-010-9564-2.

[59] S. Yin, Q. Liu, H. Liao, X. Wang, Effect of injection pressure on particle acceleration, dispersion and deposition in cold spray, Computational Materials Science. 90 (2014) 7–15. https://doi.org/10.1016/j.commatsci.2014.03.055.

[60] O.C. Ozdemir, C.A. Widener, D. Helfritch, F. Delfanian, Estimating the Effect of Helium and Nitrogen Mixing on Deposition Efficiency in Cold Spray, J Therm Spray Tech. 25 (2016) 660–671. https://doi.org/10.1007/s11666-016-0394-8.

[61] R. Huang, H. Fukanuma, Study of the Influence of Particle Velocity on Adhesive Strength of Cold Spray Deposits, J Therm Spray Tech. 21 (2012) 541–549. https://doi.org/10.1007/s11666-011-9707-0.

[62] X. Suo, S. Yin, M.-P. Planche, T. Liu, H. Liao, Strong effect of carrier gas species on particle velocity during cold spray processes, Surface and Coatings Technology. 268 (2015) 90–93. https://doi.org/10.1016/j.surfcoat.2014.04.039.

[63] M. Faizan-Ur-Rab, S.H. Zahiri, S.H. Masood, M. Jahedi, R. Nagarajah, PIV Validation of 3D Multicomponent Model for Cold Spray Within Nitrogen and Helium Supersonic Flow Field, J Therm Spray Tech. 26 (2017) 941–957. https://doi.org/10.1007/s11666-017-0567-0.

[64] W. Wong, E. Irissou, A.N. Ryabinin, J.-G. Legoux, S. Yue, Influence of Helium and Nitrogen Gases on the Properties of Cold Gas Dynamic Sprayed Pure Titanium Coatings, J Therm Spray Tech. 20 (2011) 213–226. https://doi.org/10.1007/s11666-010-9568-y.

[65] D. MacDonald, R. Fernández, F. Delloro, B. Jodoin, Cold Spraying of Armstrong Process Titanium Powder for Additive Manufacturing, J Therm Spray Tech. 26 (2017) 598–609. https://doi.org/10.1007/s11666-016-0489-2.

[66] N. Fan, J. Cizek, C. Huang, X. Xie, Z. Chlup, R. Jenkins, R. Lupoi, S. Yin, A new strategy for strengthening additively manufactured cold spray deposits through in-process densification, Additive Manufacturing. (2020) 101626. https://doi.org/10.1016/j.addma.2020.101626.

[67] S.V. Klinkov, V.F. Kosarev, M. Rein, Cold spray deposition: Significance of particle impact phenomena, Aerospace Science and Technology. 9 (2005) 582–591. https://doi.org/10.1016/j.ast.2005.03.005.

[68] A. Sova, S. Grigoriev, A. Kochetkova, I. Smurov, Influence of powder injection point position on efficiency of powder preheating in cold spray: Numerical study, Surface and Coatings Technology. 242 (2014) 226–231. https://doi.org/10.1016/j.surfcoat.2013.10.078.

[69] C.-J. Li, W.-Y. Li, H. Liao, Examination of the Critical Velocity for Deposition of Particles in Cold Spraying, Journal of Thermal Spray Technology. 15 (2006) 212–222. https://doi.org/10.1361/105996306X108093.

[70] L. Venkatesh, N.M. Chavan, G. Sundararajan, The Influence of Powder Particle Velocity and Microstructure on the Properties of Cold Sprayed Copper Coatings, J Therm Spray Tech. 20 (2011) 1009–1021. https://doi.org/10.1007/s11666-011-9614-4.

[71] X.-T. Luo, Y.-J. Li, C.-X. Li, G.-J. Yang, C.-J. Li, Effect of spray conditions on deposition behavior and microstructure of cold sprayed Ni coatings sprayed with a porous electrolytic Ni powder, Surface and Coatings Technology. 289 (2016) 85–93. https://doi.org/10.1016/j.surfcoat.2016.01.058.

[72] Q. Wang, N. Birbilis, M.-X. Zhang, Process optimisation of cold spray Al coating on AZ91 alloy, Surface Engineering. 30 (2014) 323–328. https://doi.org/10.1179/1743294413Y.0000000224.

[73] X. Meng, J. Zhang, J. Zhao, Y. Liang, Y. Zhang, Influence of Gas Temperature on Microstructure and Properties of Cold Spray 304SS Coating, Journal of Materials Science & Technology. 27 (2011) 809–815. https://doi.org/10.1016/S1005-0302(11)60147-3.

[74] J. Ajaja, D. Goldbaum, R.R. Chromik, Characterization of Ti cold spray coatings by indentation methods, Acta Astronautica. 69 (2011) 923–928. https://doi.org/10.1016/j.actaastro.2011.06.012.

[75] P. Sudharshan Phani, D. Srinivasa Rao, S.V. Joshi, G. Sundararajan, Effect of Process Parameters and Heat Treatments on Properties of Cold Sprayed Copper Coatings, J Therm Spray Tech. 16 (2007) 425–434. https://doi.org/10.1007/s11666-007-9048-1.

[76] D. Goldbaum, J. Ajaja, R.R. Chromik, W. Wong, S. Yue, E. Irissou, J.-G. Legoux, Mechanical behavior of Ti cold spray coatings determined by a multi-scale indentation method, Materials Science and Engineering: A. 530 (2011) 253–265. https://doi.org/10.1016/j.msea.2011.09.083.

[77] W. Wong, P. Vo, E. Irissou, A.N. Ryabinin, J.-G. Legoux, S. Yue, Effect of Particle Morphology and Size Distribution on Cold-Sprayed Pure Titanium Coatings, J Therm Spray Tech. 22 (2013) 1140–1153. https://doi.org/10.1007/s11666-013-9951-6.

[78] G. Bae, Y. Xiong, S. Kumar, K. Kang, C. Lee, General aspects of interface bonding in kinetic sprayed coatings, Acta Materialia. 56 (2008) 4858–4868. https://doi.org/10.1016/j.actamat.2008.06.003.

[79] A. Fardan, C.C. Berndt, R. Ahmed, Numerical modelling of particle impact and residual stresses in cold sprayed coatings: A review, Surface and Coatings Technology. 409 (2021) 126835. https://doi.org/10.1016/j.surfcoat.2021.126835.

[80] W. Li, K. Yang, D. Zhang, X. Zhou, Residual Stress Analysis of Cold-Sprayed Copper Coatings by Numerical Simulation, J Therm Spray Tech. 25 (2016) 131–142. https://doi.org/10.1007/s11666-015-0308-1.

[81] A.S.M. Ang, C.C. Berndt, A review of testing methods for thermal spray coatings, International Materials Reviews. 59 (2014) 179–223. https://doi.org/10.1179/1743280414Y.0000000029.

[82] S. Kuroda, T.W. Clyne, The quenching stress in thermally sprayed coatings, Thin Solid Films. 200 (1991) 49–66. https://doi.org/10.1016/0040-6090(91)90029-W.

[83] Y.-K. Wei, X.-T. Luo, Y. Ge, X. Chu, G.-S. Huang, C.-J. Li, Deposition of fully dense Al-based coatings via in-situ micro-forging assisted cold spray for excellent corrosion protection of AZ31B magnesium alloy, Journal of Alloys and Compounds. 806 (2019) 1116–1126. https://doi.org/10.1016/j.jallcom.2019.07.279.

[84] R. Fernandez, B. Jodoin, Cold Spray Aluminum–Alumina Cermet Coatings: Effect of Alumina Content, J Therm Spray Tech. 27 (2018) 603–623. https://doi.org/10.1007/s11666-018-0702-6.

[85] S.-L. Fu, C.-X. Li, Y.-K. Wei, X.-T. Luo, G.-J. Yang, C.-J. Li, J.-L. Li, Novel Method of Aluminum to Copper Bonding by Cold Spray, J Therm Spray Tech. 27 (2018) 624–640. https://doi.org/10.1007/s11666-018-0707-1.

[86] Y. Xie, M.-P. Planche, R. Raoelison, P. Hervé, X. Suo, P. He, H. Liao, Investigation on the influence of particle preheating temperature on bonding of cold-sprayed nickel coatings, Surface and Coatings Technology. 318 (2017) 99–105. https://doi.org/10.1016/j.surfcoat.2016.09.037.

Chapter 6 - Conclusions and Future work

6.1 Conclusions

This work focused on establishing how the initial substrate, coating, and particle impact temperatures affect the CS process performance by trying to decouple these three variables from the general spray parameters, in particular the gas stagnation temperature. To systematically investigate the effect of these temperatures on the CS deposition process, the following objectives were set:

1. Evaluate the role of the initial substrate temperature on the CS process.
2. Characterize the influence of the coating temperature on the CS process.
3. Assess the importance of the particle impact temperature on the CS process.
4. Enhance the CS process performance based on the findings of the previous objectives.

The role of the initial substrate temperature on the CS deposition process was evaluated using the soft-on-hard material combination. A few small particles bonded with the substrate when the initial substrate temperature was set at room temperature, but as the substrate temperature increased, the number and the size of deposited particles also increased. It was concluded that critical velocity was substrate-temperature dependent at the single-particle level. Higher initial substrate temperatures promoted the breakage of the substrate native-oxide layer. This facilitated the bonding process as intimate contact between particles and the substrate was achieved. The induction heating failed in retaining the initial substrate surface temperature, and thus, independently of the initial substrate temperature, the latter was always brought to the "steady-state" temperature. As the initial substrate temperature increased, minimal changes in DE were observed, and the coatings experienced no significant changes in micro-hardness values. However, a significant increase in the adhesion strength of coatings was measured. These results

confirm that the influence of higher substrate temperatures was limited to the deposition of the first layer. The FE model results discarded any significant mechanical contributions to the overall adhesion strength of the coating, and thus, the higher adhesion strength values were attributed to the improved metallic bond formation at the interface.

The influence of the coating temperature on the CS deposition process was investigated using the soft-on-hard and the hard-on-hard material combinations. Firstly, an FE analysis helped predict the eddy current density distribution experienced by pure aluminum and In718 100-μm coatings. The predicted values for In718 coatings were significantly lower in comparison to the values exhibited by pure aluminum coatings. This was attributed to the electrical conductivity for aluminum which is significantly larger in comparison to In718. The influence of the AC source and frequency values on the eddy current density distribution was investigated. The AC source had a more prominent effect over the frequency values. The coating surface time-temperature history demonstrated that the induction heating failed in maintaining a constant coating surface temperature during the spray time, but as the nozzle left the coating top surface, the coating was quickly heat up between passes promoting significant thermal softening on the already deposited layers. For the deposition of aluminum-on-Ti64, significant increases in the DE (from 50 to 75%) were observed as the coating temperature increased, but for the deposition of In718-on-Ti64, the coating temperature caused the opposite effect. A dissimilar deformation behavior between the thermally softened coating layers and the hard particles caused this different result. The aluminum coatings experienced a 20% decrease in coating micro-hardness values, and a significant increase in adhesion strength as the coating temperature increased. These results were explained by the development of an in-situ heat-treatment process that strengthened the bonds.

The importance of the particle impact temperature was assessed using the hard-on-hard material combination. The initial particle temperature was decoupled from the gas

stagnation temperature by feeding the powder in the diverging section of the nozzle. The impact temperature was estimated using a CFD model. The powder particles experienced a cooling effect once the powder was fed into the nozzle as heat was exchanged with the gas. The cooling effect must be considered when the powder is preheated prior its injection inside the nozzle as the initial temperature and the impact temperature will be different. The influence of the particle impact temperature on the coating quality was linked to the particle impact velocity.

Based on the previous findings, the CS process performance was optimized using both material combinations as feedstock materials. For the deposition of aluminum-on-Ti64 substrates, combining the coating and substrate temperatures increased the DE from 50 to almost 100%. The coating micro-hardness by 20% and the adhesion strength was raised from 0 to at least 70 MPa. It was also shown that superior adhesion could be achieved without the need of high initial substrate temperatures. Finally, combining these two temperatures increased the ductility in comparison to the baseline coupons, but the brittle behavior was still present. The superior coating mechanical properties were attributed to the development of an *in-situ* heat-treatment process. For the deposition of In718-on-Ti64 substrates, combining the coating and particle impact temperatures helped reduce the hardness dissimilarity found between the hard particles and the thermally softened coating layers resulting in a reduction in the critical velocity. Because the impingement effect was the densification mechanism due to the relatively low particle impact velocities, the repetitive impact of the relatively hard particles on the soft coating layers densified the coating.

6.2 Future Work

Several studies that further expand the understanding of the role of the initial substrate, coating and particle impact temperatures on the CS process can potentially be carried out. In the following list, some potential studies are proposed:

1. The influence of the initial substrate temperature on the deposition process for the soft-on-hard material combination was investigated, but to generalize the results, other combinations should also be tested.
2. It was proposed that higher substrate temperatures promoted the breakage of the native-oxide layer on the Ti64 substrate increasing the bonded area with the particles. However, experimental evidence using high resolution microscopy tools was not provided. Therefore, TEM analysis could be conducted at the particle/substrate interface to further understand the bonding process.
3. As a first approximation, an electromagnetic FE model was used to predict the eddy current density distribution within the coating. However, the current model does not take into account material phases, grain size, and defects. Therefore, an FE model in which these variables are included could be developed.
4. A comprehensive model in which the gas flow, the eddy current density distribution, and the nozzle pattern over the coating could be developed to further understand the role of the coating temperature on the deposition process.
5. To develop a more effective heating pattern on the coating, different coil shapes could potentially be modeled, developed and experimentally tested. The as-sprayed coating properties could also be evaluated to quantify the effectiveness of the heating pattern.
6. To explain the superior cohesion and adhesion of the coatings, it was hypothesized that high-resistivity bridges were created. Experimental evidence using high resolution microscopy tools, such as TEM or EBSD, could be used to help support this theory.

7. The micron-sized powders are only heated up by the eddy currents once they are consolidated in the form of a coating. Therefore, a potential research project could be focused on investigating if a minimum thickness is needed to have eddy currents within the coating.
8. Further investigation on the influence of the coating temperature for other materials. This will help fully characterize the benefits and potential disadvantages of increasing the coating temperature during the CS process.
9. Two different consolidation mechanisms, as a function of the particle and coating impact temperatures, were proposed in the last peer-reviewed paper. Extensive mapping of these could be done to further understand and validate the different consolidation mechanisms on the CS process.

References

[1] J.R. Davis, ed., Handbook of Thermal Spray Technology, ASM International, United States, 2004.

[2] A.N. Papyrin, ed., Cold spray technology, Elsevier, Amsterdam ; London, 2007.

[3] A. Moridi, S.M. Hassani-Gangaraj, M. Guagliano, M. Dao, Cold Spray Coating: Review of Material Systems and Future Perspectives, Surface Engineering. 30 (2014) 369–395. https://doi.org/10.1179/1743294414y.0000000270.

[4] J. Villafuerte, ed., Modern Cold Spray: Materials, Process, and Applications, Springer International Publishing, Switzerland, 2015. https://doi.org/10.1007/978-3-319-16772-5.

[5] A.N. Paryrin, ed., Cold Spray Technology, Elsevier, United Kingdom, 2007.

[6] S.H. Thurston, Method of impacting one metal upon other, 701, n.d.

[7] C.F. Rocheville, Device for treating the surface of a workpiece., 100, n.d.

[8] R. Fernandez, B. Jodoin, Effect of Particle Morphology on Cold Spray Deposition of Chromium Carbide-Nickel Chromium Cermet Powders, J Therm Spray Tech. 26 (2017) 1356–1380. https://doi.org/10.1007/s11666-017-0580-3.

[9] G. Celeste, V. Guipont, D. Missoum-Benziane, Investigation of Agglomerated and Porous Ceramic Powders Suitable for Cold Spray, in: F. Azarmi, X. Chen, J. Cizek, C. Cojocaru, B. Jodoin, H. Koivuluoto, Y.C. Lau, R. Fernandez, O. Ozdemir, H. Salimi Jazi, F. Toma (Eds.), Virtual, 2021: pp. 139–146. https://doi.org/10.31399/asm.cp.itsc2021p0139.

[10] H. Hajipour, A. Abdollah-zadeh, H. Assadi, E. Taheri-Nassaj, H. Jahed, Effect of Feedstock Powder Morphology on Cold-Sprayed Titanium Dioxide Coatings, J Therm Spray Tech. 27 (2018) 1542–1550. https://doi.org/10.1007/s11666-018-0782-3.

[11] W. Sun, A.W.Y. Tan, A. Bhowmik, I. Marinescu, X. Song, W. Zhai, F. Li, E. Liu, Deposition characteristics of cold sprayed Inconel 718 particles on Inconel 718 substrates with different surface conditions, Materials Science and Engineering: A. 720 (2018) 75–84. https://doi.org/10.1016/j.msea.2018.02.059.

[12] S. Rahmati, B. Jodoin, Physically Based Finite Element Modeling Method to Predict Metallic Bonding in Cold Spray, J Therm Spray Tech. 29 (2020) 611–629. https://doi.org/10.1007/s11666-020-01000-1.

[13] D. MacDonald, S. Rahmati, B. Jodoin, W. Birtch, An Economical Approach to Cold Spray Using In-line Nitrogen–Helium Blending, J Therm Spray Tech. 28 (2019) 161–173. https://doi.org/10.1007/s11666-018-0813-0.

[14] H. Assadi, T. Schmidt, H. Richter, J.-O. Kliemann, K. Binder, F. Gärtner, T. Klassen, H. Kreye, On Parameter Selection in Cold Spraying, J Therm Spray Tech. 20 (2011) 1161–1176. https://doi.org/10.1007/s11666-011-9662-9.

[15] T. Schmidt, F. Gärtner, H. Assadi, H. Kreye, Development of a generalized parameter window for cold spray deposition, Acta Materialia. 54 (2006) 729–742. https://doi.org/10.1016/j.actamat.2005.10.005.

[16] T. Schmidt, F. Gaertner, H. Kreye, New Developments in Cold Spray Based on Higher Gas and Particle Temperatures, Journal of Thermal Spray Technology. 15 (2006) 488–494. https://doi.org/10.1361/105996306X147144.

[17] A. Vardelle, C. Moreau, J. Akedo, H. Ashrafizadeh, C.C. Berndt, J.O. Berghaus, M. Boulos, J. Brogan, A.C. Bourtsalas, A. Dolatabadi, M. Dorfman, T.J. Eden, P. Fauchais, G. Fisher, F. Gaertner, M. Gindrat, R. Henne, M. Hyland, E. Irissou, E.H. Jordan, K.A. Khor, A. Killinger, Y.-C. Lau, C.-J. Li, L. Li, J. Longtin, N. Markocsan, P.J. Masset, J. Matejicek, G. Mauer, A. McDonald, J. Mostaghimi, S. Sampath, G. Schiller, K. Shinoda, M.F. Smith, A.A. Syed, N.J. Themelis, F.-L. Toma, J.P. Trelles, R. Vassen, P. Vuoristo, The 2016 Thermal Spray Roadmap, J Therm Spray Tech. 25 (2016) 1376–1440. https://doi.org/10.1007/s11666-016-0473-x.

[18] A. Nastic, B. Jodoin, D. Poirier, J.-G. Legoux, Particle temperature effect in cold spray: A study of soft particle deposition on hard substrate, Surface and Coatings Technology. 406 (2021) 126735. https://doi.org/10.1016/j.surfcoat.2020.126735.

[19] Y.A. Çengel, M.A. Boles, Thermodynamics: an engineering approach, Eighth edition, McGraw-Hill Education, New York, 2015.

[20] L. Ajdelsztajn, A. Zúñiga, B. Jodoin, E.J. Lavernia, Cold-Spray Processing of a Nanocrystalline Al-Cu-Mg-Fe-Ni Alloy with Sc, Journal of Thermal Spray Technology. 15 (2006) 184–190. https://doi.org/10.1361/105996306X107995.

[21] T. Stoltenhoff, H. Kreye, H.J. Richter, An Analysis of the Cold Spray Process and Its Coatings, Journal of Thermal Spray Technology. 11 (2002) 542–550. https://doi.org/10.1361/105996302770348682.

[22] H. Assadi, F. Gärtner, T. Stoltenhoff, H. Kreye, Bonding mechanism in cold gas spraying, Acta Materialia. 51 (2003) 4379–4394. https://doi.org/10.1016/S1359-6454(03)00274-X.

[23] M. Grujicic, C.L. Zhao, W.S. DeRosset, D. Helfritch, Adiabatic shear instability based mechanism for particles/substrate bonding in the cold-gas dynamic-spray process, Materials & Design. 25 (2004) 681–688. https://doi.org/10.1016/j.matdes.2004.03.008.

[24] F. Gärtner, T. Stoltenhoff, T. Schmidt, H. Kreye, The Cold Spray Process and Its Potential for Industrial Applications, Journal of Thermal Spray Technology. 15 (2006) 223–232. https://doi.org/10.1361/105996306X108110.

[25] S. Rahmati, R.G.A. Veiga, B. Jodoin, A. Zúñiga, Crystal orientation and grain boundary effects on plastic deformation of FCC particles under high velocity impacts, Materialia. 15 (2021) 101004. https://doi.org/10.1016/j.mtla.2021.101004.

[26] W. Wong, P. Vo, E. Irissou, A.N. Ryabinin, J.-G. Legoux, S. Yue, Effect of Particle Morphology and Size Distribution on Cold-Sprayed Pure Titanium Coatings, J Therm Spray Tech. 22 (2013) 1140–1153. https://doi.org/10.1007/s11666-013-9951-6.

[27] T.H. Van Steenkiste, J.R. Smith, R.E. Teets, J.J. Moleski, D.W. Gorkiewicz, R.P. Tison, D.R. Marantz, K.A. Kowalsky, W.L. Riggs, P.H. Zajchowski, B. Pilsner, R.C. McCune, K.J. Barnett, Kinetic spray coatings, Surface and Coatings Technology. 111 (1999) 62–71. https://doi.org/10.1016/S0257-8972(98)00709-9.

[28] D.L. Gilmore, R.C. Dykhuizen, R.A. Neiser, T.J. Roemer, M.F. Smith, Particle Velocity and Deposition Efficiency in the Cold Spray Process, Journal of Thermal Spray Technology. 8 (1999) 576–582. https://doi.org/10.1361/105996399770350278.

[29] M. Grujicic, J.R. Saylor, D.E. Beasley, W.S. DeRosset, D. Helfritch, Computational analysis of the interfacial bonding between feed-powder particles and the substrate in the cold-gas dynamic-spray process, Applied Surface Science. 219 (2003) 211–227. https://doi.org/10.1016/S0169-4332(03)00643-3.

[30] R. Ortiz-Fernandez, B. Jodoin, Hybrid Additive Manufacturing Technology: Induction Heating Cold Spray—Part I: Fundamentals of Deposition Process, J Therm Spray Tech. 29 (2020) 684–699. https://doi.org/10.1007/s11666-020-01005-w.

[31] Y. Watanabe, C. Yoshida, K. Atsumi, M. Yamada, M. Fukumoto, Influence of Substrate Temperature on Adhesion Strength of Cold-Sprayed Coatings, J Therm Spray Tech. (2014). https://doi.org/10.1007/s11666-014-0165-3.

[32] T.H. Van Steenkiste, J.R. Smith, R.E. Teets, Aluminum coatings via kinetic spray with relatively large powder particles, Surface and Coatings Technology. 154 (2002) 237–252. https://doi.org/10.1016/S0257-8972(02)00018-X.

[33] C.-J. Li, W.-Y. Li, H. Liao, Examination of the Critical Velocity for Deposition of Particles in Cold Spraying, Journal of Thermal Spray Technology. 15 (2006) 212–222. https://doi.org/10.1361/105996306X108093.

[34] M. Razavipour, S. Rahmati, A. Zúñiga, D. Criado, B. Jodoin, Bonding Mechanisms in Cold Spray: Influence of Surface Oxidation During Powder Storage, J Therm Spray Tech. (2020). https://doi.org/10.1007/s11666-020-01123-5.

[35] L.M. Pereira, S. Rahmati, A. Zúñiga, B. Jodoin, R.G.A. Veiga, Atomistic study of metallurgical bonding upon the high velocity impact of fcc core-shell particles, Computational Materials Science. 186 (2021) 110045. https://doi.org/10.1016/j.commatsci.2020.110045.

[36] A. Nastic, M. Vijay, A. Tieu, S. Rahmati, B. Jodoin, Experimental and Numerical Study of the Influence of Substrate Surface Preparation on Adhesion Mechanisms of Aluminum Cold Spray Coatings on 300M Steel Substrates, J Therm Spray Tech. 26 (2017) 1461–1483. https://doi.org/10.1007/s11666-017-0602-1.

[37] T. Hussain, D.G. McCartney, P.H. Shipway, D. Zhang, Bonding Mechanisms in Cold Spraying: The Contributions of Metallurgical and Mechanical Components, J Therm Spray Tech. 18 (2009) 364–379. https://doi.org/10.1007/s11666-009-9298-1.

[38] R. Fernández, D. MacDonald, A. Nastić, B. Jodoin, A. Tieu, M. Vijay, Enhancement and Prediction of Adhesion Strength of Copper Cold Spray Coatings on Steel Substrates for Nuclear Fuel Repository, J Therm Spray Tech. 25 (2016) 1577–1587. https://doi.org/10.1007/s11666-016-0467-8.

[39] T. Samson, D. MacDonald, R. Fernández, B. Jodoin, Effect of Pulsed Waterjet Surface Preparation on the Adhesion Strength of Cold Gas Dynamic Sprayed Aluminum Coatings, J Therm Spray Tech. 24 (2015) 984–993. https://doi.org/10.1007/s11666-015-0261-z.

[40] S. Yin, J. Cizek, J. Cupera, M. Hassani, X. Luo, R. Jenkins, Y. Xie, W. Li, R. Lupoi, Formation conditions of vortex-like intermixing interfaces in cold spray, Materials & Design. 200 (2021) 109444. https://doi.org/10.1016/j.matdes.2020.109444.

[41] G. Bae, Y. Xiong, S. Kumar, K. Kang, C. Lee, General aspects of interface bonding in kinetic sprayed coatings, Acta Materialia. 56 (2008) 4858–4868. https://doi.org/10.1016/j.actamat.2008.06.003.

[42] R. Ortiz-Fernandez, S. Imbriglio, R. Chromik, B. Jodoin, The Role of Substrate Preheating on the Adhesion Strength of Cold-Sprayed Soft Particles on Hard Substrates, J Therm Spray Tech. (2021). https://doi.org/10.1007/s11666-020-01148-w.

[43] S.I. Imbriglio, N. Brodusch, M. Aghasibeig, R. Gauvin, R.R. Chromik, Influence of Substrate Characteristics on Single Ti Splat Bonding to Ceramic Substrates by Cold Spray, J Therm Spray Tech. 27 (2018) 1011–1024. https://doi.org/10.1007/s11666-018-0743-x.

[44] Y. Xie, C. Chen, M.-P. Planche, S. Deng, R. Huang, Z. Ren, H. Liao, Strengthened Peening Effect on Metallurgical Bonding Formation in Cold Spray Additive Manufacturing, J Therm Spray Tech. 28 (2019) 769–779. https://doi.org/10.1007/s11666-019-00854-4.

[45] S. Yin, X. Suo, Y. Xie, W. Li, R. Lupoi, H. Liao, Effect of substrate temperature on interfacial bonding for cold spray of Ni onto Cu, J Mater Sci. 50 (2015) 7448–7457. https://doi.org/10.1007/s10853-015-9304-6.

[46] N. Bay, Mechanisms Producing Metallic Bonds in Cold Welding, Weld. J. 62 (n.d.) 137.

[47] D. Goldbaum, J.M. Shockley, R.R. Chromik, A. Rezaeian, S. Yue, J.-G. Legoux, E. Irissou, The Effect of Deposition Conditions on Adhesion Strength of Ti and Ti6Al4V Cold Spray Splats, J Therm Spray Tech. 21 (2012) 288–303. https://doi.org/10.1007/s11666-011-9720-3.

[48] S. Yin, X. Suo, Z. Guo, H. Liao, X. Wang, Deposition features of cold sprayed copper particles on preheated substrate, Surface and Coatings Technology. 268 (2015) 252–256. https://doi.org/10.1016/j.surfcoat.2014.11.009.

[49] K.-R. Ernst, J. Braeutigam, F. Gaertner, T. Klassen, Effect of Substrate Temperature on Cold-Gas-Sprayed Coatings on Ceramic Substrates, J Therm Spray Tech. 22 (2013) 422–432. https://doi.org/10.1007/s11666-012-9871-x.

[50] M. Bray, A. Cockburn, W. O'Neill, The Laser-assisted Cold Spray process and deposit characterisation, Surface and Coatings Technology. 203 (2009) 2851–2857. https://doi.org/10.1016/j.surfcoat.2009.02.135.

[51] J. Yao, L. Yang, B. Li, Z. Li, Beneficial effects of laser irradiation on the deposition process of diamond/Ni60 composite coating with cold spray, Applied Surface Science. 330 (2015) 300–308. https://doi.org/10.1016/j.apsusc.2015.01.029.

[52] M. Kulmala, P. Vuoristo, Influence of process conditions in laser-assisted low-pressure cold spraying, Surface and Coatings Technology. 202 (2008) 4503–4508. https://doi.org/10.1016/j.surfcoat.2008.04.034.

[53] D.K. Christoulis, S. Guetta, E. Irissou, V. Guipont, M.H. Berger, M. Jeandin, J.-G. Legoux, C. Moreau, S. Costil, M. Boustie, Y. Ichikawa, K. Ogawa, Cold-Spraying Coupled

to Nano-Pulsed Nd-YaG Laser Surface Pre-treatment, J Therm Spray Tech. 19 (2010) 1062–1073. https://doi.org/10.1007/s11666-010-9500-5.

[54] A. List, F. Gärtner, T. Schmidt, T. Klassen, Impact Conditions for Cold Spraying of Hard Metallic Glasses, J Therm Spray Tech. 21 (2012) 531–540. https://doi.org/10.1007/s11666-012-9750-5.

[55] J.G. Legoux, E. Irissou, C. Moreau, Effect of Substrate Temperature on the Formation Mechanism of Cold-Sprayed Aluminum, Zinc and Tin Coatings, J Therm Spray Tech. 16 (2007) 619–626. https://doi.org/10.1007/s11666-007-9091-y.

[56] X.K. Suo, M. Yu, W.Y. Li, M.P. Planche, H.L. Liao, Effect of Substrate Preheating on Bonding Strength of Cold-Sprayed Mg Coatings, J Therm Spray Tech. 21 (2012) 1091–1098. https://doi.org/10.1007/s11666-012-9803-9.

[57] Y. Xie, M.-P. Planche, R. Raoelison, H. Liao, X. Suo, P. Hervé, Effect of Substrate Preheating on Adhesive Strength of SS 316L Cold Spray Coatings, J Therm Spray Tech. 25 (2016) 123–130. https://doi.org/10.1007/s11666-015-0312-5.

[58] R. Drehmann, T. Grund, T. Lampke, B. Wielage, K. Manygoats, T. Schucknecht, D. Rafaja, Splat Formation and Adhesion Mechanisms of Cold Gas-Sprayed Al Coatings on Al2O3 Substrates, J Therm Spray Tech. 23 (2014) 68–75. https://doi.org/10.1007/s11666-013-9966-z.

[59] R. Drehmann, T. Grund, T. Lampke, B. Wielage, C. Wüstefeld, M. Motylenko, D. Rafaja, Essential Factors Influencing the Bonding Strength of Cold-Sprayed Aluminum Coatings on Ceramic Substrates, J Therm Spray Tech. 27 (2018) 446–455. https://doi.org/10.1007/s11666-018-0688-0.

[60] D.J. Barton, V.S. Bhattiprolu, G.B. Thompson, L.N. Brewer, Laser assisted cold spray of AISI 4340 steel, Surface and Coatings Technology. 400 (2020) 126218. https://doi.org/10.1016/j.surfcoat.2020.126218.

[61] D.J. Barton, V.S. Bhattiprolu, B.C. Hornbuckle, C.M. Batali, K.A. Darling, G.B. Thompson, L.N. Brewer, Residual Stress Generation in Laser-Assisted Cold Spray Deposition of Oxide Dispersion Strengthened Fe91Ni8Zr1, J Therm Spray Tech. 29 (2020) 1550–1563. https://doi.org/10.1007/s11666-020-01079-6.

[62] D.J. Barton, B.C. Hornbuckle, K.A. Darling, L.N. Brewer, G.B. Thompson, Influence of surface temperature in the laser assisted cold spray deposition of sequential oxide dispersion strengthened layers: Microstructure and hardness, Materials Science and Engineering: A. 811 (2021) 141027. https://doi.org/10.1016/j.msea.2021.141027.

[63] A. Nastic, B. Jodoin, Evaluation of Heat Transfer Transport Coefficient for Cold Spray Through Computational Fluid Dynamics and Particle In-Flight Temperature Measurement Using a High-Speed IR Camera, Journal of Thermal Spray Technology. 27 (2018) 1491–1517. https://doi.org/10.1007/s11666-018-0787-y.

[64] S. Yin, X. Wang, X. Suo, H. Liao, Z. Guo, W. Li, C. Coddet, Deposition behavior of thermally softened copper particles in cold spraying, Acta Materialia. 61 (2013) 5105–5118. https://doi.org/10.1016/j.actamat.2013.04.041.

[65] W.-Y. Li, H. Liao, G. Douchy, C. Coddet, Optimal design of a cold spray nozzle by numerical analysis of particle velocity and experimental validation with 316L stainless steel powder, Materials & Design. 28 (2007) 2129–2137. https://doi.org/10.1016/j.matdes.2006.05.016.

[66] Y. Xie, M.-P. Planche, R. Raoelison, P. Hervé, X. Suo, P. He, H. Liao, Investigation on the influence of particle preheating temperature on bonding of cold-sprayed nickel coatings, Surface and Coatings Technology. 318 (2017) 99–105. https://doi.org/10.1016/j.surfcoat.2016.09.037.

[67] C.W. Ziemian, W.J. Wright, D.E. Cipoletti, Influence of Impact Conditions on Feedstock Deposition Behavior of Cold-Sprayed Fe-Based Metallic Glass, J Therm Spray Tech. 27 (2018) 843–856. https://doi.org/10.1007/s11666-018-0720-4.

[68] A. Sova, S. Grigoriev, A. Kochetkova, I. Smurov, Influence of powder injection point position on efficiency of powder preheating in cold spray: Numerical study, Surface and Coatings Technology. 242 (2014) 226–231. https://doi.org/10.1016/j.surfcoat.2013.10.078.

[69] H.-J. Kim, C.-H. Lee, S.-Y. Hwang, Fabrication of WC–Co coatings by cold spray deposition, Surface and Coatings Technology. 191 (2005) 335–340. https://doi.org/10.1016/j.surfcoat.2004.04.058.

[70] G. Mauer, R. Singh, K.-H. Rauwald, S. Schrüfer, S. Wilson, R. Vaßen, Diagnostics of Cold-Sprayed Particle Velocities Approaching Critical Deposition Conditions, J Therm Spray Tech. 26 (2017) 1423–1433. https://doi.org/10.1007/s11666-017-0596-8.

[71] Y. Hao, J. Wang, X. Cui, J. Wu, T. Li, T. Xiong, Microstructure Characteristics and Mechanical Properties of Al-12Si Coatings on AZ31 Magnesium Alloy Produced by Cold Spray Technique, J Therm Spray Tech. 25 (2016) 1020–1028. https://doi.org/10.1007/s11666-016-0409-5.

[72] D.L. Guo, D. MacDonald, L. Zhao, B. Jodoin, Cold Spray MCrAlY Coatings on Single-Crystal Superalloy Using Nitrogen: Properties and Economics, J Therm Spray Tech. (2020). https://doi.org/10.1007/s11666-020-01058-x.

[73] M. Peters, J. Hemptenmacher, J. Kumpfert, C. Leyens, Structure and Properties of Titanium and Titanium Alloys, in: C. Leyens, M. Peters (Eds.), Titanium and Titanium Alloys, Wiley-VCH Verlag GmbH & Co. KGaA, Weinheim, FRG, 2005: pp. 1–36. https://doi.org/10.1002/3527602119.ch1.

[74] H. Guleryuz, H. Cimenoglu, Oxidation of Ti–6Al–4V alloy, Journal of Alloys and Compounds. 472 (2009) 241–246. https://doi.org/10.1016/j.jallcom.2008.04.024.

[75] F.J.J. van Loo, G.D. Rieck, Diffusion in the titanium-aluminium system—I. Interdiffusion between solid Al and Ti or Ti-Al alloys, Acta Metallurgica. 21 (1973) 61–71. https://doi.org/10.1016/0001-6160(73)90220-4.

[76] W.D. Callister, D.G. Rethwisch, Fundamentals of materials science and engineering: an integrated approach, 2019.

[77] W.B. Choi, L. Li, V. Luzin, R. Neiser, T. Gnäupel-Herold, H.J. Prask, S. Sampath, A. Gouldstone, Integrated characterization of cold sprayed aluminum coatings, Acta Materialia. 55 (2007) 857–866. https://doi.org/10.1016/j.actamat.2006.09.006.

[78] K. Ogawa, K. Ito, K. Ichimura, Y. Ichikawa, S. Ohno, N. Onda, Characterization of Low-Pressure Cold-Sprayed Aluminum Coatings, J Therm Spray Tech. 17 (2008) 728–735. https://doi.org/10.1007/s11666-008-9254-5.

[79] A. Sova, I. Smurov, M. Doubenskaia, P. Petrovskiy, Deposition of aluminum powder by cold spray micronozzle, Int J Adv Manuf Technol. 95 (2018) 3745–3752. https://doi.org/10.1007/s00170-017-1443-2.

[80] A.C. Hall, D.J. Cook, R.A. Neiser, T.J. Roemer, D.A. Hirschfeld, The Effect of a Simple Annealing Heat Treatment on the Mechanical Properties of Cold-Sprayed Aluminum, Journal of Thermal Spray Technology. 15 (2006) 233–238. https://doi.org/10.1361/105996306X108138.

[81] H. Bu, M. Yandouzi, C. Lu, B. Jodoin, Effect of heat treatment on the intermetallic layer of cold sprayed aluminum coatings on magnesium alloy, Surface and Coatings Technology. 205 (2011) 4665–4671. https://doi.org/10.1016/j.surfcoat.2011.04.018.

[82] M.M. Sharma, T.J. Eden, B.T. Golesich, Effect of Surface Preparation on the Microstructure, Adhesion, and Tensile Properties of Cold-Sprayed Aluminum Coatings on AA2024 Substrates, J Therm Spray Tech. 24 (2015) 410–422. https://doi.org/10.1007/s11666-014-0175-1.

[83] Z. Zhang, D.H.L. Seng, M. Lin, S.L. Teo, T.L. Meng, C.J.J. Lee, Z.-Q. Zhang, T. Ba, J. Guo, K. Sundaravadivelu, P.K. Aw, J. Pan, Cold spray deposition of Inconel 718 in

comparison with atmospheric plasma spray deposition, Applied Surface Science. 535 (2021) 147704. https://doi.org/10.1016/j.apsusc.2020.147704.

[84] L.I. Pérez-Andrade, F. Gärtner, M. Villa-Vidaller, T. Klassen, J. Muñoz-Saldaña, J.M. Alvarado-Orozco, Optimization of Inconel 718 thick deposits by cold spray processing and annealing, Surface and Coatings Technology. 378 (2019) 124997. https://doi.org/10.1016/j.surfcoat.2019.124997.

[85] W. Sun, A. Bhowmik, A.W.-Y. Tan, R. Li, F. Xue, I. Marinescu, E. Liu, Improving microstructural and mechanical characteristics of cold-sprayed Inconel 718 deposits via local induction heat treatment, Journal of Alloys and Compounds. 797 (2019) 1268–1279. https://doi.org/10.1016/j.jallcom.2019.05.099.

[86] D. Levasseur, S. Yue, M. Brochu, Pressureless sintering of cold sprayed Inconel 718 deposit, Materials Science and Engineering: A. 556 (2012) 343–350. https://doi.org/10.1016/j.msea.2012.06.097.

[87] W. Wong, E. Irissou, P. Vo, M. Sone, F. Bernier, J.-G. Legoux, H. Fukanuma, S. Yue, Cold Spray Forming of Inconel 718, J Therm Spray Tech. 22 (2013) 413–421. https://doi.org/10.1007/s11666-012-9827-1.

[88] R. Singh, K.-H. Rauwald, E. Wessel, G. Mauer, S. Schruefer, A. Barth, S. Wilson, R. Vassen, Effects of substrate roughness and spray-angle on deposition behavior of cold-sprayed Inconel 718, Surface and Coatings Technology. 319 (2017) 249–259. https://doi.org/10.1016/j.surfcoat.2017.03.072.

[89] R. Singh, S. Schruefer, S. Wilson, J. Gibmeier, R. Vassen, Influence of coating thickness on residual stress and adhesion-strength of cold-sprayed Inconel 718 coatings, Surface and Coatings Technology. 350 (2018) 64–73. https://doi.org/10.1016/j.surfcoat.2018.06.080.

[90] S. Bagherifard, G. Roscioli, M.V. Zuccoli, M. Hadi, G. D'Elia, A.G. Demir, B. Previtali, J. Kondás, M. Guagliano, Cold Spray Deposition of Freestanding Inconel Samples and Comparative Analysis with Selective Laser Melting, J Therm Spray Tech. 26 (2017) 1517–1526. https://doi.org/10.1007/s11666-017-0572-3.

[91] R. Vaßen, J. Fiebig, T. Kalfhaus, J. Gibmeier, A. Kostka, S. Schrüfer, Correlation of Microstructure and Properties of Cold Gas Sprayed INCONEL 718 Coatings, J Therm Spray Tech. (2020). https://doi.org/10.1007/s11666-020-00988-w.

[92] W. Ma, Y. Xie, C. Chen, H. Fukanuma, J. Wang, Z. Ren, R. Huang, Microstructural and mechanical properties of high-performance Inconel 718 alloy by cold spraying, Journal of Alloys and Compounds. 792 (2019) 456–467. https://doi.org/10.1016/j.jallcom.2019.04.045.

[93] S.Y. Kim, V. Luzin, M.L. Sesso, J. Thornton, S. Gulizia, The Effect of Low Temperature Range Heat Treatment on the Residual Stress of Cold Gas Dynamic Sprayed Inconel 718 Coatings via Neutron Diffraction, J Therm Spray Tech. 29 (2020) 1477–1497. https://doi.org/10.1007/s11666-020-01080-z.

[94] L. Perez, J. Colburn, L.N. Brewer, M. Renfro, T. McKechnie, Cold Spray Deposition of Heat-Treated Inconel 718 Powders, in: F. Azarmi, X. Chen, J. Cizek, C. Cojocaru, B. Jodoin, H. Koivuluoto, Y.C. Lau, R. Fernandez, O. Ozdemir, H. Salimi Jazi, F. Toma (Eds.), Virtual, 2021: pp. 171–176. https://doi.org/10.31399/asm.cp.itsc2021p0171.

[95] X.-T. Luo, M.-L. Yao, N. Ma, M. Takahashi, C.-J. Li, Deposition behavior, microstructure and mechanical properties of an in-situ micro-forging assisted cold spray enabled additively manufactured Inconel 718 alloy, Materials & Design. 155 (2018) 384–395. https://doi.org/10.1016/j.matdes.2018.06.024.

[96] M. Kazasidis, S. Yin, J. Cassidy, T. Volkov-Husović, M. Vlahović, S. Martinović, E. Kyriakopoulou, R. Lupoi, Microstructure and cavitation erosion performance of nickel-Inconel 718 composite coatings produced with cold spray, Surface and Coatings Technology. 382 (2020) 125195. https://doi.org/10.1016/j.surfcoat.2019.125195.

[97] W. Sun, A. Bhowmik, A.W.Y. Tan, F. Xue, I. Marinescu, F. Li, E. Liu, Strategy of incorporating Ni-based braze alloy in cold sprayed Inconel 718 coating, Surface and Coatings Technology. 358 (2019) 1006–1012. https://doi.org/10.1016/j.surfcoat.2018.12.050.

[98] W. Sun, A.W.-Y. Tan, D.J.Y. King, N.W. Khun, A. Bhowmik, I. Marinescu, E. Liu, Tribological behavior of cold sprayed Inconel 718 coatings at room and elevated temperatures, Surface and Coatings Technology. 385 (2020) 125386. https://doi.org/10.1016/j.surfcoat.2020.125386.

[99] Special Metals, Inconel 718 Properties, n.d. https://www.specialmetals.com/documents/technical-bulletins/inconel/inconel-alloy-718.pdf (accessed July 28, 2020).

[100] R.C. Reed, The Superalloys: Fundamentals and Applications, Cambridge University Press, Cambridge, 2006. https://doi.org/10.1017/CBO9780511541285.

[101] E. Akca, A. Gürsel, A Review on Superalloys and IN718 Nickel-Based INCONEL Superalloy, PEN. 3 (2015). https://doi.org/10.21533/pen.v3i1.43.

[102] T.M. Pollock, S. Tin, Nickel-Based Superalloys for Advanced Turbine Engines: Chemistry, Microstructure and Properties, Journal of Propulsion and Power. 22 (2006) 361–374. https://doi.org/10.2514/1.18239.

[103] R.E. Haimbaugh, Practical Induction Heat Treating, ASM International, United States, 2001.

[104] V. Rudnev, D. Loveless, R.L. Cook, Handbook of Induction Heating, CRC Press, United States, 2017. https://doi.org/10.1201/9781420028904.

[105] R.K. Wangsness, Electromagnetic fields, 2nd ed, Wiley, New York, 1986.

[106] J. Davies, Conduction and induction heating, P. Peregrinus Ltd. on behalf of the Institution of Electrical Engineers, London, U.K, 1990.

[107] S. Zinn, S.L. Semiatin, Elements of induction heating: design, control, and applications, ASM International, Metals Park, Ohio, 1988.

[108] N. Bowler, Eddy-current nondestructive evaluation, Springer, New York, NY, 2019.

[109] A.A. Rodríguez, A. Valli, Eddy Current Approximation of Maxwell Equations, Springer Milan, Milano, 2010. https://doi.org/10.1007/978-88-470-1506-7.

[110] Cenos, Induction Heat Treatment & Role Of Simulation Software, n.d. https://www.cenos-platform.com/post/induction-heat-treatment-role-of-simulation-software (accessed August 4, 2022).

[111] E.A. Olevsky, D.V. Dudina, Field-Assisted Sintering: Science and Applications, Springer International Publishing, Cham, 2018. https://doi.org/10.1007/978-3-319-76032-2.

[112] H.A. Jaffery, M.F. Mohd Sabri, S. Rozali, M.H. Mahdavifard, D.A. Shnawah, Effect of temperature and alloying elements (Fe and Bi) on the electrical resistivity of Sn–0.7Cu solder alloy, RSC Adv. 6 (2016) 58010–58019. https://doi.org/10.1039/C6RA08706J.

[113] C.Y. Ho, M.W. Ackerman, K.Y. Wu, T.N. Havill, R.H. Bogaard, R.A. Matula, S.G. Oh, H.M. James, Electrical Resistivity of Ten Selected Binary Alloy Systems, Journal of Physical and Chemical Reference Data. 12 (1983) 183–322. https://doi.org/10.1063/1.555684.

[114] S. Suzuki, N. Shibutani, K. Mimura, M. Isshiki, Y. Waseda, Improvement in strength and electrical conductivity of Cu–Ni–Si alloys by aging and cold rolling, Journal of Alloys and Compounds. 417 (2006) 116–120. https://doi.org/10.1016/j.jallcom.2005.09.037.

[115] R.H. Pry, R.W. Hennig, On the use of electrical resistivity as a measure of plastic deformation in copper, Acta Metallurgica. 2 (1954) 318–321. https://doi.org/10.1016/0001-6160(54)90174-1.

[116] Y. Miyajima, S.-Y. Komatsu, M. Mitsuhara, S. Hata, H. Nakashima, N. Tsuji, Change in electrical resistivity of commercial purity aluminium severely plastic deformed, Philosophical Magazine. 90 (2010) 4475–4488. https://doi.org/10.1080/14786435.2010.510453.

[117] J. Huang, X. Yan, C. Chang, Y. Xie, W. Ma, R. Huang, R. Zhao, S. Li, M. Liu, H. Liao, Pure copper components fabricated by cold spray (CS) and selective laser melting (SLM) technology, Surface and Coatings Technology. 395 (2020) 125936. https://doi.org/10.1016/j.surfcoat.2020.125936.

[118] P. Sudharshan Phani, D. Srinivasa Rao, S.V. Joshi, G. Sundararajan, Effect of Process Parameters and Heat Treatments on Properties of Cold Sprayed Copper Coatings, J Therm Spray Tech. 16 (2007) 425–434. https://doi.org/10.1007/s11666-007-9048-1.

[119] P.V. Andrews, M.B. West, C.R. Robeson, The effect of grain boundaries on the electrical resistivity of polycrystalline copper and aluminium, Philosophical Magazine. 19 (1969) 887–898. https://doi.org/10.1080/14786436908225855.

[120] H. Zeng, Y. Wu, J. Zhang, C. Kuang, M. Yue, S. Zhou, Grain size-dependent electrical resistivity of bulk nanocrystalline Gd metals, Progress in Natural Science: Materials International. 23 (2013) 18–22. https://doi.org/10.1016/j.pnsc.2013.01.003.

[121] P. Coddet, C. Verdy, C. Coddet, F. Debray, On the mechanical and electrical properties of copper-silver and copper-silver-zirconium alloys deposits manufactured by cold spray, Materials Science and Engineering: A. 662 (2016) 72–79. https://doi.org/10.1016/j.msea.2016.03.049.

[122] W.-Y. Li, C.-J. Li, H. Liao, Effect of Annealing Treatment on the Microstructure and Properties of Cold-Sprayed Cu Coating, Journal of Thermal Spray Technology. 15 (2006) 206–211. https://doi.org/10.1361/105996306X108066.

[123] T. Zedler, A. Nikanorov, Investigation of relative magnetic permeability as input data for numerical simulation of induction surface hardening, in: Modelling for Electromagnetic Processing, 2008.

[124] G.L. Ferreira-Fraga, L.A. Borba, P. Pureur, Impedance and initial magnetic permeability of the Heusler compounds Pd 2 MnSn and Pd 2 MnSb near the Curie temperature, Phys. Rev. B. 74 (2006) 064427. https://doi.org/10.1103/PhysRevB.74.064427.

[125] N. Bowler, Frequency-Dependence of Relative Permeability in Steel, in: AIP Conference Proceedings, AIP, Brunswick, Maine (USA), 2006: pp. 1269–1276. https://doi.org/10.1063/1.2184670.

[126] Z. Arabgol, M. Villa Vidaller, H. Assadi, F. Gärtner, T. Klassen, Influence of thermal properties and temperature of substrate on the quality of cold-sprayed deposits, Acta Materialia. 127 (2017) 287–301. https://doi.org/10.1016/j.actamat.2017.01.040.

[127] M. Razavipour, J.-G. Legoux, D. Poirier, B. Guerreiro, J.D. Giallonardo, B. Jodoin, Artificial Neural Networks Approach for Hardness Prediction of Copper Cold Spray Laser Heat Treated Coatings, J Therm Spray Tech. 31 (2022) 525–544. https://doi.org/10.1007/s11666-021-01311-x.

[128] D. MacDonald, R. Fernández, F. Delloro, B. Jodoin, Cold Spraying of Armstrong Process Titanium Powder for Additive Manufacturing, J Therm Spray Tech. 26 (2017) 598–609. https://doi.org/10.1007/s11666-016-0489-2.

[129] S. Yin, M. Meyer, W. Li, H. Liao, R. Lupoi, Gas Flow, Particle Acceleration, and Heat Transfer in Cold Spray: A review, J Therm Spray Tech. 25 (2016) 874–896. https://doi.org/10.1007/s11666-016-0406-8.

[130] R. Ortiz-Fernandez, B. Jodoin, Hybrid Additive Manufacturing Technology: Induction Heating Cold Spray—Part II: Coating Mechanical Properties, J Therm Spray Tech. 29 (2020) 700–713. https://doi.org/10.1007/s11666-020-01006-9.